The Cycle of Gaseous Baryons Between the Disk and Halo

Yong Zheng

Submitted in partial fulfillment of the
requirements for the degree
of Doctor of Philosophy
in the Graduate School of Arts and Sciences

COLUMBIA UNIVERSITY

2018

ABSTRACT

The Cycle of Gaseous Baryons Between the Disk and Halo

Yong Zheng

The gaseous halo surrounding a galaxy disk is often referred to as the circum-galactic medium (CGM). The boundary of the CGM is loosely defined as the virial radius of the galaxy. Recent observations and simulations have shown that the CGM is massive, multiphase, clumpy, and metal-enriched. The CGM plays an important role in galaxy formation and evolution – it serves as a massive baryonic reservoir, from which the disk accretes gas fuel to sustain the star-formation activities, and to which the disk deposits feedback material. This dissertation focuses on the gas distribution in the CGM of the Milky Way (MW) and the baryon cycle between the CGM and disk of our neighbor – the Triangulum Galaxy (M33).

Observations of the MW's CGM are unavoidably contaminated by foreground gas since we reside in the MW's disk. Conventionally, a velocity cut at $|v_{\rm LSR}| \sim 100$ km s^{-1} is used as a proxy for distance, with low-velocity ($|v_{\rm LSR}| \lesssim 100$ km s^{-1}) gas being more nearby to the Galactic disk than high-velocity gas. Using both a MW-mass simulation and all-sky QSO observations, I show that the low-velocity gas in the MW's CGM is as massive as their high-velocity counterpart, and that the MW most likely hosts a massive CGM reservoir as those $L \sim L^*$ galaxies at $z \sim 0.2$.

I further study how baryons are cycled between the disk and CGM by observing

gas accretion in M33. Using HST/COS to observe seven UV-bright stars in M33's disk, I find that there is a layer of metal-enriched inflow moving towards M33 at a rate of $\dot{M}_{\rm in} = 2.9 M_{\odot} {\rm yr}^{-1}$. The gas inflow may be related to galactic fountain process or debris falling back down due to the potential past M31-M33 interaction. This work is among the first to unambiguously reveal the existence of a disk-wide, ionized galactic inflow beyond the Milky Way. In addition, with the same set of HST/COS sightlines, I make a serendipitous discovery of an ionized very-high-velocity cloud towards M33.

Contents

List of Figures

List of Tables

ACKNOWLEDGMENTS

I feel extremely lucky to have both Mary Putman and Josh Peek as my thesis advisors. I started working with them in 2013 with a particular interest in Radio Astronomy. Over the years, they have not only taught me how single-dish observations work, but also equipped me with a broad skill set to go forward in academia. They gave me many opportunities to explore different projects, dragged me out of rabbit holes in time, instructed me how to interact with collaborators and colleagues, and patiently went through my papers and talk slides to improve my presentation skills. They set a role model for me of what a good scientist, advisor, mentor, collaborator, and colleague should be. Thank you, Mary and Josh, I would not have made it this far without your guidance.

I am very grateful to have Jess Werk as my major collaborator, mentor, and academic sibling. She led me through the complicated world of UV spectroscopy with hands-on experience, always keen to answer many of my questions, and gave me much career advice. I also want to thank many colleagues in the field, especially X. Prochaska, Jason Tumlinson, Hsiao-Wen Chen, Lia Corrales, Rongmon Bordoloi, Andrew Fox, Chris Howk, and Molly Peeples. My last year in graduate school was a big struggle. Their support and warm encouragement brought me to tears and gave me the courage to keep doing what I love to do.

Richard de Grijs first introduced me to the world of Astronomy when I was a junior in Peking University seeking for an undergrad project. He patiently taught me how to do research and encouraged me to pursue graduate study abroad. I really appreciate

his support and advice. I benefited a lot from Xiaowei Liu, who supervised my bachelor thesis. His harsh but precise lecturing style let me fascinate about spectral lines and atomic physics, which greatly influenced my research in later years. I also want to thank Maria McCormack at School of Professional Studies in Columbia, who patiently corrected many of my English pronunciation mistakes and improved my academic writing skills. I really enjoyed taking those language classes with her.

The Columbia Astronomy Department has given me the greatest opportunity to grow and mature into a junior scientist. I want to thank the faculty here for creating an encouraging and humble academic environment. In particular, I would like to thank David Schiminovich and Greg Bryan for being my committee members and for their insightful comments on all my projects. I want to thank Jacqueline van Gorkom and David Helfand for their meaningful conversations and career advice. I am also thankful to have Jennifer Sokoloski as my first-year research advisor. Since I was very interested in Radio Astronomy, she sent me to the VLA site at Socorro for a ten-week graduate intern, from which I gained much knowledge of radio interferometer.

New York is my first stop living abroad, at the beginning of which I felt pretty lost. The grads at Columbia helped me through that cultural-shock period, from whom I learned much English slang and social conventions. I want to particularly thank my lovely office mates in Pupin 207, where I spent most of my grad school time. Especially, thank you so much, Nicole Melso, Jorge Cortes, Kirsten Blancato, and Rose Gibson, for all the laughing, chatting, and complaining together. I miss those folks of my class, Susan Clark, Aleksey Generozov, Alejandro Nunez, and Stephanie Douglas, with whom I spent much

time together going through coursework and puzzling about grad school, academia, and random stuff.

I feel sincerely fortunate to be loved and supported by my friends and families. I want to thank Yingci Sun, who hear me and understand me deeply. I would like to thank Long Wang, Wei Chen, and Wen Li, who are always on my side and listen to my complaints patiently. I also want to send my heartfelt thanks to my wonderful brother, Yonghui Zheng, who takes over many family responsibilities since I am studying abroad.

My parents, Qintao Zheng and Xue Lin, have given me tremendous support over the years. They are hard-working, generous to their families and friends, and trustworthy to their co-workers. They are the kind of person I want to grow up to be. They let me grow freely without pressure, and always told me to "do whatever you want as long as you are happy". I could not wish for better words. Thank you for your unconditional support and trust.

Yong Zheng

Manhattan, New York

Chapter 1

Introduction

The circum-galactic medium (CGM) is a large volume of plasma surrounding a galaxy disk and is gravitationally bound to the galaxy. The study of CGM is critical in understanding galaxy formation and evolution. For star-forming galaxies, the disks thrive on baryonic inflows from the CGM, while the CGM is enriched and heated by outflows from the disks. For elliptical galaxies and dwarf irregulars, the CGM may also contain a considerable amount of baryons expelled from the hosts, shedding light on the evolution of the galaxies. This dissertation is dedicated to studying the properties of the CGM at $z = 0$ using both observations and simulations. In particular, I focus on studying the gas distribution in the CGM of the Milky Way (MW) as well as gas inflows in one of our neighbours – the Triangulum Galaxy (M33).

Recent years have seen great progress in understanding the CGM with various observational techniques, which will be briefly summarized in this chapter. I will first build a theoretical framework to define the CGM in terms of virial radius and virial mass (§ 1.1).

Then I will provide two arguments – the missing baryon problem and the gas consumption problem – to support the existence of the CGM (§ 1.2). Finally, I will elaborate on the CGM properties based on multi-wavelength studies in the literature (§1.3).

1.1 The CGM Extension, Virial Radius, and Virial Mass

A galaxy's gaseous CGM does not end abruptly. The CGM connects to the galaxy's disk and the surrounding intergalactic medium through inflows and outflows (see reviews by Putman et al. 2012; Somerville & Davé 2015; Tumlinson et al. 2017). Conventionally, the boundary of the CGM is loosely defined as the virial radius $R_{\rm vir}$ of the dark-matter halo. Here I derive $R_{\rm vir}$ and other related quantities of the CGM following the discussion in Binney & Tremaine (2008) and Shull (2014).

In a cosmological context, galaxies form when the density perturbations turn around from the Hubble expansion at $\bar{\rho} \gtrsim 5.55\bar{\rho}_m$ and collapse, where $\bar{\rho}_m$ is the mean matter density of the universe at the turn-around time. Once the galaxy halo reaches dynamical equilibrium, the whole system can be described by the virial theorem which states that the gravitational energy (U) of the system equals to twice its kinetic or thermal energy (E): $U = -2E$. The virial radius $R_{\rm vir}$ of the dark-matter halo is often approximated by the radius within which the mean halo density $\bar{\rho}_h$ is Δ_c times higher than the critical density

of the universe*:

$$\bar{\rho}_h = \Delta_{\rm c}\rho_{\rm crit}, \text{ and, } \Delta_{\rm c} = 200, \tag{1.1}$$

where $\rho_{\rm crit} \equiv 3H_0^2/8\pi G$, $H_0 = 67.8 {\rm kms}^{-1}{\rm Mpc}^{-1}$ is the present-day Hubble constant (Planck Collaboration et al. 2016) and G is the gravitational constant. The virial mass of the dark-matter halo can be calculated as:

$$M_{\rm h} = \frac{4\pi}{3} R_{\rm vir}^3 \bar{\rho}_h = \frac{4\pi}{3} R_{\rm vir}^3 \Delta_c \rho_{\rm crit}, \tag{1.2}$$

which in turn provides an estimate of the virial radius:

$$\begin{aligned} R_{\rm vir} &= (\tfrac{4\pi}{3})^{-1/3} M_h^{1/3} \Delta_{\rm c}^{-1/3} \rho_{\rm crit}^{-1/3} \\ &\approx (211 \text{ kpc}) (\tfrac{M_h}{10^{12}\, M_\odot})^{1/3} (\tfrac{\Delta_{\rm c}}{200})^{-1/3} (\tfrac{H_0}{67.8 \text{ km s}^{-1} \text{ Mpc}^{-1}})^{-2/3}. \end{aligned} \tag{1.3}$$

Observationally, the values of M_h are often inferred from galaxies' stellar masses or luminosities with the halo abundance matching technique, which assumes that the most massive (or luminous) galaxies are associated with the most massive halos monotonically (e.g., Behroozi et al. 2010). Note that here $R_{\rm vir}$ is calculated with present-day values of Δ_c and H. For higher-redshift dark-matter halos, Shull (2014) solved for an analytical expression of $R_{\rm vir}(z)$ by taking into account the evolution of the over-density $\Delta_c(z)$† and

*Note that in some literature $R_{\rm vir}$ is differently defined. It is related to the mean matter density $\bar{\rho}_m$ as $\bar{\rho}_h = \Delta\bar{\rho}_m = \Delta_m \Omega_m \rho_{\rm crit}$ (e.g. Klypin et al. 2011; van der Marel et al. 2012; Shull 2014; Bland-Hawthorn & Gerhard 2016); these authors adopted a value of $\Delta_m = 340 - 360$. If adopting this definition, the virial radius $R_{\rm vir}$ derived in Eq. (1.3) will be increased by a factor of $[\Delta_c/(\Delta_m\Omega_m)]^{1/3} \approx 1.25$. Therefore, for a dark-matter halo with mass of $M_h \approx 10^{12}\, M_\odot$, its virial radius is $R_{\rm vir} \sim 260$ kpc.

†Bryan & Norman (1998) provided an approximate solution for $\Delta_c(z)$ in a flat ΛCGM cosmology with curvature $\Omega_k = 0$ as $\Delta_c(z) \equiv \rho(z)/\rho_{\rm crit} = 18\pi^2 + 82x - 39x^2$, where $x = \Omega_m(z) - 1$ and $\Omega_m \equiv \rho_m/\rho_{crit}$ is the matter density parameter.

the Hubble constant $H(z)$[‡].

We can also derive the virial temperature of the dark-matter halo using the virial theorem. For a spherical volume with a homogeneous density distribution $\rho(r)$ inside $R_{\rm vir}$, the potential energy of the system is

$$U = -4\pi G \int_0^{R_{\rm vir}} r\rho(r)M(r)dr = -\frac{3}{5}\frac{GM_h^2}{R_{\rm vir}}, \tag{1.4}$$

following the derivation in Chapter 2 in Binney & Tremaine (2008). Assuming that the CGM consists of monatomic gas, the ideal gas law shows that the kinetic energy of the system is

$$E = \frac{1}{2}M_h\bar{v^2} = \frac{M_h}{\mu m_p}\frac{3}{2}k_B T, \tag{1.5}$$

where $\mu = 0.59$ for completely ionized gas assuming a primordial composition of $X = 0.75, Y = 0.25, Z = 0$, and X is the mass fraction of hydrogen, Y for helium, and Z for other elements heavier than helium. Combining Eq. (1.4) and (1.5) and applying the virial theorem, $2E + U = 0$, we have

$$\begin{aligned} T_{\rm vir} &= \tfrac{\mu m_p}{5k_B}\tfrac{GM_h}{R_{\rm vir}} \\ &\approx (10^{5.4}\ {\rm K})(\tfrac{\mu}{0.59})(\tfrac{M_{\rm h}}{10^{12}\ M_\odot})(\tfrac{R_{\rm vir}}{211{\rm kpc}})^{-1}. \end{aligned} \tag{1.6}$$

Note that we assume the gas is isothermal with $T(r) = T =$ constant, which may not

[‡]The Hubble constant is related to the present-day value as $H(z) = H_0(\Omega_m a^{-3} + \Omega_{\rm rad}a^{-4} + \Omega_k a^{-1} + \Omega_{\Lambda,0})^{1/2} \approx H_0(\Omega_m a^{-3} + \Omega_\Lambda)^{1/2}$, where $a = 1/(1+z)$ is the scale factor. The four Ω_x in the equation are dimensionless present-day density parameters with $\Omega_x \equiv \rho_x(t = t0)/\rho_{\rm crit}$, where x represents m for matter, *rad* for radiation, Λ for dark energy, and k for curvature. The matter density parameter Ω_m can be further divided into two terms: $\Omega_m = \Omega_{\rm DM} + \Omega_b$, where $\Omega_{\rm DM}$ is for dark matter and Ω_b for baryon. The Planck 2015 results for cosmology parameters give $\Omega_m = 0.3089$, $\Omega_\Lambda = 0.6911$, $\Omega_b = 0.0486$, and $\Omega_k = 0.000 \pm 0.005$.

be practical since the CGM has been found to be multiphase in both observations and simulations (See § 1.3 for more discussion on multi-wavelength observations of CGM). However, the practice in Eq. (1.3) and (1.6) to derive $R_{\rm vir}$ and $T_{\rm vir}$ provides an order of magnitude estimate on the CGM properties, which is helpful to set the anchor for the following discussion on various CGM observations.

1.2 Why Should the CGM Exist?

Two arguments are often used to support the existence of the CGM and its importance in galaxy formation. One is the missing baryon problem, which states that the total baryonic mass found in collapsed forms (galaxies, clusters, and groups) is less than 50% the amount predicted by the Lambda CDM cosmology (Fukugita et al. 1998; Shull et al. 2012; Tumlinson et al. 2017). The other is the gas consumption problem, which indicates that star-forming galaxies would run out of gas fuel in a few Gyrs should the star formation activities keep going at current rates without gas replenishment. Both arguments regard the CGM as a massive baryonic reservoir that connects the stellar component of a galaxy to the large-scale cosmic web the galaxies are embedded in. Below I will briefly summarize these two arguments quantitatively. Other arguments supporting the CGM existence can be found in Putman (2017) and Tumlinson et al. (2017).

1.2.1 The Missing Baryon Problem and the Observed Baryon Budget

The deficit of baryons occurs on both large scales and individual galaxy scales in the low-redshift universe (Persic & Salucci 1992; Fukugita et al. 1998; Shull et al. 2012). On large scales, the Planck 2015 results for cosmology parameters suggest the cosmic baryon density parameter is $\Omega_b \equiv \rho_b/\rho_{\rm crit} = 0.0486$. However, Persic & Salucci (1992) found that less than 10% of these baryons exist in the collapsed form of stars in galaxies ($\Omega_b^{\rm star} \sim 0.002$) and hot gas in groups and clusters ($\Omega_b^{\rm hot\ gas} \sim 0.001$). These values are consistent with those estimates by Fukugita et al. (1998), who found $\Omega_b^{\rm star} \sim 0.0019 - 0.0057$[§] for baryons in spheroid, disk and irregular galaxies, and $\Omega_b^{\rm cold\ gas} \sim 0.0005 - 0.0008$ in atomic and molecular gas. The remaining $\sim 90\%$ of baryons are suggested to exist in ionized form in the low-z intergalactic medium (Cen & Ostriker 1999; Bregman 2007; Shull 2014).

On individual galaxy scales, one should expect the total baryonic mass within the dark-matter halo to be $M_b \equiv \frac{\Omega_b}{\Omega_m} M_h \approx 0.16 M_h \approx 1.6 \times 10^{11}\ M_\odot (\frac{M_h}{10^{12}\ M_\odot})$ if baryons collapse together with the cold dark-matter during galaxy formation as predicted by ΛCDM. However, Behroozi et al. (2010) showed that only $10 - 20\%$ of the expected M_b are locked in stars by investigating the $M_* - M_h$ relation at $z < 4$ with the halo abundance matching technique[†]. For the cold gas component with H I and H_2, Peeples & Shankar (2011) parameterized the gas fraction $F_g \equiv M_g/M_*$ as a function of stellar mass M_* with a power-law fit: $\log F_g \approx 5.5 - 0.57 \log(M_*/\ M_\odot)$ (see their figure 2 and table 3), which is derived by considering the H I and H_2 measurements of nearby galaxies at $z \sim 0$ by McGaugh (2005),

[§]Sum of line 1-3 in table 3 in Fukugita et al. (1998). The range is from the minimum/maximum values.

[†]See equation (21) and table 2 in Behroozi et al. (2010) for an analytical expression of the $M_* - M_h$ relation as a function of redshift based on the halo abundance matching technique.

Leroy et al. (2008), and Garcia-Appadoo et al. (2009). For a galaxy with $\log(M_*/M_\odot) = 10.5$, the cold gas mass is $F_g = 10^{5.5-0.57*10.5} \sim 33\%$ of the total stellar mass M_*, or $\sim 5\%$[‡] of the expected baryonic mass M_b. Therefore, the stellar and gas components together only contribute $\lesssim 25\%$ to the expected value.

So far the best-known budget of the baryon distribution in galaxies is from the observations of our own MW. In Table 1.1, I provide a summary of the Galactic baryon mass in various stellar and cold gas forms; readers interested in more details than the provided values can find discussion in Putman et al. (2012) and Bland-Hawthorn & Gerhard (2016). For the total stellar mass of the MW, Bland-Hawthorn & Gerhard (2016) suggested a value of $M_*^{\rm MW} = (5 \pm 1) \times 10^{10}\ M_\odot$ or $\log(M_*^{\rm MW}/\ M_\odot) = 10.7$, which is roughly 28% of the expected baryonic mass. The total cold gas mass is $M_{\rm HI}^{\rm MW} \sim 4 \times 10^9\ M_\odot$ or $\log(M_{\rm HI}^{\rm MW}/\ M_\odot) = 9.6$, which contributes $\sim 2\%$ of baryons. The rest 70% of baryons is missing and is suggested to be in the surrounding CGM and IGM.

The arguments above suggest that $\sim 70-90\%$ of the baryons are not contained in stars and cold gas. They are most likely expelled from galaxies via outflows and reside in the CGM and IGM in the form of ionized gas at various phases. In recent years, researchers have made great progress in detecting the missing baryons in multiple phases in the CGM and IGM, which I will summarize in § 1.3.

[‡]i.e., $33\% \times (10 - 20\%) \sim 5\%$

Table 1.1: Milky Way Baryon Budget for Stellar and Cold Gas Components

Component	Mass ($M_\odot$)	Baryon Fraction $f_b \equiv M_x/M_b$ [†]	Reference
DM halo mass M_h (M_{200})	$(1.1 \pm 0.3) \times 10^{12}\ M_\odot$	-	1
Expected baryon mass ($M_b \equiv \frac{\Omega_b}{\Omega_m} M_h$)	$\sim 1.8 \times 10^{11}$	100%	2
Observed Stellar Mass			
Thin Disk	$(3.5 \pm 1) \times 10^{10}$	$\sim 19.4\%$	3
Thick Disk	$(6 \pm 3) \times 10^{9}$	$\sim 3.3\%$	3
Bulge	$(1.4 - 1.7) \times 10^{10}$	$\sim 8.6\%$	4
Stellar Halo	$(4 - 7) \times 10^{8}$	$\sim 0.3\%$	5
Total Stellar Mass	$\mathbf{(5 \pm 1) \times 10^{10}}$	$\mathbf{\sim 27.8\%}$	6
Observed Cold Gas Mass			
H I-Disk	$\sim 3 \times 10^{9}$	$\sim 1.7\%$	7
H I-HVC	$\sim 2.6 \times 10^{7}$	$\sim 0.014\%$	8
H I-LMC/SMC	$\sim 7 \times 10^{8}$	$\sim 0.39\%$	9
H I-MS	$\sim 3 \times 10^{8}$	$\sim 0.17\%$	10
Total H I Mass	$\mathbf{\sim 4 \times 10^{9}}$	$\mathbf{\sim 2.2\%}$	11

[†] x represents the component in each entry, such as the thin disk, stellar halo, and H I-HVC. Note that the calculated f_b will vary if a different M_h value is adopted.

[1] The average Galaxy mass M_{200} from Table 8 of Bland-Hawthorn & Gerhard (2016).

[2] See §1.1. $\Omega_b = 0.0486$ and $\Omega_m = 0.3089$ are the present-day baryon and matter density parameter from Planck 2015 results, respectively.

[3] See Bland-Hawthorn & Gerhard (2016), page 570.

[4] See Bland-Hawthorn & Gerhard (2016), page 551.

[5] See Bland-Hawthorn & Gerhard (2016), page 575.

[6] See Bland-Hawthorn & Gerhard (2016), page 583. Total mass in the MW's thin disk, thick disk, bulge, and stellar halo.

[7] From Table 1.2 in Draine (2011).

[8] See Putman et al. (2012), page 499. A majority of the mass in HVC is contributed by 13 large HVC complexes with known distances, while the remaining small cloud mass are estimated with an assumed distance of 10 kpc.

[9] See Putman et al. (2012), page 499.

[10] See Putman et al. (2012), page 499. The Magellanic Stream mass is calculated with a distance of 55 kpc.

[11] Total H I mass in the MW's disk, HVC, LMC/SMC, and MS.

Abbreviation: DM - Dark Matter; HVC - High Velocity Cloud; MS - Magellanic Stream; LMC - Large Magellanic Cloud; SMC - Small Magellanic Cloud.

1.2.2 The Gas Consumption Problem

The gas consumption problem addresses the importance of the CGM from a different aspect that focuses on star-forming galaxies. Conventionally, the star formation activities over galactic scales can be described by the gas depletion time scale: $\tau \equiv M_{\rm gas}/{\rm SFR}$, where $M_{\rm gas}$ is the total mass in H I and/or H_2 contained in the disk, and SFR is the star-formation rate. The reciprocal of τ, termed as the star-formation efficiency (SFE[†]), is also often used to quantify the star formation activities (e.g., Leroy et al. 2008). For example, the MW has an H I mass of $3 \times 10^9\ M_\odot$ (see Table 1.1) and SFR $\approx 1.9\ M_\odot {\rm yr}^{-1}$ (Chomiuk & Povich 2011), thus its gas depletion time scale is $\tau_{\rm MW} \sim 1.6$ Gyrs and ${\rm SFE}_{\rm MW} \sim 6 \times 10^{-10}\ {\rm yr}^{-1}$.

Low-mass galaxies tend to have higher gas depletion time scales and thus lower star-formation efficiencies than their high-mass counterparts, although the τ variation among different galaxy masses is only up to a few Gyrs. For example, Schiminovich et al. (2010) measured the H I mass, stellar mass, and SFRs for $\sim$ 190 nearby galaxies with $\log(M_*/M_\odot) > 10$, and found $\tau \sim 3$ Gyrs and SFE $\sim 10^{-9.5}\ {\rm yr}^{-1}$. Leroy et al. (2008) studied the SFE and gas depletion time scales in 23 nearby galaxies; the 11 dwarf galaxies [$\log(M_*/M_\odot) < 10$] in their sample have a median gas depletion timescale of ~ 7 Gyrs[‡]. In their review paper, Tumlinson et al. (2017) found $\tau \sim (4-8)$ Gyrs for galaxies with $\log(M_*/M_\odot) = 8.5$, $\sim (2-5)$ Gyrs at $\log(M_*/M_\odot) = 10.5$, and $\sim (1-3)$ Gyrs at $\log(M_*/M_\odot) = 11.5$ (see their figure 2).

[†]SFE can be defined in various ways, please see Leroy et al. (2008) for some discussion on SFE.

[‡]Note that Leroy et al. (2008) adopted a different definition SFE: SFE $\equiv \Sigma_{\rm SFR}/\Sigma_{\rm gas}$, where $\Sigma_{\rm SFR}$ is the star-formation rate surface density and $\Sigma_{\rm gas}$ is the H I+H_2 surface density. To keep the consistency, the ~ 7 Gyrs listed here is the median value computed from the ratios of $M_{\rm HI}$ to SFR for the 11 dwarf galaxies (from DDO154 to NGC0925) in their Table 4.

There may also exist a weak dependency of gas depletion time scale on redshift. Genzel et al. (2010) conducted a collective study of star-formation activities as a function of redshift by compiling a large sample of molecular data of normal star-forming galaxies from $z \sim 0$ (Kennicutt 1998; Leroy et al. 2008, 2009; Kuno et al. 2007) to $z \sim 1.0 - 3.5$ (e.g., Erb et al. 2006; Daddi et al. 2010; Tacconi et al. 2010; see § 2 in Genzel et al. 2010 for a full list of references). They found $\tau \sim 0.5$ Gyrs at $z \sim 2$ and ~ 1.5 Gyrs at $z \sim 0$. Note that here the τ value at $z \sim 0$ is not directly comparable to those estimates mentioned above (Schiminovich et al. 2010; Leroy et al. 2008; Tumlinson et al. 2017), since molecular gas mass instead of neutral hydrogen mass is used.

In all, the short Gyr-scale gas depletion time suggests that the ISM of spiral galaxies has to be replenished continuously to sustain the star-formation activities in the disks. The CGM surrounding the disks thus serves as a massive reservoir, from which the disks accrete gas fuel (i.e., inflows) and to which the disks expel post-star-formation material (i.e., outflows and feedback). Searching for signatures of inflows and outflows is a very active area of research (e.g., Heckman et al. 2000; Weiner et al. 2009; Martin et al. 2012; Rubin et al. 2012, 2014; Chisholm et al. 2016); various efforts are made to quantify inflow/outflow activities with respect to host galaxy properties, which provide insights into the question of how the CGM and disks interact with each other and how they mutualistically exist as the galaxies evolve.

1.3 CGM Observations with Different Tracers

Over the past couple of decades, our understanding of the CGM has rapidly evolved thanks to the development of observational and modeling techniques. Both ground-based (e.g., Keck and SDSS) and space telescopes (e.g., FUSE and HST) are used to study the CGM properties in various contexts, such as host-galaxy type, ionization state, density structure, and cloud populations. Simulations of galaxy formation and evolution explore the CGM properties on both large (e.g, kpc-Mpc) and small (pc-sub Kpc) scales, providing unique ways to study how the CGM and disks interact with each other through gas inflows and outflows.

So far, studies of the CGM have found that the CGM is massive in various phases, clumpy with density structures, rich in ionization states, and metal enriched. However, a complete picture of the CGM and its role in galaxy formation is yet to come, partially due to the limits in observational techniques, sample sizes, and the lack of self-consistent theories to incorporate all observational evidence. In this section I will briefly highlight some observations made with different tracers to illustrate the complexity of the CGM. Note that this is by no means an exhaustive list of the efforts that have been made to study the CGM, but it provides a general view of what can be done and what has been done. Readers interested in more detailed discussion on CGM observations and simulations should consult the review articles by Putman et al. (2012) on the MW's gaseous CGM, Somerville & Davé (2015) on cosmological simulations of galaxy formation, and Tumlinson et al. (2017) on CGM observations and techniques in extragalactic systems.

1.3.1 H I 21cm Emission

Hydrogen is the most abundant element in the universe. Neutral hydrogen (H I) is detectable in $\lambda \approx 21$ cm (or $\nu = 1.42$Gz) in emission due to the hyper-fine transition at its ground state. The three large blind H I surveys (LAB, HI4PI, GALFA-HI) reach an H I column density [N(H I)] limit of a few times 10^{18} cm^{-2} over 1 km s^{-1} at 1σ (Kalberla et al. 2005; HI4PI Collaboration et al. 2016; see Table 1 in Peek et al. 2018). And surveys with particular scientific goals[†] are designed to achieve different N(H I) limits of $\sim 10^{17-19}$ cm^{-2}. Due to the sensitivity limit of radio observations, H I 21cm emission is usually used to probe gas in the ISM, in the vicinity of galaxy disks within a few kpc, and in nearby satellite galaxies.

Our own MW provides the best place to study H I in its inner CGM. H I high-velocity clouds (HVCs) are found to be in configuration of large complexes (van Woerden et al. 2004; Wakker 2004) and small cloudlets (Saul et al. 2012) at a typical distance of ~ 10 kpc from the Galactic disk. The total mass of H I HVCs amounts to 2.6×10^7 $M_\odot$ (see Table 1.1). The Magellanic Stream spans $\sim 200^\circ \times 10^\circ$ over the Galactic sky and contributes 3×10^8 $M_\odot$ of H I assuming a distance of $\gtrsim 55$ kpc (Putman et al. 2003; Nidever et al. 2010). For satellite galaxies in the MW halo, most are found to be devoid of H I (Grcevich & Putman 2009; Spekkens et al. 2014); a few gas-rich satellite galaxies such as the Magellanic Clouds (LMC/SMC), contribute an H I mass of $\sim 7 \times 10^8$ $M_\odot$ (see Table 1.1).

[†]For instance, the CHILES survey is designed to create H I maps at a 1σ limit of N(H I)$\sim 5 \times 10^{19}$ cm^{-2} for galaxies at $z = 0 - 0.45$ to investigate H I properties as a function of redshift, galaxy mass, color, and environment (Fernández et al. 2013). The ALFALFA survey observes galaxies out to $z \sim 0.06$ to determine the faint end of the H I mass function at a sensitivity of N(H I)$\sim 1.6 \times 10^{18}$ cm^{-2} over 10 km s^{-1} at 6σ (Giovanelli et al. 2005). AGES aims at studying H I properties in different environment down to N(H I)$\sim 2 \times 10^{18}$ cm^{-2} over 50 km s^{-1} at 3σ (Auld et al. 2006). In the region near M33, AGES data reaches a limiting column density of 1.5×10^{17} cm^{-2} over 10 km s^{-1} at 1σ (Keenan et al. 2016).

For extragalactic systems, the detection of H I 21cm signal from neutral gas in the CGM is less common. Braun & Thilker (2004) found that M33 and M31 are possibly connected by an H I bridge at a 3σ detection limit of N(H I)= 1.5×10^{17} cm^{-2} over 30 km s^{-1}. This diffuse H I emission was later confirmed by Wolfe et al. (2016) with higher-resolution GBT data. Other searches of H I in the CGM often focus on the so-called extraplanar gas of nearby spiral galaxies (Fraternali et al. 2001, 2002; Sancisi et al. 2008), although the H I extension is usually within a few-ten kpc. For example, NGC891 is found to have extraplanar H I extending up to 15 kpc (Fraternali et al. 2005).

To briefly summarize, H I 21cm emission is sensitive to gas-rich systems with N(H I)$\gtrsim 10^{17-18}$ cm^{-2}, which limits its use in observing the CGM in which hydrogen is mostly ionized (see § 1.3.4 and § 1.3.5).

1.3.2 Hydrogen Lyα Absorbers Against Background QSOs

Low column density H I in the CGM can be probed by hydrogen absorption lines in the continua of background quasars (QSOs) observed with pencil-beam sightlines. Often the Lyα line at $\lambda = 1215.67$Å is used and other higher-order Lyman-series lines are adopted when Lyα becomes saturated. When the spectral quality is too poor to yield meaningful Voigt-profile analyses for individual kinematic components, the equivalent width (W_λ[†]) of the corresponding line is computed, which measures the total power missing from the continua due to the presence of H I along the line of sight.

The column density of H I can be inferred from W_λ based on the curve-of-growth

[†] $W_\lambda \equiv \int_{\lambda_1}^{\lambda_2}(1 - F_\lambda/F_0)d\lambda$, where $[\lambda_1, \lambda_2]$ indicates the wavelength range over which the absorption line occurs, F_λ is the flux of the absorption line, and F_0 is the continuum of the background target.

analysis (see Chapter 9, Draine 2011). For absorbers with optically thin line profiles at N(H I) $\lesssim 10^{14}$ cm^{-2}, the curve of growth shows that the H I column density scales linearly with the equivalent width: N(H I) = $1.836 \times 10^{14} W_\lambda$ cm^{-2}, where W_λ is in unit of Å (see equation 9.15 in Draine 2011). These are the absorbers often identified in Lyα Forest[†] in high-z QSO spectra, tracing low-density diffuse H I in the IGM (e.g., Adelberger et al. 2003; Rudie et al. 2012). Then over the range of $10^{14} \lesssim$ N(H I)[‡] $\lesssim 10^{18}$ cm^{-2}, the equivalent width becomes insensitive to H I column density with $W_\lambda \propto b\sqrt{\ln[N(\mathrm{HI})/b]}$, where b is the Doppler Width. Estimates of N(H I) based on W_λ is unreliable over this range. For high column density system with N(H I) $\gtrsim 10^{18}$ cm^{-2}, W_λ scales with the square root of N(H I): $W_\lambda \propto \sqrt{N(\mathrm{HI})}$. These are the systems most likely resembling galaxy disks or gas-rich satellites in the halos (see § 1.3.1).

Rudie et al. (2012) conducted a study of H I absorbers at $z \sim 2.0 - 2.8$ using the Keck Baryonic Structure Survey (KBSS). They searched for Lyα absorbers in the Lyα Forest of 15 QSOs at $z \sim 2.5 - 2.9$, and ran Voigt-profile analyses to simultaneously fit over several Lyman series lines (e.g., Lyα, Lyβ, Lyγ; see their figure 4) to measure H I absorbers' column densities, equivalent widths, and redshifts. They correlated the H I absorbers with 886 star-forming galaxies at similar redshifts within projected separation of ≤ 3 Mpc. They

[†]H I absorbers are classified into three different categories: Lyα Forest with N(HI) $\lesssim 10^{17}$ cm^{-2} (see a review by Rauch 1998), Lyman Limit System (LLS) with $10^{17} \lesssim N(\mathrm{HI}) \lesssim 10^{20.3}$ cm^{-2} (e.g., Steidel 1990; Prochaska 1999), and Damped Lyman Alpha (DLA) system with N(HI) $\gtrsim 10^{20.3}$ cm^{-2} (see a review by Wolfe et al. 2005). These three absorbers can be easily recognized based on their different spectroscopic features. Briefly, Lyα Forest are discrete Lyα absorption lines blue-ward of the rest-frame Lyα emission line of the QSOs themselves. LLSs show up as a sharp break of flux in the QSO continuum blue-ward of the rest-frame $\lambda = 912$ Å, due to the presence of high-density regions that are optically thick to ionizing photons with $E > 13.6$ eV. DLAs are those with large absorption troughs and damping wings which maybe destroyed by intervening Lyα Forest lines. DLAs usually have $W_\lambda > 5$Å (see § 1.2 in Wolfe et al. 2005). Note that hydrogen is mostly neutral in DLAs, but is dominantly ionized in LLSs and Lyα forest.

[‡]The N(H I) = 10^{14} and 10^{18} cm^{-2} values are rough estimates that separate the linear, flat, and damped parts of the curve of growth for H I Lyα absorption line, according to figure 9.2 in Draine (2011).

found that denser H I absorbers ($10^{14} \lesssim$N(H I)$\lesssim 10^{17}$ cm^{-2}) are more likely to apprear near galaxies, usually within 300 kpc and $|\Delta v| \lesssim 300$ km s^{-1} of the host galaxies' positions and systemic velocities (see their figure 10).

Rudie et al. (2012) also compared their work with other Lyα absorber studies at lower redshifts (Chen et al. 2001b; Wakker & Savage 2009; Prochaska et al. 2011) and tabulated the results in their table 6. Generally speaking, stronger H I absorbers with $W_\lambda \sim 0.1-1.0$Å (See figure 4, Tumlinson et al. 2017) are deemed a CGM association if the absorber-QSO pairs are close in position-velocity space. For example, Prochaska et al. (2011) found a near-unity covering fraction for Lyα absorbers with $W_\lambda \geq 50$mÅ for $L \geq 0.01L^*$ galaxies at $z \leq 0.4$ within 300 kpc and $|\Delta v| \leq 400$ km s^{-1}. They also found that the W_λ and covering fraction of Lyα decline as a function of impact parameter out to 1Mpc despite large scatters in the data (see their figure 6; see also Borthakur et al. 2015). A total CGM baryonic mass of $M_{\rm CGM}^{\rm HI} \sim 10^{10.5\pm0.3}\ M_\odot$ was derived by assuming a constant N(H I)= 10^{19} cm^{-2} column density profile out to 300 kpc.

Borthakur et al. (2015) investigated on the correlation between Lyα absorbers in the CGM and host galaxy properties. They focused on a sample of 45 $L \sim L^*$ gas-rich galaxies over a mass range of $\log(M_*/M_\odot) = 10.1 - 11.1$ at $z \sim 0.026 - 0.049$. The CGM of the target galaxies were probed with HST/COS QSO sightlines at impact parameters of 63−231 kpc from the corresponding hosts. They performed Voigt-profile fitting to evaluate the centroid velocities of the Lyα absorbers since most of the lines are saturated (with $W_\lambda \geq 0.3$Å). The Lyα equivalent widths W_λ are found to correlate well with the neutral gas fraction $f_{\rm HI} \equiv M_{\rm HI}/M_*$ in the disks at nearly 3σ level, but no correlation is observed

between W_λ and galaxy inclinations. Thus they concluded that the Lyα absorbers in the CGM distribute in a spherical configuration with respect to the central host and that the $W_\lambda - f_{\rm HI}$ connection hints at some gas accretion history.

In summary, Lyα absorbers observed with high-z QSO sightlines provide an useful tool to study the diffuse and predominantly ionized CGM gas down to N(H I)$\gtrsim 10^{13}$ cm^{-2} (e.g., see Table 6 in Rudie et al. 2012 and references therein). The Lyα measurements, combined with UV metal absorption lines and proper ionization modelings, give critical constraints on CGM properties, such as metallicity, temperature, ionization state, baryonic mass, and radial density profiles (see § 1.3.4).

1.3.3 Lyα Emission Mapping

Hydrogen Lyα photons emitted by sources at $z \sim 2-6$ are red-shifted to $\sim 2400-4900$Å, which are accessible by ground-based telescopes. Many Lyα emitting sources have been discovered by narrow-band imaging or integral field unit (IFU) observations; these sources usually have projected extensions of a few tens physical kpc to a few hundreds across. It seems unclear how these extended Lyα emitting sources are produced, or whether they resemble the CGM detected in UV absorbers (see § 1.3.4) or hot X-rays (see § 1.3.5). Here I briefly review some properties of the Lyα emitting sources which could be potentially CGM-related.

Different names, such as Lyα nebulae, Lyα blobs, and Lyα halos, are used to describe the extended Lyα emitting sources. It seems that Lyα Nebulae are preferentially assigned to those sources detected near AGNs with projected sizes of $\gtrsim 100$ physical kpc (pkpc)

(e.g., Cantalupo et al. 2014; Hennawi et al. 2015; Borisova et al. 2016). Lyα Blobs are more generically used to describe various Lyα emitting sources, including Lyα Nebulae and other targets with seemingly smaller[‡] sizes (e.g., Steidel et al. 2000; Matsuda et al. 2004). Lyα halos are reported surrounding star-forming/Lyα-emitting galaxies, and they are presumably fainter and smaller than the sources in the other two categories (e.g., Wisotzki et al. 2016).

It is unknown how Lyα emitting sources relate to their central hosts. For example, Matsuda et al. (2004) found 35 Lyα blobs with projected extension of $\sim 30 - 110$ pkpc[¶] at $z = 3.1$ with Subaru Telescope. Among these, 17 are associated with Lyα emitters (Hayashino et al. 2004) and the other eight are related to known Lyman break galaxies (Steidel et al. 2003). Cantalupo et al. (2014) detected a giant Lyα nebula, the Slug Nebula, with a projected size of 460 pkpc (at a limited surface brightness of SB $> 10^{-18}$ erg s^{-1} cm^{-2} arcsec^{-2}) surrounding a radio-quiet QSO at $z \sim 2.3$. Borisova et al. (2016) found 100% detection rate of Lyα nebulae around 17 QSOs at $3 < z < 4$ with projected size of $100 - 320$ pkpc with MUSE using the same SB limit as Cantalupo et al. (2014).

Despite the difference in shape, size, luminosity, and central host, Borisova et al. (2016) suggested that the azimuthal-averaged SB profiles of Lyα emitting sources can be similarly described by a power-law fit of SB $\propto r^{-1.8}$ (see their figure 5), except for the Lyα halos (Wisotzki et al. 2016). In their work, Wisotzki et al. (2016) investigated the extended

[‡]Note that different authors quoted different flux limits to define the Lyα emitting sources, which make it difficult to directly compare the source extension. For example, the > 100pkpc Lyα nebulae in Borisova et al. (2016) are defined with surface brightness level $> 10^{-18}$ erg s^{-1} cm^{-2} arcsec^{-2}, while Matsuda et al. (2004) chose Lyα blobs (with area of $16 - 200$ arcsec^2) based on a requirement that the isophotal area should be brighter than 0.7×10^{-16} erg s^{-1} cm^{-2}.

[¶]Matsuda et al. (2004) found that their sources have sizes of $16 - 200$ arcsec^2. The $\sim 30 - 110$ kpc projected sizes are converted from these angular area estimates, with $1'' \approx 7.6$ kpc at $z = 3.1$.

Lyα emission around star-forming galaxies at $z = 3 - 6$, and found that the Lyα halos extend to $\sim 10 - 25$ kpc in radius at a detection limit of SB $\sim 1 \times 10^{-19}$ erg s^{-1} cm^{-2} arcsec^{-2} (see their figure 7). The SB distribution tends to follow an exponential profile rather than a power law.

The sometimes interchangeable names and various central hosts add mysteries to these high-z extended Lyα emitting sources, so does its unclear production mechanism. The Lyα emitting sources could be produced in cooling gas in collapsed dark-matter halos where gravitational energy is released in Lyα emission (e.g, Haiman et al. 2000). Some authors suggested that it could be due to cool extended gas being illuminated (photoionized) by rest-frame UV sources obscured from the lines of sight or due to Lyα photons being scattered off by the extended neutral hydrogen (e.g., quasars; Matsuda et al. 2004; Cantalupo et al. 2014; Borisova et al. 2016).

A detailed discussion of Lyα emission and the production mechanism are certainly beyond the scope here. The giant Lyα nebulae seem to be related to cosmic-web filaments (e.g., Cantalupo et al. 2014), while Lyα halos are more likely to be gravitationally bound within the CGM given their smaller physical extension from host galaxies (e.g., Wisotzki et al. 2016). Kinematically resolved observations with IFUs and other metal emission-line observations as predicted by simulations (Corlies & Schiminovich 2016) will better understand these Lyα emitting sources and their connection to the CGM.

1.3.4 Metal Absorption Lines Probing Cool CGM at $T \sim 10^{4-5.5}$ K

Metal absorption lines together with Lyα absorbers as discussed in § 1.3.2 provide so-far the best constraints on the mass, metallicity, density profile, and kinematics of cool CGM. Large samples of QSO-galaxy pairs are collected to statistically study the CGM properties using a wide range of ions (e.g., Mg II, Si II, C II, Si III, and Si III). In this section, I will briefly summarize some results on observing the cool CGM with ground-based telescopes (Mg II; § 1.3.4.1) and with space spectrographs (UV lines; § 1.3.4.2).

1.3.4.1 Mg II Doublet Observed With Ground-Based Optical & Infrared Instruments

The strong Mg II doublets $\lambda\lambda 2796, 2803$Å are commonly used to study the CGM and IGM at low ionization states at $z \sim 0.3 - 2.5$ with optical telescopes (e.g., Chen & Tinker 2008; Chen et al. 2010b; Zhu & Ménard 2013) and at $1.9 < z < 6$ with infrared instruments (e.g., Matejek & Simcoe 2012). Broadly speaking, three approaches are adopted: (1) Mg II absorbers are blindly searched for along high-z QSO sightlines (e.g., Matejek & Simcoe 2012; Zhu & Ménard 2013; Chen et al. 2017; see also Rudie et al. 2012 for a similar study of Lyα absorbers), (2) QSO absorber-galaxy pairs are selected to study the halos of known galaxies (e.g., Chen & Tinker 2008; Chen et al. 2010b; Nielsen et al. 2013), and (3) down-the-barrel observations of Mg II lines in the spectra of host galaxies (e.g., Weiner et al. 2009; Coil et al. 2011; Rubin et al. 2014).

First, blind searches of Mg II absorbers at $0.4 < z < 7$ using high-z QSOs found two distinct populations that evolve differently as a function of redshift (e.g., Matejek & Simcoe 2012; Zhu & Ménard 2013; Chen et al. 2017). For example, Zhu & Ménard (2013)

detected $\sim 40,000$ Mg II absorbers at $0.4 < z < 2.3$ and combined them with 110 absorbers at $1.9 < z < 5.3$ (Matejek & Simcoe 2012). The total sample shows that the number density of weak Mg II absorbers ($0.6 < W_\lambda^{2796} < 1$Å) does not evolve significantly over the redshift span, while strong absorbers ($W_\lambda^{2796} > 1$Å) correlates well with the cosmic star-formation density which peaks at $z \sim 3$ and declines at higher and lower z (see their figure 13).

Second, studies of QSO absorber-galaxy pairs focus on quantifying Mg II detection around low-z galaxies within projected separation (impact parameter) of a few $10 - 100$ kpc (e.g., Chen et al. 2010a; Bordoloi et al. 2011; Nielsen et al. 2013, 2016; Ho et al. 2017). The rest-frame equivalent width, W_λ^{2796}, is used to correlate Mg II measurements with other galaxy properties, such as galaxy type and halo mass (e.g., Chen et al. 2010b; Gauthier et al. 2010; Nielsen et al. 2016), gas kinematics and disk orientation (e.g, Bouché et al. 2012; Ho et al. 2017), and star formation activities (e.g., Ménard et al. 2011). It has been found that more luminous galaxies host more extended Mg II halos (e.g., Chen et al. 2010a), the size of which can be parameterized with a Holmberg-like luminosity scaling relation as $R_{\rm MgII} = R^*_{\rm MgII}(L_B/L^*_B)^\beta$, where $R^*_{\rm MgII}$ is the radius of the Mg II halo for a $L \sim L^*_B$ galaxy in B band. For example, Chen & Tinker (2008) suggested $\beta = 0.35$ and $R^*_{\rm MgII} = 91h^{-1}$ using 23 QSO absorber-galaxy pair at $< z >= 0.38$. Chen et al. (2010a) estimated a value of $M_b \sim (6-9)\times10^9\ M_\odot$ for cool CGM of $L \sim L^*$ galaxies by considering Mg II cloud size ($1-2$ kpc), total cloud number ($2\times10^5 h^{-2}$), and metallicity ($0.05-0.1Z_\odot$) within a $R = 75h^{-1}$ kpc halo assuming that the Mg II-bearing gas is photoionized.

To quantify the distribution of Mg II absorbers in the CGM, covering fractions (κ) at certain W_λ^{2796} values within certain radii are often quoted (e.g., Bowen et al. 1995; Kacprzak

et al. 2008; Chen et al. 2010a; Gauthier et al. 2010). For example, Chen et al. (2010a) found $\kappa \sim 70\%$ for absorbers with $W_\lambda^{2796} \gtrsim 0.3$Å within $75h^{-1}$ kpc of host galaxies, a majority of which are $\sim L^*$ galaxies with $M_{\rm DM} = 10^{11-12.5}h^{-1}\ M_\odot$. At higher-mass end, Gauthier et al. (2010) found $\kappa \sim 20-30\%$ at $W_\lambda^{2796} = 0.5$Å within $100h^{-1}$ for Mg II absorbers around luminous red galaxies (i.e., old and passive galaxies) with $M_{\rm DM} > 10^{-13}h^{-1}\ M_\odot$ (see their figure 3). Although different authors report various κ values, these literature together indicates that: (1) star-forming galaxies tend to have higher detention rates of Mg II absorbers within their virial radii than passive galaxies, (2) κ is less than unity in all cases, and (3) W_λ^{2796} values drop at large impact parameters.

Third, down-the-barrel observations which directly search for Mg II absorption lines in the spectra of host galaxies have found ubiquitous Mg II-bearing outflows (e.g., Weiner et al. 2009; Coil et al. 2011; Rubin et al. 2014). In their work, Rubin et al. (2014) analyzed Mg II line profiles of 105 star-forming galaxies with $\log(M_*/M_\odot) \gtrsim 9.6$ at $< z > \sim 0.5$, and found that 66% of their galaxies host large-scale outflows at velocities of $\sim 150-550$ km s^{-1}(i.e., blue-shifted absorption lines; see their figures 6 and 14). Outflows are more commonly detected in nearly face-on disks than in edge-on systems (see their figure 13), suggesting that star-forming galaxies can launch outflows biconically with opening angle of $\sim 100^\circ$. The collimation of outflows found in Rubin et al. (2014) echoes the studies of a number of authors who suggested that stronger Mg II absorbers (with larger W_λ^{2796}) locate closer to the minor axes of host galaxies (e.g., Bordoloi et al. 2011; Bouché et al. 2012).

In summary, ground-based telescopes provide useful tools to study the high-z CGM with ion absorbers whose rest-frame wavelengths are stretched into the optical and in-

frared regimes. Besides Mg II absorbers, other similar ions (e.g, Fe II and Ca II; Zhu & Ménard 2013) as well as highly ionized species (e.g., C IV, O VI; Cooksey et al. 2013; Turner et al. 2015) are also used, and data samples with sightline number on the order of $\sim 100 - 10,000$ can be aggregated to yield statistically significant estimates on the high-z CGM properties. The phase of the CGM probed by Mg II is most likely similar to the phase probed by UV ions at low-intermediate ionization states (see next section) that are also predominantly photoionized.

1.3.4.2 UV Absorption Lines Observed With Space Telescopes

The cool CGM at low redshifts can also be probed by ions at low-intermediate ionization states, such as Si II, Si III, Si IV, C II, C IV, which are only accessible by space telescopes. The installation of the Cosmic Origin Spectrograph (COS) on the Hubble Space Telescope (HST) has spurred the studies of cool CGM at $z \lesssim 0.2$ over the past couple of decades. Below I briefly summarize some CGM studies using HST/COS.

The COS-Halos survey analyzed the mass, density profile, and metallicity of the cool CGM of $0.1 \lesssim L \lesssim 3L^*$ galaxies[‖] using 44 QSO-galaxy pairs at $z \sim 0.2$ (Werk et al. 2012, 2013; Tumlinson et al. 2013; Werk et al. 2014; Prochaska et al. 2017). The QSO sightlines probed the CGM within 160 kpc ($\rho \lesssim 0.55R_{\rm vir}$) of the host galaxies, and detected a wide range of ions (e.g., H I Lyα, Si III, Si IV, O VI). Werk et al. (2013) found that 33/44 of the galaxy halos were detected with significant metal absorption, indicating the CGM of $L \sim L^*$ galaxies are metal-enriched with a median metallicity of $\sim 0.3Z_\odot$ (Prochaska et al.

[‖]Their galaxy sample have a median $\log(M_*/M_\odot) = 10.5$, nearly 70% of which are star-forming galaxies with sSFR $> 5 \times 10^{-12}$ yr^{-1}, and the rest are passive galaxies (see figure 3 in Tumlinson et al. 2011).

2017). Their Voigt-profile fits showed that the centroid velocities of these ion absorbers are within $|\Delta v| \lesssim 400$ km s^{-1} of the systemic velocities of the host galaxies, indicating that most absorbers in the CGM are gravitationally bound to the dark-matter halos (see figure 15 in Werk et al. 2013). Both the covering fraction and column density of the absorbers decrease as a function of the impact parameter with a radial dependence of $N_H \propto (R/R_{\rm vir})^{-1}$ at 99% confidence (see equations 4 and 6 in Werk et al. 2014).

The COS-Halos team found the mass of the cool, photoionized CGM to be on the order of a few times 10^{10} $M_\odot$ out to the virial radii of $L \sim L^*$ galaxies at $z \sim 0.2$. Werk et al. (2013) gave a preferred lower limit** of the cool CGM mass at $M^{\rm cool}_{\rm CGM}(R \lesssim R_{\rm vir}) = 6.5 \times 10^{10}$ $M_\odot$ for $L \sim L^*$ galaxies. This mass is obtained by integrating the hydrogen surface density $N_{\rm H}$ from 0 to 1 $R_{\rm vir}$, where $< R_{\rm vir} >= 300$ kpc for $L \sim L^*$ galaxies in their sample. They derived the $N_{\rm H}(r)$ profile by applying ionization correction to the measured N(H I) with CLOUDY modeling (see their equation 4 and figure 10); even so, the mass estimate was deemed a lower limit since the H I lines detected in $\sim$ 20 of the absorber systems were saturated (Tumlinson et al. 2013). A higher mass estimate of $M^{\rm cool}_{\rm CGM}$(R < 160 kpc) = (9.2±4.3)×10^{10} $M_\odot$ was obtained by Prochaska et al. (2017) with a new subset of QSO sightlines from the COS-Halos survey, which was designed to yield more accurate N(H I) by computing the optical depths of the continua at rest-frame $\lambda_{912} = 912$Å, where a sharp drop in flux occurs blueward of λ_{912} (see their figure 1) due to the missing of $E > 13.6eV$ photons absorbed by

**Another two mass estimates were also given by Werk et al. (2013). First, they derived a strict lower limit with $M^{\rm cool}_{\rm CGM}(R \leq 0.55R_{\rm vir}) = 2.1 \times 10^{10}$ $M_\odot$, where the lowest ionization parameter is adopted in the CLOUDY modeling. And they only integrated $N_{\rm H}$ out to 0.55 $R_{\rm vir}$, which is the boundary of their sightline distribution. Second, they adopted a similar volume-filling-method as used in Stocke et al. (2013) and found $M^{\rm cool}_{\rm CGM}(R \leq 0.55R_{\rm vir}) = 3.2 \times 10^{10}$ $M_\odot$, which is based on CGM cloud population estimates with CLOUDY modeling.

dense neutral hydrogen along the lines of sight. In addition, Stern et al. (2016) developed a new CGM model which described the cloud population with a hierarchical density structure and found $M_{\rm CGM}^{\rm cool}(\rm R < R_{vir}) = (1.3 \pm 0.4) \times 10^{10}$ $\rm M_\odot$. Note that Stern et al. (2016) used the UV background from Haardt & Madau (2012), while Werk et al. (2013) and Prochaska et al. (2017) adopted the spectra from Haardt & Madau (2001) (see also Keeney et al. 2017 for discussion on the effect of using different UV background intensity spectra in the CLOUDY modeling).

Other COS programs are independently carried out by different authors, which are complementary to the COS-Halos survey in target selection and sightline coverage. Stocke et al. (2013) studied the cool CGM of galaxies with different morphology types ranging from massive spirals to dwarf irregulars. Their sample included 11 QSO-galaxy pairs at $z < 0.02$ and ~ 60 serendipitous archival pairs at $z < 0.2$ (see also Keeney et al. 2017). This sample covered a wider impact parameter ($0.1 - 1.5R_{\rm vir}$) and broader luminosity range (from dwarfs with $\sim 0.01L^*$ to super-L^*) than those of the COS-Halos. For $L \gtrsim 0.1L^*$ galaxies, Stocke et al. (2013) found that the covering fraction of the metal absorbers is $C_f \sim 1$ within $\rm R < 0.5R_{vir}$ and ~ 0.75 over $[0.5, 1]\rm R_{vir}$, which is similar to the COS-Halos result. Dwarf galaxies with $L \sim [0.01, 0.1]L^*$ have $C_f \sim 0.5$, although this value is less certain due to the limited sample size. The cloud population in the CGM was carefully studied, which was based on CLOUDY modeling and Voigt-profile fitting to derive the cloud sizes and numbers along the lines of sight. Stocke et al. (2013) found an average cloud component number of $S = 1.4 \pm 0.2$ for each sightline, a cloud size range of $0.1 - 30$ kpc, and a volume filling factor of $10 - 15\%$ for the cool CGM of $L \gtrsim 0.1L^*$ galaxies. Summing all the cloud

masses together, they estimated a total mass of $M_{\rm CGM}^{\rm cool} \sim 10^{10}\ M_{\odot}$ within the viral radius. Keeney et al. (2017) updated Stocke et al. (2013)'s result with new profile modeling and CLOUDY modeling, and refined the CGM mass to $M_{\rm CGM}^{\rm cool}(\rm R < R_{vir}) = 10^{10.5\pm0.3}\ M_{\odot}$ after taking into account the different choices of extra-galactic UV background[§] between their work and that of the COS-Halos.

Despite the good agreement in cool CGM mass, the COS-Halos survey (Werk et al. 2013, 2014; Prochaska et al. 2017) found that the metal column density and ionization parameter decrease with the impact parameter, while Stocke et al. (2013) and Keeney et al. (2017) did not find such trend in their sample. Keeney et al. (2017) suggested that this difference could be partially due to the different impact parameter ranges: the sample in Keeney et al. (2017) mainly probed absorbers at $0.5 < \rm R < 1.5R_{vir}$ while the COS-Halos sightlines are mostly in the inner halo at $\rm R \leq 0.55R_{vir}$. A combined sample of the COS-Halos data and those of Keeney et al. (2017) showed that the gas column density declines from 0 to 1 $R_{\rm vir}$ and flattens beyond this range, a trend that can be generally described by a singal power-law distribution (see figure 3 in Keeney et al. 2017).

The CGM of our own MW has also been carefully studied in many aspects using UV absorption lines from background QSOs and MW halo stars. To name a few, Savage & Wakker (2009) parameterized the ionized gas extension[‡] above the Galactic disk with an exponential density profile and a flat-slab plane-parallel geometry. They found that

[§]Werk et al. (2014) and Prochaska et al. (2017) adopted a background radiation field from Haardt & Madau (2001) in their CLOUDY modeling, while Stocke et al. (2013), Stern et al. (2016), and Keeney et al. (2017) assumed the spectra from Haardt & Madau (2012). Please see detailed discussion on the different UV radiation fields by Shull et al. (2015) and Keeney et al. (2017).

[‡]The ionized gas that is a few kpc above the Galactic disk is often referred to as the gaseous thick disk (Savage & Wakker 2009) or the disk-halo interface (Putman et al. 2012). In extragalactic studies, this gas is also called the extraplanar gas (Ho et al. 2017) or the diffuse ionized gas (DIG; Haffner et al. 2009; Boettcher et al. 2016).

the low-velocity gas ($|v_{\rm LSR}| \lesssim 100$ km s^{-1}) detected in H I, Al III, Si IV, C IV, and O VI can be respectively fit with scale heights of 0.24, 0.90, 3.2, 3.6, and 2.6 kpc in their flat-slab model (see also, e.g., Savage et al. 2003; Bowen et al. 2008; Wakker et al. 2012; and Chapter 3). Ionized high-velocity gas in the MW halo is commonly found in the vicinity of H I HVCs (see § 1.3.1), and the coincidence in position-velocity space and similar metallicity measurements are often used to infer the connection between the ionized and neutral gas (e.g., Wakker 2004; Fox et al. 2006; Shull et al. 2009; Lehner et al. 2012; Fox et al. 2014; Fox 2015; Richter et al. 2017; Bordoloi et al. 2017). The MW's CGM is also found to be clumpy as probed by sightlines with sub-degree separation (Howk et al. 2002; see also Chapter 4). And the kinematic behavior of the multiphase gas near the Galactic disk has been modelled with lagging layers and Galactic fountains under the influence of stellar feedback from the disk (e.g., Shapiro & Field 1976; Bregman 1980; Marasco & Fraternali 2011; Marasco et al. 2013).

To briefly summarize, extragalactic studies of the CGM with ions at low-intermediate ionization states suggest that the mass of the cool, photoionized CGM is on the order of 10^{10} $M_\odot$ (Werk et al. 2013; Stocke et al. 2013; Stern et al. 2016; Keeney et al. 2017; Prochaska et al. 2017), which corresponds to $\sim$ 30 – 100% of the expected baryons of a $L \sim L^*$ galaxy (see § 1.2.1). The large uncertainties in the estimates of the CGM mass and baryon fraction stem from many factors, such as CLOUDY modeling, density profile fitting, gas clumpiness, and metallicity estimates. For the MW CGM studies, the physical extension of the halo gas can not be as easily estimated as in those extragalactic work since we reside inside the Galactic disk. Accurate distance information is difficult to obtain unless close

pairs of halo stars in the foreground and background of the target clouds can be found to bracket the distance. I will further discuss the MW CGM observations and the difficulties in studying the kinematics and distribution of the MW halo gas in Chapters 2 and 3.

1.3.5 The Warm-Hot CGM with $T \sim 10^{5-7}$ K

Cosmological simulations predict that 30 – 40% of the baryons are in the warm-hot intergalactic medium at temperatures of 10^{5-7} K (Cen & Ostriker 1999). Within galaxy halos, the warm-hot gas with $T > T_{\rm vir}$ can host a considerable amount of baryons ($\sim 10^{10}\ M_\odot$) which shine in highly ionized transition lines in the UV and soft X-ray, such as O VI, O VII, O VIII, Ne VIII, and Mg X (Bregman 2007; Miller & Bregman 2015). Among these ions, the O VI doublet $\lambda\lambda$1031.9, 1037.6Å can be observed in the UV with space telescopes (Nicastro et al. 2003; Sembach et al. 2003; Savage et al. 2003; Stocke et al. 2006; Prochaska et al. 2011; Tumlinson et al. 2011), the Ne VIII $\lambda\lambda$770.409, 780.32Å lines are identified in $z \sim 0.2 - 0.7$ absorbers with FUSE and HST/COS (Savage et al. 2005; Meiring et al. 2013; Pachat et al. 2017), and the Mg X doublet $\lambda\lambda$609.8, 624.9 Å has been found in a $z \approx 1.2$ system (Qu & Bregman 2016). The O VII (λ21.602Å) and O VIII (λ18.967Å) lines are in the soft X-ray regime, which can be observed with the Chandra X-Ray Observatory and XMM-Newton (Gupta et al. 2012). Except for O VI and soft X-ray absorbers, the detection of other ions is less common.

Tumlinson et al. (2011) studied the O VI absorbers in the CGM of 42 $L \sim L^*$ galaxies within 160 kpc at $z \sim 0.2$ (the COS-Halos survey; Tumlinson et al. 2013; Werk et al. 2013). Among them, 30 are star-forming galaxies with sSFR $\sim 5 \times 10^{-12}$ yr^{-1} and the rest

are passive galaxies (see their figure 3). At 99.9% confidence level they found the O VI presence in the halo strongly correlates with the host's star-formation activity: star-forming galaxies have ubiquitous O VI absorbers in their CGM with a typical value of logN(O VI)= 14.5 and a covering fraction of $C_f \geq 0.8$, while only 4/12 passive galaxies have O VI detection with logN(O VI)$\sim$ 13.7 – 14.3. They reached a lower-limit mass estimate for the O VI-probed CGM at $2 \times 10^9\ M_\odot$ by assuming a solar metallicity $Z = Z_\odot$, a maximum ionization correction $f = 0.2$ from O VI to O at $T \sim 10^{5-6}$ K (see their figure 4), and a spherical volume of $R = 150$ kpc. This mass value could be substantially larger if O VI is not dominantly photoionized at its peak temperature as is assumed in Tumlinson et al. (2011) (see also Peeples et al. 2014 for an estimate of the O VI-probed CGM mass with a power-law O VI density profile out to 300 kpc).

In fact, how O VI is produced in the CGM is still subject to debate. For example, Werk et al. (2014) found that the O VI column densities cannot be fully accounted for in their photoionization modeling, and other mechanisms such as collisional ionization, should be considered. However, Stern et al. (2016) argued that O VI can be produced in photoionized gas whose density structure follows hierarchical manner (i.e., high-density weakly-ionized clouds are embedded in low-density highly-ionized gas). Werk et al. (2016) stressed that any O VI ionization models should self-consistently explain the high-column density [logN(O VI)= 14.5; figure 2, Tumlinson et al. 2011], the various line-widths ($b \sim 10 - 100$ km s^{-1}; figure 6, Werk et al. 2016), the detection dichotomy between star-forming and passive galaxies (figure 3, Tumlinson et al. 2011), and the similar kinematics between low ions and O VI (figure 11, Werk et al. 2013).

Gupta et al. (2012) searched for the O VII and O VIII absorbers in the MW halo with the Chandra X-Ray Observatory. They compared their absorption line measurements with the X-ray emission to estimate the electron volume density n_e and gas extension R of the halo. Briefly, absorption lines provide column density measurements of N $\propto n_e R$ and the emission measure scales with density square as EM $\propto n_e^2 R$, therefore the combination of these two gives constraint on n_e and R. Gupta et al. (2012) found $n_e = (2.0 \pm 0.6) \times 10^{-4}$ cm^{-3} and $R = 239 \pm 100$ kpc. Assuming $f_{\rm OVII} = 0.5$, $Z = 0.3 Z_\odot$, and $T = 10^{6.1-6.4}$ K with collisional ionization equilibrium, they derived a total mass for the hot-phase MW's CGM of 2.3×10^{11} $M_\odot$[‡]. Miller & Bregman (2015) found a substantially smaller mass of $M_{\rm MW}^{\rm hot}(R < 250\,{\rm kpc}) = 4.3^{+0.9}_{-0.8} \times 10^{10}$ $M_\odot$ by the fitting O VIII observations with a β-model halo density profile assuming gas metallicity of $Z = 0.3 Z_\odot$ (see also Anderson & Bregman 2010; Miller & Bregman 2013).

In brief, highly ionized species (e.g., O VI, O VII, O VII, Ne VIII, Mg X) probe a much hotter phase of the CGM than those low-intermediate ions (§ 1.3.4). Mass estimates found that this phase contains a large amount of baryons with mass of 10^{10-11} $M_\odot$. Except for O VI, detailed kinematic studies of gas in this phase remain difficult due to the low spectral grating[††] of soft X-ray observations.

[‡]The total mass is $\sim 1.2 \times 10^{10}$ $M_\odot$ if using solar metallicity.

[††]For Chandra, the low-energy grating is FWHM = 0.05Å or $\sim$ 750 km s^{-1} at 20Å, and the high-energy grating is FWHM = 0.023Å or $\sim$ 345 km s^{-1} at 20Å, see Gupta et al. (2012)

1.4 Structure of the Dissertation

This dissertation is dedicated to understanding the gas distribution in the MW's CGM as well as the baryon cycle between the CGM and the galaxy disk in M33 using UV spectroscopy and H I 21cm observations. In Chapter 2, I study the fraction of the low-velocity gas in the MW's CGM being blocked by the foreground ISM by conducting synthetic observations using a MW-like simulated galaxy. In Chapter 3, I further investigate the distribution of the low-velocity gas in the MW's halo using ~ 132 HST/COS archival QSO sightlines. The sub-degree scale clumpiness of the CGM and a mysterious Wright's Cloud near the direction of M33 is studied in Chapter 4. Finally, the cycle of baryons between the CGM and the disk is studied in Chapter 5 by observing gas accretion onto M33 using seven HST/COS stellar sightlines. I briefly conclude in Chapter 6.

Chapter 2

The Circumgalactic Medium of the Milky Way is Half Hidden. I: Synthetic Observations

2.1 Introduction

Studies of the circumgalactic medium (CGM) help us to understand the origin of a galaxy's star formation fuel and the impact of galactic feedback. Assessing the amount and state of the baryons in galaxy halos is a key active area in galaxy formation research. Due to its proximity, the CGM of the Milky Way (MW) has been studied in the most detail, and this has helped us interpret the nature of the multiphase medium and the potential interactions with the galactic disk.

This chapter is a reproduction of a paper by Zheng, Putman, Peek, & Joung (2015) published on The Astrophysical Journal.

To calculate the mass of the multiphase CGM in the MW, numerous spectroscopic observations towards high-velocity line features have been conducted. High velocity clouds (HVCs), mapped in H I surveys via the 21 cm hyperfine transition line, trace the coldest component of the Galactic halo. HVCs have been found to largely reside within 15 kpc of the disk with the exception of the complexes associated with the Magellanic System which are at least at $\sim$ 55 kpc (Wakker & van Woerden 1997; Putman et al. 2012, hereafter PPJ12). The H I mass of the non-Magellanic System HVCs is $\sim 3 \times 10^7\ M_\odot$ (PPJ12), and thus is a very small fraction of the Galaxy's baryons (see § 1.2.1). Observations of the ion absorption lines in the spectra of background quasars show an order of magnitude more mass is associated with the warmer ionized gas ($T \sim 10^{4-6}$ K) in the Galactic halo (Sembach et al. 2003; Shull et al. 2009; PPJ12). X-ray observations of hot gas ($T > 10^6$ K) in emission and absorption (O VII, O VIII) do not have strong constraints from spectral line observations, but currently indicate a mass of $\sim 10^{10}\ M_\odot$ if extended out to 250 kpc (Anderson & Bregman 2010; Miller & Bregman 2013, 2015).

The MW's CGM can be compared to that of other $L \sim L^*$ galaxies now with the increase in absorption line probes made available with the Cosmic Origins Spectrograph (COS). Discrepancies in both mass and column density have been found. At first glance, the total mass of the MW's CGM with $T \leq 10^6$ K appears to be $1-2$ orders of magnitude lower than the CGM mass of other $L \sim L^*$ spirals ($\sim 10^{10}\ M_\odot$; Stocke et al. 2013; Werk et al. 2014). As for the column density, Tumlinson et al. (2011) found a typical value of $\log N_{OVI} = 14.5$ in the CGM of $L \sim L^*$ galaxies with specific star formation rate (sSFR) $> 10^{-11}$ yr^{-1} in the COS-Halos sample, while the MW's CGM instead has $\log \left\langle N_{OVI} \right\rangle = 14.0$

(Sembach et al. 2003) with sSFR $\sim 2-6\times10^{-11}$ yr^{-1} (SFR $\sim 1-4$ $M_{\odot}$ yr^{-1}, Robitaille & Whitney 2010; Diehl et al. 2006; log M$_{*}$ $\sim$ 10.8, McMillan 2011). These differences between the MW and external $L \sim L^{*}$ galaxies raise several questions. Is the MW's CGM an outlier with much less mass than other $L \sim L^{*}$ spirals? Or are our observations of the MW's CGM still incomplete?

Observations of the MW's CGM specifically suffer from obscuration by the dense foreground disk gas that can be moving at a similar radial velocity as the gas in the MW's CGM. The disk gas causes studies of the MW's CGM to apply velocity cutoffs with commonly adopted values of $|v_{\rm LSR}| < 90-100$ km s^{-1} (Wakker 1991a; Sembach et al. 2003; Lehner et al. 2012; PPJ12). It is also common to exclude gas with deviation velocity $|v_{\rm DEV}| < 50-75$ km s^{-1} which is the amount a cloud's velocity deviates from a simple disk rotation model (Wakker 1991a; PPJ12). However, estimates of the obscured MW's CGM mass due to these velocity cutoffs are rarely presented since it is usually impossible to distinguish signals of low velocity halo gas from that of disk gas.

In this work, we conduct synthetic observations of the CGM of a simulated MW-mass galaxy. Observational conditions of the MW's CGM are reproduced so that the influence of foreground disk material on the observed CGM properties can be evaluated. Following the definitions in Wakker (1991a), two velocity cutoffs ($|v_{\rm LSR}| \geq 100$ km s^{-1} and $|v_{\rm DEV}| \geq 50$ km s^{-1}) are adopted to define the high velocity gas that is observable in the simulated CGM. We do not perform sophisticated modelling of the gas ionization state, but rather approximate the CGM gas phases by several temperature ranges: cold, $T \leq 10^{4}$ K; warm, $T \sim 10^{4-5}$ K; warm-hot, $T \sim 10^{5-6}$ K; hot, $T > 10^{6}$ K. These loosely correspond to

gas traced by atomic hydrogen (H I), low and intermediate ions (e.g., Si II, Si III, Si IV, C II, C III, C IV), high ions (e.g., O VI), and X-ray emitting/absorbing ions (e.g., O VII, O VIII), respectively. With this setup, we can understand the CGM distribution in high and low velocity regimes at various phases, which will shed light upon the question of whether the MW's CGM is abnormal or current observations are incomplete.

This chapter is organized as follows: § 2.2 briefly describes the setup of the numerical simulation and gas kinematics of the simulated CGM; § 2.3 outlines the methods we use to conduct synthetic observations on the simulated CGM with a view from within the simulated disk. The properties of obscured low velocity gas in the simulated CGM through spectroscopic observations are shown in § 2.4, and comparisons with current observations of the MW and other $L \sim L^*$ galaxies are discussed in § 2.5. We conclude in § 2.6 with our main findings.

2.2 Simulation of a MW-mass Galaxy

Our investigation of gas kinematics in the MW's CGM is based on a high-resolution cosmological simulation of a MW-mass galaxy. The simulation was performed by Joung et al. (2012b) with *Enzo*, an Eulerian hydrodynamics adaptive refinement code. A low-resolution run was first performed which identified four MW-mass halos in Local-Group-like volumes; then one of the halos was re-simulated, achieving a mass resolution of $\sim 10^5\ M_\odot$ and spatial resolution of $136 - 272$ pc physical (or better at all times). The code includes metallicity-dependent cooling, photoionization by UV extragalactic radiation, shielding of UV radiation by H I, and photoelectric heating of the interstellar medium.

Star formation and stellar feedback (but no AGN feedback) are implemented. We refer the reader to the work done by Joung et al. (2012b) and Fernández et al. (2012) for detailed information on the performance of the simulation, and only report their key results here.

The total mass of the simulated dark matter halo is 1.4×10^{12} $M_{\odot}$ within its virial radius (250 kpc). Warm-hot and hot ionized gas dominate the mass accretion over large radii with an accretion rate of $\dot{M} = 3 - 5$ $M_{\odot}\mathrm{yr}^{-1}$. Nearly 70% of such flow enters the virial radius along filamentary structures. This inflowing gas interacts with existing halo gas, with its cooling rate and heating rate generally balanced over large radii. Only a small fraction of the filamentary flows manage to reach regions close to the disk in the form of cold clouds (H I). Another source of H I is the stripped gas from satellites as they move through the simulated CGM. Inflows and the stripped satellite gas contribute comparable amounts of H I to the halo. Galactic winds also affect the gaseous CGM. Large-scale collimated outflows driven by supernova feedback have been reported in the simulated galaxy (also see § 2.3); these winds generally carry very hot metal-enriched gas and move at high velocities extending from $\sim$ 200 to $\sim$ 1000 km s^{-1} (PPJ12).

2.3 Synthetic Observations

In this work, the *simulated disk* is defined as a cylindrical region with a size of $R \leq 18$ kpc and $|z| \leq 2$ kpc following the terminology used in Joung et al. (2012b). The *simulated CGM* defines a spherical volume with a radius of 250 kpc with the central simulated disk manually masked. We use the *yt* analysis toolkit (Turk et al. 2011) to study the properties of the simulated CGM from a view within the simulated disk, and perform analyses on the

CGM gas with all the temperature available in the simulation unless otherwise specified. The synthetic observations account for the galactic differential rotation of the simulated disk and the off-center location of the mock observer (Local Standard of Rest; LSR), which is the case for observations of the MW's CGM.

We construct a mock Galactic coordinate system analogous to that of the MW, and specify observing sightlines using galactic longitude l and galactic latitude b. We then build a disk rotation model by synthesizing H I 21cm emission from the simulated disk in order to determine the velocity ranges allowed by disk rotation, within which low velocity gas in the simulated CGM at similar velocities will be obscured.

2.3.1 Constructing the Mock Galactic Coordinates System

The simulated disk is centered at the point of maximum baryon density, close to the center of mass of the disk. The rotation axis of the simulated disk is aligned with the angular momentum vector of the disk cylinder. In the mid-plane of the simulated disk, we place a mock observer at a distance of $R_0 = 8.0$ kpc * from the disk center. This location is used to set up the LSR frame for the synthetic observations, which is the reference point for the kinematic properties of the simulated CGM unless otherwise specified. In § 2.4.2.3, we will additionally examine whether the observed kinematic properties depend on the location of the LSR by relocating the mock observer to seven other locations in the mid-plane at the same galactocentric distance.

*We note that $R_0 = 8.0$ kpc is slightly shorter than the current best estimate of the Galactic distance of the Sun ($R_0 = 8.34 \pm 0.16$ kpc, Reid et al. 2014). We calculate the observable mass fraction f_m (see § 2.4.2 for detailed description of f_m) with 8.34 kpc and find it only changes by 0.15%, thus the effect of increasing R_0 by 0.3 kpc is negligible.

Originating from the LSR, we define $\vec{\mathrm{U}}\vec{\mathrm{V}}\vec{\mathrm{W}}$ axes under the right-handed convention: $\vec{\mathrm{U}}$ points towards the galactic anti-center and $\vec{\mathrm{W}}$ aligns with the disk rotation axis. The direction of a sightline is specified by the galactic longitude and latitude (l, b) computed using:

$$b = \frac{\pi}{2} - \arccos(\vec{w} \cdot \vec{r}) \tag{2.1}$$

and

$$l = \begin{cases} \pi + \arccos(\vec{u} \cdot \vec{r}_{uv}) & \text{if } 0 \leq \arccos(\vec{v} \cdot \vec{r}) < \frac{\pi}{2} \\ \pi - \arccos(\vec{u} \cdot \vec{r}_{uv}) & \text{if } \frac{\pi}{2} \leq \arccos(\vec{v} \cdot \vec{r}) \leq \pi, \end{cases} \tag{2.2}$$

where $\vec{r}_{uv}$ is the sightline vector $\vec{r}$ projected onto the disk $\vec{\mathrm{U}}\vec{\mathrm{V}}$ plane, and $\vec{u}$, $\vec{v}$, $\vec{w}$ are unit vectors along the $\vec{\mathrm{U}}\vec{\mathrm{V}}\vec{\mathrm{W}}$ axes, respectively.

The mock observer co-rotates with the simulated disk, and its circular velocity is approximated by the bulk motion of baryons within 1.0 kpc of the LSR. To visualize the overall gas motions in the simulated CGM with respect to the mock observer, we generate sightlines with a spatial interval of $(\delta l, \delta b) = (1^\circ, 1^\circ)$ and calculate the mass fraction of red-shifted gas ($v_{\mathrm{LSR}} > 0$) along each sightline. Figure 2.1 shows the spatial variation of the mass ratio in Aitoff projection, with the galactic center located at the center of the figure and galactic longitude increasing leftwards. Velocity segregation across $l = 180^\circ$ can be observed: gas at $0^\circ < l < 180^\circ$ is largely red-shifted and that at $-180^\circ < l < 0^\circ$ blue-shifted. This is consistent with observations of the MW's CGM whose velocities are greatly shaped by the Galactic differential rotation in the view of local observers (e.g, Wakker & van Woerden 1991; Sembach et al. 2003; Collins et al. 2005; Shull et al. 2009).

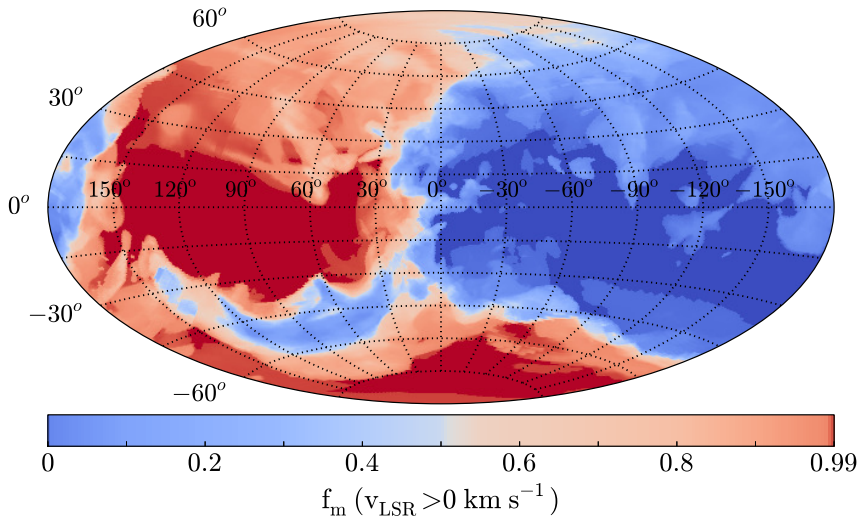

Figure 2.1: Mass fraction of red-shifted gas ($v_{\rm LSR} > 0$ km s^{-1}) in the simulated CGM. The map is in Aitoff projection with galactic center at the center of the figure and galactic longitude increasing leftwards. Due to the circular motion of the LSR, the sky is heavily red-shifted in directions at $0° < l < 180°$ and blue-shifted at $-180° < l < 0°$. The diminishing color scales towards higher latitudes indicate the existance of both red-shifted and blue-shifted gas.

2.3.2 Kinematic Ranges of the Simulated Disk Rotation

The strong emission or absorption from the disk gas has long plagued observations of the MW's CGM. In most directions the Galactic disk gas appears as low-velocity spectral line features that can be efficiently excluded with certain velocity cutoffs. The adopted velocity range for the gas associated with the MW disk is often $|v_{\rm LSR}| < 90 - 100$ km s^{-1} (Wakker 1991a; Wakker & van Woerden 1997; Sembach et al. 2003; Lehner et al. 2012) where $v_{\rm LSR}$ is the velocity with respect to the LSR. A more accurate value is $|v_{\rm DEV}| < 50 - 75$ km s^{-1} (Wakker 1991a; PPJ12) where $v_{\rm DEV}$ is the deviation velocity given by Wakker (1991a) as,

$$v_{\rm DEV} = \begin{cases} v_{\rm LSR} - v_{\rm min} & \text{if } v_{\rm LSR} < 0 \\ v_{\rm LSR} - v_{\rm max} & \text{if } v_{\rm LSR} \geq 0 \end{cases} \tag{2.3}$$

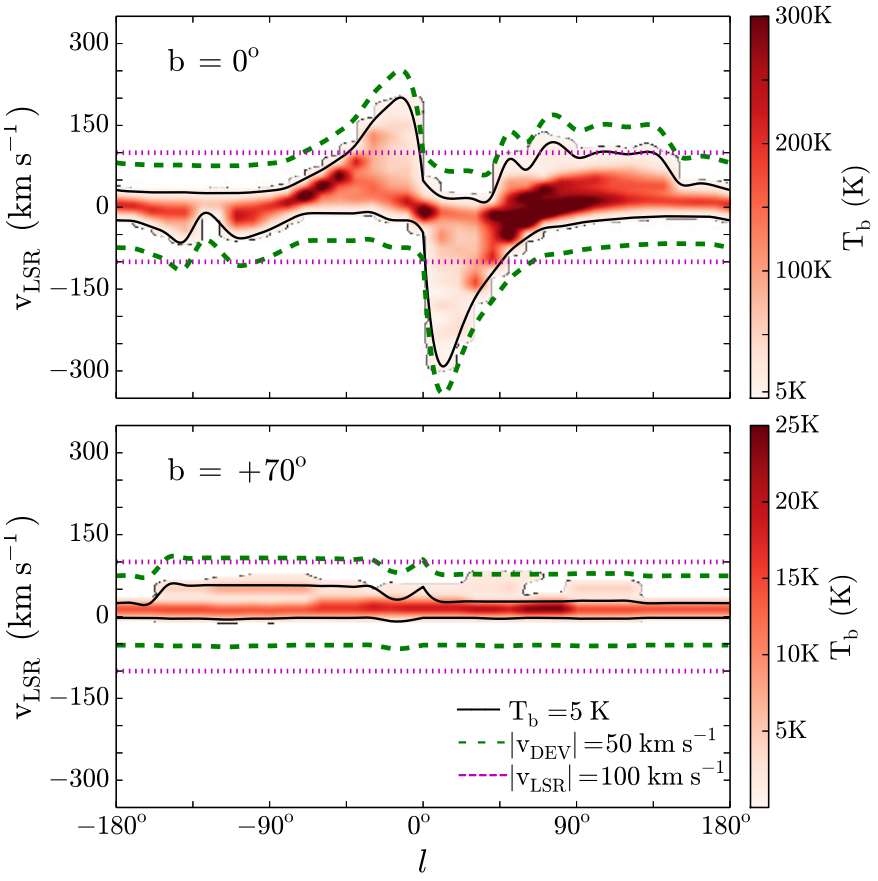

Figure 2.2: H I intensity as a function of LSR velocity and galactic longitude (l) at $b = 0°$ (top) and $b = 70°$ (bottom). The black solid curves represent the $T_b = 5$ K contour used to set the galactic rotation limits (v_{min}, v_{max}) in this work. The green dashed curves show the $|v_{\rm DEV}| = 50$ km s^{-1} dividing lines beyond which the gas in the simulated CGM is observable and the horizontal magenta lines show the $|v_{\rm LSR}| = 100$ km s^{-1} dividing lines.

. The (v_{min}, v_{max}) above is the minimum and maximum LSR velocities compatible with the Galactic differential rotation in a given direction. This can be obtained either by assuming a simple Galactic rotation model or tracking the motions of neutral hydrogen or molecular clouds in the disk (Hartmann & Burton 1997; Dame et al. 2001).

In our synthetic observations, the (v_{min}, v_{max}) is calculated from the synthesized H I 21 cm emission line from the simulated disk (following the description in Draine 2011; also see Kim et al. 2014). We approximate the (v_{min}, v_{max}) by the velocities beyond which

the H I brightness temperature T_b drops below 5 K in an H I spectrum. Figure 2.2 shows two H I position-velocity maps at $b = 0°$ and $b = 70°$, respectively. The 5 K temperature threshold defining the (v_{min}, v_{max}) is marked by two black solid curves. As seen in the top panel, the (v_{min}, v_{max}) are very direction-sensitive which indicates the strong impact of the circular motion of the LSR on the observed radial velocities at low galactic latitudes. In the simulated disk, a small warp is found in the $+\vec{V}$ direction bending towards the $-\vec{W}$ axis and slightly goes beyond the surface of the disk cylindrical region (also see Figure 2.7). This causes the asymmetry of the H I 21cm intensities at $l = \pm 90°$ in top panel. H I intensities below 5 K do not extend significantly, indicating that this cutoff encompasses most of the H I 21 cm emission from the simulated disk.

Using (v_{min}, v_{max}), we define two velocity cutoffs to mask out the low velocity gas in the simulated disk: $|v_{\rm DEV}| \geq 50$ km s^{-1}, which closely traces the shape of the galactic rotation in each direction; and $|v_{\rm LSR}| \geq 100$ km s^{-1}, which is insensitive to direction but also independent of disk rotation models. Gas with velocities beyond (within) these ranges will be referred as "high (low) velocity gas" throughout the paper. In Figure 2.2, the $|v_{\rm LSR}| = 100$ km s^{-1} and $|v_{\rm DEV}| = 50$ km s^{-1} velocity cutoffs are shown as the dotted magenta lines and the dashed green curves. The velocity cutoff of $|v_{\rm LSR}| \geq 100$ km s^{-1} fails to cover high velocity gas near the galactic center which is still associated with the disk, while in other directions it is so wide that excess gas in the simulated CGM is excluded.

2.4 Results

2.4.1 Kinematic Similarities: Simulated CGM vs. $L \sim L^*$ Galaxies

We first compare the kinematic properties of the simulated CGM ($T \leq 10^6$ K) and that observed for the MW. For each sightline through the simulated CGM, we calculate the mass-weighted LSR velocity ($v_{\rm LSR}$) over all of the simulated gas cells as shown in Figure 2.3. Observations of high velocity gas in the MW's CGM from various metal lines are shown as color-coded symbols (e.g., Si II, Si III, and O VI; Sembach et al. 2003; Shull et al. 2009; Lehner et al. 2012), and shades represent the simulated CGM. When the observed CGM gas associated with the Magellanic System is excluded (open symbols at generally $|v_{\rm LSR}| \geq 200$ km s^{-1}), there is overall consistency in the gas kinematics between the simulated CGM and the MW's CGM. The velocity spread of the gas in the simulated CGM is narrower than that of the actual MW. This is most likely due to the mass-weighted algorithm which smooths out high-velocity low-density features. Though the simulated MW does have small satellites, they are not at the scale of the Magellanic System and contribute negligible mass flux (Joung et al. 2012b). In addition, three of four satellites in the simulation at $z \sim 0$ are at velocities ≤ 200 km s^{-1} with respect to the galaxy systemic velocity.

Synthetic observations of the simulated CGM from external views are also conducted so that we can make connections with other $L \sim L^*$ galaxies. We observed the simulated CGM ($T \leq 10^6$ K) with three disk inclinations: 0° (face-on), 45°, and 90° (edge-on). From each inclination, we calculate the line of sight velocities for 500×500 sightlines on a square

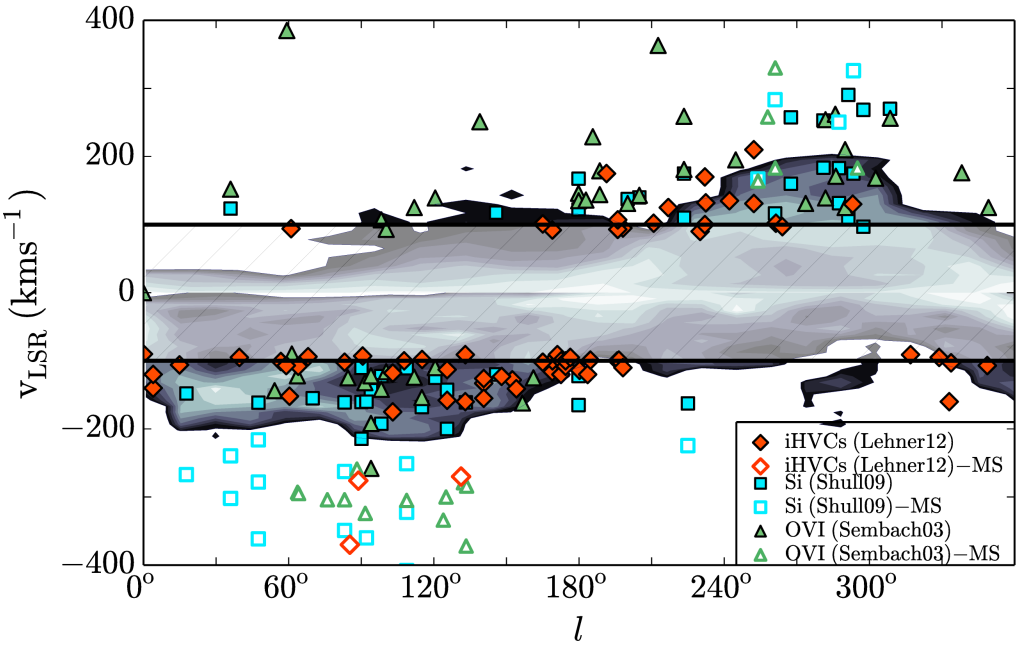

Figure 2.3: The position-velocity (LSR) distribution of the CGM ($T \leq 10^6$ K) when observed from within the simulated disk is shown by the shaded region. The mass-weighted LSR velocities of the simulated CGM gas are shown, with lighter shades indicating a higher density of material. The velocity cutoff at $|v_{\rm LSR}| = 100$ km s^{-1} is shown by the horizontal black lines and the simulated CGM within this cutoff is lightened. Color-coded symbols show the velocity centroids of high-velocity gas in the MW's CGM from observations (Lehner et al. 2012; Shull et al. 2009; Sembach et al. 2003). Open symbols indicate the association of the observed high-velocity gas with the Magellanic System (MS).

grid that spans -250 kpc to 250 kpc (with intervals of 1 kpc) from the galactic center. In Figure 2.4, the line of sight velocity δv with respect to the galaxy systemic velocity as a function of impact parameter is plotted as the gray shades for the simulated CGM. The observation symbols are from the COS-Halos survey (Tumlinson et al. 2013; Werk et al. 2013) and are similarly color and shape-coded as Figure 2.3 showing the observed velocity centroids of different species (i.e., H I, Mg II, C II, C III, Si III and O VI) in the CGM of $L \sim L^*$ galaxies at $z \sim 0.2$. The velocity dispersion of the simulated CGM is $\sigma \approx 53$ km s^{-1}, which is smaller than that derived from the COS-Halos survey ($\sigma \approx 85$ km s^{-1} from the metal lines by Werk et al. 2013 and $\sigma \approx 200$ km s^{-1} in the H I by Tumlinson et al. 2013). Some of

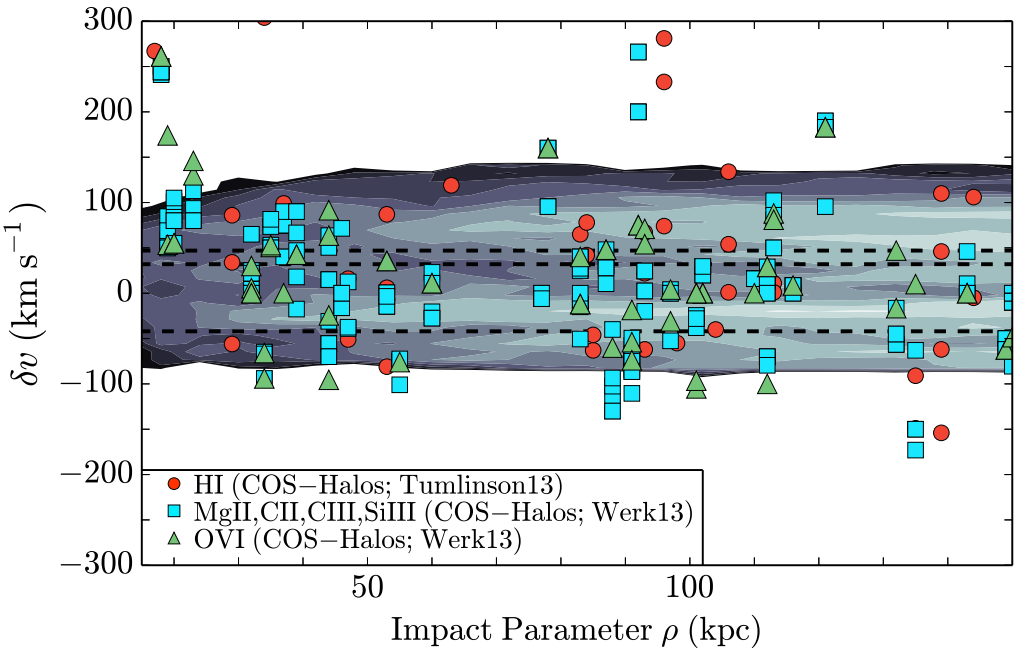

Figure 2.4: The velocities of the CGM ($T \leq 10^6$ K) with respect to the galaxy systemic velocity as a function of impact parameter. The gray shades show the line-of-sight mass-weighted velocities of the gas in the simulated CGM when observed from three external views: edge-on, 45° and face-on. The three horizontal dash lines indicate the median values of the gas velocities from the edge-on view (bottom), 45° (middle) and face-on view (top). Color-coded symbols show the gas centroid velocities of different transition lines from the COS-Halos survey (Tumlinson et al. 2013; Werk et al. 2013). Multiple data points at the same impact parameters represent the multiple component structures along the corresponding line of sight which results from individual Voigt profile component analysis.

the difference could be the lack of AGN feedback in the simulation, but more important effect is likely that only one simulated galaxy is examined in our synthetic observations while in the COS-Halos' sample galaxies may slightly vary in mass, gas content and so on. High velocity outliers can be seen from the H I data (Tumlinson et al. 2013), that may come from potential fast moving satellites in the CGM of the $L \sim L^*$ galaxies or non-relevant cold gas parcels beyond the CGM but intersected by the sightlines. Overall, the kinematics of gas in the simulated CGM when viewed externally is in good agreement with the observations of the CGM of other $L \sim L^*$ galaxies.

When viewed from different inclinations, the mass-weighted velocity of the CGM gas shows asymmetric distributions. This is indicated by the dashed lines in Figure 2.4, which are the median values of the velocity distributions for edge-on (bottom), 45 degree (middle) and face-on (top) views. We find a bulk motion of the simulated CGM with respect to the entire galaxy in a direction parallel to the disk plane with δv of 30 km s^{-1}. This bulk flow therefore contributes to the line of sight velocities of the simulated CGM from the edge-on view, while observations with the face-on view will largely miss it. This is consistent with Kacprzak et al. (2010) who showed that the Mg II absorption line profiles in their sample favor one side of the galaxy systemic velocity, suggesting that the observed velocity spreads may depend on galaxy inclinations.

2.4.2 Gas Observability in the Simulated CGM

2.4.2.1 Overall Gas Observability

We first calculate the mass fraction and spatial distribution of high velocity gas in the simulated CGM. For a given sightline (l, b), the mass fraction f_m of high velocity gas along a path length of 250 kpc is computed. The top (bottom) panel in Figure 2.5 shows the variation of f_m across the simulated galactic sky with a velocity cutoff of $|v_{\rm DEV}| \geq 50$ km s^{-1} ($|v_{\rm LSR}| \geq 100$ km s^{-1}). Close to $l \pm 90^\circ$, large patches with $f_m \rightarrow 1$ are observed. This indicates that most gas along corresponding sightlines move at high velocities which are observable to the mock observer. As mentioned in § 2.3.2, the velocity cutoff $|v_{\rm LSR}| \geq 100$ km s^{-1} is generally too broad for most directions, resulting in more obscuration of the simulated CGM. This reflects in Figure 2.5 (and Table 2.1), where f_m with $|v_{\rm LSR}| \geq 100$ km s^{-1} is

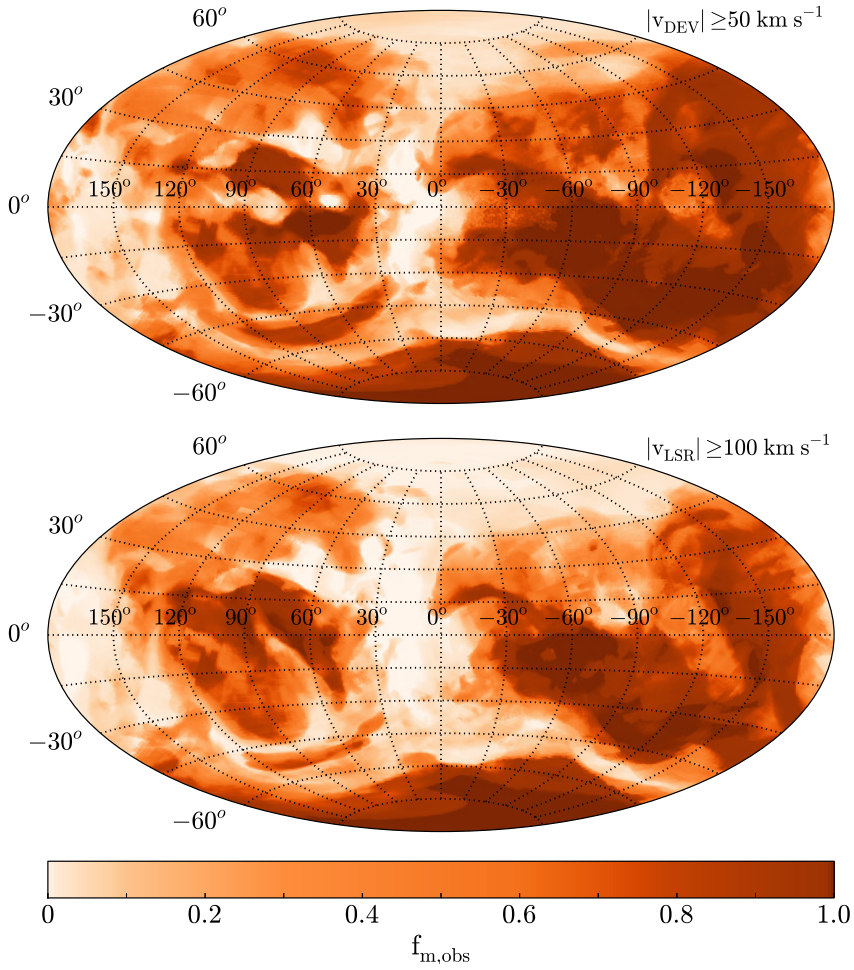

Figure 2.5: Observable mass fraction f_m of the simulated CGM with velocity cutoffs $|v_{DEV}| \geq 50$ km s^{-1} (top) and $|v_{LSR}| \geq 100$ km s^{-1} (bottom). Panels are in the same configuration as Figure 2.1. Sightlines that contain primarily high-velocity CGM are the darkest, while regions where the CGM is largely obscured are the lightest.

generally lower than that with $|v_{DEV}| \geq 50$ km s^{-1}. At the bottom of both panels exists a large orange patch, resulting from high velocity SN-driven outflows from the simulated disk (Joung et al. 2012b). This outflowing gas can also be found in the phase diagrams (Figure 2.6) at temperature above 10^6 K.

Integrating f_m over the whole spherical volume ($r \leq 250$ kpc), we obtain the total mass fraction of high velocity gas for different CGM components defined by temperature

Table 2.1. Observability

Components (1)	Norm. Mass (2)	$f_{m,v_{\rm DEV}}$ (3)	$f_{m,v_{\rm LSR}}$ (4)
CGM ($r \leq 250$ kpc)	1.00	0.54	0.45
$\lvert b\rvert \geq 10^{\circ}$	–	0.44	0.40
$\lvert b\rvert \geq 20^{\circ}$	–	0.33	0.35
$T < 10^5$ K	0.08	0.62	0.55
$10^5 \leq T < 10^6$ K	0.70	0.54	0.44
$T \geq 10^6$ K	0.22	0.53	0.44

Note. — Column 2: Gas mass normalized to the total mass of the halo. Column 3: Mass fraction of high velocity gas with $\lvert v_{\rm DEV}\rvert \geq 50$ km s^{-1}. Column 4: Gas mass fraction with $\lvert v_{\rm LSR}\rvert \geq 100$ km s^{-1}. Row 2: Overall gas observability in the simulated CGM. Row 3: Observability of halo gas at $\lvert b\rvert \geq 10^{\circ}$ and $\lvert b\rvert \geq 20^{\circ}$. Row 4: Gas observability within temperature ranges $T < 10^5$ K, $10^5 \leq T < 10^6$ K and $T \geq 10^6$ K, respectively.

ranges and galactic latitudes. In Table 2.1, column 2 shows the mass of each component normalized to the total gas mass of the simulated CGM. The $f_{m,v_{\rm DEV}}$ ($f_{m,v_{\rm LSR}}$) in column 3 (4) indicates the mass fraction of high velocity gas with the velocity cutoff $\lvert v_{\rm DEV}\rvert \geq 50$ km s^{-1} ($\lvert v_{\rm LSR}\rvert \geq 100$ km s^{-1}). *We find that generally only* ~ 0.5 *of the CGM mass is carried by high velocity gas; this means that nearly half of the mass of the simulated CGM is obscured from observations due to velocity cutoffs*. This is one of the key results of this paper.

Specifically, the mass fractions at $\lvert b\rvert \geq 10^{\circ}$ and $\lvert b\rvert \geq 20^{\circ}$ are computed since low latitude regions in the actual MW's CGM are usually avoided by absorption line experiments due to Galactic emission or absorption. We find that the $f_{m,v_{\rm DEV}}$ ($f_{m,v_{\rm LSR}}$) decreases to ~ 0.4 at $\lvert b\rvert \geq 10^{\circ}$ (~ 0.3 at $\lvert b\rvert \geq 20^{\circ}$), indicating that the observations of the actual MW's CGM may miss more than half of the gas mass. It is notable from Figure 2.5 that the simulated southern sky is covered by more high velocity gas than the northern sky. The MW (and

other actual galaxies) may have this type of imbalance but it is biased by the presence of the Magellanic System in the southern sky.

2.4.2.2 Gas Observability at Various Phases and Galactocentric Radii

In order to study if velocity cutoffs preferentially select gas at certain phases, we calculate the mass fraction of high velocity gas for gas with temperature $T < 10^5$ K, $10^5 \leq T < 10^6$ K and $T \geq 10^6$ K. The last row in Table 2.1 shows that the mass fraction of high velocity gas remains nearly 50% for gas at different phases in spite of their distinct contributions to the total CGM mass. We compare the phase properties of the high velocity and low velocity gas in the simulated CGM in Figure 2.6, and find that they occupy similar regions in the phase space (see below). This indicates that observations of the MW's CGM using various metal lines from different ionization states may miss similar amounts of low velocity gas no matter which temperature ranges they probe.

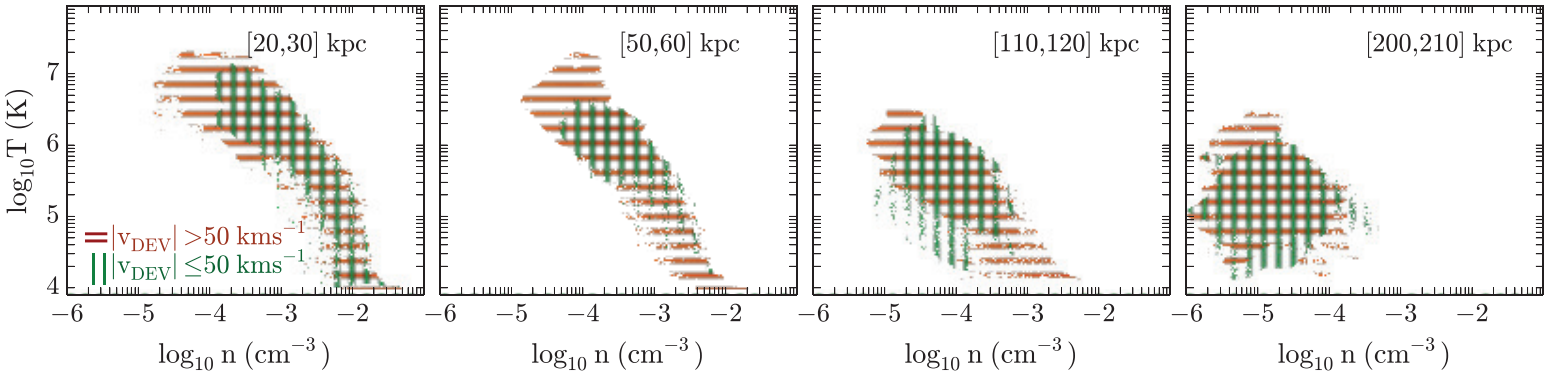

Figure 2.6: Phase diagrams of the simulated CGM in galactocentric shells at [20, 30], [50, 60], [110, 120], [200, 210] kpc. High velocity gas moving at $|v_{\rm DEV}| \geq 50$ km s^{-1} (i.e., observable) is shown by horizontal red strips, while that with $|v_{\rm DEV}| < 50$ km s^{-1} is marked by vertical green.

The H I HVCs in the actual MW's CGM are generally observed within 0.06 $R_{\rm vir,MW}$ while the COS-Halos team finds CGM out to 0.55 $R_{\rm vir,COS}$ [†]. To study if velocity cutoffs preferentially select high velocity gas at certain radii, we decompose the volume of the simulated CGM into a set of galactocentric shells, each with a thickness of Δr = 10 kpc. We separately calculate the mass fraction of high velocity gas within each shell, and find that f_m fluctuates very little from r = 10 kpc to r = 250 kpc, with an average of 0.54 ± 0.03 for $|v_{\rm DEV}| \geq 50$ km s^{-1} (0.44 ± 0.03 for $|v_{\rm LSR}| \geq 100$ km s^{-1}). Such constant f_m throughout the simulated CGM can be explained if the gas velocities of the simulated CGM are relatively continuous along radial directions (see § 2.4.4 for further discussion).

Figure 2.6 shows the phase of high and low velocity gas within the different galactocentric shells. Only the result with $|v_{\rm DEV}| \geq 50$ km s^{-1} is shown since that with $|v_{\rm LSR}| \geq 100$ km s^{-1} is similar. Though the high and low velocity gas in the simulated CGM do generally occupy similar phase space, the high velocity gas is more extended to the high-temperature, low-density region (the top left corner) which corresponds to high velocity, hot outflows in the simulation (Joung et al. 2012b; PPJ12). There is also some high density, low temperature gas in the shells between 50-120 kpc that is only found in the high velocity regime. This corresponds to gas stripped from recently accreted satellites (Joung et al. 2012b) and is a negligible fraction of the total CGM mass. We also examined the simulated CGM at different metallicity bins ranging from 0 − 0.1 $Z\odot$ to > 1 $Z\odot$, and find that the mass fractions of high velocity gas are similar ($f_m \sim 0.6$) in spite of the distinct mass distribution at each bin. These results suggest that we are not biased towards high

[†]We adopt $R_{\rm vir,MW}$ as 250 kpc, same as the value we used for our synthetic observations; and $R_{\rm vir,COS} \approx 300$ kpc is given by the COS-halo teams (Werk et al. 2014).

velocity gas ($T \leq 10^6$ K) having specific properties that may represent distinct origins.

Within each galactocentric shell, high velocity gas can generally be found at directions towards $l \pm 90^\circ$ which is similar to the spatial distribution of the overall case shown in Figure 2.5. This is to say, the velocity fields in the simulated CGM are closely correlated in space throughout the volume. This spatial coherence is in large part due to the circular motion of the LSR, which shifts halo gas around $l \pm 90^\circ$ to high velocity by adding extra components to the gas radial velocity with respect to the LSR. On the other hand, such large scale velocity correlation is also aided by the presence of large scale gas flows, such as feeding filaments and polar outflows.

2.4.2.3 Varying the Location of the Mock Observer

Gas observability in the simulated CGM discussed above can be biased since the mock observer is so far fixed at one location in the disk mid-plane. Local activities such as turbulence and SN-driven outflows may cause non-negligible effects on the corresponding synthetic observations. In this section, we vary the location of the mock observer in the disk mid-plane and study if the change of the reference LSR affects the observed gas kinematics in the simulated CGM.

We relocate the mock observer to seven other places in the simulated disk with an angular separation of $\phi = 45^\circ$, where ϕ is the polar angle on the fiducial $\vec{U}\vec{V}$ plane defined in § 2.3 with $+\vec{U}$ being the polar axis. Each location is 8.0 kpc from the galactic center and the velocity of a given LSR is again averaged over the baryons in its local neighbourhood in order to closely represent the circular motion of the disk rotation at that location. We

Table 2.2. Variation of Observability

ϕ	0°	45°	90°	135°	180°	225°	270°	315°
$f_{m,v_{\rm LSR}}$	0.45	0.39	0.55	0.70	0.67	0.64	0.53	0.45

Note. — Mass fraction of high velocity gas as a function of the locations of the mock observer. Velocity cutoff is set as $|v_{\rm LSR}| \geq 100$ km s^{-1}. Each location is 8.0 kpc from the galactic center, and $\phi = 45^{\circ}$ apart where ϕ is the polar angle on the $\vec{\rm U}\vec{\rm V}$ plane defined in § 2.3.

follow the same procedures described in § 2.4.2.1 and calculate the mass fraction of high velocity gas in the simulated CGM from corresponding new locations. We only apply $|v_{\rm LSR}| \geq 100$ km s^{-1} in our calculations but note that the values with $|v_{\rm DEV}| \geq 50$ km s^{-1} will be similar considering the results in § 2.4.2.1.

Table 2.2 shows the mass fraction $f_{m,v_{\rm LSR}}$ of high velocity gas in the simulated CGM as observed from new locations. $f_{m,v_{\rm LSR}} = 0.45$ at $\phi = 0^{\circ}$ corresponds to the value from the original LSR, which has been shown in Table 2.1. The gas observability in the simulated CGM varies from 0.39 to 0.75 (with a mean of 0.55) as the angular location of the mock observer changes. As indicated in § 2.4.1, a net bulk flow ($\delta v \sim 30$ km s^{-1}) of the simulated CGM with respect to the galaxy is observed in our simulation. This may largely cause the variation of $f_{m,v_{\rm LSR}}$ since the calculations of the velocities of the LSR only consider the bulk motions of local neighbourhood.

We examine the spatial distribution of high velocity gas in the simulated CGM as observed from these eight different locations, and find similar high velocity patterns as have been seen in Figure 2.5. Except for the hot outflowing gas towards the poles, most high velocity gas is observed in directions around $l \pm 90^{\circ}$, indicating that gas velocities at

low galactic latitudes are greatly shaped by the circular motion of the LSR in the disk (see also Figure 2.1). In all cases, we still find that nearly half of the CGM mass is carried by low velocity gas, which is obscured due to velocity cutoffs in spite of different locations of mock observers in the disk plane.

2.4.3 H I Observability in the Simulated CGM

In this section, we calculate the distribution and covering fraction of high velocity H I in the simulated CGM. We only present the H I behaviors with velocity cutoff $|v_{\rm DEV}| \geq 50$ km s^{-1}, with the knowledge that the results with $|v_{\rm LSR}| \geq 100$ km s^{-1} are similar according to Figure 2.5. For a given sightline, we compute the column density of high velocity H I ($N_{\rm HI}$) by summing up the H I retained by all the simulated gas cells with $|v_{\rm DEV}| \geq 50$ km s^{-1} along the corresponding path ($\sim$ 250 kpc). We also use different path lengths ranging from 50 to 300 kpc and find little variations among those $N_{\rm HI}$ values we have obtained. This is because most of the H I resides at radii close to the disk except for satellites, an increase in path length will not necessarily gather more H I.

Figure 2.7 shows the spatial distribution of high velocity H I in the simulated CGM. The high $N_{\rm HI}$ clumps near $(l, b) = (-90^\circ, -30^\circ)$ are the warp of the disk bending downwards which was not included in the cylindrical disk region as defined in § 2.3.2 (see also Fernández et al. 2012). This uneven distribution of H I at $l = \pm 90^\circ$ causes the asymmetric H I 21 cm emission in Figure 2.2. At higher elevation above the disk plane, elongated structures can be seen which may relate to gas-rich satellites or accreted gas along filamentary streams in the simulated CGM (Joung et al. 2012b; Fernández et al. 2012). Besides these

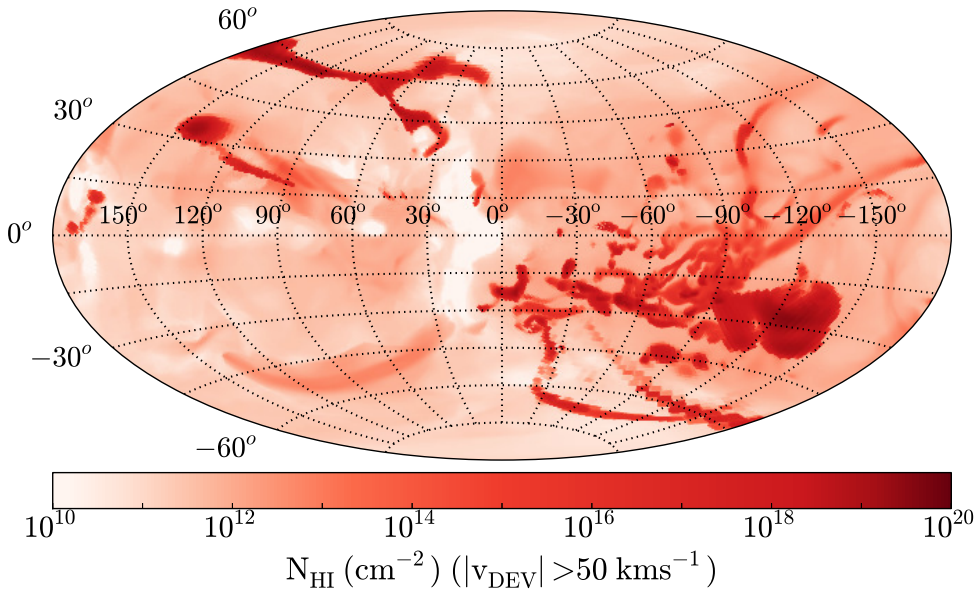

Figure 2.7: Column density of high velocity H I ($|v_{\rm DEV}| > 50$ km s^{-1}) in Aitoff projection. The galactic center is located at the center of the figure, and galactic longitude l increases from left to right.

distinct dense structures, most of the simulated galactic sky is covered by very diffuse H I.

Figure 2.8 shows the covering fractions of high velocity H I and the H I without velocity cutoffs in the simulated CGM at different column sensitivities. Regions at $|b| < 20°$ are purposely omitted in order to link to the actual observations of the MW's CGM. A comparison between the black solid line (without velocity cutoffs) and the green-dash lines (with velocity cutoffs) indicates that the covering fraction of the high velocity H I is reduced to only 0.29 (from 0.48) at $N_{\rm HI} \geq 10^{18}$ cm^{-2}. More generally, the covering fractions of the high velocity H I are ~ 0.2 less than those without velocity cutoffs at a given column density sensitivity. Color-coded symbols at $N_{\rm HI} \sim 10^{18}$ cm^{-2} mark the measured covering fractions of HVCs in the actual MW's CGM: 0.18 at $N_{\rm HI} > 2\times10^{18}$ cm^{-2} (Wakker 1991a)‡, 0.37 at $N_{\rm HI} > 7\times10^{17}$ cm^{-2} (Murphy et al. 1995), and 0.37 at $N_{\rm HI} > 8\times10^{17}$ cm^{-2} (Lockman

‡No latitude limitation $|b| \geq 20^{\circ}$ was adopted by Wakker (1991a).

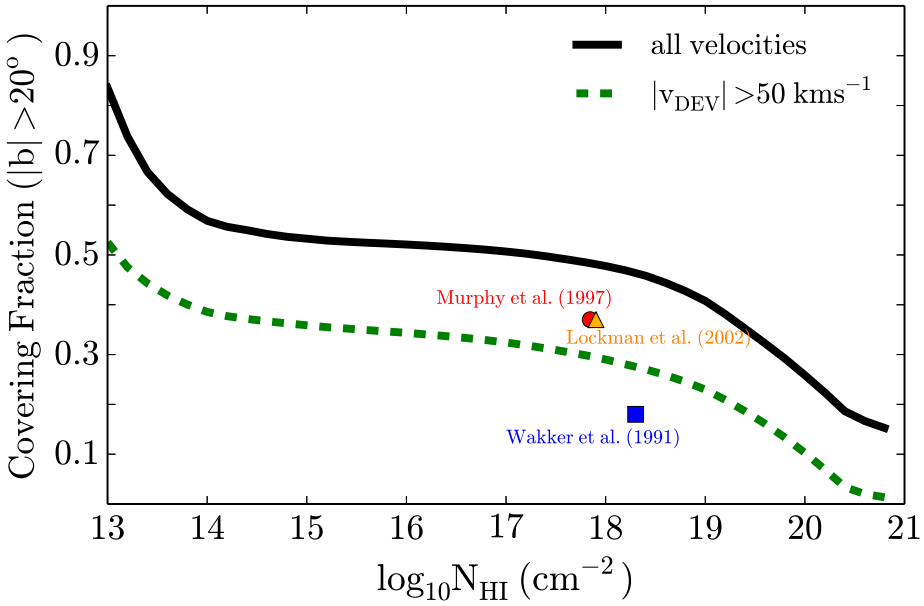

Figure 2.8: H I covering fractions vs. H I column sensitivities in the simulated CGM ($|b| \geq 20°$). Black solid line: H I without any velocity cutoffs; green dashed line: H I with $|v_{DEV}| \geq 50$ km s^{-1}. Color-coded symbols: observed H I HVCs covering fractions in the actual MW's CGM by Wakker (1991a), Lockman et al. (2002) and Murphy et al. (1995).

et al. 2002). The consistency between the measured H I HVCs and the simulated high velocity H I column density indicates that a considerable fraction of low velocity H I may remain hidden in the actual MW's CGM (see § 2.5.3 for a detailed discussion of potential missing low velocity H I complexes).

2.4.4 Additional Mass Obscuration in the Outer Halo

Apart from the mass obscuration due to foreground low velocity disk gas, high velocity gas in the outer halo may be additionally blocked by nearby halo gas if it moves at similar velocities. In another words, even at high velocity regimes spectral lines from the gas in the outer halo may blend with signals from nearby gas if line separations (i.e., velocity differences) are too small to detect. Recognition of these close line profiles will depend on

the resolution of observations.

To quantify this issue, we extract two data sets from the simulation which represent an inner halo ($r \leq$30 kpc) and an outer halo ($50 \leq r \leq 150$ kpc), respectively. Maps of high velocity gas in both halos in Aitoff projection show similar patterns as those in Figure 2.5. For a given sightline, we calculate the velocity differences between the high velocity gas in the inner halo and that in the outer halo. This is separately performed for red-shifted and blue-shifted gas. Gas in the outer halo is observable only if: (1) its velocity is high enough to survive the $|v_{\rm DEV}| \geq 50$ km s^{-1} or $|v_{\rm LSR}| \geq 100$ km s^{-1} cutoffs; (2) its velocity differs from that of the gas in the inner halo by a number Δv which is the chosen minimum detectable line separation.

Table 2.3 shows the observable mass fraction of high velocity gas in the outer halo that satisfies both criteria under a set of minimum detectable line separations Δv ranging from 0 km s^{-1} to 30 km s^{-1}. If the spectral resolution is high enough ($0 < \Delta v \leq 10$ km s^{-1}) so that gas at similar velocities in the inner and outer halo would be distinguishable, we find that the observable mass fraction in the outer halo is 0.47 at $|v_{\rm DEV}| \geq 50$ km s^{-1} (0.43 at $|v_{\rm LSR}| \geq 100$ km s^{-1}). However, the observable mass fraction in the outer halo decreases as the spectral resolution falls off (i.e., Δv becomes larger). For example, it is significantly reduced by a factor of two (from 0.47 to 0.23) if $\Delta v = 30$ km s^{-1}. This indicates that less than 50% of gas is accessible to local observers due to a combination effect of velocity cutoffs and obscuration by nearby halo gas. In particular, this has a potential influence on the mass estimate of the ionized HVCs by Lehner et al. (2012) who compared the covering fractions from a stellar sample with that from a QSO sample, and constrain the clouds to

Table 2.3. Gas observability in the outer halo ($50 \leq r \leq 150$ kpc)

Min. Sep. Δv	0 km s^{-1}	10 km s^{-1}	20 km s^{-1}	30 km s^{-1}
$f_{m,v_{\rm DEV}}$	0.47	0.39	0.30	0.23
$f_{m,v_{\rm LSR}}$	0.43	0.31	0.23	0.16

Note. — Δv means a minimum detectable line separation in spectroscopic observations; $f_{m,v_{\rm DEV}}$ and $f_{m,v_{\rm LSR}}$ are the observable mass fractions of gas in the outer halo at $|v_{\rm DEV}| \geq 50$ km s^{-1} ($|v_{\rm LSR}| \geq 100$ km s^{-1}) with the corresponding Δv.

be within 5 – 15 kpc.

2.5 Discussion

The CGM is key to our understanding of galactic accretion and feedback processes. It has been claimed that the CGM can solve the "missing baryon problem" from studies with both observations (e.g., Werk et al. 2014) and simulations (e.g., Cen & Ostriker 2006; Sommer-Larsen 2006). In this section, we re-evaluate the total mass of the MW's CGM taking into account the obscured mass due to the velocity cutoffs, and compare the obscuration-corrected MW's CGM with the CGM of other $L \sim L^*$ galaxies. In the end of this section, we discuss potential observations of obscured low velocity gas in the MW's CGM through non-kinematic methods.

2.5.1 Obscuration-corrected Mass of the MW's CGM

Cold gas ($T < 10^4$ K) in the actual MW's CGM has been broadly studied with H I 21 cm observations, while the warm ($\sim 10^{4-5}$ K) and warm-hot gas ($\sim 10^{5-6}$ K) has been revealed by UV absorption lines in the spectra of background sources (stars or QSOs) and Hα emission. Mass estimates of this gas focus on available high velocity lines in spectra, with little evaluation of the mass contribution from low velocity obscured halo gas. Thus in this section we apply the observable mass fraction $f_m = 0.5$ to current mass estimates of the MW's CGM and obtain an obscuration-corrected mass for CGM gas at various phases. We do not apply the correction to gas from the Magellanic System as this system is moving at high velocity relative to the MW (Kallivayalil et al. 2013) and the vast majority of the gas is likely to be observable based on predictions from the models (Besla et al. 2010; Connors et al. 2006). This type of large accretion event is also not presently occurring in our simulated galaxy halo, and is rare in observations of MW-like galaxies (Tollerud et al. 2011).

Cold gas in the MW's CGM is usually in the form of discrete H I structures called HVCs. Galactic HVCs have a total mass of $M_{HI} \sim 3 \times 10^7\ M_\odot$, excluding the HVCs associated with the Magellanic System. This includes 13 H I complexes within 10 kpc of the disk and the remaining small HVCs placed at a general distance of 10 kpc (PPJ12). Considering the 50% mass obscuration, the total mass of Galactic HVCs is therefore corrected to $M_{HI}^{corr} \sim 6 \times 10^7\ M_\odot$. This corrected H I mass in the MW's CGM without the Magellanic System is consistent with observations of M31's halo gas (Thilker et al. 2004). If we include the mass from the high velocity gas of the Magellanic System (excluding

the Magellanic Clouds themselves), the mass increases by $M_{HI} = 3 \times 10^8 (d/55\ \mathrm{kpc})^2\ M_\odot$ (Putman et al. 2003; Brüns et al. 2005).

There are recent mass estimates of warm and warm-hot gas in the MW's CGM. Lehner & Howk (2011a) found that the ionized HVCs reside within 5-15 kpc using the constraint from halo stars. The total mass of warm and warm-hot gas is thus $M_{\mathrm{warm}} \sim 1.1 \times 10^8 (d/12\ \mathrm{kpc})^2\ M_\odot$ (see also Shull et al. 2009). If the observable mass fraction $f_m = 0.5$ is applied, the mass of warm and warm-hot gas will be $M_{\mathrm{warm}}^{\mathrm{corr}} \sim 2.2 \times 10^8 (d/12\ \mathrm{kpc})^2\ M_\odot$. This mass is almost certainly a lower limit given the consistent finding of warm and warm-hot gas at large radii in the CGM of other galaxies (e.g., Tumlinson et al. 2011; Chen et al. 2010b; Werk et al. 2014). Some of the MW's CGM at large radii may be too diffuse to detect from within the disk using background QSOs. One should also consider that in § 2.4.4 we show that distant gas in the CGM can be obscured by nearby gas if they are moving at similar velocities. This shadowing effects from high velocity gas in the inner halo may cause an additional 50% of mass obscuration in the outer halo in observations with a spectral resolution of ≥ 30 km s^{-1}. Thus the mass estimate by Lehner et al. (2012) shall be interpreted with caution as they do not take into account the local halo shadowing effects. We do not attempt to correct for this additional obscuration here or calculate a mass for gas that does not have a distance constraint. A recent estimate of the total mass in warm and warm-hot gas from the Magellanic System (excluding the Magellanic Clouds) is $M_{\mathrm{warm,MS}} \approx 1.5 \times 10^9 (d/55\ \mathrm{kpc})^2\ M_\odot$ (Fox et al. 2014).

Miller & Bregman (2015) estimate the mass of hot gas ($T \gtrsim 10^6$ K) in the MW's CGM to be $4.3 \times 10^{10}\ M_\odot$ within 250 kpc (or $3.8 \times 10^9\ M_\odot$ within 50 kpc) using O VII and O VIII

lines through X-ray observations (see also Gupta et al. 2012). This mass is consistent with non-spectroscopic observations (see Anderson & Bregman 2010 for a detailed discussion). Given the low velocity resolution of X-ray observations, the mass estimates of hot halo gas are usually based on line profile fitting to exclude local emission components rather than applying velocity cutoffs. Thus our mass obscuration correction is not applicable to their mass estimates. In Figure 2.6, we also show that the gas that would be at highest velocities and potentially directly detectable is the most diffuse and hot and the most difficult to detect.

2.5.2 Is the MW's CGM an Outlier?

In this section we compare the MW's CGM to that of other $L \sim L^*$ galaxies for which large amounts of warm and warm-hot (10^{4-6} K) have been found. We start by looking at the mass estimates and then, given the modeling required to obtain total masses, assess the difference in terms of the column density. As shown in Figure 2.4, external galaxies do not have the same obscuration effect; the observations of background QSOs often show gas in CGM very close to the systemic velocity of the galaxy.

2.5.2.1 CGM Mass

Stocke et al. (2013) found $\sim 10^{10}$ $M_\odot$ of CGM ($T \sim 10^4$ K) within the virial radius of late-type galaxies at $z \leq 0.2$ (with 75% of the mass contained in the inner half of the virial radius). Werk et al. (2014) also suggest a conservative estimate of 2×10^{10} $M_\odot$ for the 10^4 K CGM gas within 160 kpc of the $L \sim L^*$ galaxies at $z \sim 0.2$. This is $\sim 3 \times 10^9$ $M_\odot$ within 50

kpc of the disk and $\sim 4 \times 10^8$ $M_\odot$ within 15 kpc based on the gas surface density profile they adopt. The value is comparable to the MW estimate (Section 2.5.1) within small radii, but the MW value is still low and the external galaxy results indicate there is most likely a large amount of gas undetected at large radii.

Since the COS results are for galaxies at somewhat higher redshift, we examined the simulated CGM at different redshifts to assess if any discrepancy could be due to gaseous halo evolution with time. Negligible variation is found for the mass of the simulated CGM from $z = 0.3$ to $z = 0.0$ (within a fixed radius of 250 kpc). This is consistent with Stinson et al. (2012) who examined the CGM gas content in an $L = 1\,L^*$ star-forming galaxy, and found little variation of CGM mass within the virial radius since $z = 0.5$. Thus, the difference in redshift of the external galaxies and the MW is not expected to greatly affect the CGM mass.

There are some remaining issues with the CGM mass estimates for external galaxies. The warm CGM pressure that Stocke et al. (2013) derive ($P/k \sim 10$ cm^{-3} K) is an order of magnitude lower than that typically found from observations of clouds in the halo of the Milky Way (Fox et al. 2010; Hsu et al. 2011). This may be due to uncertainties related to the photoionization modeling. In addition, one of the mass estimates for the 10^4 K CGM by Werk et al. (2014) is based on the assumption that the $n_{\rm HI}$ along each sightline is representative of all of the gas at a given impact parameter. However, observations of the MW's CGM (e.g., Sembach et al. 2003; Shull et al. 2009) and external galaxies (e.g., Werk et al. 2014) indicate that multiple discrete absorbers exist along sightlines. Our synthetic observations from external views and from within the simulated galaxy also

suggest multiple absorbers at discrete velocities. Although the other method that Werk et al. (2014) applied takes into account the volume filling factor, this mass estimate comes with large uncertainty since it is largely dependent on the calculation of $N_{\rm HI}$ and $n_{\rm HI}$.

Thus far, we cannot confirm that the MW is an outlier in CGM mass. Other potential factors, such as the completeness of observations and the gas density profile of the CGM, need to be more fully considered.

2.5.2.2 CGM Column Density

Column densities of metal lines detected in the MW's CGM are generally lower than those of external galaxies. For example, Tumlinson et al. (2011) found a typical value of $\log {\rm N_{OVI}} = 14.5$ for 27 out of 30 star-forming galaxies with sSFR $\geq 10^{-11}$ yr^{-1}, which is higher than the mean value of $\log \left\langle {\rm N_{OVI}} \right\rangle = 14.0$ (at sSFR $\sim 2-6\times10^{-11}$ yr^{-1}) for the MW's CGM (Sembach et al. 2003). To evaluate this discrepancy in column density, variations of path length from observations of the MW's CGM to those of external galaxies need to be considered as well as the velocity obscuration effect.

As an approximation, we compute the column densities of warm-hot gas $\rm N_{wh}$ in the simulated halo. We calculate the ratio of $\rm N^{ex}_{wh}/N^{in}_{wh}$, where "ex" indicates column densities of the warm-hot CGM as observed from external views (edge-on, 45° and face-on), and "in" for that with an internal view as described in § 2.3. For $\rm N^{in}_{wh}$, we sum up all the material along the sightlines and do not separate high velocity and low velocity halo gas so that the influence of path length difference independent of disk obscuration effects can be evaluated. We find that the ratio of external to internal column density varies from

0.9 to 5.0 with a mean of 2.34. This implies that the column densities of CGM in external galaxies are intrinsically higher by a factor of $\sim$ 2.0 than those of the MW because of the difference in path length. Taking this into account, we can correct the column densities of the MW's CGM to $\log \left\langle N_{OVI} \right\rangle = 14.30$, similar to other $L \sim L^*$ galaxies. This is a lower limit given that the low velocity gas obscured by MW's disk could make an additional contribution to the average column density. Thus we find the MW's halo detected in O VI is not an outlier in column density.

2.5.3 Obscured Low Velocity H I complexes

In this section we examine the obscured halo gas in the context of complexes of HI gas that may exist in the Milky Way halo. These complexes would be low velocity halo clouds (LVHCs), or halo clouds that have LSR velocities indistinguishable from those in the MW disk, but are otherwise akin to HVCs (Wakker 1991b; Peek et al. 2008). These LVHCs may represent bulk flows within the MW halo that have been missed by standard HVC studies due to our location in the disk.

There is some evidence for MW LVHCs from far-infrared (FIR) studies of low velocity clouds that find a small number have undetectable FIR emission, similar to HVCs (Peek et al. 2009; Saul et al. 2014). This lack of FIR emission in HVCs is likely due to some combination of low dust content and weak dust heating from the interstellar radiation field. Peek et al. (2009) examined the ratio of dust FIR emission to H I gas column density and found several potential LVHCs, in particular L2 and L5 noted in Figure 2.9. Saul et al. (2014) examined this ratio for a larger population of low velocity clouds and identified

an entire complex of potential LHVCs in a region of sky near a HVC complex known as the WA complex. Saul et al. (2012) referred to this potential LVHC population as the +WQ3 clouds. As can be seen in the left panel of Figure 2.9, there is a position-velocity link between the +WQ3 clouds, the WA complex, and L2 and L5, indicating these clouds represent a bulk flow that was not previously recognized in halo gas studies.

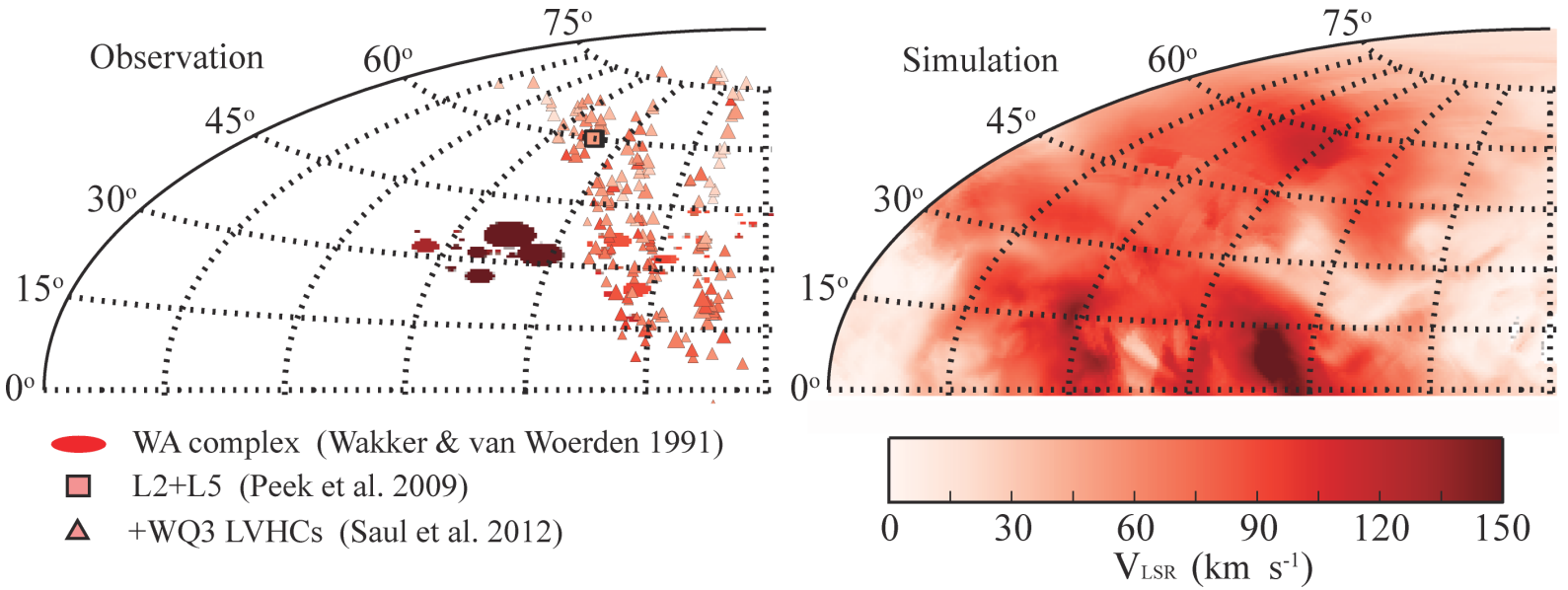

Figure 2.9: Left: the WA complex from the HVC catalog of Wakker & van Woerden (1991) is shown in ellipses. The size of the ellipse indicates the sky coverage of each WA HVC, but does not correspond to the shape of the observed WA HVCs on the sky. The L2+L5 (Peek et al. 2009) and +WQ3 LVHCs (Saul et al. 2012) are indicated by squares and triangles respectively, although their sizes are not accurately indicated. The color of the symbols indicates the LSR velocities. Right: the mass-weighted LSR velocities of the simulated CGM of the same patch of sky. The velocities shown in both panels are in the same color scale as is indicated by the color bar. A velocity gradient can be clearly seen both in the MW and the simulated CGM.

To examine if we see similar LVHC features in the simulated CGM, we plot the LSR velocities of gas in the simulated CGM for the same patch of sky as the clouds discussed above in the right panel of Figure 2.9. We find a velocity gradient in the simulated galactic sky, which is consistent with the observed pattern from complex WA to the L2, L5 and +WQ3 LVHCs. This implies that those regions with low $v_{\rm LSR}$ towards the galactic center and anti-galactic center in the simulated halo have populations of LVHCs, similar to what the MW FIR studies seem to be finding. Since the low $v_{\rm LSR}$ regions (i.e., the low f_m regions in Figure 2.5) are spatially coherent, we expect there are additional large LVHC complexes in the MW's CGM which have been missed entirely due to the velocity cutoffs provided by the disk emission.

2.6 Conclusion

When we observe the MW's CGM, the low velocity gas is missing and we are biased towards high velocity gas due to disk contamination. To assess the amount of obscured low velocity halo gas and its contribution to the MW CGM's baryon mass, we conduct synthetic observations of a simulated MW-mass galaxy. We embed mock observers inside the simulated disk and observe outward to examine gas kinematics as shaped by galactic rotation. We also observe the simulated CGM externally for three different disk inclination angles. The synthetic observations of the simulated CGM with inside-out views and external views show comparable kinematic properties with the MW's CGM and that of other $L \sim L^*$ galaxies.

Our main results can be summarized as follows:

1. The mean mass fraction of high velocity (observable) gas in the simulated CGM is 0.55 (Figure 2.5; Table 2.1) as is seen by the mock observer in the simulated disk. This value fluctuates from 0.39 to 0.75 as the location of the mock observer changes.

2. Large spatially-coherent velocity fields are seen in the simulated CGM, where most of the high velocity gas is at low galactic latitudes and the low velocity gas generally exists at higher galactic latitudes. This suggests that large H I complexes moving at low velocities in the MW's CGM may be missed by observers located at solar radius.

3. Given the similarity between the simulation and the MW's CGM kinematics, we find that the obscuration-corrected mass of the MW's CGM ($T \leq 10^6$ K) is 2.8×10^8 $M_\odot$ excluding the Magellanic System. This gives the lower bound of the CGM mass since current mass estimates are limited to the inner halo where reliable distance constraints can be found. Although the corrected mass of the MW's CGM is below the CGM mass of other $L \sim L^*$ galaxies, we find similar column densities for O VI lines after correcting for the difference in path length between observations of the MW's CGM and that of external galaxies.

4. Obscured low velocity gas and observable high velocity gas in the simulated CGM closely overlap in phase space, indicating that this 50% obscuration in mass affects observations of gas at most phases at $T < 10^6$ K (Figure 2.6). This is to say, observations of the MW's CGM using various metal lines at different ionization states generally miss 50% of CGM gas because it moves at low velocities. In addition, no significant difference in metallicity is found between the low velocity and high

velocity gas.

5. Breaking the simulated CGM into a series of galactocentric shells, we find that the observable mass fraction does not vary with galactocentric distance (Figure 2.6). The spatially coherent distribution of high velocity gas in the inner and outer halo may significantly reduce the gas observability in the outskirts of the MW's CGM. This happens if distant high velocity halo gas moves at velocities close to that of the nearby halo gas so that their line separations in spectra are too small to recognize.

Acknowledgement. We thank Greg Bryan for useful discussions on the interpretation of multiphase gas and kinematics in the simulation throughout this project, and Jessica K. Werk and Nicolas Lehner for helpful discussions on gas column densities. MEP acknowledges funding from NSF Awards AST-1008134 and AST-1312888, and the Clare Boothe Luce Program. MRJ acknowledges funding from AST-1312888. JEGP was supported by HST-HF-51295.01A, provided by NASA through a Hubble Fellowship grant from STScI, which is operated by AURA under NASA contract NAS5-26555.

Chapter 3

The Circumgalactic Medium of the Milky Way is Half Hidden. II: HST/COS Observations with 132 Background Quasars

3.1 Introduction

The star-forming disk of a galaxy is embedded in a massive multiphase plasma, the so called circumgalactic medium (CGM). The galaxy grows by accreting material from the CGM, while the CGM is enriched, heated, and stirred by outflows from the galaxy (Putman

This chapter is a reproduction of a paper by Zheng, Peek, Putman & Werk (2018). This paper was still under peer review at the time of the completion of this dissertation. Please find the updated version of this chapter at https://arxiv.org/abs/1710.10703.

et al. 2012; Tumlinson et al. 2017). One of the tools proven most useful for studying the CGM of galaxies is absorption-line observations towards background quasars (QSOs), providing rest-frame observations of the multi-phase CGM with weakly (e.g., Mg II, Si II) or highly ionized metals (e.g., O VI). Significant evidence has been found for the CGM as a massive, multiphase reservoir for sub- to super-L^* galaxies at $z \lesssim 0.5$ (e.g., Chen et al. 2010a; Prochaska et al. 2011; Stocke et al. 2013; Werk et al. 2014; Bordoloi et al. 2014; Liang & Chen 2014; Burchett et al. 2016; Prochaska et al. 2017; Keeney et al. 2017).

The star-forming disk and CGM are closely connected via inflows and outflows, forming an active disk-halo interface. The interface is difficult to probe due to its spatial and kinematic proximity to the dense disk material and the complicated inflow and outflow interplay. For nearby extragalactic systems, the disk-halo interface can be studied in edge-on star-forming galaxies in Hα or H I 21cm emission lines, often recognized as the diffuse ionized gas (DIG) or the extraplanar gas (e.g., Rand 1997, 2000; Fraternali et al. 2005; Boettcher et al. 2016). Recent galaxy surveys with integral field units (IFU), such as the SAMI Galaxy Survey (Allen et al. 2015; Ho et al. 2016) and MaNGA (Bundy et al. 2015; Bizyaev et al. 2017), also detect the disk-halo interface in Hα in several dozens of edge-on nearby galaxies.

The disk-halo interface is commonly found to co-rotate with the disk. The rotation velocity of the gas at the interface gradually declines as a function of distance from a galaxy plane. This is referred to as halo lagging. Deep H I observations of edge-on galaxies in the local universe show a halo lagging of $dv_{\rm rot}/dz \sim 15 \pm 4$ km s^{-1} kpc^{-1}, where z is the distance from the disk plane (Marasco & Fraternali 2011). A similar vertical falloff

of 22 ± 6 km s^{-1} kpc^{-1} is found within 100 pc of the MW's plane (Levine et al. 2008). With a sample of 67 edge-on galaxies from the MaNGA survey, Bizyaev et al. (2017) found that the halo lagging scales with galaxy stellar mass: low mass galaxies ($M_* \sim 10^{9.5}$ $M_\odot$) tend to have lower lagging with $dv_{\rm rot}/dz \lesssim 10$ km s^{-1} kpc^{-1}, while massive systems ($M_* \sim 10^{10.5}$ $M_\odot$) are more likely to have larger halo lagging with $dv_{\rm rot}/dz \sim 40$ km s^{-1} kpc^{-1}.

The MW's disk-halo interface, also often referred to as the gaseous Galactic thick disk (Savage et al. 2003; Savage & Wakker 2009, hereafter SW09; Wakker et al. 2012, hereafter W12), is the only one that has been broadly observed and studied. Its multiple gas phases, temperature gradient, scale height, and kinematics are among those properties that are of great interest. The H I layer of the MW's disk has a thickness of ≤ 220 pc at $R < R_\odot$ and flares dramatically beyond the solar circle (Dickey & Lockman 1990). The ionized gas with different phases occupies various vertical layers beyond the H I plane (Putman et al. 2012), usually modeled as symmetrical flat slabs with exponential density profiles (Savage et al. 1997; Savage et al. 2003; Bowen et al. 2008; SW09; W12). By investigating ionic absorption lines within $|v_{\rm LSR}| \lesssim 100$ km s^{-1} seen toward MW's halo stars and background QSOs, SW09 found that the scale heights of the MW's disk-halo interface are $\sim 3-4$ kpc for Si IV, C IV, and O VI if modeled with flat slabs. We will discuss their analyses further in § 3.4.1. Here we note that SW09 included 15 QSOs and six stellar sightlines in the Large/Small Magellanic Clouds (LMC/SMC) to determine the flat-slab scale height, which may result in bias since it is unclear where the ionized gas lies along the line of sight toward these distant targets.

Unlike halo star spectra, every QSO spectrum contains absorption-line signatures

from the MW's interstellar (ISM), disk-halo interface, and CGM. In fact, Savage et al. (2003) report that a flat slab is a poor fit to the O VI absorption-line data observed with QSO sightlines. We raise the question as to whether the QSO absorption-line measurements are suitable for MW disk-halo studies in the context of a flat slab near the Galactic disk. More specifically, we ask what the origin of the ionized gas moving at $|v_{\rm LSR}| \lesssim 100$ km s^{-1} is. Although traditional studies have often associated this gas with the Galactic disk-halo, the origin remains uncertain since the distance to the gas is poorly constrained. In particular, many studies have indicated that the MW is embedded in a warm-hot medium with mass on the order of $\sim 10^{10-11}$ $M_\odot$ out to the virial radius (e.g., Anderson & Bregman 2010; Gupta et al. 2012). Therefore, it is likely that a QSO sightline going through the MW's CGM would collect cool ion absorbers embedded in the warm-hot medium. A synthetic observation (Zheng et al. 2015) has shown that there is likely to be an equally massive amount of gas moving at low velocity as compared to the commonly studied high-velocity gas in the MW's CGM.

Here we leverage the HST Spectroscopic Legacy Archive (HSLA; Peeples et al. 2017) to revisit the ion distribution in the Galactic disk-halo interface and halo. The HSLA dataset provides medium resolution COS spectra at G130M and/or G160M gratings. Low ions, such as C II, Si II, and Si III, are so strong that they are often fully saturated and can only be used to study the gas at $|v_{\rm LSR}| > 100$ km s^{-1}. For gas moving at $|v_{\rm LSR}| \leq 100$ km s^{-1}, usually transition lines at high-ionization stages are used, such as Al III, Si IV, C IV, and O VI (e.g., Savage et al. 2003, SW09, W12). In this work, we focus on the Si IV doublet at 1393/1402 Å to study the gas at $|v_{\rm LSR}| \leq 100$ km s^{-1} over the Galactic sky. Hereafter we

refer to the velocity range of $|v_{\rm LSR}| \leq 100$ km s^{-1} as the *low-intermediate* velocity, and refer to the range of $|v_{\rm LSR}| > 100$ km s^{-1} as the *high* velocity.

This chapter is organized as follows: § 3.2 introduces our data reduction of the *HST*/COS spectra, including continuum fitting, column density and centroid velocity calculations, and evaluation of line saturation. We make our continuum-normalized spectra publicly available as described in § 3.2.2, and the dataset can be found here: [10.17909/T9N677]. In § 3.3 we study the all-sky distribution of the low-intermediate Si IV absorbers. We compare our QSO measurements with SW09's flat-slab model prediction in § 3.4.1, and propose a new two-component model in § 3.4.2. In § 3.5, we discuss the caveats of SW09's and our models (§ 3.5.1), investigate the origin of the global component (§ 3.5.2), and finally conduct an order-of-magnitude mass estimate for the global component in the context of the MW's CGM (§ 3.5.3). We conclude in § 3.6.

3.2 Data

3.2.1 General Overview

We obtain our QSO spectra from HSLA (Peeples et al. 2017). The first release of HSLA (February 2017) delivers uniformly reduced and co-added *HST*/COS spectra with M-mode (medium-resolution/ G130M and G160M) and L-mode (low-resolution/ G140L) observations. For each target, the spectra from different programs, epochs, and gratings are co-added to improve the signal-to-noise ratio (SNR) and the wavelength coverage. HSLA arranges targets into different categories, such as *Solar System and Exoplanets*, *Stars*

and *Galaxies and Clusters*; in this work, we make use of those spectra under the category of *QSOs, AGNs, and Seyferts*, which we will henceforth refer to as the HSLA QSO catalog.

For M-mode observations, the HSLA QSO catalog includes co-added spectra of 467 QSOs with the G130M grating and 305 QSOs with the G160M grating. In total there are 511 QSOs, among which 261 QSOs were observed with both G130M and G160M. HSLA characterizes each spectrum with an average SNR, defined as the mean of the SNR values per resolution element (taken to be six pixels) calculated over 10 Å windows every 1000 Å starting from 1150 Å (Peeples et al. 2017). Our analyses focus on those QSOs with SNR $\geq$ 5, which includes 385 (246) QSOs with the G130M (G160M) grating. In total there are 401 QSOs, among which 230 QSOs have both G130M and G160M observations.

For the 401 QSOs with SNR $\geq$ 5, we perform continuum normalization for a series of interstellar absorption lines, including Fe II 1142/1143/1144/1608 Å, P II 1152 Å, S II 1250/1253/1259 Å, Si II 1190/1193/1206/1526 Å, Si III 1260 Å, Si IV 1393/1402 Å, C II 1334 Å, and C IV 1548/1550 Å. We focus on the spectral region within ±1000 km s^{-1} of the rest wavelength of each line of interest, and use Linetools* package (Prochaska et al. 2016) to conduct the continuum normalization. Linetools is an in-development open-source 1D spectral analysis package. Its continuum normalization function† makes use of an Akima Spline to generate the continua from absorption-free regions near the lines of interest. An interactive interface is generated for each spectrum, and we visually inspect the suggested continua and make local correction to account for higher-order continuum variation if needed. We make our dataset publicly available along with the publication of

*https://github.com/linetools/linetools
†http://linetools.readthedocs.io/en/latest/xspectrum1d.html

this manuscript. The details of the data release can be found in § 3.2.2.

3.2.2 Data Publication

We make our continuum-normalized COS spectra publicly available as the COS Quasar Database for Galactic Absorption Lines (COS-GAL). This database includes 401 QSOs that were observed with the G130M and/or G160M gratings. For each target, we perform continuum normalization for a number of interstellar lines, including Fe II 1142/1143/1144/1608 Å, P II 1152 Å, S II 1250/1253/1259 Å, Si II 1190/1193/1206/1526 Å, Si III 1260 Å, Si IV 1393/1402 Å, C II 1334 Å, and C IV 1548/1550 Å. We extract the spectrum within ±1000 km s^{-1} of the rest wavelength of each line of interest, and write the data into fits format. Each file includes the original spectral line data, the absorption-line-free continuum, the continuum-normalized flux, and the errors. Note that these continuum-normalized spectra are specifically processed to study the absorption lines associated with the ionized gas of the MW. They are not ideal for the studies of any broad features, especially those that are intrinsic to the host QSOs. Users interested in these features should examine the original spectra instead.

Along with the ion lines, we provide H I 21cm emission line spectra extracted at the position of each QSO. We retrieve the H I 21cm lines from three H I surveys: GALFA-H I (Peek et al. 2018), HI4PI (HI4PI Collaboration et al. 2016), and LAB (Kalberla et al. 2005). GALFA-H I covers 32% of the sky with fine spatial and velocity (4′/0.18 km s^{-1}) resolution, while the other two surveys are for the full Galactic sky but with lower resolution (16.2′/1.49 km s^{-1} for HI4PI and 36′/1.25 km s^{-1} for LAB). We refer the reader to Table 1

in HI4PI Collaboration et al. (2016) for a comparison of the three surveys. For each QSO, we retrieve H I 21cm lines from GALFA-H I averaged over a 4′ and a 1° beam, from HI4PI averaged over a 16.2′ and a 1° beam, and from LAB averaged over a 1° beam.

Note that the COS spectra are observed with an aperture size of only 2.5″, which is much smaller than the radio beam sizes of the H I surveys. Thus, we caution that the ionized gas studied by COS-GAL and the neutral gas extracted from these HI surveys may not be entirely co-spatial. We provide the HI spectra at various resolutions to partially investigate this and refer the reader to a study by Wakker et al. (2001) that examines the influence of different radio beam sizes on studies of high and low-intermediate velocity clouds.

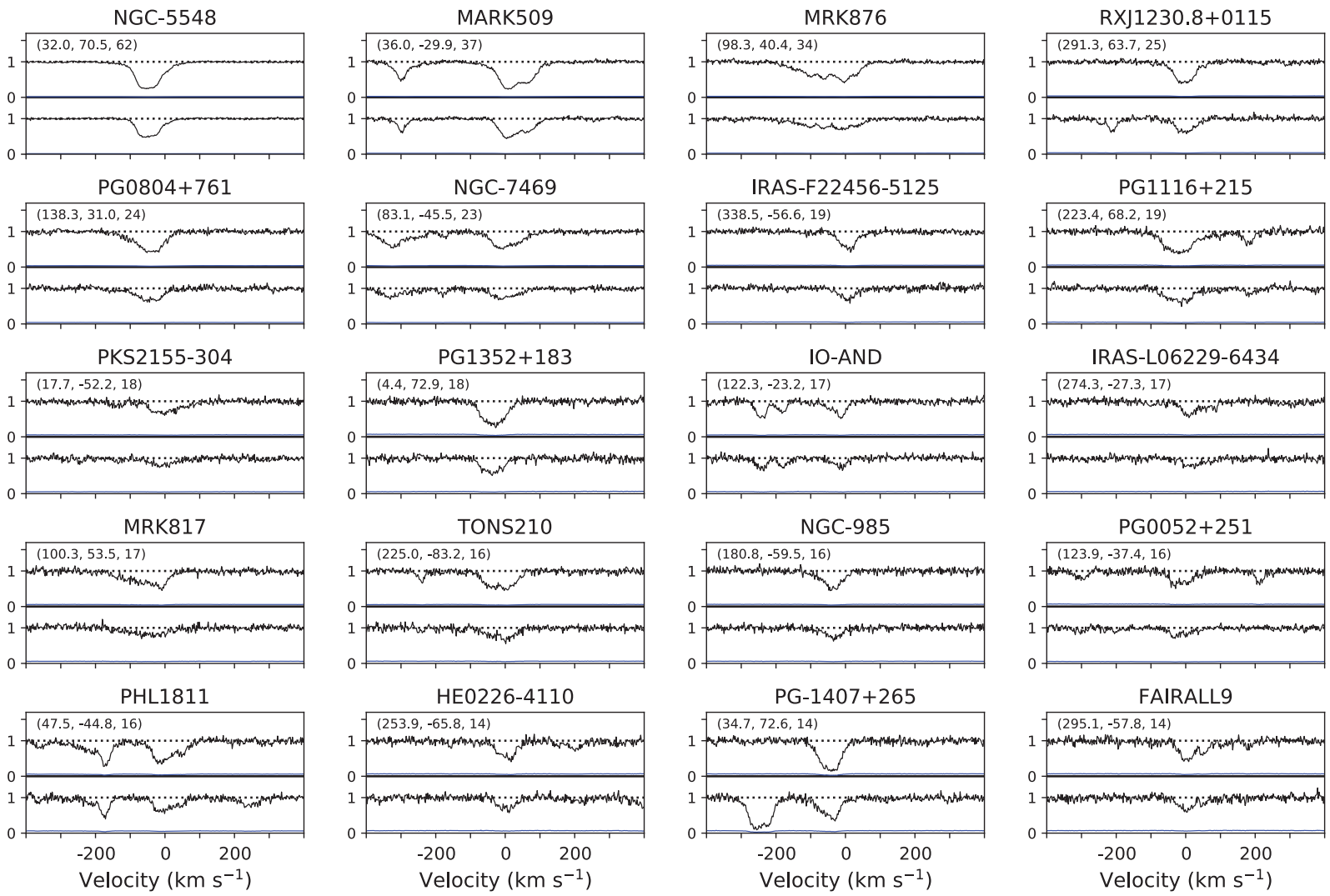

Figure 3.1: Continuum-normalized flux (black) and error (blue) of Si IV doublets. All the spectra are in their original spectral resolution. Each frame is noted with a QSO ID, and (Galactic longitude, Galactic latitude, SNR per pixel) in parentheses. From panel to panel, the spectra are arranged from high to low SNR per pixel. The 120 QSOs in this figure are classified as spectrally resolved with $Q = 0$, please see § 3.2.3 for more details.

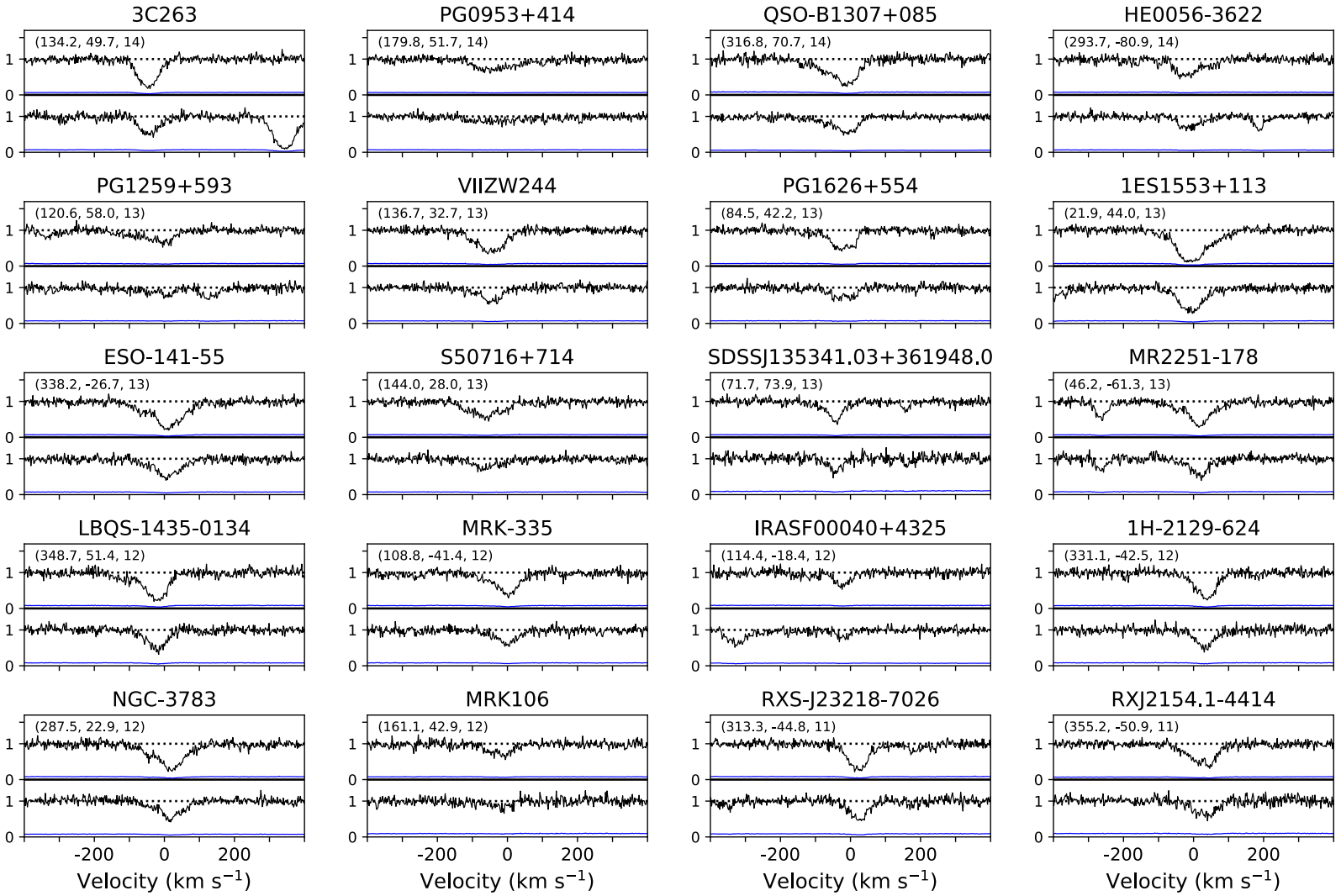

Figure 3.1 continued.

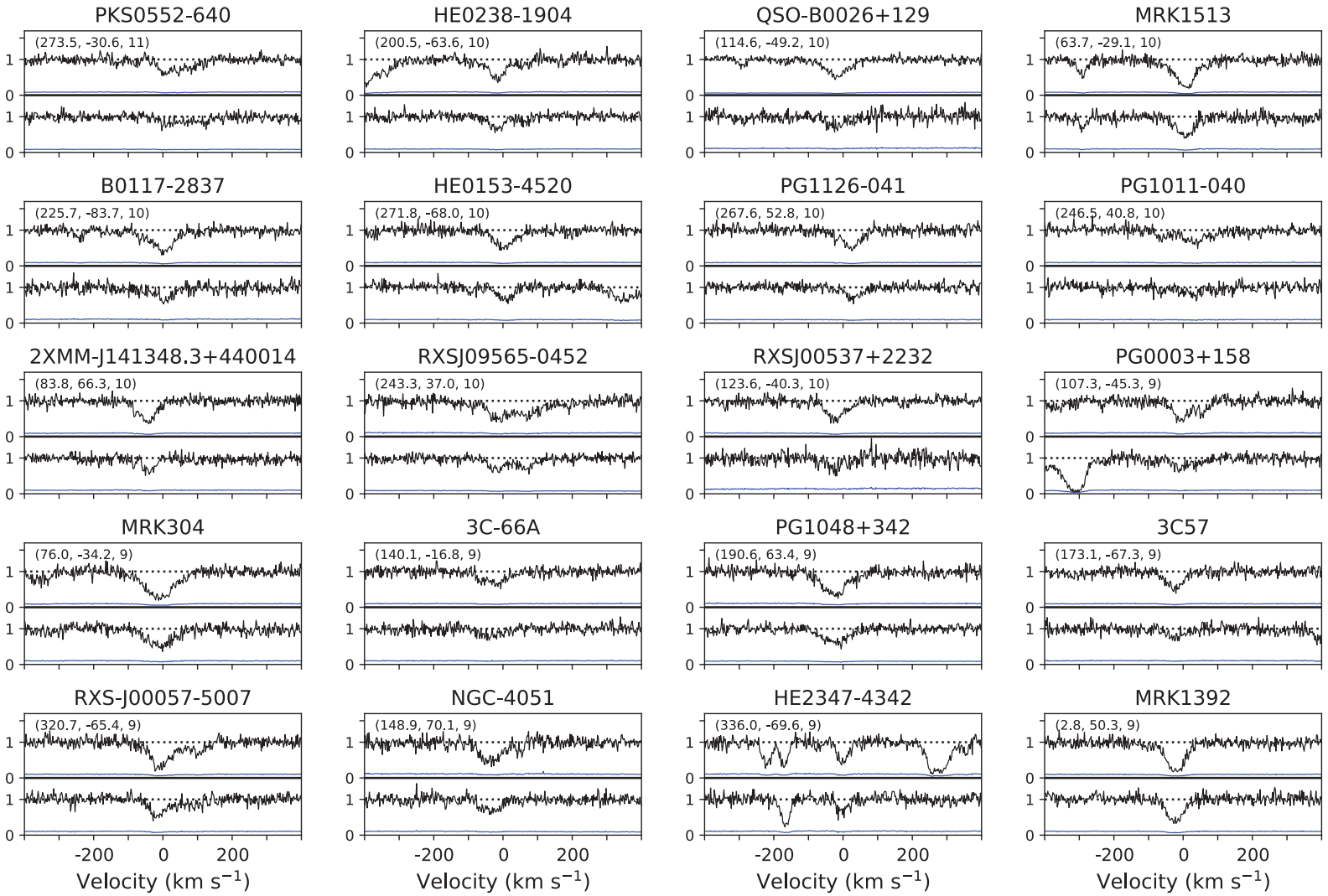

Figure 3.1 continued.

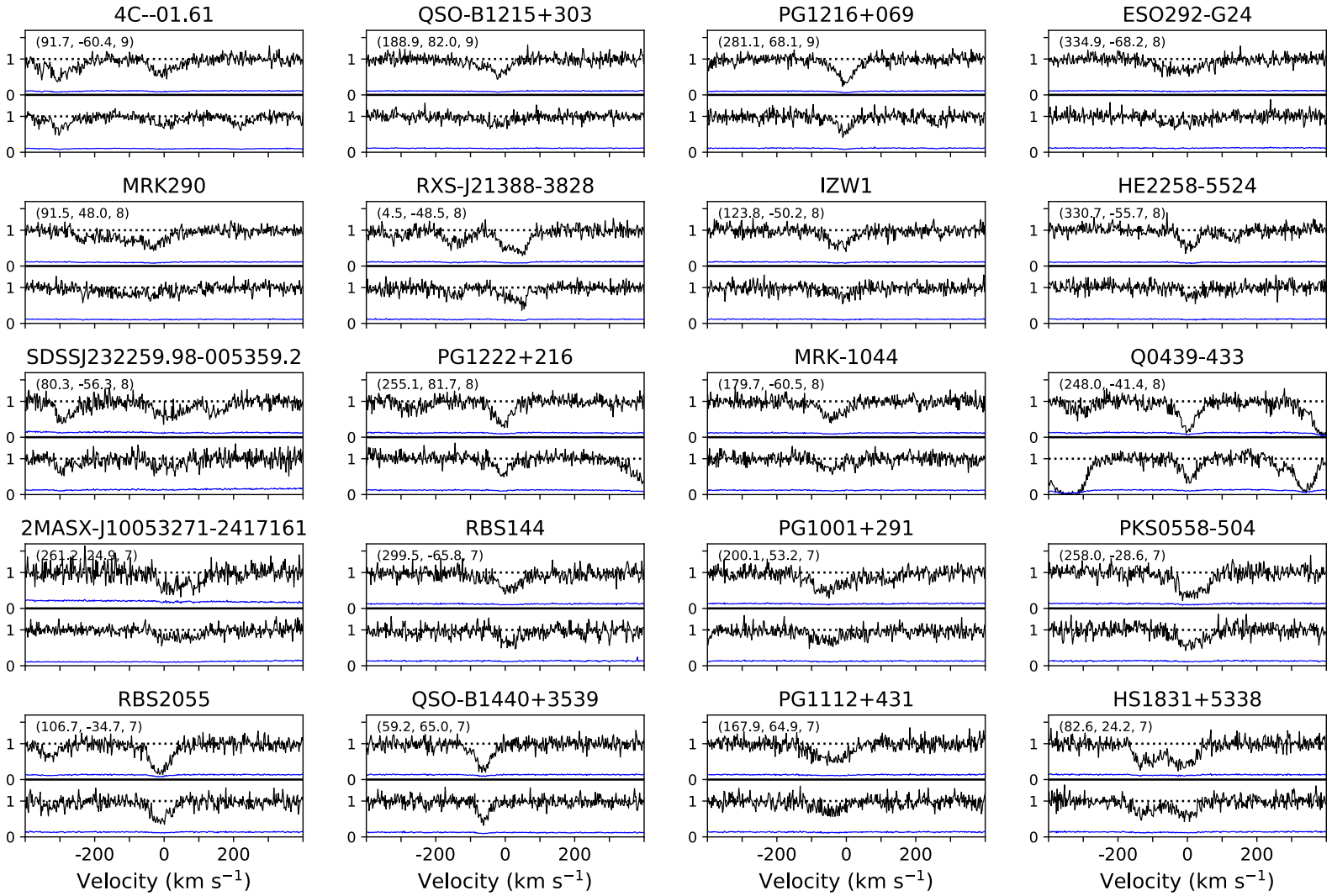

Figure 3.1 continued.

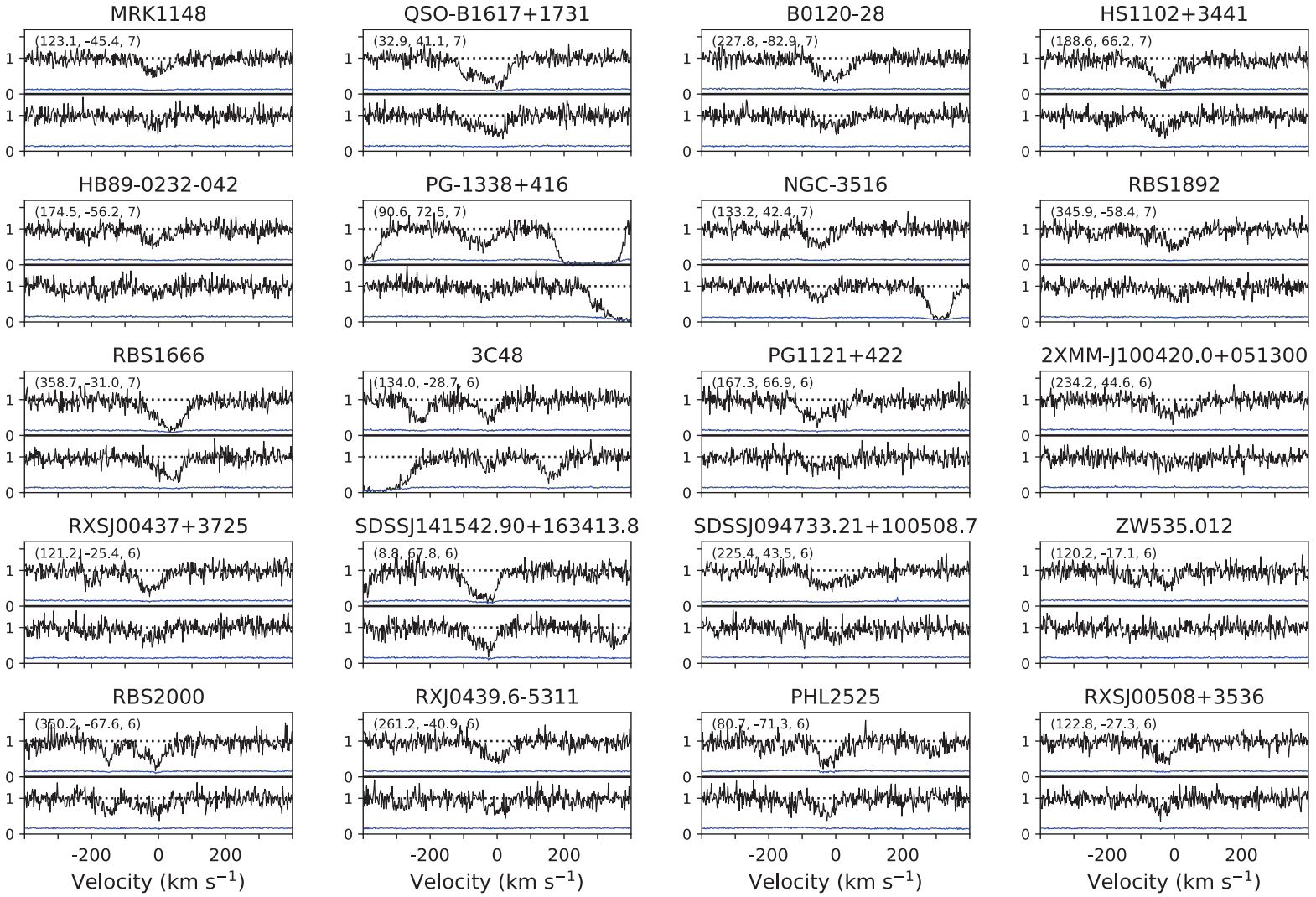

Figure 3.1 continued.

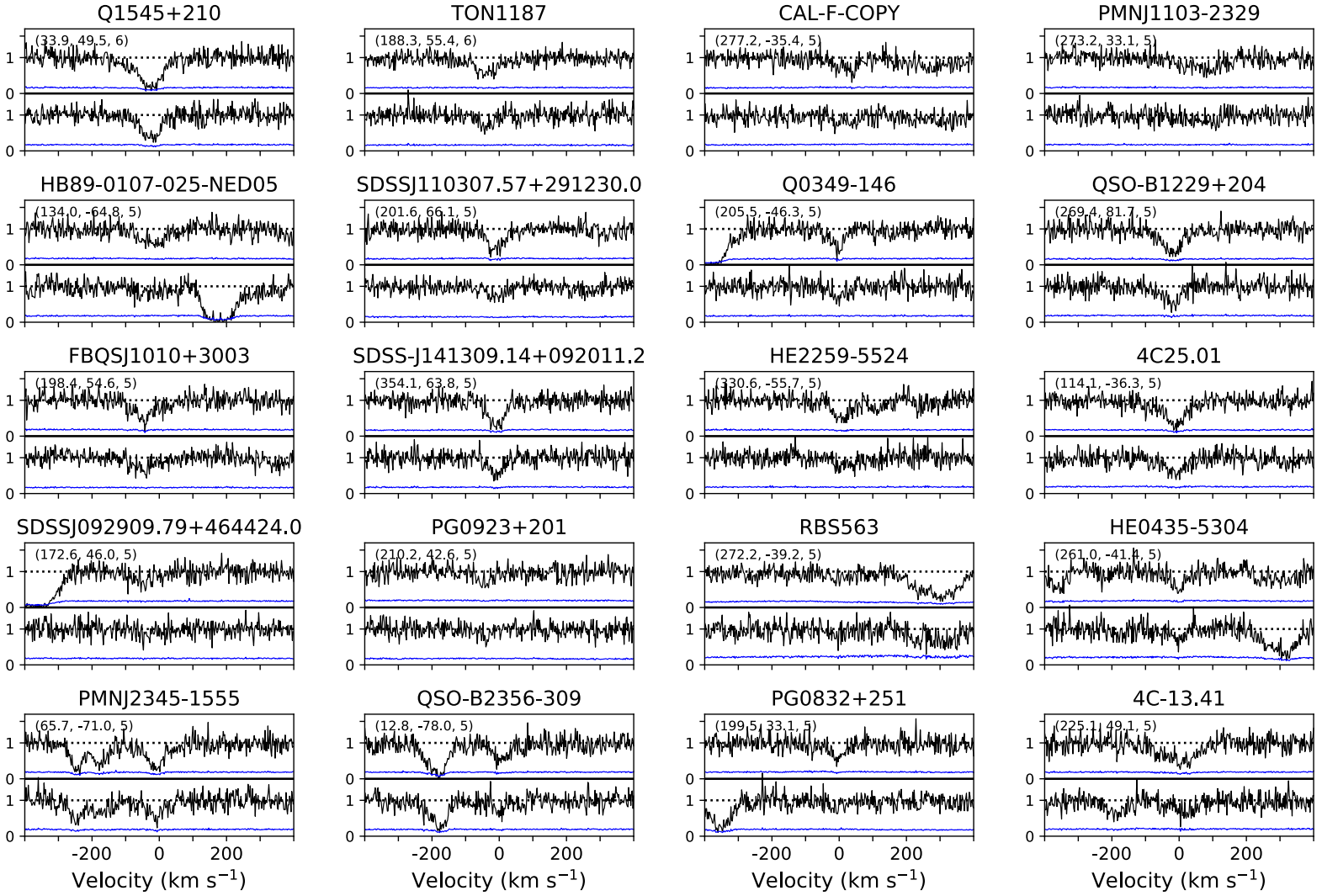

Figure 3.1 continued.

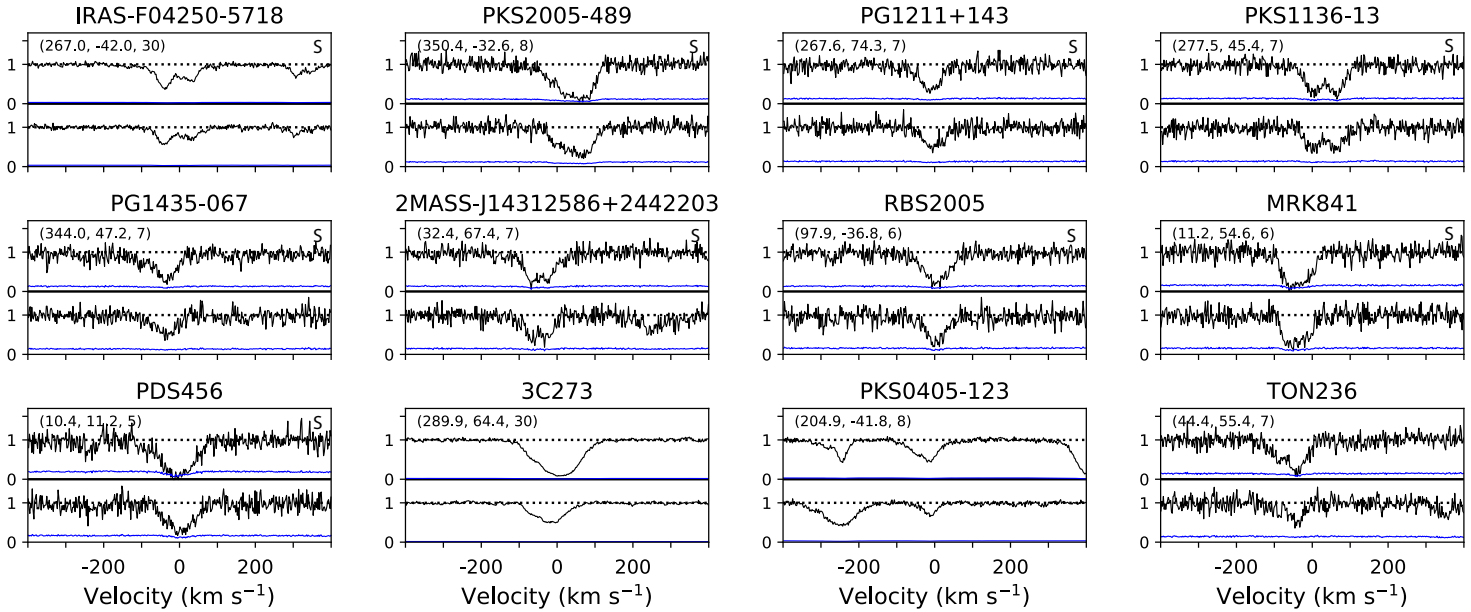

Figure 3.2: The first nine sightlines have unresolved saturation in the Si IV doublet, because their column density measurements do not match Eq. 3.4 or their normalized flux is below 0.1 (i.e., PDS456). These targets are shown in red in Fig 3.3 and tagged with $Q = 1$ in Table 3.1. The last three targets have abnormally strong Si IV 1393 Å profiles; we tag them with $Q = -1$ in the table and do not use them for future analyses. Please see § 3.2.3 for more details.

3.2.3 Data Reduction Focused on The Si IV Doublet

In the following we focus on the Si IV doublet at 1393.76 Å and 1402.77 Å to study the warm-ionized gas associated with the MW's disk-halo and halo. These two lines are observed with the G130M gratings, therefore there are 385 QSO available in the HSLA QSO catalog. We examine the continuum-normalized Si IV doublet for each of the 385 QSOs and identify 291 QSOs with reliable absorption lines. The other 94 QSOs are mostly with unmatched absorption components, or the spectral data quality is so poor that no good judgment can be made. For the adopted 291 QSOs, we calculate the SNR per pixel for the non-absorption continuum region between 1394 Å and 1401Å. We find 132 QSOs with SNR per pixel ≥ 5, which form the core sample of our following analyses. For each spectrum, we correct the velocity to the LSR frame with

$$v_{\rm LSR} = v_{\rm hel} + 9\cos(l)\cos(b) + 12\sin(l)\cos(b) + 7\sin(b), \tag{3.1}$$

where $v_{\rm hel}$ is the heliocentric velocity used in the HSLA and COS spectra. In Figure 3.1 we show the doublet spectra of 120 QSOs that we classify as spectrally resolved with $Q = 0$, and in Figure 3.2 we show the spectra of nine QSOs with unresolved saturation ($Q = 1$) and three with uncertain contamination ($Q = -1$). The judgment of the line saturation and the Q value is based on the apparent column density measurements as described next.

We adopt the apparent optical depth (AOD) method (Savage & Sembach 1991, 1996)

to calculate the apparent column density profiles $N_{1393}(v)$ and $N_{1402}(v)$, which is,

$$\begin{aligned} N_\lambda(v) &= \frac{m_e c}{\pi e^2} \frac{-\ln[F_n(v)]}{f\lambda} \\ &= 3.768 \times 10^{14} \frac{-\ln[F_n(v)]}{f\lambda(\text{Å})} [\text{atoms cm}^{-2}(\text{km s}^{-1})^{-1}], \end{aligned} \tag{3.2}$$

where $F_n(v)$ is the continuum-normalized spectrum, and the wavelength λ = 1393.76 (1402.77) Å and the oscillator strength f = 0.513 (0.254) are adopted from Morton (2003). For both lines, we calculate the total column density and centroid velocity as,

$$\begin{aligned} N_\lambda &= \int_{v_-}^{v_+} N_\lambda(v) \mathrm{d}v \\ v_\lambda &= \int_{v_-}^{v_+} v N_\lambda(v) \mathrm{d}v / \int_{v_-}^{v_+} N_\lambda(v) \mathrm{d}v, \end{aligned} \tag{3.3}$$

where $v_- = -100$ km s^{-1} and $v_+ = +100$ km s^{-1}, respectively. We tabulate the integrated column density and centroid velocity in Table 3.1.

Savage & Sembach (1991) pointed out that there might exist spectrally unresolved saturation even though the absorption line profiles appear to be shallow. This effect is most significant when the full width half maximum (FWHM) of a strong absorption line is comparable to or smaller than the FWHM of the instrument's line-spread function. The unresolved saturation can also occur if multiple absorption components with various line widths co-exist at similar velocity regions; the original absorption line profiles end up being smeared into broader but shallower profiles. Savage & Sembach (1991) suggested that for ions with more than one transition line, an efficient way to identify unresolved saturation is to compare the apparent column density profiles $N_\lambda(v)$ or the integrated apparent column density N_λ over a certain velocity range. A well-resolved spectrum

should yield consistent $N_\lambda(v)$ profiles among the multiplet absorption lines and consistent integrated N_λ values. This method has been widely used to identify smearing effect of unresolved saturation in the spectra (e.g., Howk et al. 2006; W12).

W12 identify unresolved saturation by comparing the doublet N_λ measurements for all the ions they studied, such as Si IV, N V, C IV, and O VI. They require the column density difference between the ion doublet to be within the linearly combined measurement errors. Here we adopt a similar approach, but require,

$$\begin{aligned} &\delta \log N \equiv |\log N_{1393} - \log N_{1402}| \leq \sigma_c, \\ &\sigma_c \equiv (\sigma_{1393}^2 + \sigma_{1402}^2)^{\frac{1}{2}}, \end{aligned} \tag{3.4}$$

where σ_c is the combined quadrature error of the doublet column density difference, and σ_{1393} and σ_{1402} are the measured logarithmic errors of the corresponding $\log N_{1393}$ and $\log N_{1402}$ values, respectively. Among the 132 QSOs, we identify 121 QSOs satisfying Eq. 3.4, suggesting that these QSOs have well resolved doublet spectra. We carefully inspect each of the spectra and find that one of the targets, PDS456, has a minimum flux of $F_{\rm n} \leq 0.1$ in Si IV 1393 Å. Since COS spectra is empirically known to be saturated at this level, we classify PDS456 as spectrally saturated with $Q = 1$. Eventually we have 120 QSOs with well resolved Si IV doublet ($Q = 0$) as shown in Figure 3.1, and the comparison between of the doublet column density measurements for $Q = 0$ targets is shown as black dots in Fig 3.3.

For the rest of the QSOs, we classify nine of them as spectrally saturated with $Q = 1$ and show their doublet spectra in Fig 3.2. These include PDS456 which we describe above

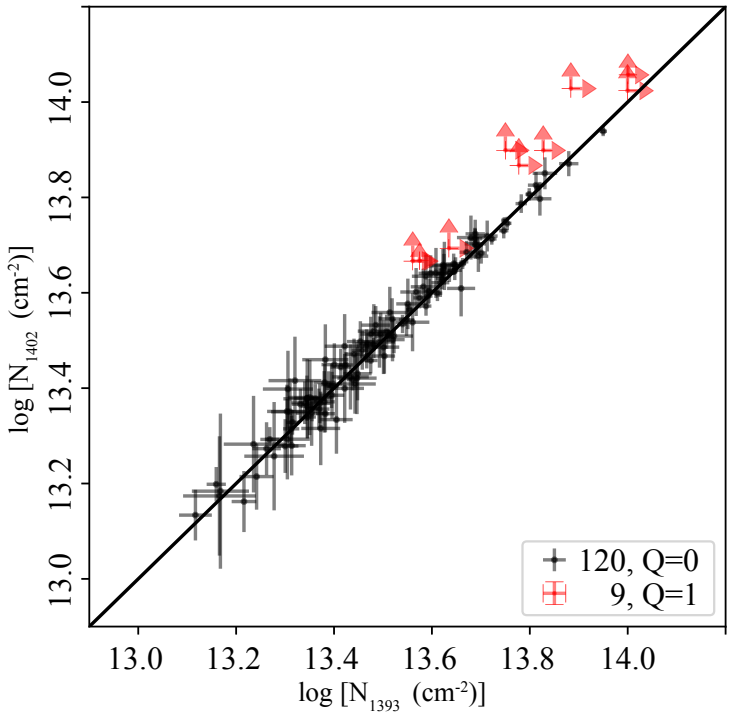

Figure 3.3: Comparison of Si IV doublet column density measurements. In black are the 120 QSO sightlines with spectrally resolved doublet profiles ($Q = 0$), i.e., meeting the criterion in Eq. 3.4. In red are the nine sightlines with unresolved saturation ($Q = 1$) in their doublet spectra (see § 3.2.3).

and the other eight QSOs that do not satisfy Eq. 3.4. The column density measurements with these QSOs are shown as red crosses in Fig 3.3, from which we find that saturation mostly occurs at high column densities. Savage & Sembach (1991) provide column density correction for unresolved saturation, which is based on a simulation of an isolated Gaussian component being smeared by instrument's line-spread function with different FHWM. However, as they pointed out, the correction are most precise if the doublet's logarithm column density difference is less than 0.05 dex; for targets with larger difference, the column density correction itself could vary up to $0.1-0.3$ dex if the lines have multiple components. Given that our log$N$ measurement errors are ~ 0.05 dex for most of the low

SNR sightlines, and that the broad line profiles are probably caused by multi-components, it is unrealistic to apply SW09's column density correction to our data. We only list the column density as lower limits for these nine QSOs in Table 3.1.

For the remaining three QSOs, TON236, 3C273, and PKS0405-123, we find that their Si IV 1393 Å is abnormally stronger than the 1402 Å with $\log N_{1393} > \log N_{1402} + \sigma_c$. Their spectra are shown in the last three panels in Fig 3.2. For 3C273, W12 suggests that the 1393 Å line may suffer from blending with Lyα. For PKS0405-123, we measure $\log N_{1393} = 13.45 \pm 0.01$, consistent with W12's FUSE value of $\log N_{1393} = 13.43 \pm 0.04$; note that the QSO is listed as PKS0405-12 in their work. However, for 1402 Å we find $\log N_{1402} = 13.27 \pm 0.02$ while W12 find $13.40 \pm .07$. Neither line shows signs of a peculiar profile in our COS spectra (Figure 3.2) despite the $\log N$ difference. As W12 did not provide the original FUSE spectra for PKS0405-123, we cannot conduct a close inspection of the line profiles to further compare results. For TON236, the 1393Å line may be contaminated by an additional line at $v_{\rm LSR} \sim -90$ km s^{-1} that does not have a corresponding component at 1402 Å. For these three QSOs, we tag them as $Q = -1$, and do not use them for future analyses.

Among the 132 QSOs, we found 19 sightlines in common with the *FUSE* sightlines used in W12. We note these sightlines with asterisks in the first column of Table 3.1. Among them, 16 have spectrally resolved ($Q = 0$) doublet profiles observed with COS. For these sightlines, we calculate the integrated column density over the same velocity range as W12 adopted. We find that $\log N_{1393}$ agrees within ±0.08 dex and $\log N_{1402}$ agrees within ±0.09 dex, except RXJ1230.8+0115 for which our measurements show $\log N_{1393} =$

$\log N_{1402}$ = 13.51±0.01, while W12 gave $\log N_{1393}$ = 13.47 ± 0.04 and $\log N_{1402}$ = 13.30 ± 0.09. Since our doublet values are consistent and they match W12's Si IV 1393Å value, it is likely that W12 overestimated the continuum of 1402Å for this target.

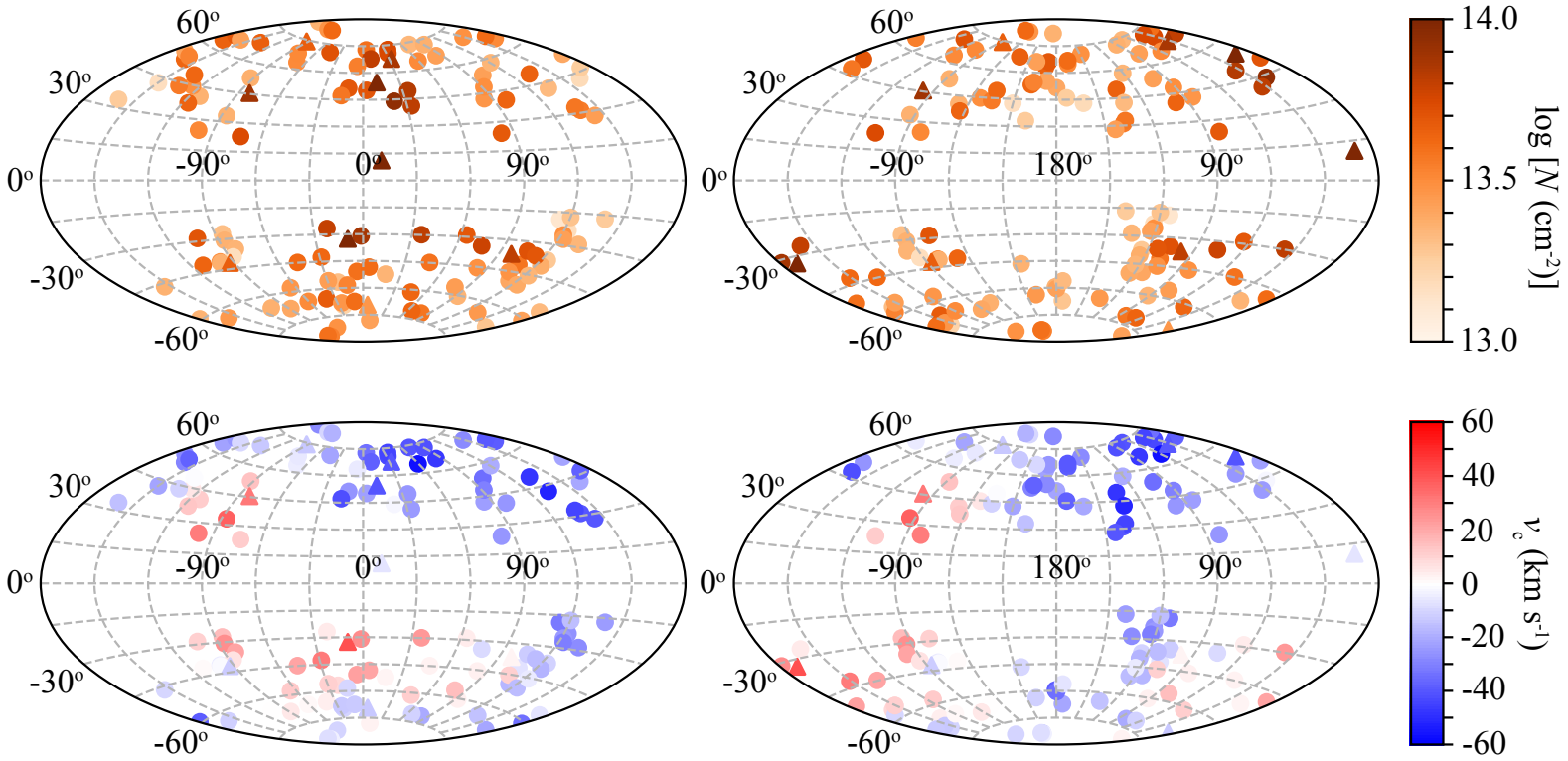

Figure 3.4: The top two panels show the all-sky distribution of the Si IV column density integrated from −100 to +100 km s^{-1}, with the left panel centered at the Galactic center and the right panel at anti-Galactic center. For each spectrally resolved sightline (Q = 0, dots), we show the mean column density of the doublet; and for each saturated sightline (Q = 1, upward triangles), we show the column density of logN_{1402} as the lower limit, given that Si IV 1402Å is weaker thus is less saturated than 1393Å. The bottom two panels show the distribution of the centroid velocity v_c over the sky, which is the mean centroid velocity of the doublet regardless of a target's Q value (see § 3.3).

Table 3.1: Si IV Data Sample

No.	HSLA-ID	l	b	RA	DEC	z	SNR	Q	logN_{1393}	$v_{c,1393}$	logN_{1402}	$v_{c,1402}$
		(°)	(°)	(°)	(°)		(per pix)			km s^{-1}		km s^{-1}
(0)	(1)	(2)	(3)	(4)	(5)	(6)	(7)	(8)	(9)	(10)	(11)	(12)
1*†	NGC-5548	31.96	70.50	214.50	25.14	0.017	62.7	0	13.75±0.00	-42.7± 0.3	13.75±0.00	-44.7± 0.5
2*†	MARK509	35.97	-29.86	311.04	-10.72	0.034	37.8	0	13.82±0.00	24.2± 0.3	13.82±0.00	27.6± 0.6
3*	MRK876	98.27	40.38	243.49	65.72	0.129	34.6	0	13.64±0.00	-24.5± 0.5	13.64±0.01	-19.9± 1.0
4*	RXJ1230.8+0115	291.26	63.66	187.71	1.26	0.117	25.1	0	13.51±0.01	-4.6± 0.8	13.51±0.01	-4.3± 1.7
5	PG0804+761	138.28	31.03	122.74	76.04	0.100	24.2	0	13.55±0.01	-39.7± 1.0	13.56±0.01	-39.8± 2.0
6*	NGC-7469	83.10	-45.47	345.82	8.87	0.016	23.6	0	13.48±0.01	3.3± 1.0	13.49±0.01	-1.0± 1.8
7	IRAS-F22456-5125	338.51	-56.63	342.17	-51.16	0.100	19.1	0	13.32±0.01	9.1± 1.6	13.33±0.03	10.9± 3.4
8	PG1116+215	223.36	68.21	169.79	21.32	0.176	19.1	0	13.66±0.01	-12.8± 0.9	13.66±0.01	-12.1± 1.5
9*	PKS2155-304	17.73	-52.25	329.72	-30.23	0.116	18.6	0	13.35±0.01	2.6± 1.7	13.36±0.02	-1.0± 3.1
10†	PG1352+183	4.37	72.87	208.65	18.09	0.152	18.1	0	13.61±0.01	-33.6± 1.4	13.60±0.02	-36.0± 2.5
11	IO-AND	122.28	-23.18	12.08	39.69	0.134	17.5	0	13.16±0.02	-25.5± 2.8	13.20±0.04	-15.1± 4.8
12	IRAS-L06229-6434	274.31	-27.32	95.78	-64.61	0.128	17.3	0	13.31±0.02	15.9± 2.2	13.31±0.03	24.5± 4.3
13	MRK817	100.30	53.48	219.09	58.79	0.031	17.2	0	13.44±0.01	-34.2± 1.7	13.42±0.02	-34.1± 3.5
14*	TONS210	224.97	-83.16	20.46	-28.35	0.116	16.8	0	13.54±0.01	-14.4± 1.2	13.53±0.02	-10.4± 2.5
15	NGC-985	180.84	-59.49	38.66	-8.79	0.042	16.5	0	13.35±0.01	-38.3± 2.2	13.36±0.03	-30.7± 4.0
16	PG0052+251	123.91	-37.44	13.72	25.43	0.154	16.3	0	13.27±0.02	-10.7± 2.5	13.29±0.03	-15.4± 3.4
17*	PHL1811	47.47	-44.82	328.76	-9.37	0.190	16.1	0	13.59±0.01	3.2± 1.1	13.59±0.02	3.5± 2.1
18*	HE0226-4110	253.94	-65.77	37.06	-40.95	0.493	14.8	0	13.36±0.02	0.1± 2.0	13.38±0.03	4.9± 3.9
19	PG-1407+265	34.67	72.59	212.35	26.31	0.940	14.7	0	13.75±0.01	-43.7± 1.3	13.75±0.01	-41.8± 2.2
20	FAIRALL9	295.07	-57.83	20.94	-58.81	0.047	14.5	0	13.47±0.01	12.2± 1.7	13.47±0.03	18.6± 3.5

Col (0): QSOs are arranged from high to low SNR per pixel. QSOs noted with ∗ have *FUSE* spectra as used in Wakker et al. (2012) (see § 3.2.3), while those with † are potentially related to the Fermi Bubbles given their spatial proximity (see § 3.3).
Col (1): QSO ID as adopted by HSLA (Peeples et al. 2017).
Col (2) & (3): Galactic longitude and latitude in degree.
Col (4) & (5): Right Ascension and Declination in degree.
Col (6): QSO redshift as adopted by HSLA (Peeples et al. 2017).
Col (7): SNR per pixel for the absorption-free region between 1394Å and 1401Å.
Col (8): Quality flagging (see § 3.2.3): $Q = 0$ means this target has spectrally resolved doublet profiles, $Q = 1$ means its Si IV lines are likely to be saturated, and $Q = -1$ means its 1393 Å line is abnormally stronger than 1402 Å. We do not use $Q = -1$ target in our analyses.
Col (9) & (10): logarithmic apparent column density and centroid velocity for Si IV 1393Å integrated from −100 to 100 km s^{-1}.
Col (11) & (12): Same as Col (9) & (10), but for Si IV 1402 Å.

No.	HSLA-ID	l	b	RA	DEC	z	SNR	Q	logN_{1393}	$v_{c,1393}$	logN_{1402}	$v_{c,1402}$
		(°)	(°)	(°)	(°)		(per pix)			km s^{-1}		km s^{-1}
(0)	(1)	(2)	(3)	(4)	(5)	(6)	(7)	(8)	(9)	(10)	(11)	(12)
21	3C263	134.16	49.74	174.99	65.80	0.646	14.5	0	13.65±0.01	-47.7± 1.7	13.66±0.02	-41.3± 2.7
22*	PG0953+414	179.79	51.71	149.22	41.26	0.234	14.4	0	13.39±0.02	-21.1± 2.1	13.41±0.03	-12.6± 3.8
23	QSO-B1307+085	316.79	70.71	197.45	8.33	0.155	14.4	0	13.72±0.01	-21.5± 1.2	13.71±0.01	-20.6± 1.6
24	HE0056-3622	293.72	-80.90	14.66	-36.10	0.164	14.0	0	13.47±0.02	-10.0± 1.9	13.49±0.02	-5.9± 2.8
25*	PG1259+593	120.56	58.05	195.30	59.04	0.477	13.9	0	13.33±0.02	-19.3± 2.4	13.37±0.03	-10.5± 4.3
26	VIIZW244	136.66	32.68	131.19	76.89	0.131	13.8	0	13.59±0.01	-43.9± 1.8	13.57±0.02	-40.9± 3.3
27	PG1626+554	84.51	42.19	246.98	55.38	0.133	13.8	0	13.47±0.01	-22.8± 1.8	13.46±0.03	-26.9± 3.8
28†	1ES1553+113	21.91	43.96	238.93	11.19	0.360	13.7	0	13.95±0.01	-2.3± 0.7	13.94±0.01	-5.5± 1.2
29*†	ESO-141-55	338.18	-26.71	290.31	-58.67	0.037	13.6	0	13.80±0.01	4.7± 0.9	13.81±0.01	5.0± 1.6
30	S50716+714	143.98	28.02	110.47	71.34	0.300	13.6	0	13.42±0.02	-39.5± 2.4	13.45±0.03	-41.4± 4.4
31	SDSSJ135341.03+361948.0	71.67	73.91	208.42	36.33	0.146	13.1	0	13.35±0.02	-40.3± 2.7	13.34±0.04	-48.9± 7.7
32	MR2251-178	46.20	-61.33	343.52	-17.58	0.063	13.0	0	13.64±0.01	11.7± 1.2	13.64±0.02	14.8± 2.5
33†	LBQS-1435-0134	348.72	51.37	219.45	-1.79	1.310	12.7	0	13.69±0.01	-25.0± 1.4	13.70±0.02	-22.4± 2.4
34*	MRK-335	108.76	-41.42	1.58	20.20	0.025	12.5	0	13.57±0.01	-6.6± 1.5	13.59±0.02	-3.7± 2.7
35	IRASF00040+4325	114.42	-18.42	1.65	43.71	0.166	12.4	0	13.12±0.03	-31.0± 4.9	13.13±0.05	-25.4± 7.6
36	1H-2129-624	331.14	-42.52	324.10	-62.40	0.058	12.2	0	13.62±0.01	31.2± 1.7	13.64±0.02	31.0± 3.0
37*	NGC-3783	287.46	22.95	174.76	-37.74	0.009	12.2	0	13.75±0.01	11.8± 1.1	13.73±0.02	14.8± 2.0
38	MRK106	161.14	42.88	139.98	55.36	0.123	12.1	0	13.22±0.03	-20.4± 3.4	13.16±0.06	-27.2± 9.3
39	RXS-J23218-7026	313.29	-44.84	350.46	-70.45	0.300	11.9	0	13.62±0.01	21.2± 1.5	13.63±0.02	26.4± 3.0
40	RXJ2154.1-4414	355.18	-50.86	328.71	-44.23	0.344	11.7	0	13.59±0.01	22.3± 1.4	13.60±0.03	29.3± 3.7
41	PKS0552-640	273.47	-30.61	88.10	-64.04	0.680	11.7	0	13.38±0.02	26.5± 2.8	13.35±0.04	37.0± 6.1
42	HE0238-1904	200.48	-63.63	40.14	-18.86	0.631	10.8	0	13.44±0.02	-11.1± 2.3	13.47±0.03	1.3± 4.2
43	QSO-B0026+129	114.64	-49.25	7.31	13.27	0.142	10.8	0	13.40±0.01	-17.1± 1.9	13.40±0.05	-9.9± 6.1
44	MRK1513	63.67	-29.07	323.12	10.14	0.062	10.6	0	13.70±0.01	4.5± 1.2	13.68±0.02	4.3± 2.7
45	B0117-2837	225.73	-83.65	19.90	-28.36	0.348	10.6	0	13.55±0.02	-3.5± 1.9	13.54±0.03	-3.3± 4.3
46	HE0153-4520	271.80	-67.97	28.80	-45.10	0.451	10.5	0	13.38±0.02	5.5± 2.7	13.41±0.04	-7.5± 5.0
47	PG1126-041	267.63	52.75	172.32	-4.40	0.061	10.5	0	13.37±0.02	14.5± 2.8	13.37±0.04	26.3± 5.9
48	PG1011-040	246.50	40.75	153.59	-4.31	0.058	10.4	0	13.37±0.02	12.1± 2.9	13.36±0.04	17.6± 5.9
49	2XMM-J141348.3+440014	83.83	66.35	213.45	44.00	0.089	10.2	0	13.41±0.02	-46.7± 3.5	13.44±0.04	-29.3± 5.7
50	RXSJ09565-0452	243.33	37.00	149.13	-4.89	0.157	10.1	0	13.65±0.01	13.3± 1.9	13.65±0.02	17.5± 2.8

Note. — Table 3.1 continued

No.	HSLA-ID	l	b	RA	DEC	z	SNR	Q	logN_{1393}	$v_{c,1393}$	logN_{1402}	$v_{c,1402}$
		(°)	(°)	(°)	(°)		(per pix)			km s^{-1}		km s^{-1}
(0)	(1)	(2)	(3)	(4)	(5)	(6)	(7)	(8)	(9)	(10)	(11)	(12)
51	RXSJ00537+2232	123.64	-40.33	13.44	22.54	0.148	10.0	0	13.38±0.02	-17.8± 2.7	13.37±0.06	-26.0± 8.9
52	PG0003+158	107.32	-45.33	1.50	16.16	0.450	9.9	0	13.47±0.02	11.2± 2.5	13.49±0.03	0.1± 4.5
53	MRK304	75.99	-34.22	334.30	14.24	0.065	9.9	0	13.78±0.01	-8.5± 1.2	13.79±0.02	-6.9± 2.4
54	3C-66A	140.14	-16.77	35.66	43.04	0.444	9.8	0	13.26±0.03	-23.0± 4.0	13.27±0.06	-40.2± 8.8
55	PG1048+342	190.60	63.44	162.93	33.99	0.167	9.8	0	13.64±0.02	-21.7± 1.9	13.66±0.02	-21.1± 2.9
56	3C57	173.08	-67.26	30.49	-11.54	0.670	9.8	0	13.30±0.03	-20.9± 3.6	13.28±0.06	-19.3± 7.7
57	RXS-J00057-5007	320.71	-65.41	1.43	-50.12	0.033	9.7	0	13.67±0.01	4.2± 1.6	13.69±0.02	8.3± 3.0
58	NGC-4051	148.88	70.09	180.79	44.53	0.002	9.6	0	13.50±0.02	-27.6± 3.0	13.47±0.04	-29.2± 5.3
59	HE2347-4342	336.03	-69.57	357.64	-43.43	2.885	9.6	0	13.24±0.03	-10.0± 4.3	13.21±0.07	2.3± 8.8
60	MRK1392	2.75	50.26	226.49	3.71	0.036	9.6	0	13.69±0.02	-22.5± 1.7	13.71±0.02	-24.0± 3.0
61	4C–01.61	91.66	-60.36	357.98	-1.15	0.173	9.1	0	13.34±0.03	3.6± 3.4	13.37±0.04	2.6± 5.7
62	QSO-B1215+303	188.87	82.05	184.47	30.12	0.130	9.1	0	13.34±0.03	-27.3± 3.7	13.38±0.05	-21.2± 6.6
63*	PG1216+069	281.07	68.14	184.84	6.64	0.331	9.0	0	13.51±0.02	-5.5± 2.1	13.52±0.04	-2.9± 4.5
64	ESO292-G24	334.90	-68.16	356.75	-44.76	0.030	8.9	0	13.46±0.02	-13.1± 2.9	13.48±0.04	-13.2± 5.5
65	MRK290	91.49	47.95	233.97	57.90	0.029	8.7	0	13.48±0.02	-29.6± 3.1	13.51±0.04	-17.2± 5.0
66	RXS-J21388-3828	4.51	-48.46	324.71	-38.48	0.182	8.7	0	13.62±0.02	21.1± 2.3	13.62±0.03	26.8± 4.2
67	IZW1	123.75	-50.17	13.40	12.69	0.058	8.7	0	13.40±0.03	-15.5± 3.3	13.39±0.05	-14.7± 6.5
68	HE2258-5524	330.72	-55.67	345.47	-55.14	0.141	8.6	0	13.31±0.03	11.1± 3.6	13.28±0.06	18.7± 8.5
69	SDSSJ232259.98-005359.2	80.27	-56.26	350.75	-0.90	0.150	8.6	0	13.45±0.03	15.4± 3.6	13.43±0.06	9.7± 7.1
70	PG1222+216	255.07	81.66	186.23	21.38	0.432	8.3	0	13.45±0.03	-9.5± 3.0	13.50±0.04	-7.9± 5.3
71	MRK-1044	179.69	-60.48	37.52	-9.00	0.016	8.3	0	13.40±0.03	-33.5± 3.9	13.45±0.04	-35.8± 6.8
72	Q0439-433	247.98	-41.38	70.32	-43.23	0.593	8.0	0	13.62±0.02	1.3± 2.1	13.66±0.03	-0.1± 3.8
73	2MASX-J10053271-2417161	261.23	24.85	151.39	-24.29	0.153	7.8	0	13.52±0.04	30.8± 5.7	13.51±0.04	35.1± 5.6
74	RBS144	299.48	-65.84	15.11	-51.23	0.062	7.6	0	13.50±0.02	1.6± 2.9	13.51±0.05	20.8± 6.0
75	PG1001+291	200.08	53.21	151.01	28.93	0.327	7.5	0	13.62±0.02	-28.6± 3.2	13.65±0.03	-25.1± 4.6
76	PKS0558-504	257.96	-28.57	89.95	-50.45	0.137	7.4	0	13.69±0.02	11.1± 2.2	13.72±0.03	9.5± 3.6
77	RBS2055	106.67	-34.66	357.97	26.33	0.040	7.4	0	13.71±0.02	-11.8± 2.0	13.72±0.03	-10.0± 3.7
78	QSO-B1440+3539	59.24	65.03	220.53	35.44	0.079	7.3	0	13.49±0.03	-55.9± 5.6	13.53±0.04	-46.0± 6.8
79	PG1112+431	167.89	64.94	168.78	42.83	0.301	7.3	0	13.52±0.02	-38.3± 3.9	13.50±0.05	-42.5± 7.4
80	HS1831+5338	82.59	24.21	278.21	53.67	0.039	7.3	0	13.69±0.02	-24.8± 2.6	13.68±0.03	-19.6± 4.3

Note. — Table 3.1 continued

No.	HSLA-ID	l	b	RA	DEC	z	SNR	Q	logN_{1393}	$v_{c,1393}$	logN_{1402}	$v_{c,1402}$
		(°)	(°)	(°)	(°)		(per pix)			km s^{-1}		km s^{-1}
(0)	(1)	(2)	(3)	(4)	(5)	(6)	(7)	(8)	(9)	(10)	(11)	(12)
81	MRK1148	123.09	-45.44	12.98	17.43	0.064	7.2	0	13.35±0.03	-5.1± 3.9	13.35±0.07	-20.7± 9.2
82†	QSO-B1617+1731	32.89	41.08	245.05	17.41	0.112	7.2	0	13.81±0.02	-23.5± 2.0	13.83±0.03	-20.7± 3.4
83	B0120-28	227.78	-82.93	20.65	-28.72	0.436	7.2	0	13.58±0.03	-7.7± 2.8	13.61±0.04	-4.3± 4.7
84	HS1102+3441	188.56	66.22	166.42	34.43	0.508	7.2	0	13.69±0.02	-24.6± 2.7	13.70±0.03	-26.6± 4.4
85	HB89-0232-042	174.46	-56.16	38.78	-4.03	1.437	7.1	0	13.31±0.04	-6.5± 4.7	13.35±0.07	0.9± 8.9
86	PG-1338+416	90.59	72.48	205.25	41.39	1.217	7.1	0	13.40±0.03	-41.0± 5.3	13.33±0.07	-33.2±10.7
87*	NGC-3516	133.24	42.40	166.70	72.57	0.008	7.1	0	13.30±0.04	-51.4± 7.2	13.35±0.06	-51.7± 9.9
88	RBS1892	345.90	-58.37	341.33	-46.87	0.200	7.0	0	13.52±0.03	-9.7± 3.2	13.55±0.04	-1.6± 5.4
89†	RBS1666	358.73	-31.00	301.47	-41.58	0.079	7.0	0	13.88±0.02	26.8± 2.4	13.87±0.03	27.0± 3.5
90	3C48	133.96	-28.72	24.42	33.16	0.367	6.9	0	13.37±0.04	-26.8± 5.2	13.32±0.08	-17.5±10.2
91	PG1121+422	167.26	66.86	171.16	42.03	0.225	6.9	0	13.60±0.02	-39.2± 3.9	13.64±0.04	-23.1± 5.3
92	2XMM-J100420.0+051300	234.16	44.62	151.08	5.22	0.161	6.8	0	13.49±0.03	5.8± 3.8	13.50±0.05	11.4± 7.1
93	RXSJ00437+3725	121.23	-25.42	10.93	37.42	0.079	6.6	0	13.50±0.03	-23.9± 4.1	13.49±0.06	-34.1± 8.3
94†	SDSSJ141542.90+163413.8	8.85	67.83	213.93	16.57	0.743	6.5	0	13.82±0.02	-37.4± 3.3	13.80±0.04	-37.9± 5.2
95	SDSSJ094733.21+100508.7	225.37	43.54	146.89	10.09	0.139	6.5	0	13.55±0.02	-10.5± 2.9	13.58±0.05	-21.2± 7.2
96	ZW535.012	120.17	-17.13	9.09	45.66	0.047	6.4	0	13.30±0.05	-15.2± 5.8	13.29±0.08	-20.5±11.5
97	RBS2000	350.20	-67.58	351.19	-40.68	0.173	6.4	0	13.59±0.03	-12.5± 3.1	13.63±0.05	-16.1± 5.7
98	RXJ0439.6-5311	261.22	-40.93	69.91	-53.19	0.243	6.3	0	13.48±0.03	-4.7± 3.6	13.52±0.06	-0.7± 6.8
99	PHL2525	80.68	-71.32	0.10	-12.76	0.198	6.3	0	13.57±0.03	-20.0± 3.9	13.60±0.05	-30.0± 7.0
100	RXSJ00508+3536	122.80	-27.26	12.71	35.61	0.058	6.2	0	13.43±0.04	-30.1± 5.2	13.42±0.07	-21.2± 9.3
101†	Q1545+210	33.90	49.46	236.93	20.87	0.264	6.0	0	13.83±0.03	-24.7± 2.7	13.85±0.03	-24.2± 4.2
102	TON1187	188.33	55.38	153.26	35.86	0.079	6.0	0	13.42±0.04	-27.2± 5.4	13.40±0.07	-23.1± 9.8
103	CAL-F-COPY	277.18	-35.42	75.77	-66.56	0.064	5.9	0	13.31±0.05	21.5± 6.8	13.40±0.08	15.8±10.3
104	PMNJ1103-2329	273.19	33.08	165.91	-23.49	0.186	5.9	0	13.35±0.04	37.4± 7.2	13.38±0.08	25.9±11.7
105	HB89-0107-025-NED05	134.03	-64.78	17.57	-2.31	0.956	5.9	0	13.42±0.04	-14.4± 5.0	13.49±0.07	-18.9± 9.2
106	SDSSJ110307.57+291230.0	201.56	66.09	165.78	29.21	0.365	5.9	0	13.44±0.04	-9.2± 4.7	13.41±0.06	-16.5± 8.0
107	Q0349-146	205.48	-46.32	57.87	-14.49	0.616	5.8	0	13.35±0.05	-9.5± 5.4	13.38±0.08	0.1±10.1
108	QSO-B1229+204	269.44	81.74	188.01	20.16	0.063	5.8	0	13.61±0.03	-18.0± 3.3	13.64±0.05	-31.1± 7.2
109	FBQSJ1010+3003	198.43	54.63	152.50	30.06	0.256	5.7	0	13.51±0.04	-37.0± 5.7	13.56±0.05	-36.4± 8.4
110	SDSS-J141309.14+092011.2	354.10	63.76	213.29	9.34	0.460	5.6	0	13.56±0.03	-4.8± 3.5	13.54±0.06	-9.3± 7.2

Note. — Table 3.1 continued

No.	HSLA-ID	l	b	RA	DEC	z	SNR	Q	logN_{1393}	$v_{c,1393}$	logN_{1402}	$v_{c,1402}$
		(°)	(°)	(°)	(°)		(per pix)			km s^{-1}		km s^{-1}
(0)	(1)	(2)	(3)	(4)	(5)	(6)	(7)	(8)	(9)	(10)	(11)	(12)
111	HE2259-5524	330.64	-55.72	345.59	-55.14	0.854	5.6	0	13.45±0.04	11.2± 4.8	13.42±0.08	12.6± 9.9
112	4C25.01	114.07	-36.28	4.92	26.05	0.284	5.6	0	13.68±0.03	-15.6± 3.1	13.72±0.05	-12.2± 5.7
113	SDSSJ092909.79+464424.0	172.58	46.01	142.29	46.74	0.239	5.5	0	13.24±0.06	-37.2± 9.8	13.28±0.10	-6.2±13.1
114	PG0923+201	210.18	42.65	141.48	19.90	0.192	5.5	0	13.17±0.07	-21.3±10.3	13.17±0.13	-31.3±18.7
115	RBS563	272.25	-39.23	69.62	-61.80	0.069	5.4	0	13.17±0.06	-0.9±7.6	13.18±0.16	6.1±21.2
116	HE0435-5304	261.02	-41.37	69.21	-52.98	1.231	5.3	0	13.32±0.05	-1.3± 6.2	13.42±0.09	-14.1±12.1
117	PMNJ2345-1555	65.67	-70.99	356.30	-15.92	0.621	5.3	0	13.63±0.03	-10.4± 3.5	13.66±0.05	-14.4± 6.1
118	QSO-B2356-309	12.84	-78.04	359.78	-30.63	0.165	5.3	0	13.38±0.05	3.2± 5.7	13.46±0.07	-5.8± 9.4
119	PG0832+251	199.49	33.15	128.90	24.99	0.329	5.3	0	13.28±0.06	-15.0± 7.8	13.26±0.11	0.1±14.3
120	4C-13.41	225.12	49.12	151.86	12.82	0.240	5.2	0	13.66±0.03	-0.8± 3.3	13.61±0.06	12.8± 7.3
121	IRAS-F04250-5718	266.99	-42.00	66.50	-57.20	0.104	30.2	1	≥13.57	-11.9± 0.6	≥13.67	-10.7± 1.0
122†	PKS2005-489	350.37	-32.60	302.36	-48.83	0.071	8.6	1	≥14.00	41.1± 2.5	≥14.06	43.4± 2.5
123*	PG1211+143	267.55	74.31	183.57	14.05	0.080	7.6	1	≥13.56	-12.7± 2.6	≥13.67	-3.0± 3.7
124	PKS1136-13	277.53	45.43	174.79	-13.85	0.556	7.4	1	≥13.83	29.8± 2.4	≥13.90	30.5± 3.2
125†	PG1435-067	343.98	47.21	219.57	-6.97	0.126	7.4	1	≥13.63	-35.3± 3.1	≥13.69	-33.7± 4.8
126	2MASS-J14312586+2442203	32.42	67.42	217.86	24.71	0.406	7.0	1	≥13.78	-39.8± 3.2	≥13.87	-43.2± 4.5
127	RBS2005	97.94	-36.80	351.48	21.89	0.120	6.7	1	≥13.75	2.4± 1.8	≥13.90	3.1± 2.8
128†	MRK841	11.21	54.63	226.00	10.44	0.036	6.4	1	≥13.88	-40.0± 3.5	≥14.03	-41.8± 3.9
129†	PDS456	10.39	11.16	262.08	-14.27	0.184	5.8	1	≥14.00	-6.4± 1.9	≥14.02	1.6± 2.5
130*	3C273	289.95	64.36	187.28	2.05	0.158	30.2	-1	-	-	-	0.0± 0.0
131*	PKS0405-123	204.93	-41.76	61.95	-12.19	0.572	8.6	-1	-	-	-	0.0± 0.0
132	TON236	44.43	55.35	232.17	28.42	0.450	7.6	-1	-	-	-	0.0± 0.0

Note. — Table 3.1 continued

3.3 The All-Sky Distribution of Si IV

Moving at $|v_{\rm LSR}| \leq 100$ km s^{-1}

In this section we study the column density (log$N$) and centroid velocity (v_c) distribution of the low-intermediate velocity Si IV over the Galactic sky, as shown in Figures 3.4 and 3.5. For each $Q = 0$ sightline, log$N$ is the mean column densities of the doublet measurements; and for each $Q = 1$ sightline, log$N$ is taken to be the values of logN_{1402} since Si IV 1402Å is weaker thus is less saturated. The centroid velocity v_c is the average value of the doublet measurements for each QSO regardless of the target's Q value. Overall the north and south are roughly evenly sampled with 61 and 68 QSO sightlines, respectively. For $Q = 0$ sightlines with spectrally resolved doublet profiles, the minimum and maximum values of log$N$ are 13.13 and 13.94, with an average of 13.50 and a standard deviation of 0.17 dex. If excluding those sightlines potentially associated with the Fermi Bubbles (see next), we find that the maximum log$N$ is 13.78, and the rest of the sample has an average log$N$ of 13.48 and a standard deviation of 0.15 dex. The general scatter range of Si IV is consistent with the Si IV measurements by W12 using *FUSE* spectra (see their Figure 7).

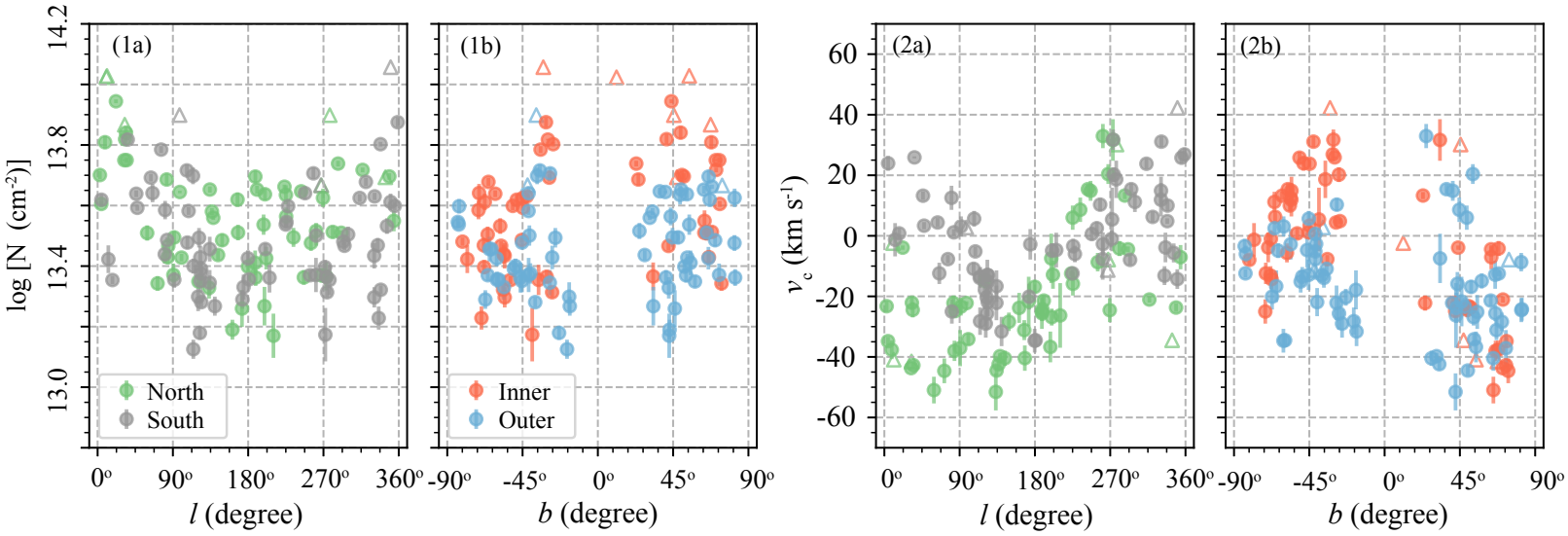

Figure 3.5: Panels (1a) and (1b) show the log$N$ distribution as functions of Galactic longitude (l) and latitude (b), respectively. For $Q = 0$ sightlines, we calculate the mean value of the doublet column density (dots); for $Q = 1$ sightlines, we show the logN_{1402} value as the lower limits (upward triangles). In panel (1a), we color-code the data into North ($b > 0°$, green) and South ($b \leq 0°$, grey); in panel (1b), we split the data into Inner ($0° < l < 90°$ or $270° < l < 360°$, red) and Outer ($90° < l < 270°$, blue). Panels (2a) and (2b) show the v_c distribution as functions of l and b; the symbols are color-coded the same way as those in panel (1a) and (1b), respectively. The centroid velocity is the mean of the doublet measurements for both the spectrally resolved and saturated sightlines.

We find a log$N$ enhancement towards the Galactic center near $|l| \lesssim 30^\circ$ and $-40^\circ \lesssim b \lesssim 80^\circ$, which roughly coincides with the Fermi Bubbles (Ackermann et al. 2014; Fox et al. 2015; Bordoloi et al. 2017). Sightlines within this region have log$N$ generally ~ 0.2 dex higher than others as is better shown in panel (1a) in Figure 3.5, although the centroid velocities are not significantly different. There are 14 sightlines that are likely to be associated with the Fermi Bubbles, which are indicated with † in Table 3.1. Ten of these sightlines are in common with the sightlines used for the study of the north Fermi Bubble by Bordoloi et al. (2017). One of them, PDS456, lies inside the Fermi Bubble at $l = 10.4^\circ$ and $b = 11.2^\circ$. Our AOD analyses show that the Si IV doublet of this sightline are saturated (see § 3.2.3) with log$N \geq 14.02$, while Bordoloi et al. (2017) gave a consistent estimate of log$N > 14.05$ based on Voigt profile fitting (see also Fox et al. 2015 for a detailed study of PDS456 through the Galactic center). The other nine sightlines all lie outside of the north Fermi Bubble but generally within $10^\circ - 20^\circ$ of the bubble boundaries.

Except for these 14 sightlines, we find that the log$N$ distribution in the north and south are similar as shown in Figures 3.4 and 3.5. This is different from the observations of the low-intermediate velocity O VI in the Galactic halo as studied by Savage et al. (2003). There they found that the O VI column density at $b > 45^\circ$ is ~ 0.25 dex higher than other regions of the Galactic sky.

Kinematically, we find that in the north a significant fraction of the Si IV-bearing gas is moving towards us at $v_c \gtrsim -50$ km s^{-1}, as seen from the centroid velocity distribution in Figures 3.4 and 3.5. The blue-shifted pattern near $l \sim 180^\circ$ cannot be simply explained by co-rotation or halo lagging of ionized gas at the MW's disk-halo interface, which would

otherwise show a clear segregation pattern of blue- and red-shifted velocity at $l = 180°$ (Wakker 2004). As most sightlines are at high Galactic latitudes, their centroid velocities suffer only modest projection effects. The blue-shifted gas in the north implies an excess of inflowing gas toward the disk. In the south, no obvious trend of gas inflows is found.

We detect Si IV absorption along every COS sightline studied in this work, indicating the low-intermediate velocity Si IV has a covering fraction (i.e., detection rate) of $C_f = 100\%$ over the Galactic sky at $|b| \gtrsim 30°$. This is very different from the results of the ionized high-velocity gas (Fox et al. 2006; Shull et al. 2009; Collins et al. 2009; Lehner et al. 2012; Richter et al. 2017). For example, Shull et al. (2009) show that the HVC sky coverage is $81\% \pm 5\%$ based on a search of Si III absorbers in *HST*/COS and *FUSE* spectra of 37 AGNs, while Richter et al. (2017) found a covering fraction of 74% for high-velocity Si III using COS observations. Collins et al. (2009) nevertheless found a very high detection rate of $91\% \pm 4\%$ for Si III using *HST*/STIS archival data. With a different set of ions (e.g., C II, C IV, Si III, Si IV), Lehner et al. (2012) found a covering fraction of 68% for gas moving at $|v| > 90$ km s^{-1} at $|b| > 20°$. The non-unity covering fraction of the ionized high-velocity gas can also be inferred from our doublet spectra (Figures 3.1 and 3.2), where not every sightline has absorption features at $|v| > 100$ km s^{-1}.

3.4 Models for the All-Sky Distribution of Si IV

Without distance constraints, it is difficult to trace the origins of the Si IV-bearing gas. The spectrum of a QSO sightline going through the Galactic halo is likely to contain absorption line information from the ISM, disk-halo interface, and the MW's CGM in a large volume

simultaneously. A number of authors attribute the QSO-probed Galactic Si IV to the MW's disk-halo interface with a plane-parallel flat slab geometry (e.g., Savage et al. 1990; SW09; W12), assuming that there is very small amount of low-intermediate velocity Si IV existing in the MW's CGM. In § 3.4.1, we briefly review SW09's flat-slab model for the Galactic Si IV moving at low-intermediate velocities. Then in § 3.4.2, we propose a better-fit model to the data with a global component that is likely to resemble the contribution of the MW's CGM.

3.4.1 A Commonly Adopted Flat Slab Model

SW09's flat-slab model assumes a simple physical scenario that most of the Galactic Si IV at $|v| \lesssim 100$ km s^{-1} concentrated on the MW's disk-halo interface. The flat slab has an exponential density profile, $n(z) = n_0 e^{-|z|/z_h}$, extending above and below the Galactic disk. In this equation, z is the vertical distance from the Galactic plane, z_h is the scale height of the gas, and n_0 is the mid-plane number density. z_h and n_0 can be constrained in the following way: for a star at height z_s from the Galactic plane, the modeled column density seen towards the star projected along the vertical direction is $N_{mod,\perp} = \int_0^{z_s} n(z, X) dz$. $N_{mod,\perp}$ can then be related to the observed column density towards the star as $N_{mod,\perp} = N_{obs} \sin|b|$, where b is the star's Galactic latitude. Since the number density of the flat slab drops dramatically above z_h, the value of $N_{mod,\perp}$ flattens as we probe background stars at vertical distances much larger than z_h. For extragalactic targets, such as QSO sightlines and stars in LMC/SMC, the flat-slab model expects that the Si IV column densities measured along these sightlines should be consistent with those of halo stars at distances much higher

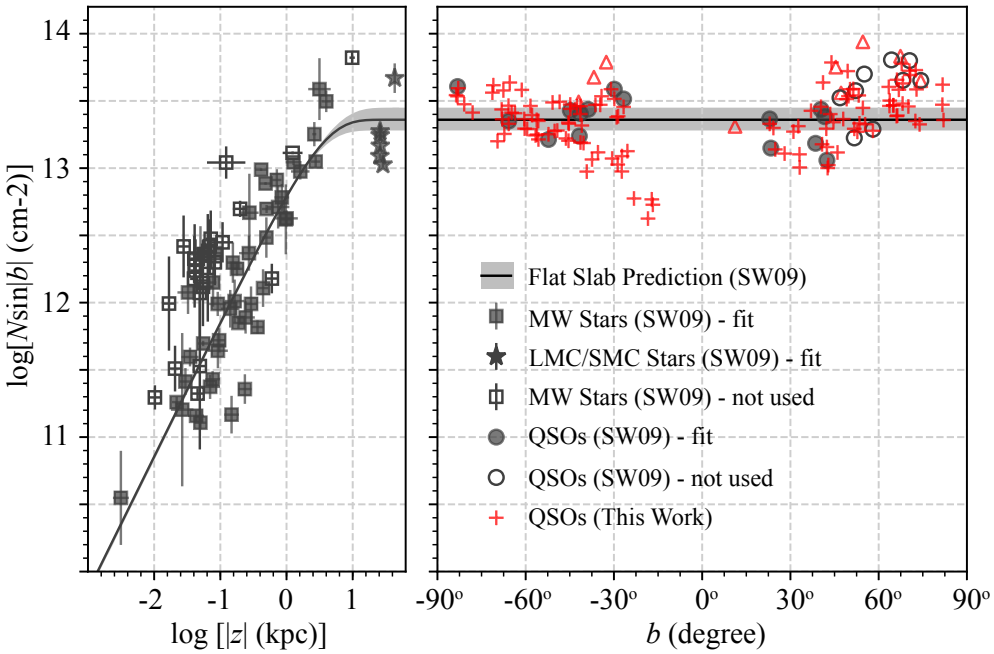

Figure 3.6: The log(Nsin|b|)-log|z| relation on the left panel for stellar sightlines, and log(Nsin|b|)-b on the right for QSO sightlines, respectively. The black symbols are those used by SW09: filled symbols were used in their flat-slab model fitting, while open symbols were excluded due to sightlines intercepting specific ISM/halo structures. See § 3.4.1 for more details. This plot is adopted from their Si IV panel of Figure 2 in SW09, although we do not include their upper/lower limit data. The black curve and gray shaded regions show the predicted log$N_{\rm mod,\perp}$ and 1σ from SW09's flat-slab model. The red crosses/upward triangles are our Si IV measurements of resolved (Q = 0)/saturated (Q = 1) sightlines, respectively; error bars are approximately equal to the size of the symbol. Our QSO data show that log(Nsin|b|) increases as |b| increases, which cannot be explained by the flat slab geometry.

than $z_{\rm h}$.

SW09 conducted a thorough study of the flat-slab model for the warm-hot ionized gas moving at low-intermediate velocities. They searched the literature and collected the column densities of a number of ions (e.g., H I, Al III, Si IV, C IV, O VI) for 109 halo star sightlines and 30 QSO sightlines from a number of authors (e.g., Jenkins 1978; Lehner & Howk 2007; Bowen et al. 2008; W12; see Table 2 of SW09 for a complete list of references). Different authors have varied choices of velocity ranges over which the ion column densities were integrated, but the adopted ranges are all near $[-100, 100]$ km s^{-1}. For example,

Bowen et al. (2008) calculated the O VI AOD column densities within ±120 km s^{-1} for all their stellar sightlines while W12 deliberately determined the velocity range of each absorption line for every QSO they used.

SW09 examined the log($N_{\rm obs}$sin|b|)-log|z| relation, and found that log($N_{\rm obs}$sin|b|) increases with log|z| for most of their halo star sightlines but the relation reaches a plateau for stars beyond certain heights. We reproduce SW09's flat-slab experiment using their published stellar/QSO Si IV data, which are shown as black symbols in Figure 3.6. In the left panel, the filled black symbols show the stellar sightlines used in their flat slab parameter fitting, including 44 MW halo stars (shown in filled squares) broadly distributed from log|z| ~ -2.5 to ~ 0.5 and six LMC/SMC stellar sightlines (shown in filled stars) at log|z| ~ 1.7. Sightlines noted as open symbols were not considered in their fitting due to either prominent H II regions, X-ray sources, or supernova remnants along the lines of sight. They also excluded a halo star vZ 1182 at log|z| ~ 1.0 and $b \sim 79^\circ$ because of the concern of contamination from the potential excess region near the north Galactic pole, as revealed by the O VI all-sky distribution (Savage et al. 2003). The right panel shows the QSO measurements as a function of Galactic latitude b. The 15 QSOs shown in filled black circles were used by SW09 for the flat slab modeling, and there are ten QSO sightlines at $b > 45^\circ$ (open circles) that were discarded to avoid the O VI-enhanced region near the north Galactic pole (Savage et al. 2003). SW09's data show that the value of log($N_{\rm obs}$sin|b|) peak at ~ 13.3 for stars at $z \sim 5 - 10$ kpc (i.e., log|z| $\gtrsim 0.5$), and the QSO measurements scatter around this value. The straight line and shaded area spanning from the left to right panels in Figure 3.6 show the model prediction of the log$N_{\rm mod,\perp}$-log|z| relation from

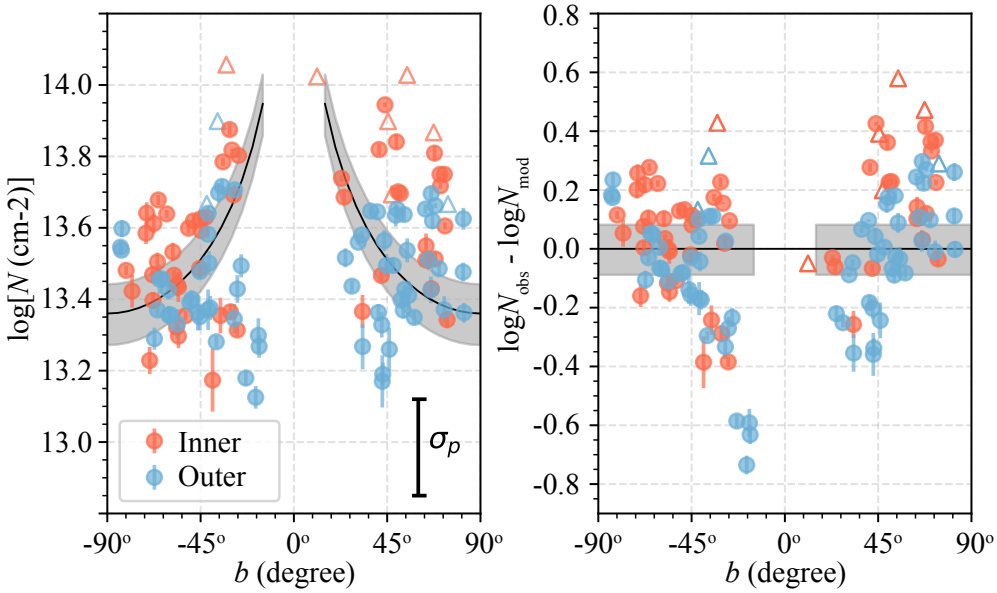

Figure 3.7: Left: log$N$-b relation for the low-intermediate Si IV from our QSO data. The data points are the same as those in panel (1b) of Figure 3.5. Black curves show SW09's flat-slab model prediction, and the gray shades are the 1σ ranges. The σ_p = 0.27 dex in the bottom right is the patchiness parameter that SW09 adopted, which we discuss in § 3.4.2. Right: Residuals of the observed and model-predicted Si IV column densities, δlog$N$=log$N_{\rm obs}$-log$N_{\rm mod}$. A good model fit should yield a random distribution of δlog$N$ around 0.0 dex, however, the actual residuals show that the flat-slab model overpredicts the log$N$ value at low b and underpredicts those at high b.

SW09's flat slab model. They found a best-fit scale height of $z_h = 3.2^{+1.0}_{-0.6}$ kpc and mid-plane density of $n_0 = 2.3 \times 10^{-9}$ cm^{-3} for the Si IV flat slab.

SW09's flat-slab model reproduces the general trend of the projected Si IV column densities seen towards halo stars and a number of QSO sightlines at $b < 45°$. However, as we populate the Galactic sky with more QSO measurements shown in red crosses (resolved, $Q = 0$) and upward triangles (saturated, $Q = 1$) in the right panel of Figure 3.6, we find that the flat slab cannot describe the log($N_{\rm obs}$sin$|b|$)-b trend as revealed by our large QSO sample. A Spearman test between log($N_{\rm obs}$sin$|b|$) and $|b|$ find a correlation coefficient of $r_{\rm s} = 0.53$, implying log($N_{\rm obs}$sin$|b|$) is likely to increase monotonically with

$|b|$. A separate test for north- and south-only sightlines finds $r_{s,n} = 0.54$ and $r_{s,s} = 0.50$. Since the flat-slab model regards QSO sightlines as those with path lengths of infinity, the $\log(N_{obs}\sin|b|)$ values from QSOs should always be $\log(N_{obs}\sin|b|) = \log(n_0 z_h) = 13.36$ (SW09). The monotonic $\log N_{obs}\sin|b|$-$|b|$ trend indicates that a flat-slab geometry with an exponential density distribution is not adequate to explain the Si IV content along the QSO sightlines, which we discuss in more detail next.

The mismatch between our QSO measurements and SW09's flat-slab model prediction is further illustrated in Figure 3.7, where we directly compare the column density values without the $\sin|b|$ projection. The data points in the left panel are the same as those in panel (1b) of Figure 3.5. The black curves and gray shades show the $\log N$ prediction from SW09's best-fit flat slab model: a QSO sightline at $b = 30°$ would have twice as much column density as a QSO at $b = 90°$. However, our measurements of $\log N$ show no such strong dependence on b. We find that $\log N$ generally fluctuates between 13.1 to 14.0 dex regardless of their b value. The right panel shows the column density residuals $\delta\log N$ between our measurements and SW09's flat-slab model prediction. A good model fit should yield residuals that randomly scatter around 0.0 dex, which is not the case here. The flat slab model over-predicts $\log N$ at low b and under-predicts those sightlines at high b, resulting in an increasing $\delta\log N$ at higher b.

We note that this mis-match between the measured $\log N$ and flat-slab prediction has also been found in studies of Galactic O VI (Figure 12 of Savage et al. 2003) and C IV (Figure 8 of W12) moving at low-intermediate velocities. In their work, Savage et al. (2003) analyzed *FUSE* spectra of 100 extragalactic targets and pointed out that a symmetrical flat

slab with an exponential density profile cannot accurately depict the overall distribution of O VI moving at $|v| \lesssim 100$ km s^{-1}. They also found that the O VI centroid velocities do not fit into the scenario of a flat slab co-rotating with the Galactic disk. C IV is likely to be a better proxy than O VI for Si IV given their comparable ionization potentials (33eV for Si IV and 48eV for C IV). In the flat-slab model, SW09 found a scale height of z_h = 3.6 kpc for C IV, which is similar to Si IV's scale height of 3.2 kpc. W12 show their log$N$ measurements of C IV at low-intermediate velocity in their Figure 8, overplotted with SW09's flat-slab predictions. Their northern sightlines show a similar data-model mismatch to what we show in Figure 3.7. Their southern sightlines follow the general trend of the flat slab; however, since they only have 13 sightlines in the south, it is hard to clearly declare a 1/sin|b| effect.

To briefly summarize, we find a flat-slab geometry cannot accurately describe the overall distribution of the Si IV moving at low-intermediate velocities as seen from QSO sightlines. In the following section, we proceed with a new model for the Si IV distribution by adding in a global component to the flat slab model. Then we further discuss the caveats of SW09's flat-slab model and our model in § 3.5.1.

3.4.2 A New Two-Component Model

The flat-slab model predicts a strong dependence of log$N$ on b, i.e., QSO sightlines near the pole regions have the shortest path lengths through the flat slab and thus should have the least Si IV, while those near the Galactic plane would have the longest paths and thus the most Si IV (see left panel of Figure 3.7). However, the observed log$N$ does not follow

this predicted trend closely – log$N$ seems to have a flat, but scattered distribution from low to high b. Inspired by this b-independent distribution, here we propose a new model which includes two column density components along each QSO sightline: a disk-halo component resembling SW09's flat slab, and a global component indicating a constant column density background. We refer to this model as the *two-component* model in the following text. The model expects the total column density for a given line of sight to be:

$$N_{\rm tot} = N_{\rm DH,\perp}/\sin|b| + N_{\rm global}, \tag{3.5}$$

where b is the Galactic latitude, $N_{\rm DH,\perp}$ represents the projected Si IV column density as predicted by a flat slab, and $N_{\rm global}$ is contributed by a global background. At low latitudes, the material at the disk-halo interface dominates the column densities owing to a substantially increased path length through it (a factor of 2 for gas at $b = 30^\circ$ compared to $b = 90^\circ$). Thus, the $N_{\rm DH,\perp}$ term provides an excellent description of the bulk of the material at low Galactic latitudes. At higher Galactic latitudes, the uniformly distributed global component $N_{\rm global}$ provides a relatively larger contribution to the observed total column density owing to the shorter path length through the disk-halo flat slab.

Solving Eq. 3.5 is a straight line fit to the data in the linear N-1/sin$|b|$ space, where ($N_{\rm DH,\perp}$, $N_{\rm global}$) are the coefficients we are solving for. We use the 120 QSOs sightlines that have spectrally resolved Si IV doublets ($Q = 0$). Excluding the nine sightlines with saturated profiles ($Q = 1$) will not change our results significantly given that the quantity is small and that they are mostly at $|b| > 30^\circ$. We discuss further in § 3.5.1 how low-b data may affect our fitting. We conduct a linear chi-square fit to the data by minimizing

$\chi^2 = \sum_{i=1}^{120}(\frac{N_i - N_{\rm fit}}{\sigma_m})^2$, where N_i is the measured total column density for each sightline and $N_{\rm fit}$ is the corresponding fit. $\sigma_m \equiv (\sigma_i^2 + \sigma_p^2)^{1/2}$ is the combined quadrature error of the measured column density error σ_i and an artificially introduced term σ_p. Since σ_i is much smaller ($\sim 10^{11-12}$ cm^{-2}; $\lesssim 0.05$ dex) than the scatter of column density (see Figure 3.5) which has a standard deviation order of magnitude higher (3.15×10^{13} cm^{-2}; 0.17 dex), we include the σ_p to regulate the χ^2 minimization so that the fitting will not be driven by those high-quality data points with the smallest σ_i.

The introduction of σ_p is inspired by the fitting method adopted by SW09. In their work, a similar σ_p was incorporated into the measurement errors so that the reduced χ^2 could be forced to 1.0 at their best fits. Their derived σ_p has a value of 0.27 dex as shown in Figure 3.7. Without σ_p, the reduced χ^2 would be $\gg$1.0 and the best-fit parameters would be determined by those measurements with the smallest errors. As they emphasized, σ_p measures the degree of patchiness in the data, which is a remedy for the over-simplified model setup that has a smooth density distribution. Our two-component model suffers the same problem that it is inadequate to describe the patchiness/clumpiness of the intervening ionized gas. Physically we expect σ_p to reflect the column density variation from sightline to sightline, thus it is given the value of the standard deviation of our column density measurements at $\sigma_p = 3.15 \times 10^{13}$ cm^{-2}, or 0.17 dex for logarithmic column densities. This is consistent with SW09's choice of σ_p.

We conduct bootstrapping on the data to estimate the confidence level of the ($N_{\rm DH,\perp}$, $N_{\rm global}$) solution. This is done by randomly sampling the data sightlines with replacements, and running the linear chi-square fit on every experiment so that a distribution of $N_{\rm DH,\perp}$

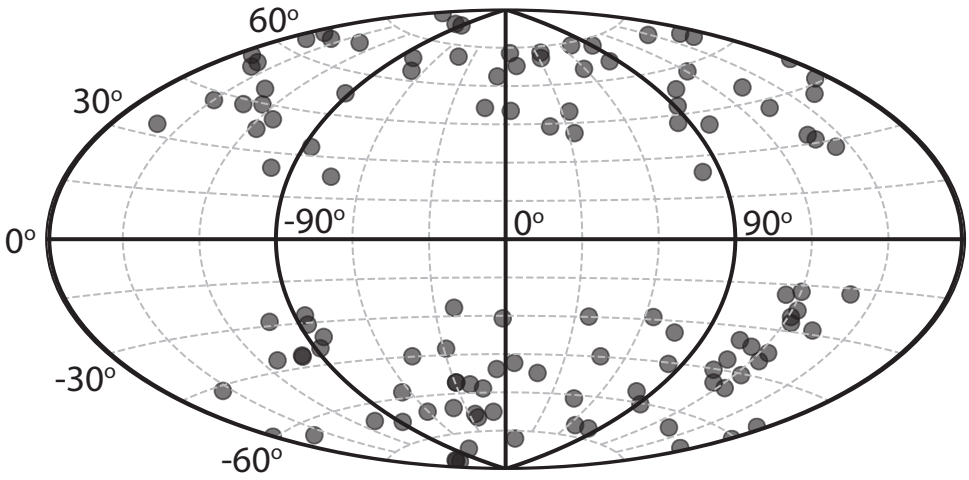

Figure 3.8: The distribution of the 120 QSOs with spectrally resolved Si IV profiles ($Q = 0$). Black lines divide the sky into the eight segments, which we use in block bootstrapping in § 3.4.2. From top left to bottom right, the number of sightlines in each segment is 19, 7, 13, 16, 11, 21, 12, 21, respectively.

and $N_{\rm global}$ can be obtained. Although our data have sampled the north (61 QSOs) and south (68 QSOs) sky quite evenly (§ 3.3), it is possible that some sightlines are correlated at certain spatial scales given the large neutral/ionized HVC structures seen in the Galactic halo (van Woerden et al. 2004; Putman et al. 2012). For example, as we show in § 3.3, there are 14 sightlines toward the Galactic center with enhanced column densities that are likely to be associated with the Fermi Bubbles. Bootstrapping on the original sample may not be able to break the degeneracy introduced by these structures. Therefore we perform block bootstrapping by dividing the Galactic sky into octants as shown in Figure 3.8. The selection of $90^\circ \times 90^\circ$ segments is for two reasons. First, the spatial extensions of the prominent H I HVCs and IVCs are at similar scales (van Woerden et al. 2004; Putman et al. 2012). Second, by bootstrapping these eight segments, we efficiently test how the $N_{\rm DH,\perp}$ and $N_{\rm global}$ values are influenced by those sightlines with the lowest or

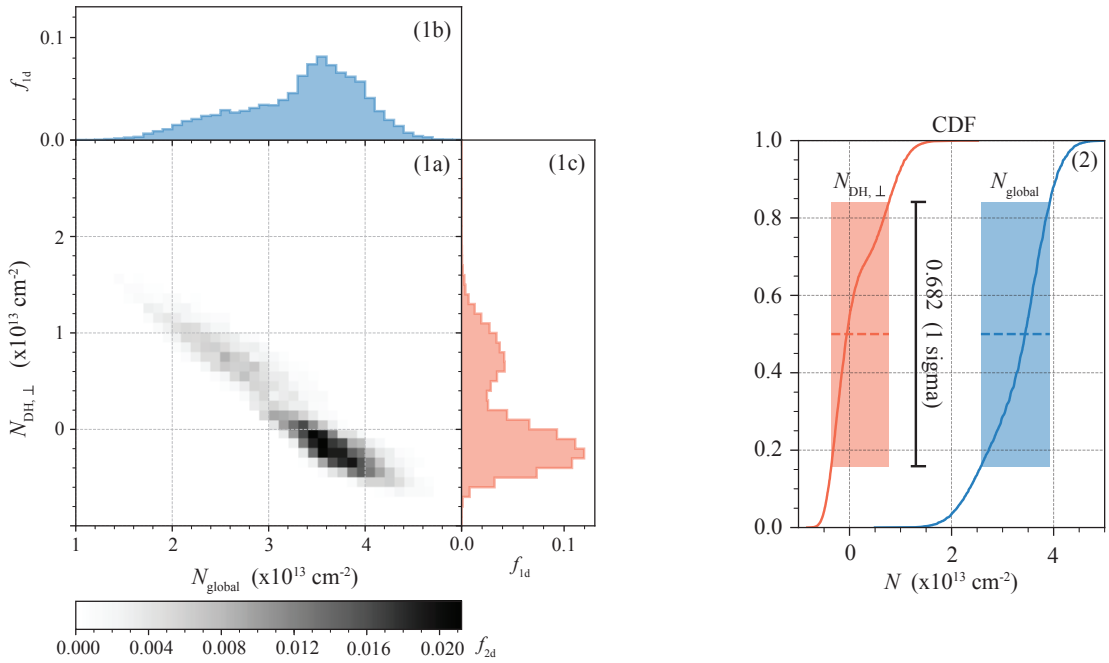

Figure 3.9: (1): 1D and 2D histograms of the ($N_{\rm DH,\perp}$, $N_{\rm global}$) solutions drawn from 10^5 block bootstrapping experiments. Panel (1a) shows the fraction of experiments within each bin in step size of 10^{12} cm^{-2}. Panel (1b) shows the marginal probability distribution for the global component and (1c) for the disk-halo component. (2): the cumulative distribution function for the global component (blue, right) and for the disk-halo component (red, left). The square patches shows the 1σ (68.2% confidence) range of the $N_{\rm global}$ and $N_{\rm DH,\perp}$ values.

highest column densities in certain regions. We also run block bootstrapping by dividing the data sample into smaller segments (e.g., $30^\circ \times 30^\circ$, $45^\circ \times 45^\circ$, or $60^\circ \times 60^\circ$), and find smaller uncertainties of the fitting parameters as we show in Figure 3.9. Therefore, the octant block bootstrapping serves as the most conservative estimates on how underlying structures could affect our estimates.

Figure 3.9 shows our result of block bootstrapping on octants. In panel (1a/1b/3c), we show the 1D and 2D histograms of ($N_{\rm DH,\perp}$, $N_{\rm global}$) solutions obtained from 10^5 block bootstrapping experiments. The data are binned in step of 10^{12} cm^{-2} for both $N_{\rm DH,\perp}$ and $N_{\rm global}$. $f_{\rm 2d}$ is defined as the fraction of experiments within each bin, which can also be

interpreted as the probability that a certain ($N_{\rm DH,\perp}$, $N_{\rm global}$) value is taken. Panel (1b) and (1c) show the marginal probability distribution for $N_{\rm DH,\perp}$ and $N_{\rm global}$, respectively. The disk-halo component $N_{\rm DH,\perp}$ shows a double-peak distribution while the global component $N_{\rm global}$ has a broad base with a peak at $\sim 3.6 \times 10^{13}$ cm^{-2}. As we explain in Eq. 3.5, the $N_{\rm DH,\perp}$ becomes prominent at low b where 1/sin|b| becomes larger, while at high b the $N_{\rm global}$ dominates the total column density. Therefore, the peaks at $N_{\rm DH,\perp} \sim 0$ and $N_{\rm global} \sim 3.6 \times 10^{13}$ cm^{-2} are likely to be caused by sampling on blocks that contain sightlines at low b with low column density measurements, where the model fitting strongly disfavors the disk-halo contribution. On the other hand, the second peak at $N_{\rm DH,\perp} \sim 0.7{\times}10^{13}$ cm^{-2} and the corresponding low-value $N_{\rm global}$ bump result from sampling on blocks with sufficient low-b sightlines with high column density measurements, thus the fitting favors more disk-halo contribution.

We show the cumulative distribution functions (CDF) of $N_{\rm DH,\perp}$ and $N_{\rm global}$ in the right panel of Figure 3.9. At CDF = 0.5, we find a median value of $N_{\rm DH,\perp} = -5.2 \times 10^{11}$ cm^{-2} and $N_{\rm global} = 3.4 \times 10^{13}$ cm^{-2}. At the 68.2% confidence level we find $N_{\rm DH,\perp} \lesssim 7.7 \times 10^{12}$ cm^{-2} and $2.6 \times 10^{13} \lesssim N_{\rm global} \lesssim 3.9 \times 10^{13}$ cm^{-2}. These equal to log$N_{\rm DH,\perp} \lesssim 12.89$ and $13.41 \lesssim$log$N_{\rm global} \lesssim 13.59$. The negative values of $N_{\rm DH,\perp}$ do not have physical implications on the properties of the Galactic halo medium. However, they suggest that our QSO sample might not have enough sightlines at low Galactic latitudes (e.g., $|b| < 30°$) to effectively study the disk-halo component $N_{\rm DH,\perp}$, which is a caveat we will discuss in § 3.5.1.

In Figure 3.10, we compare the column density prediction of the two-component

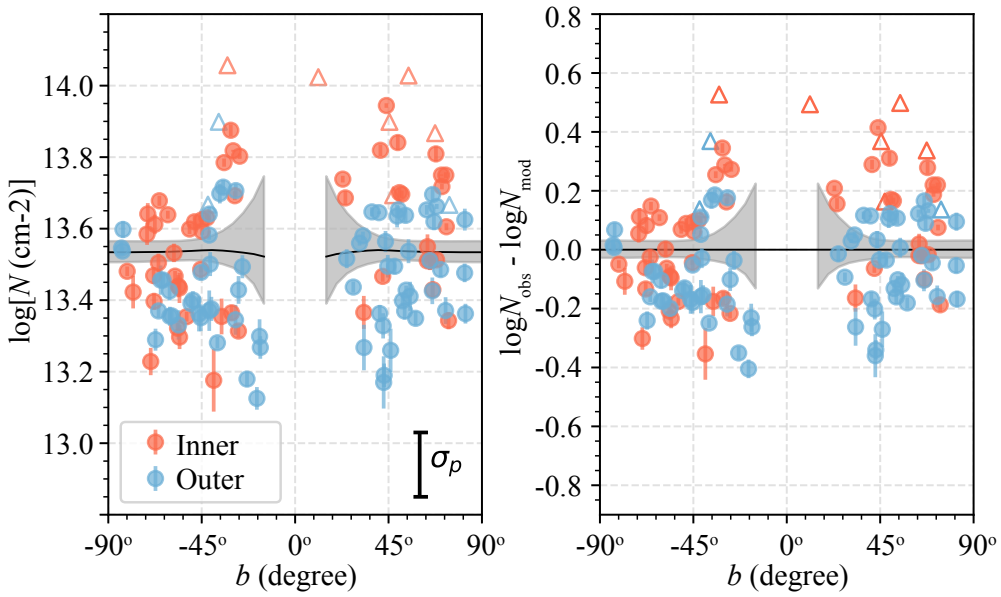

Figure 3.10: Left: log$N$-b distribution. The data points are the same as those in Figures 3.5 and 3.7. The black line shows the median values of log$N_{\rm tot}$ as predicted by the two-component model based on block bootstrapping. The gray shades indicate the 68.2% (1σ) confidence range as inferred from the CDF (Figure 3.9). The σ_p = 0.17 dex in the bottom right is the patchiness parameter used in the two-component model fitting to account for the scatter of log$N$ (see § 3.4.2). Right: column density residuals of the observed and model-predicted Si IV column densities, $\delta\log N = \log N_{\rm obs} - \log N_{\rm mod}$. Note that the abnormal trend of $\delta\log N$ increasing with larger b as shown in Figure 3.7 has now disappeared, implying that our two-component model is likely a better representation of the Si IV seen towards QSOs than the commonly adopted flat-slab model.

model with the QSO measurements. The data symbols are the same as those in Figure 3.7. The black line shows the predicted total column density from the median value drawn from the 10^5 bootstraps at each b, while the gray shades show the corresponding 68.2% confidence range. Although $N_{\rm DH,\perp}$ and $N_{\rm CGM}$ show broad distribution (see Figure 3.9), they together produce tight $N_{\rm tot}$ value regulated by the straight line fit in Eq. 3.5. In general our two-component model can recover the Si IV column density distribution over the Galactic sky, despite the large scatter of the column densities. As we describe previously, the large scatter is most likely due to the patchy nature of the halo medium, which is accounted for by the patchiness parameter σ_p in our model. Notably, the prominent b-dependent column

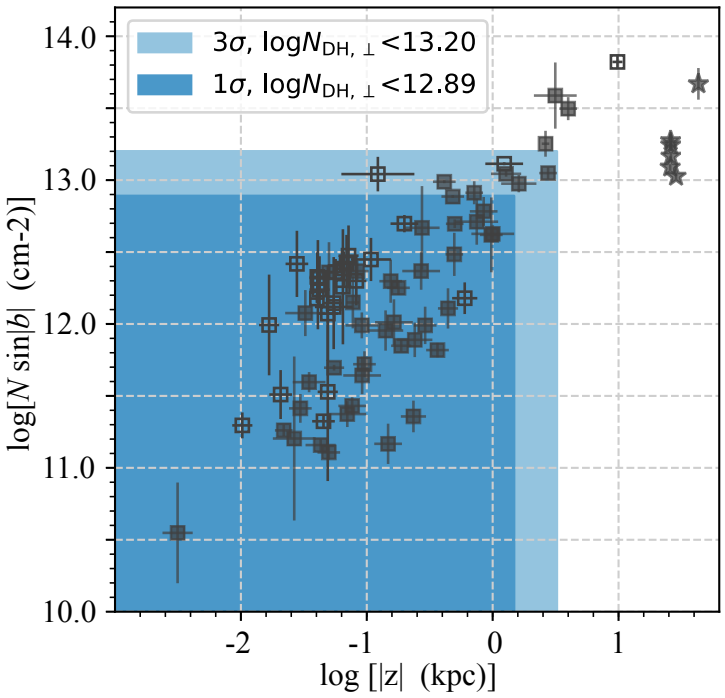

Figure 3.11: Comparisons between the predicted disk-halo component $\log N_{\rm DH,\perp}$ and the observed values $\log(N_{\rm obs}\sin|b|)$ towards SW09's stellar sightlines. The data symbols are the same as those in the left panel of Figure 3.6. The dark-blue patch shows the 1σ range of $\log N_{\rm DH,\perp}$ as we derive from the CDF in Figure 3.9, and the light-blue patch shows the 3σ range. The boundaries of the patches on the x axis are determined by the stars with the higher $\log|z|$ within each patch.

density residuals found in SW09's flat-slab model (Figure 3.7) now mostly disappears.

Since our two-component model does not have distance information, the exact locations of the disk-halo and global components are ambiguous. In § 3.5.2, we discuss the potential origin(s) of the global component. For the disk-halo component, it is by design to represent the flat-slab geometry as adopted in SW09 as well as to reflect the observational evidence of the flat disk-halo interface seen in nearby edge-on galaxies (e.g., Rand 1997, 2000; Fraternali et al. 2005; Boettcher et al. 2016). For this component, we compare the model-predicted $\log N_{\rm DH,\perp}$ value with SW09's stellar data in Figure 3.11. From the block bootstrapping we find that at 1σ the disk-halo component has $N_{\rm DH,\perp} < 7.7 \times 10^{12}$

cm^{-2} or $\log N_{DH,\perp} \lesssim 12.89$; this is shown as the dark-blue patch in Figure 3.11. For stellar sightlines within this range, we find that the maximum height is $\log|z| \sim 0$ or $|z| \sim 1$ kpc. The light-blue patch shows the 3σ value of $\log N_{DH,\perp} \lesssim 13.20$ dex, within which the highest star is at $\log|z| \sim 0.5$ or $|z| \sim 3$ kpc. This implies that our two-component model is able to reproduce the column densities towards stars within 3 kpc. Stellar sightlines beyond this height and those in the LMC/SMC start to collect more Si IV associated with the global component along the sightline path.

3.5 Discussion

In the previous section, we briefly reviewed SW09's flat-slab model and proposed a two-component model to better describe the all-sky distribution of Si IV absorption at low-intermediate velocity. Here, we first discuss the caveats of both models (§ 3.5.1). We proceed by discussing the potential origin(s) of the Si IV global component, which dominates over the disk-halo component in column density (§ 3.5.2). Finally, we conduct order-of-magnitude mass calculations for the global component in the context of the MW's CGM (§ 3.5.3).

3.5.1 Caveats of the Models

A considerable degree of column density scatter can be seen in both SW09's star/QSO sample and our QSO sample, indicating that the Si IV-bearing gas is patchy. There are several reasons why a disk-halo and halo medium would be patchy. For example, the

Galactic fountain (Shapiro & Field 1976) that circulates material between the disk and halo may be responsible for some of the scatter. Along the trajectory of a fountain gas parcel, the gas may experience several phase changes due to different cooling rates at different locations (Marasco et al. 2012), resulting in a clumpy and inhomogeneous medium.

The patchiness parameter σ_p adopted by both SW09's and our models is designed to account for the column density scatter. The inclusion of σ_p is to ensure that the χ^2 minimization algorithm would not be driven by those few data points with the most accurate measurements. However, the value of σ_p itself does not convey any deep physical meaning. Ideally, a comprehensive model would include a physically-motivated parameter that independently describes the clumpiness or volume filling factor. Unfortunately, our current dataset offers no insight as to what such a parameter's true value may be and determining its value is beyond the scope of this work.

The second caveat pertaining to both SW09's and our model is rooted in the sample selection. The halo stars in SW09 lie mostly at $|b| < 15^\circ$ and towards the inner Galaxy direction. Their sightlines at higher Galactic latitudes consist of 15 QSOs at $b < 45^\circ$ and six stars in the LMC/SMC. Along the QSO and LMC/SMC stellar sightlines, the sources of and distances to the foreground low-intermediate velocity absorbers are not well-constrained. This inhomogeneous sample selection and the inclusion of distant sighltines likely overestimate the flat-slab scale height. In contrast, our sample is dominated by QSOs at $|b| \gtrsim 30^\circ$ and our two-component model does not have distance information on the gas as limited by the QSO data sample. Although our disk-halo component can predict most of column densities measured toward SW09's halo stars within 3 kpc (Figure 3.11),

ideally one should combine the QSOs and halo stars together to provide better constraints on the locations of the disk-halo and global components.

3.5.2 Origin(s) of the Si IV Global Component

Here we discuss the origin(s) of the global component revealed in § 3.4.2. We attempt to consider all of the possible ionized structures that the QSO paths may intercept.

First, we consider a Galactic ISM origin. It is unlikely that our QSO sightlines would suffer strong contamination from dense spiral-arm regions or warps at the outskirts of the MW's disk since the QSOs are mostly at $|b| \gtrsim 30°$. However, all sightlines must leave the disk through the Local Bubble, a cavity in the ISM at the location of the Sun with a radius of $\sim$ 100 pc. SW09's halo star sample contains three objects within 1 kpc of the Sun (HD_38666, HD_52463, HD_116658). The mean Si IV column density measured along these sightlines is log$N \sim$ 12.5 dex, which accounts for only $\sim$ 10% of the Si IV toward distant QSOs. Furthermore, Savage & Lehner (2006) found that the local bubble contributes only $\sim$ 9% of column density to the total O VI content in the MW halo by comparing UV spectra of nearby white dwarfs at a mean distance of $\sim$ 109 pc with those of MW halo stars. Based on this result, SW09 suggest that Si IV from the local bubble would not have a significant effect, despite the potential phase difference between the O VI- and Si IV-traced material.

Second, superbubbles breaking out of the ISM near the solar neighborhood are unlikely to be the source. This is primarily because the upstreaming material should be found with mostly positive radial velocities, in stark contrast with our velocity centroid measurements (Figure 3.4) that predominantly trace negative radial velocities. However,

it is possible that we are seeing the remnants of a past superbubble break-out, where the bulk of the previously-ejected material is now falling back down. In this scenario, the fall-back gas is not distinguishable from the observed ionized IVCs and HVCs, which we will discuss shortly.

Third, as our sightlines cover most of the Galactic sky at $|b| \gtrsim 30^{\circ}$, any particular substructures covering small areas of the sky cannot be the dominant sources, but are likely to contribute to the column density scatter. The potential structures include: (1) the Fermi Bubbles (e.g., Fox et al. 2015; Bordoloi et al. 2017) which we have discussed in § 3.3, (2) the CGM of M31 in the southern sky (Lehner et al. 2015), and (3) cool filamentary structures embedded in the $10^5 - 10^7$ K warm-hot intergalactic medium in the Local Group (e.g., Nicastro et al. 2003; Richter et al. 2017). As we divide the sky into octants for block bootstrapping, the influence of sightlines potentially associated with small-area structures have been reflected in the distribution of the ($N_{\rm DH,\perp}$, $N_{\rm global}$) solutions (Figure 3.9).

Fourth, we consider that the global component may be associated with the widespread HI structures observed in the inner Galactic halo. IVCs are defined as discrete H I clouds moving at $|v| < 100$ km s^{-1} (van Woerden et al. 2004; Albert & Danly 2004; Wakker 2004) at distances of $\sim 1 - 5$ kpc above the Galactic plane (see Table 2 in Albert & Danly 2004), and HVCs are those moving at $|v| > 100$ km s^{-1} at further distances around ~ 10 kpc (van Woerden et al. 2004; Putman et al. 2012; Lehner et al. 2012; Richter et al. 2017). Since we only consider the origin of the Si IV global component at low-intermediate velocities, ionized HVCs themselves are not the possible culprits; however, clouds have been found with similar properties to HVCs moving at lower velocities (Peek et al. 2009; Saul et al.

2014) as expected from models (Wakker 1991b). If the global component represents the ionized counterparts of the IVCs or HVCs, one would expect the Si IV-bearing clouds to be distributed in a spherical configuration so that the column densitites have minimal dependence on $|b|$.

Ultimately, we consider that the global component may represent a contribution from material occupying the MW's CGM, extending to $\sim 0.5\ R_{\rm vir}$. All QSO sightlines would intercept the extended CGM material of the MW. The MW's CGM is typically studied at high velocities ($|v| > 100$ km s^{-1}) to avoid contamination from more nearby low-intermediate velocity gas (e.g., Fox et al. 2006; Shull et al. 2009; Collins et al. 2009; Lehner et al. 2012; Richter et al. 2017). However, in Chapter 2 we found that $\sim 65\%$ of the MW's CGM mass above $|b| \geq 20^{\circ}$ is likely to be hidden at $|v| \leq 100$ km s^{-1} regardless of the gas phase, based on a synthetic observation of a simulated MW-mass galaxy from a cosmological simulation (Joung et al. 2012b). Empirically, as found in extragalactic CGM studies, highly ionized, metal-enriched gas can extend to nearly half the virial radii of the host galaxies with centroid velocity largely within $|v| \lesssim 150$ km s^{-1} of the systemic velocities of host galaxies (e.g., Werk et al. 2014; Liang & Chen 2014; Burchett et al. 2016). Therefore, it is likely that the Si IV in the MW's CGM extends beyond the inner Galactic halo and casts absorption features at low-intermediate velocity ranges.

To summarize, we find that the global component is unlikely to be dominated by the Local Bubble, superbubble breakouts, Fermi Bubble, M31's CGM, or the Local Group medium. The global component is most likely to represent the ionized counterparts to nearby IVCs/HVCs, and/or the MW's extended, ionized CGM that occupies a much larger

volume, although its exact location is unknown. In each of these potential scenarios, spherical-like geometry better describes the data than the flat-slab cylindrical geometry since there is not an observed dependence on $|b|$ for the Si IV column densities (Figures 3.5, 3.7, and 3.10). The dominant global component over the disk-halo component shows that there is likely to be a large amount of ionized gas moving at low-intermediate velocities hidden in the MW's CGM.

3.5.3 Order-of-Magnitude Calculation of the MW's CGM Mass

In this section, we conduct an order-of-magnitude calculation for the mass of the low-intermediate velocity Si IV-bearing gas in the context of the MW's CGM. We provide two mass estimates: one adopts a radius of 160 kpc (i.e., $\sim 0.5\ R_{\rm vir}$) under the assumption that the MW's CGM is similar to that of $\sim L*$ galaxies studied at lower redshifts (e.g., Werk et al. 2014; Liang & Chen 2014; Keeney et al. 2017; Prochaska et al. 2017); the other limits the radius to 30 kpc under the assumption that the global component traces the ionized IVC/HVC counterparts in the inner Galactic halo.

3.5.3.1 MW's extended CGM within $R = 160$ Kpc

We first consider the case that the global component is associated with MW's extended CGM in a spherical volume with $R = 160$ kpc, a value based on the impact parameters probed by the COS-Halos survey (Tumlinson et al. 2011; Werk et al. 2014; Prochaska et al. 2017). We consider a uniform distribution of the global component with a covering fraction of $C_f = 1$, given that the detection rate of Si IV is 100% in our observations (§ 3.3).

Note that this assumption is unlikely to be realistic since the Galactic halo is often found to be clumpy with large column density scatter (see § 3.3 and § 3.4). The Si IV mass at low-intermediate velocities is,

$$\begin{aligned} M_{\rm SiIV,low} &= 4\pi R^2 C_f m_{\rm Si} N_{\rm global} \\ &= (1.9-2.8)\times 10^6\ M_\odot (\tfrac{C_f}{1})(\tfrac{R}{160\ {\rm kpc}})^2, \end{aligned} \tag{3.6}$$

where $m_{\rm Si}$ is the mass of a silicon atom, $4\pi R^2$ is the area of the spherical surface, and $N_{\rm global}$ is the surface density which is taken to be the column density of the global component. The range in the parentheses is based on the 1σ lower and upper values of $N_{\rm global}$ as derived in § 3.4.2.

We can further convert the Si IV mass into a hydrogen mass by assuming that the Si IV-bearing gas represents the bulk property of the MW's CGM at cool phases:

$$\begin{aligned} M_{\rm H,low} &= (\tfrac{M_{\rm SiIV,low}}{m_{\rm Si}}) 1.4 m_{\rm H} f_{\rm SiIV}^{-1} ({\rm Si/H})_\odot^{-1} {\rm Z}^{-1} \\ &= (2.4-3.6)\times 10^{10}\ M_\odot \\ &\quad (\tfrac{C_f}{1})(\tfrac{R}{160\ {\rm kpc}})^2 (\tfrac{f_{\rm SiIV}}{0.4})^{-1} (\tfrac{\rm Z}{0.3\ {\rm Z}_\odot})^{-1}, \end{aligned} \tag{3.7}$$

where 1.4 is to account for the presence of helium and $m_{\rm H}$ is the mass of a hydrogen atom. We adopt $({\rm Si/H})_\odot = 10^{-4.49}$ from Asplund et al. (2009), which is the silicon abundance in the present-day solar photosphere relative to hydrogen. We assume the metallicity as Z = 0.3 $Z_\odot$, based on the COS-Halos mean CGM metallicity estimate (Prochaska et al. 2017). The most uncertain term is the ionization fraction $f_{\rm SiIV}$, defined as the ratio of the Si IV to all the silicon in various neutral and ionized states. Photoionization, collisional ionization,

and other non-equilibrium processes such as shock ionization, conductive interfaces, and turbulence mixing may contribute to producing Si IV (e.g., Fox et al. 2005; W12). As we only aim for an order-of-magnitude mass calculation, we do not conduct sophisticated ionization modelings to determine $f_{\rm SiIV}$. Based on a collisional ionization model of Gnat & Sternberg (2007), we adopt $f_{\rm SiIV} = 0.4$ which is the maximum ionization fraction of Si IV at $Z = 0.1\ Z_\odot$. This is the closest ionization data to our adopted $Z = 0.3\ Z_\odot$ value from Gnat & Sternberg (2007)'s ionization models. We also examine the ionization fraction produced by CLOUDY (v13.03; Ferland et al. 1998, 2013) in an extragalactic UV background (Haardt & Madau 2001) at H I column density of 10^{20} cm^{-2}. We find $f_{\rm SiIV}$ peaks at ~ 0.3 for $Z = 0.1 - 0.3\ Z_\odot$, similar to the collisional ionization prediction by Gnat & Sternberg (2007).

Based on the synthetic observation of a simulated MW-mass galaxy, Zheng et al. (2015) found that the mass ratio of the high to low-intermediate velocity gas in the MW halo at $|b| \geq 20^\circ$ is 0.35 : 0.65 and this mass radio does not vary significantly from 10 kpc to 250 kpc. If we apply this ratio to the calculated mass in Eq. 3.6 and 3.7, we find that the total Si IV and hydrogen mass in the MW's CGM is,

$$\begin{aligned} M_{\rm SiIV,all} &= M_{\rm SiIV,low}/0.65 = (2.9 - 4.3) \times 10^6\ M_\odot \\ M_{\rm H,all} &= M_{\rm H,low}/0.65 = (3.7 - 5.6) \times 10^{10}\ M_\odot, \end{aligned} \tag{3.8}$$

Our mass calculation for the MW's extended CGM is accurate only as an order-of-magnitude estimate. We caution the Si IV ionization fraction is highly uncertain without fully understanding its ionization mechanism (e.g. W12; Werk et al. 2016). Furthermore, metallicity measurements for the ionized gas are notoriously difficult to obtain. Large sys-

tematic uncertainties in gas ionization state, metallicity and medium clumpiness plague all mass estimates based upon ionized gas absorption lines. When compared to the literature, we find that our derived mass of the MW's extended CGM is comparable to the most recent CGM mass estimates from the COS-Halos team (Prochaska et al. 2017), who found that the total mass of the cool, photoionized CGM of $L \sim L*$ galaxies at redshift ~ 0.2 is $(9.2 \pm 4.3) \times 10^{10}\ M_{\odot}(\frac{R}{160\ \mathrm{kpc}})^2$. On the other hand, our estimated CGM value is higher than the mass of M31's CGM as recently placed by Lehner et al. (2015). They derived a total Si mass of $M_{\mathrm{Si}} = 2.1 \times 10^6 M_{\odot}(\frac{R}{50\mathrm{kpc}})^2$ by considering Si II, Si III, and Si IV simultaneously. This corresponds to a total hydrogen mass of $\sim 4 \times 10^9(\frac{R}{160})^2(\frac{Z}{0.3Z_{\odot}})^{-1}$ adopting our assumption of the metallicity. Note that they assumed solar metallicity for the CGM of M31.

Our mass calculation is different from the one used by Stocke et al. (2013) who estimated the CGM mass of late-type galaxies with a volume filling factor of 3% – 5%. Briefly, they determined the volume filling factor of warm CGM clouds by taking into account the cover fraction, the average number of ion absorption components along the sightlines, and the physical cloud sizes as inferred from photoionization modelings (see their Eq. 5). The total CGM mass was derived by summing up the mass of all available clouds with the assumption that the warm clouds represent the whole CGM cloud population. Werk et al. (2014) calculated the CGM mass for the COS-Halos sample with both the surface density method (as we adopt here) and the volume-filling method. With a volume filling factor of 11%, they found consistent CGM mass results between the two methods. The volume-filling method has two requirements: (1) an estimate of cloud sizes based on CLOUDY modeling, and (2) an estimate of the average number of ion

absorption components along the sightlines based on Voigt-profile fitting. Since neither of these is used in this work, we are unable to conduct mass estimate with the volume-filling method.

3.5.3.2 MW's inner CGM within R=30 Kpc

Here we consider the scenario that the global component is associated with the gas in the inner Galactic halo, potentially related to the ionized counterpart of H I IVCs/HVCs. Since the Galactic disk extends out to $\sim$ 25 kpc as observed in H I (Levine et al. 2006), here we adopt a spherical volume with R = 30 kpc to ensure the inclusion of the entire disk. Adopting Eq. 3.6 but with a smaller radius, we find $M_{\rm SiIV,low} = (6.6 - 9.9) \times 10^4$ $\rm M_\odot (\frac{R}{30\ kpc})^2$ at 1σ. To convert it to the hydrogen mass, we again assume Z = 0.3 $\rm Z_\odot$ and $f_{\rm SiIV} = 0.4$, and find $M_{\rm H,low} \sim (0.9 - 1.3) \times 10^9$ $\rm M_\odot (\frac{R}{30\ kpc})^2 (\frac{f_{SiIV}}{0.4})^{-1} (\frac{Z}{0.3\ Z_\odot})^{-1}$. If we apply the same mass ratio of high to intermediate-velocity gas of 0.35 : 0.65 (Zheng et al. 2015), the hydrogen mass of the high-velocity gas in the inner Galactic halo is $M_{\rm H,high} \sim (4.6 - 6.9) \times 10^8$ $\rm M_\odot (\frac{R}{30\ kpc})^2$ and the total mass of the gas at all velocities is $M_{\rm H,all} \sim (1.3 - 2.0) \times 10^9$ $\rm M_\odot (\frac{R}{30\ kpc})^2$.

This mass calculation has the caveat that we assume a spherical volume centers at the Sun instead of the Galactic center. This caveat is negligible for the calculation in § 3.5.3.1 since a much larger volume is assumed, but becomes nontrivial here for a spherical volume with R = 30 kpc. We adopt this 30 kpc value to ensure that most of the ionized gas near the Galactic disk is taken into account; however, the mass could be overestimated by including too much volume beyond the disk. The same caveat exists in Lehner et al. (2012)'s method of estimating the total mass of ionized HVCs in the Galactic halo. They

adopted a spherical volume of 12 kpc, and found $M_{\rm iHVCs} = 1.1{\times}10^8\,M_\odot(\frac{d}{12\ \rm kpc})^2(\frac{C_f}{0.5})(\frac{\rm Z}{0.2\ \rm Z_\odot})^{-1}$. A radius of 12 kpc from the Sun would result in a spherical volume directly cutting through the Galactic disk, which may not represent the real distribution of gas clouds in the inner Galactic halo.

3.6 Conclusion

For MW absorption-line studies that rely on background QSOs, the lines of sight unavoidably intercept the ISM, the disk-halo interface, and the CGM of the Galaxy. Therefore every QSO spectrum contains mixed absorption-line features from these sources. High velocity gas ($|v| > 100$ km s^{-1}) is traditionally assumed to relate to the CGM, while low-intermediate velocity gas ($|v| \leq 100$ km s^{-1}) is considered to be more nearby. In this work, we study the all-sky distribution and origins of the Si IV-bearing gas at low-intermediate velocity with co-added G130M COS spectra of 132 QSOs obtained from HSLA (Peeples et al. 2017). Our results are summarized as follows.

First, we find that the Si IV column density log$N$ does not significantly correlate with the Galactic latitude or longitude, except sightlines near the Fermi Bubbles (see § 3.3). For other directions, we find similar log$N$ distributions in the north and south. As for the centroid velocity v_c, we find most sightlines in the north show gas moving at negative velocities toward the LSR at $v_{\rm c} \gtrsim -50$ km s^{-1}, which implies potential inflow. Sightlines in the south do not show such velocity preference.

Second, we compare our Si IV column density measurements with the predicted values from SW09's flat-slab model (§ 3.4.1). The flat slab has an exponential density profile

along the direction perpendicular to the Galactic plane. We find that the column density residuals between the QSO data and the model prediction show strong dependence on the Galactic latitude, which cannot be explained by the assumed plane-parallel geometry. The flat-slab model overestimates the column densities of sightlines at low Galactic latitudes and underestimates those at high Galactic latitudes.

We propose a two-component model which consists of a disk-halo and a global component in § 3.4.2. The disk-halo component $N_{\rm DH,\perp}$ is assumed to follow the flat-slab geometry, thus the line of sight column density scales with $1/\sin|b|$. The global component $N_{\rm global}$ represents a general background that contributes identically from sightline to sightline in the homogeneous case. We conduct block bootstrapping to solve for the values of the disk-halo and global components, and find $\log N_{\rm DH,\perp} \lesssim 12.89$ and $13.41 \lesssim \log N_{\rm global} \lesssim 13.59$ at 1σ. Our two-component model is able to reproduce the column density distribution seen towards distant QSOs and those stellar sightlines within 3 kpc of the Galactic plane.

We examine the potential origin(s) of the global component in § 3.5.2, and find that it is most likely to be associated with the MW's CGM, although its exact location is difficult to constrain without distance measurements. We conduct order-of-magnitude mass estimates for the global component with two different volume assumptions. If the global component exists in a large volume with $R = 160$ kpc, we find that the MW's extended CGM has a total hydrogen mass of $(3.7 - 5.6) \times 10^{10}\ M_{\odot}$ (§ 3.5.3.1); this mass estimate is roughly consistent with the CGM mass of $L \sim L^{*}$ galaxies at low redshifts. If the global component were related to the inner Galactic halo within 30 kpc, we find a total mass of $(1.3 - 2.0) \times 10^{9}\ {\rm M}_{\odot}$; note that this value might be overestimated since we assume

a spherical volume from the Sun (see § 3.5.3.2). Our analyses of the low-intermediate velocity Si IV absorbers and the two-component model show that there is likely to be a large amount of ionized gas moving at low-intermediate velocity hidden in the MW's CGM that has been ignored in previous studies.

In conducting this study, we perform continuum normalization for a total of 401 QSO spectra (§ 3.2.1) observed with HST/COS, which is based on a subset of HSLA (Peeples et al. 2017). Each co-added spectrum has G130M and/or G160M gratings and has a SNR $\geq$ 5.0 over the wavelength span. Our continuum normalization focuses on interstellar absorption lines, including Fe II 1142/1143/1144/1608 Å, P II 1152 Å, S II 1250/1253/1259 Å, Si II 1190/1193/1206/1526 Å, Si III 1260 Å, Si IV 1393/1402 Å, C II 1334 Å, and C IV 1548/1550 Å. For each QSO we also retrieve H I 21cm emission lines from three H I surveys: GALFA-H I (Peek et al. 2018), LAB (Kalberla et al. 2005), and HI4PI (HI4PI Collaboration et al. 2016). The QSO continua, individual line spectra, and the corresponding H I 21cm lines together form our COS-GAL dataset, which we release to the public at [10.17909/T9N677] (§ 3.2.2).

Critical information is missing when relying on QSO sightlines to probe the MW halo – the distance. For future studies, we will add in new halo star samples to constraint the distance to the Si IV content associated with the MW's disk-halo interface, thus shed light on the location of the low-intermediate velocity gas hidden in the MW's CGM. In future applications of the COS-GAL dataset, we will use other ions present in the COS spectra to study the MW's disk-halo and halo. Our COS-GAL dataset has broad potential usage, such as studying the global phenomena of ionized HVCs, gas flows in different directions,

the ionized gas properties in specific regions of the MW, or the surroundings of galaxies in the Local Group.

Acknowledgement. We are very grateful to B. Wakker and B. Savage for pointing out a critical systemic error in calculating the Si IV apparent column density in the previous version of this manuscript. We thank K. Tchernyshyov for useful discussions on COS ion absorption lines and apparent column density profile derivations. We thank M. Peeples for answering many of our questions about HSLA. We thank S. Flemming for assisting us in turning the COS-GAL dataset into a high-level science product hosted at the Mikulski Archive for Space Telescopes (MAST). We acknowledge support from HST-GO-13706, HST-GO-13383, and HST-GO-13382 which were provided by NASA through grants from the Space Telescope Science Institute (STScI). STScI is operated by the Association of Universities for Research in Astronomy, Inc., under NASA contract NAS5-26555. Most of the data presented in this paper were obtained from the MAST. We also acknowledge support from the National Science Foundation under Grant No. AST-1410800 and AST-1312888. In this research, we use software of Astropy (Astropy Collaboration et al. 2013), Linetools (Prochaska et al. 2016), IPython package (Pérez & Granger 2007), matplotlib (Hunter 2007).

Chapter 4

The Discovery and Origin of A Very-High Velocity Cloud Toward M33

4.1 Introduction

The inner halo ($\lesssim 20$ kpc) of the Milky Way (MW) is populated by neutral H I high-velocity clouds (HVCs) and their ionized counterparts (ionized HVCs). HVCs are usually defined to have velocities of $|v_{\rm LSR}| > 90$ km s^{-1}, where $v_{\rm LSR}$ is the velocity in the rest frame of the Local Standard-of-Rest (LSR) with respect to the Sun. The neutral and ionized HVCs exist at an interface where outflows from the Galactic disk is likely to be closely interacting with inflows from the halo (see Putman et al. 2012 and references therein). HVCs are commonly arranged in large complexes observed in H I 21-cm emission (Wakker & van Woerden 1991); on the other hand, ionized HVCs are detected via optical or ultraviolet

This chapter is a reproduction of a paper by Zheng, Werk, Peek, & Putman (2017) published on The Astrophysical Journal.

(UV) absorption lines toward background stars or quasars (see van Woerden et al. 2004 and references therein). The metallicities of HVCs vary from ~ 0.1 solar (e.g., complex A, WD), to $\sim 0.1-0.3$ solar (e.g., complex C; Tripp et al. 2003; Shull et al. 2011) and likely near solar (e.g., complex M, WB), complicating the interpretation of the origins (van Woerden et al. 2004). Distances to HVCs are difficult to obtain; the only direct means is to bracket the distance via the detection (non-detection) of absorption lines at similar velocities toward background (foreground) stars projected along the line of sight to the clouds (e.g, Thom et al. 2006; Thom & Chen 2008; Lehner & Howk 2010; Smoker et al. 2011; Peek et al. 2016). So far, it is generally suggested that most of the clouds lie within 5-15 kpc of the Sun (e.g., Wakker 2001; Wakker et al. 2008; Lehner et al. 2012).

One H I complex that does not lie in MW's inner halo is the Magellanic Stream, a $\sim 200^{\circ}$ long H I structure that originates from the Magellanic Clouds (MCs; Putman et al. 2003; Nidever et al. 2008, 2010). The Stream has been stripped from the MCs by tides and/or ram pressure forces as the two galaxies move through the MW halo (e.g., Murai & Fujimoto 1980; Gardiner et al. 1994; Besla et al. 2010). The closest distance of the Stream is likely ~ 55 kpc near the MCs while the most distant point is suggested to be at ~ 100 kpc near the tail based on tidal models (Besla et al. 2012) and geometrodynamical calculation (Jin & Lynden-Bell 2008). Except very close to the MCs, the metallicity of the Stream is ~ 0.1 solar, measured from several QSO sightlines that pass through different locations of the Stream (Fox et al. 2010, 2013; Richter et al. 2013; Gibson et al. 2000). Near the Stream, numerous small individual H I HVCs are found moving at Magellanic-like velocities (Braun & Thilker 2004; Brüns et al. 2005; Stanimirović et al. 2008; Nidever et al.

2010). In addition, Fox et al. (2014, hereafter F14) found that the Magellanic System, including the Stream, the Bridge and the Leading Arm, is likely to be surrounded by an ionized extended envelope with a cross-section of ≈ 11000 deg^2, which is nearly four times larger that its H I-bright region. Excluding the MCs themselves, the Magellanic H I-bright regions* have total mass of M(H I+H II)$\sim 1.4 \times 10^9 (d/55 \text{ kpc})^2$ M$_\odot$ (Brüns et al. 2005; F14), and its ionized envelope beyond the main body has an ionized mass of M(H II)$\sim 5.5 \times 10^8 (d/55 \text{ kpc})^2$ M$_\odot$ (F14).

On the projected sky, the ionized envelope of the Magellanic Stream near its tip may overlap with M31's and M33's circumgalactic medium (CGM) seen toward extragalactic sources (e.g., quasars; QSOs) and in emission, complicating the interpretation of the gas velocities in this region (F14; Nidever et al. 2010; Lehner et al. 2015). The tip of the Stream and its surrounding H I clouds move at $-500 \lesssim v_{\rm LSR} \lesssim -300$ km s^{-1} (F14; Nidever et al. 2010; Lehner et al. 2015). Since M31's and M33's systemic velocities are -301 km s^{-1} (Courteau & van den Bergh 1999) and -179 km s^{-1} (Corbelli & Schneider 1997) respectively, it is possible that the CGM of these two galaxies may have velocities comparable to the Magellanic Stream (Lockman et al. 2012; Lehner et al. 2015; Wolfe et al. 2016). In addition, this region is close to the area studied in Richter et al. (2016) who suggested nearby absorbers are likely to be streaming toward the Local Group center.

To intensify the intrigue of this Magellanic-M33-M31 overlap region, here we report the detection of a VHVC along five sightlines toward M33, and therefore the VHVC lies in front of M33's disk. As shown in Figure 4.1, between M33 and MW, there are five possibilities that may cause the absorption: A – a MW CGM cloud, B – the ionized

*Including the Magellanic Stream, the Magellanic Bridge, the Leading Arm, see F14.

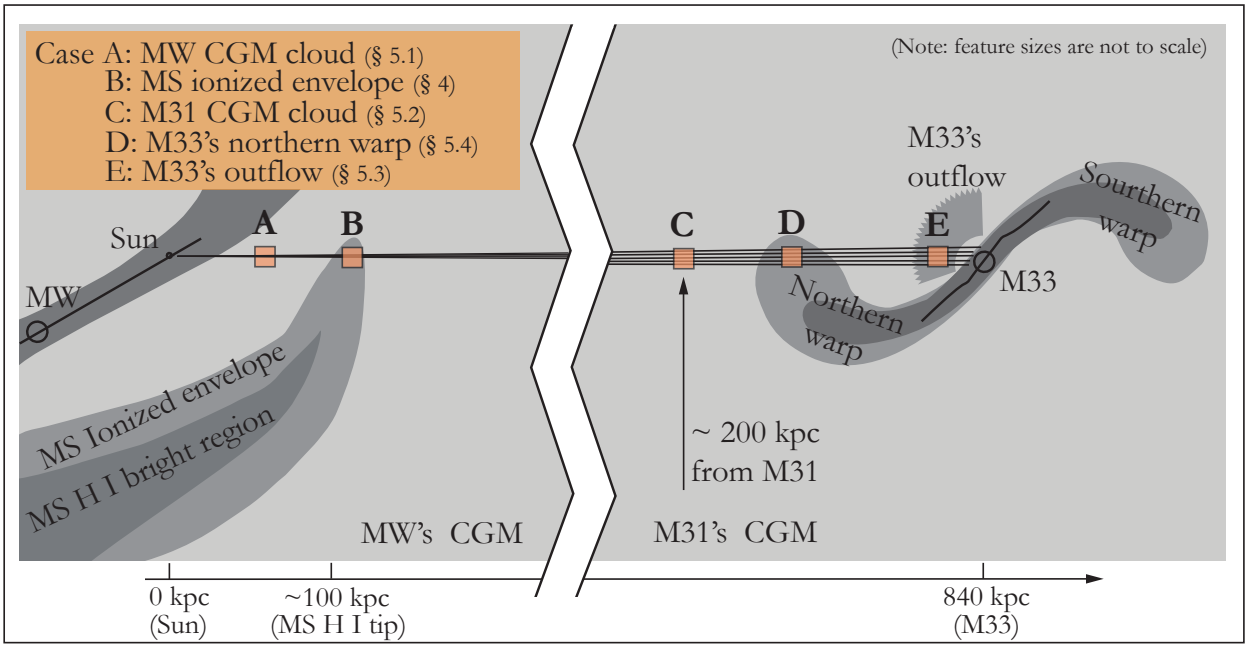

Figure 4.1: A cartoon showing the potential locations (A/B/C/D/E) of the VHVC along the *HST*/COS sightlines. Feature sizes are not to scale and the sizes of the orange squares at different locations are arbitrary. H I features are shown in dark gray while ionized features are indicated in light gray. We will discuss Case B – the ionized envelope of the Magellanic Stream in § 4.4, and the other cases in § 4.5.

envelope of the Magellanic Stream, C – an M31 CGM cloud, D – M33's northern warp, and E – M33's outflow. In addition, on the projected sky the VHVC is ~ 2° from an H I-VHVC – Wright's Cloud (Wright 1974; Wright 1979, hereafter, W79) and they are at similar velocities. The distance to Wright's Cloud is not clear yet; we discuss the relation of the VHVC and Wright's Cloud and the implication in § 4.5.5.

In the following, we present our data and discuss the origin possibilities of the VHVC and its possible connections with nearby H I structures. In § 4.2 we show absorption-line data obtained from *HST*/COS, and H I 21-cm data from the Arecibo Galaxy Environment Survey (AGES; Keenan et al. 2016) and the Galactic Arecibo L-Band Feed Array H I survey (GALFA-H I; Peek et al. 2011). In § 4.3, we calculate the O I abundance and show the gas

properties over sub-degree scale for the VHVC. In § 4.4, we discuss the inferences that can be drawn from the metallicity and the spatial patchiness of the VHVC in relation to the Magellanic Stream (Case B in Figure 4.1). We discuss the possible origins (Case A, C, D, and E in Figure 4.1) of the VHVC in § 4.5 and summarize our findings in § 4.6.

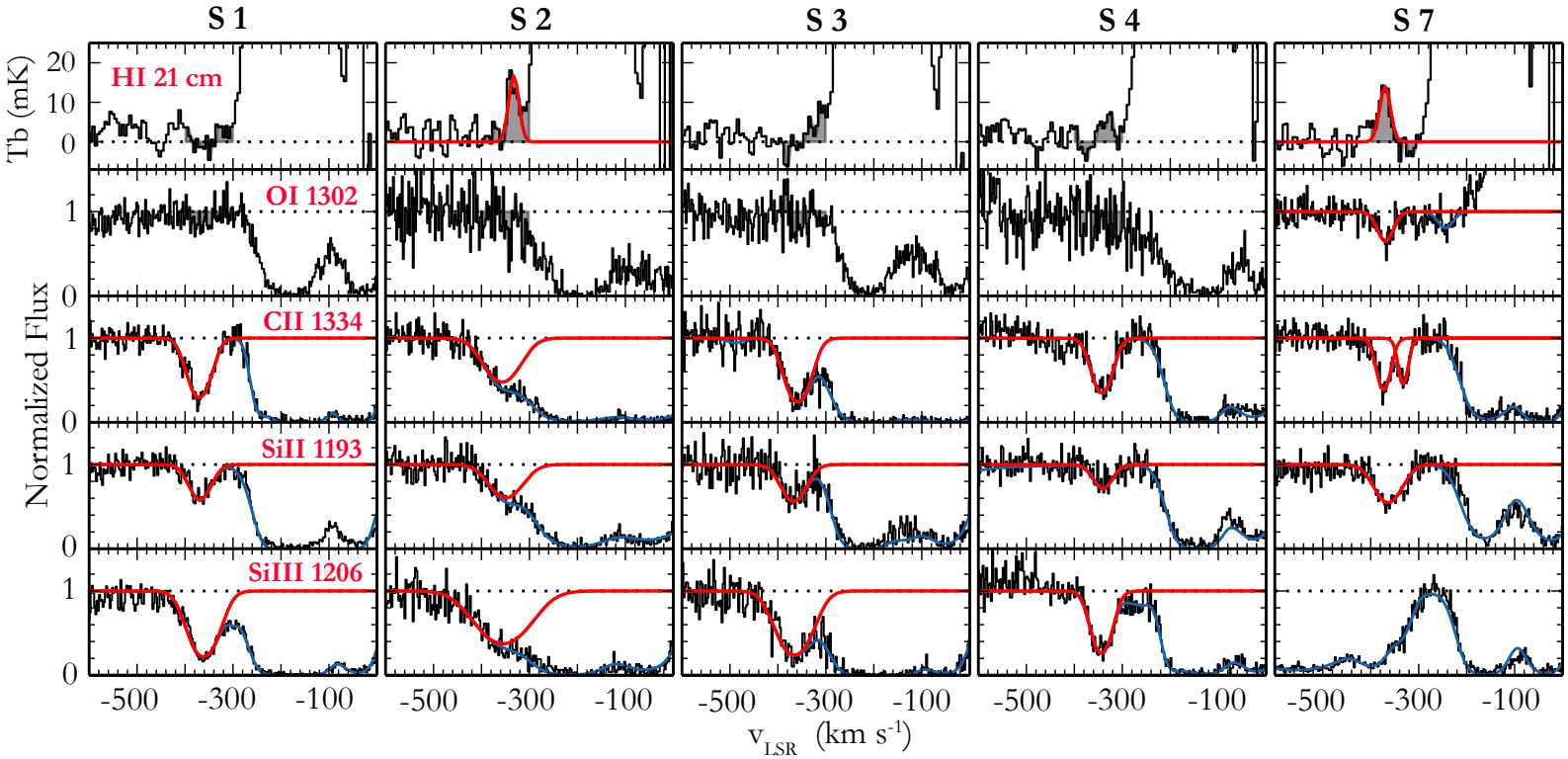

Figure 4.2: The top row shows the H I 21cm spectra from AGES; the red curves are Gaussian fits to the two possible H I detections with $> 2\sigma$ significance. The data have a brightness temperature sensitivity of 4-8 mK (Auld et al. 2006). The bottom four rows show the continuum-normalized O I, C II, Si II, and Si III absorption lines and their Voigt-profile fits (red); the underlying blue curves indicate the overall fits. The absorption components at $v_{\rm LSR} \sim -350$ km s^{-1} are associated with the VHVC, and those at $-300 < v_{\rm LSR} < -100$ km s^{-1} (~ 0 km s^{-1}) are from M33 (MW).

4.2 Data and Measurement

4.2.1 HST/COS Observations

The VHVC is a serendipitous detection in the observations described in Chapter 5. Among the seven sightlines (S1-S7) that were used in Chapter 5, five show significant ion absorption lines at $v_{\rm LSR} \sim -350$ km s^{-1}, while the other two are heavily contaminated by stellar lines and/or M33's interstellar absorption lines at the corresponding velocities. Therefore, in this work we only use the five sightlines, which are M33-UIT-236, M33-FUV-350, M33-FUV-444, NGC 592, and M33-FUV-016. Hereafter we use their sightline ID S1, S2, S3, S4, S7, same as those in Chapter 5 for consistency.

The VHVC is detected in absorption lines of O I λ1302, C II λ1334, Si II $\lambda\lambda$1190, 1193[†], and Si III λ1206. Hereafter we refer to these ions as "low ions" since they represent low ionization states that require < 20 eV to be produced[‡]. We do not detect Fe II, S II, P II, Si IV absorption lines at similar velocities even though our data cover these ionic species; the lack of these ions may reflect some limits on metallicity and ionization condition, which we decide not to explore further since it requires sophisticated ionization assumptions and modelings.

The *HST*/COS observations will be thoroughly described in Chapter 5, here we briefly summarize relevant details. The spectra were obtained using the G130M FUV grating with a central wavelength of 1291 Å and a wavelength coverage of 1134-1431 Å. The velocity resolution (FWHM) is 14 – 19 km s^{-1} per resolution element (COS data handbook; Fox

[†]We do not use Si II λ 1260 Å because it is blended with S II λ 1259 Å absorption from M33 (Chapter 5)
[‡]Si II/Si III/C II need 8.15/16.35/11.26 eV to be ionized from their previous states, respectively.

2015). The spectra were taken with the Primary Science Aperature which has an aperture size of 2.5″. We retrieved the calibrated and co-added data from the Mikulski Archive from Space Telescopes (MAST). The spectra have been processed by the standard CalCOS pipeline (version 3.0). In Chapter 5, we have justified the CalCOS products are reliable for our scientific analysis, mainly benefiting from the simple setup of our observations. The COS spectra used in this work can be found here: 10.17909/T9FG6R.

Among the detected ionic absorption lines, those of O I 1302 Å require special treatment. From the original CalCOS co-added spectra, we find a clear O I absorption line along S7. The other four spectra are dominated by strong air-glow emission at the expected velocities due to O I in the exosphere of the Earth. To confirm the S7 detection and to check if other sightlines also show similar O I signals, we conducted night-only data reduction following the night-only calibration tutorial[§] provided by Justin Ely. Briefly, we installed the CalCOS v3.0 pipeline locally and retrieved new calibration reference files using the *HST* Calibration Reference Data System (CRDS). We used the TimeFilter python module to select the night-only photons from the raw data, then constructed the O I night-only spectra for the five sightlines. From the night-only spectra, we find that S7 presents the same O I λ1302 absorption as seen in the original spectrum but with a noisier profile due to the reduced number of photons. However, S1-S4 still do not show O I absorption, which is most likely due to the low S/N ratio of the night-only spectra.

With the reduced spectra, we perform continuum and Voigt-profile fitting following the procedures outlined in Chapter 5. Briefly, for singular transition we normalize the absorption profile by fitting stellar continuum and stellar lines with Legendre polynomi-

[§]https://justincely.github.io/AAS224/timefilter_tutorial.html

nals within ±1000 km s^{-1} from the line center. The fitting is evaluated using the reduced χ^2 values. For the Voigt-profile fitting, we fit one component for each line unless obvious multiple components exist. The Voigt-profile fits give estimates for the centroid velocity v, Doppler width b, and column density log $N_{\rm ion}$, and the fitting is performed multiple times iteratively so that these parameters converge. In Figure 4.2, we show the O I, C II, Si II, and Si III absorption lines which have been continuum-normalized and Voigt-profile fitted, and in Table 4.1 we tabulate the best-fit v, log N, and FWHM($\equiv 1.667b$). Overall, all lines yield straightforward solutions except those detected along S2, which has considerable larger uncertainties due to the blending with M33's interstellar absorption at less negative velocities. In addition, for O I absorption lines in Figure 4.2, we use the night-only spectra for S1-S4 since their original spectra at $v_{\rm LSR} \sim -350$ km s^{-1} are dominated by geocoronal airglow emission. For S7, we use the original CalCOS co-added spectrum because the absorption is isolated from the airglow emission at $v_{\rm LSR} > -200$ km s^{-1} and this spectrum has a higher S/N than the night-only.

4.2.2 H I 21-cm data

The H I 21-cm spectra shown in the top row of Figure 4.2 are from the Arecibo Galaxy Environment Survey (AGES; Keenan et al. 2016). AGES data have an angular resolution of $\sim 4'$, spectral resolution of ~ 5.2 km s^{-1}, and a 1σ sensitivity of $\sim 1.5 \times 10^{17}$ cm^{-2} over 10 km s^{-1}. Only S2 and S7 indicate $> 2\sigma$ emission signals, which we fit with Gaussian components. S1, S3, and S4 do not show significant detection above the noise level, thus we integrate the spectra from -400 to -300 km s^{-1} to derive a 3σ upper limit. Note

Table 4.1: Ion Properties

Sightline[a]	v[b] km s^{-1}	log N[c] cm^{-2}	FWHM[d] km s^{-1}
	H I		
S1	[−400, −300]	<17.68	-
S2	−332.7	17.91±0.13	25.3
S3	[−400, −300]	<17.94	-
S4	[−400, −300]	<17.92	-
S7	−370.3	17.87±0.14	27.0
Mean[e]	−351.5±18.8	17.89±0.02	26.1±0.8
	O I		
S1	[−400, −300]	<14.29	-
S2	[−400, −300]	<14.43	-
S3	[−400, −300]	<14.18	-
S4	[−400, −300]	<14.38	-
S7	−354.1±2.7	14.00±0.07	33.5
Mean	−354.1	14.00	33.5
	Si II		
S1	−354.9±1.8	13.26±0.01	47.8
S2	−334.6±6.8	13.41±0.09	74.0
S3	−353.2±3.9	13.35±0.06	55.3
S4	−325.8±3.4	13.01±0.07	42.8
S7	−348.5±2.1	13.40±0.03	60.5
Mean	−343.4±11.3	13.29±0.15	56.1±10.8
	Si III		
S1	−347.5±1.2	13.29±0.02	62.5
S2	−340.8±6.4	13.37±0.04	116.7
S3	−351.8±5.5	13.33±0.06	73.2
S4	−328.6±1.9	13.09±0.04	42.5
S7	-[f]	-	-
Mean	−342.2±8.8	13.27±0.11	73.7±27.1
	C II		
S1	−356.6±1.2	14.17±0.02	48.7
S2	−342.5±6.5	14.14±0.10	78.0
S3	−345.1±2.3	14.26±0.04	52.8
S4	−327.4±1.5	14.05±0.03	43.3
S7	−357.7±1.5	13.85±0.04	29.0
	−316.8±1.5	13.63±0.06	19.8
Mean	−341.8±9.6	14.13±0.08	54.3±12.2

Note. — (*a*) S1: M33-UIT-236; S2: M33-FUV-350; S3: M33-FUV-444; S4: NGC 592; S7: M33-FUV-016. See Table 5.1 in Chapter 5 for more information. (*b*): the Gaussian (Voigt-profile) fitted centroid velocities for H I (O I, C II, Si II, and Si III). (*c*): Gaussian (Voigt-profile) fitted logarithm column densities; if there is no detection a 3σ upper limit is indicated. (*d*): For H I, FWHM≡ 2.355σ where σ is from Gaussian fits. For O I, C II, Si II, and Si III, FWHM≡ 1.667*b* where *b* is the Doppler width values from Voigt-profile fits. (*e*): the mean and the standard deviation of the measured values. For C II along S7, the two components are considered as one while calculating the overall mean and standard deviation. (*f*): Si III along S7 is contaminated by strong stellar lines, so we do not use it.

that this $[-400, -300]$ km s^{-1} integration range is relatively broad as compared to the narrow H I lines detected in S2 and S7; the derived 3σ upper limits should be conservative estimates for the H I along S1, S3, and S4. We tabulate the Gaussian-fitted H I velocities and column densities and the integrated upper limits in Table 4.1; the column density values are calculated using N(H I) = $1.823 \times 10^{18} \int_{-400}^{-300} T_{\rm B}\, dv$ cm^{-2} (Draine 2011). Note that H I-bearing gas may not be entirely co-spatial with the VHVC detected along *HST*/COS sightlines, since AGES beam size ($\sim 4'$) is ~ 100 times larger than the COS aperture size ($2.5''$). Still, the high-sensitivty AGES data provide the best available estimate of the H I for the VHVC.

In addition, we use H I 21-cm data from the Galactic Arecibo L-Band Feed Array H I survey (GALFA-H I; Peek et al. 2011). The GALFA-H I data is from its second data release (Peek et al. 2018), with an angular resolution of $\sim 4'$, a spectral resolution of ~ 0.18 km s^{-1}, and a 1σ noise level of 140 mK in an integrated 1 km s^{-1} velocity channel. We use the GALFA-H I data to create maps to study H I features near the VHVC in § 4.5.5.

4.3 Gas Properties of the VHVC

4.3.1 Metallicity

The O I detection along S7 provides us a direct metallicity measurement for the VHVC without assuming any ionization correction. This is because O I and H I have comparable ionization potentials from their ground states, and O I is not likely to be heavily depleted onto dust (Jenkins 2009). As shown in Table 4.1, we find log N(O I) = 14.00 ± 0.07 cm^{-2}

and log N(H I) = 17.87 ± 0.14 cm^{-2} for S7. Thus the gas-phase abundance is 12+log(O/H) = 8.13±0.16. Using the oxygen solar abundance (12+log(O/H)$_\odot$ = 8.69±0.05; Asplund et al. 2009), we measure [O I/H I] ≡ log(O/H) − log(O/H)$_\odot$ = −0.56 ± 0.17 dex, corresponding to a metallicity of Z≡ $10^{[OI/HI]}$ = 0.28 ± 0.11 Z$_\odot$ for the VHVC. In addition, sightline S2 shows similar H I emission although O I only has a 3σ upper limit. For S2, we found a 3σ upper limit of [O I/H I] ≤ −0.17 dex and Z ≤ 0.68 Z$_\odot$, consistent with the value estimated from S7.

4.3.2 Sub-Degree Scale Variation

For each ion, we calculate the mean and standard deviation values of v, log$N$, and FWHM among the five sightlines, which are tabulated in Table 4.1. Both H I and the four ions show similar mean centroid velocities at $v_{\rm LSR} \sim -350$ km s^{-1} with a standard deviation of $\sim$ 15 km s^{-1}. Column densities vary up to 0.15 dex as measured from Si II; in most cases the differences among the sightlines remain $\lesssim$ 0.1 dex. As for the FWHM, a relatively large standard deviation of 27 km s^{-1} is seen in Si III, contributed by the blended Si III absorption line along S2. Otherwise the FWHM values of all the transition lines remain $\lesssim$ 70 km s^{-1}.

The above standard deviations are measured among five sightlines with projected angular separations of $\sim 0.06 - 0.4^\circ$. To determine how the absorption properties fluctuate over this sub-degree scale, we group the five sightlines into pairs and calculate the absolute values of the differences: |log N$_i$−log N$_j$|, and $|v_i - v_j|$. From the top panel of Figure 4.3, we find that the maximum log N difference is $\sim$ 0.4 dex with an average of $\sim$ 0.15 dex. The

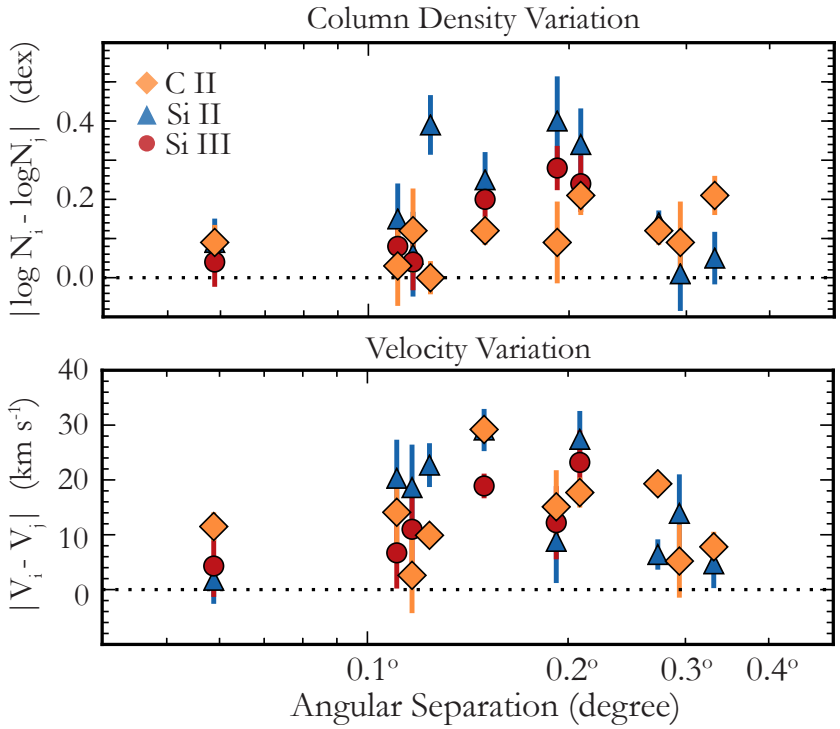

Figure 4.3: The absolute values of ion column density differences (top) and centroid velocity differences (bottom) of paired sightlines over sub-degree scales. C II/Si II/Si III are shown as orange diamonds/blue triangles/red circles, respectively. Data points without error bars mean the errors are smaller than the sizes of the symbols.

bottom panel shows that the centroid velocity differences between sightlines vary up to 30 km s^{-1} with an average of $\sim$ 14 km s^{-1}, which is well within COS velocity resolution. The small sightline-to-sightline variations suggest that the VHVC is relatively smooth on sub-degree scales. To better interpret the smooth distribution, it is necessary to know the physical separations between the five sightlines. We will investigate this in § 4.5 where the potential origins of the VHVC are discussed.

4.4 Is the VHVC Related to the Magellanic Stream?

In the vicinity of the Magellanic System, large amounts of ionized gas have been found to move at expected Magellanic velocities (F14; Nidever et al. 2008). The expected velocities are defined by extrapolating from the H I velocity fields at certain longitudes in the Magellanic coordinate system. Based on this position-velocity proximity, F14 suggested the nearby ionized gas is physically associated with the Magellanic System[¶], forming an ionized envelope surrounding the System. The ionized envelope has a total mass of M(H II) $\sim 5.5\times10^8$(d/55kpc)^2 $M_\odot$, contributing $\sim$ 20% of the total mass to the System (excluding the MCs themselves). It extends $\approx 11,000$ deg^2 on the sky, including the region where we find the VHVC, which is $\sim 40^\circ$ from the tip of the Magellanic Stream, as is shown in Figure 4.4 and Case B in Figure 4.1 (see also Richter et al. 2016 for a even larger estimate on the cross-section for the Magellanic System). Thus, this close projected distance naturally leads us to examine whether the VHVC originates from the Magellanic Stream.

Our main argument against a Magellanic origin is based on the single metallicity we measured from the COS spectrum of S7. The VHVC has a metallicity of [O I/H I] = -0.56 ± 0.17 dex ($Z = 0.28 \pm 0.11$ $Z_\odot$; see § 4.3.1). As for the Magellanic Stream, its metallicity has been measured at four locations (see Figure 4.4). Richter et al. (2013) found that the Stream close to the MCs has [S/H] = -0.30 ± 0.04 (0.50 $Z_\odot$; see also Gibson et al. 2000) toward Fairall 9. This material is likely to be recently stripped metal-rich gas that originated from the LMC. Except at the Fairall 9 position, the main body of the Stream has a mean metallicity of [X/H] = -1.12 dex, as calculated at three other positions:

[¶]Including the Magellanic Stream, the Magellanic Bridge, and the Leading Arm; see F14.

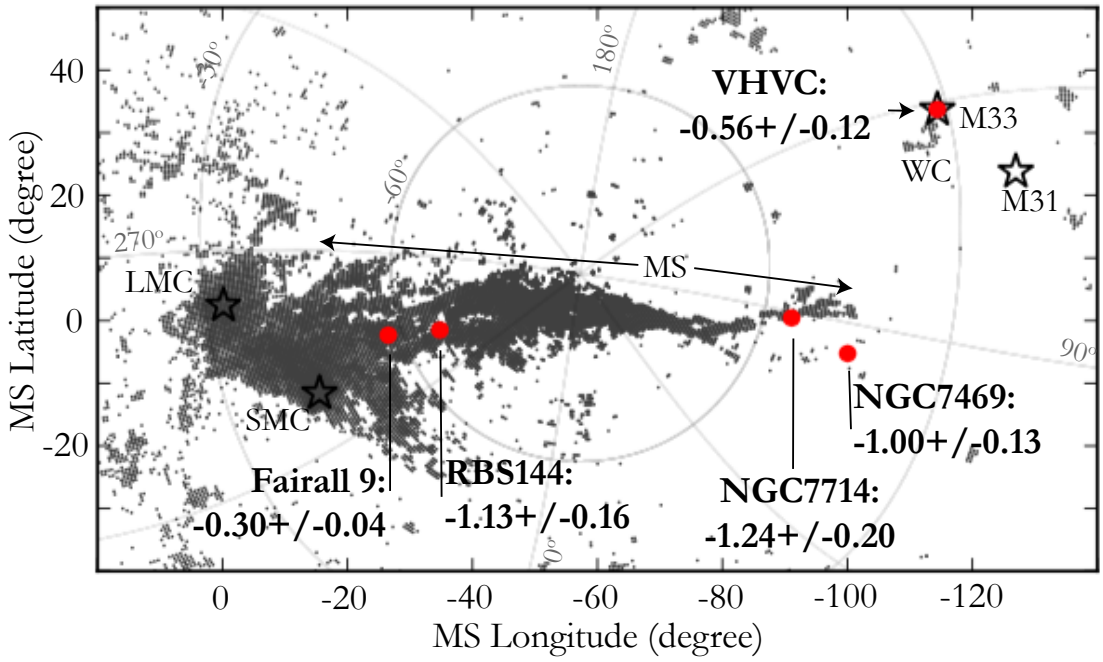

Figure 4.4: The positions of the VHVC, M33, M31, Wright's Cloud (WC), the MCs (LMC, SMC), the Magellanic Stream (MS) trailing the MCs, and four QSO sightlines (Fairall 9, RBS 144, NGC 7714, NGC 7469) with metallicity estimates for the Magellanic Stream. Note that the VHVC is at the same position as M33 and in front of the galaxy. The gray patches are H I data from Nidever et al. (2008), which include more structures besides the Magellanic Stream. The map is in the Magellanic coordinate system (Nidever et al. 2008).

[S II/H I] = -1.13 ± 0.16 (~ 0.07 $Z_\odot$) toward RBS 144 (Fox et al. 2013), [O I/H I] = -1.24 ± 0.20 (~ 0.064 $Z_\odot$) toward NGC7714 (Fox et al. 2013), and [O I/H I] = -1.00 ± 0.13 (~ 0.10 $Z_\odot$) toward NGC7469 (Fox et al. 2010). Therefore, the metallicity of the VHVC is at least 0.56 dex (3.3σ) higher than the mean metallicity of the Magellanic Stream. In particular, it is 0.68 dex (4σ) higher than the metallicity measured at the tip of the Magellanic Stream toward NGC 7714, which is the closest point to the VHVC in projection (see Figure 4.4).

We also compare the ionic column densities of the VHVC with those of the nearby ionized gas that is presumably associated with the Magellanic Stream. The top panel of Figure 4.5 shows the $v_{\rm LSR}$ velocities of Magellanic-related ionized absorbers found in F14.

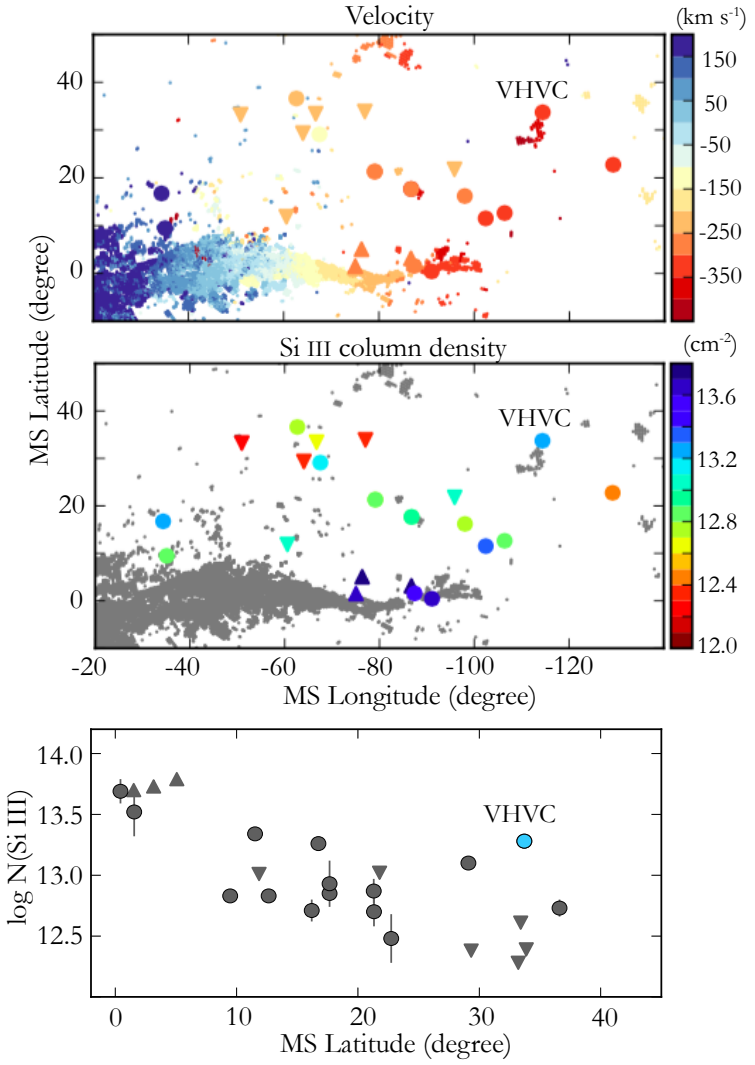

Figure 4.5: Gas velocities (top) and column densities (middle; bottom) near the tip of the Magellanic Stream. The ionized gas absorbers, for which we use Si III as a representative transition, are detected through background QSOs and indicated by circles (good measurements), upward (lower limits) and downward (upper limits) triangles. All the spectra were taken with COS/G130M, so there is no systematic difference due to instrumental difference in comparing the ion column densities. The Magellanic-associated gas absorber measurements are from F14 and the VHVC measurement is from this work. We show the H I tip of the Magellanic Stream; the H I velocities and column densities are from Nidever et al. (2008). In the bottom panel, data points without error bars mean the errors are smaller than the sizes of the symbols.

This velocity map shows that the ionized gas, regardless of their origins, move at similar velocities in this region. The potential diversity of gas origins can be seen in the middle and bottom panels. In the middle panel, we show the log N(Si III) values for the ionized

gas; the majority of the Magellanic ionized stream near the tip has log $N_{SiIII} \lesssim 13.0$ dex, which is ~ 0.3 dex lower than that of the VHVC (log $N_{SiIII} \sim 13.3$ dex). This difference is shown more obviously when we plot the log N(Si III) values against Magellanic latitude. The VHVC's column density is $\gtrsim 0.5$ dex higher than those of the Magellanic Stream at similar latitude. Similar trends can also be found in Si II and C II. The ionized envelope of the Magellanic Stream tends to become more and more diffuse at further distances from its H I-bright main body. The VHVC, with higher ionic column densities, is unlikely to be associated with the Stream.

We conclude that *the VHVC is unlikely to originate from the Magellanic Stream*. Nearby our VHVC, there is an H I-VHVC – Wright's Cloud – moving at a similar Magellanic velocity. Some authors have suggested Wright's Cloud may be related to the Magellanic Stream due to their proximity in position-velocity space (W79; Braun & Thilker 2004; Putman et al. 2009; Nidever et al. 2010). Indeed, F14 included Wright's Cloud as one of the H I-bright regions of the Magellanic System, thus extended the Magellanic ionized envelope 30° beyond Wright's Cloud (see Figure 1 in F14). However, as we discuss in § 4.5.5, Wright's Cloud's origin is unclear due to its unknown distance. Therefore, we cast doubt on the existence of the Magellanic ionized envelope within 30° of Wright's Cloud where there is no other Magellanic-associated H I emission or QSO absorbers. The highly uncertain origin of Wrights Cloud and the evidence that the VHVC is not part of the Stream together suggest that the ionized envelope of the Magellanic Stream may not extend to cover the region of the sky in the direction of M33.

4.5 The Origin of the VHVC

In this section we discuss the multiple possibilities for the origin of the VHVC given the complex velocity field on this projected sky. Apart from the Magellanic scenario (Case B) that we argue against in the previous section, there are four other plausible scenarios that could cause the absorption, which we illustrate in Figure 4.1 as: A – a MW CGM cloud, C – an M31 CGM cloud, D – M33's northern warp, and E – M33's outflow. Here we evaluate each of these possibilities separately.

4.5.1 A MW CGM Cloud?

As we annotate as Case A in Figure 4.1, the VHVC could be a cloud at an unknown distance in MW's CGM. Though we have shown in § 4.4 that the VHVC is unlikely to be part of the Stream, it could be closer in the MW's inner halo similar to other MW HVCs. The $\sim$ 0.3 $Z_{\odot}$ metallicity of the VHVC makes it similar to some H I complexes, such as Complex C ($Z = 0.1 - 0.3\ Z_{\odot}$; Tripp et al. 2003; Shull et al. 2011). In Figure 4.6, we compare the column density (log$N$) variations of the VHVC with those MW HVCs detected in Si III between 58 QSO sightlines with angular separation of $\leq 30^{\circ}$ (Collins et al. 2009). In the top panel, we find that the VHVC's log N values vary up to $\sim$ 0.4 dex over 0.4°, while those of the MW HVCs are $\sim$ 3 times larger. The larger variations of the MW HVCs still hold when we separate Collins et al.'s sample by positive/negative HVC velocities and by northern/southern QSO sightlines.

We note that the direct comparison in angular seperation between our VHVC and the MW HVCs may not be informative since it does not reflect the actual physical separations

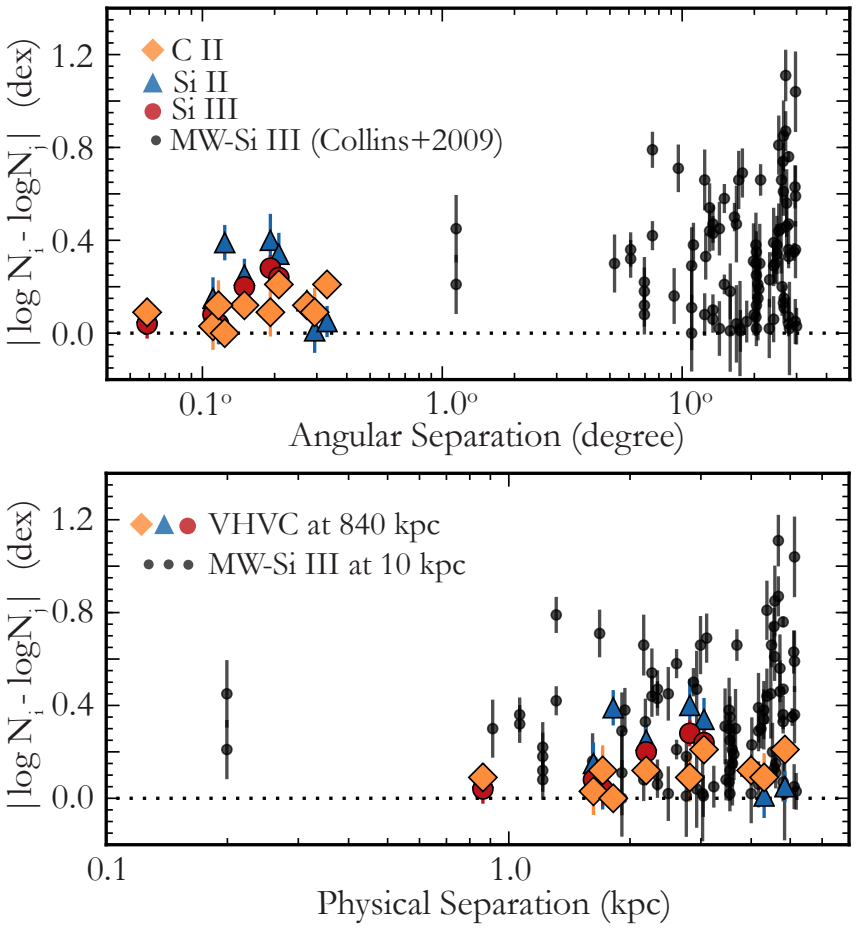

Figure 4.6: The log-log angular variation of the ion column densities. The orange diamonds, blue triangles, and red circles are respectively the C II, Si II, and Si III logarithmic column density differences of the VHVC along our sightline pairs; same as those in Figure 4.3. The black dots are the Si III logarithmic column density differences of MW HVCs measured toward sightline pairs with angular separations less than 30° (Collins et al. 2009). Data points without error bars mean the errors are smaller than the sizes of the symbols.

of the paired sightlines on the sky. The MW HVCs are generally at distance of 5-15 kpc from the Sun (Wakker 2001; Wakker et al. 2008; Lehner et al. 2012); we assume them at d = 10 kpc and find physical separations of $\lesssim$ 5 kpc for these MW paired sightlines as shown in the bottom panel of Figure 4.6. In order to make our VHVC's physical scale comparable to those of the MW HVCs, we find its distance would have to be ~ 840 kpc, which is beyond the virial radius of the Galaxy and is as far as M33. Therefore, our

sightlines toward the VHVC should probe a smoother medium on sub-degree scales than those in Collins et al. (2009) if it belongs to the MW's CGM. However, if the VHVC is instead associated with M33 as we discuss in § 4.5.3 and § 4.5.4, the smoother column density variation in the bottom panel suggests that the VHVC is unlikely to represent HVC-like features in M33's CGM, assuming that M33 has similar HVC population as MW.

4.5.2 An M31 CGM Cloud?

The VHVC moves at $v_{\rm LSR} \sim -350$ km s^{-1} while M31's systemic velocity is $v_{\rm LSR} = -301$ km s^{-1} (Courteau & van den Bergh 1999). If put at M31's distance, the VHVC would be $\sim$ 200 kpc from the galaxy in projection. We show this possibility as Case C in Figure 4.1. By comparing the ion column densities of the VHVC with those detected in M31's CGM by Lehner et al. (2015), we find that the VHVC generally has higher C II, Si II, and Si III column densities. Beyond 50 kpc of M31's CGM, Lehner et al. (2015) reported no significant detection of Si II with an upper limits of log N(Si II) $\lesssim$ 13.19. In addition, Si III absorption lines were detected along four sightlines with <log N(Si III)>= 12.53, while C II column densities are mostly upper limits (log N(C II) < 13.70) with only one detection at log N(C II)=13.16. These measurements indicate that the ionized gas in the outskirt of M31's CGM is most likely to be diffuse, with column densities lower than those we measured for the VHVC: <log N(Si II)>= 13.29, <log N(Si III)>= 13.27, and <log N(C II)>= 14.13. Given the column density mismatch, we disfavor an origin of the VHVC being part of M31's CGM. Note that M31's CGM may be patchy, similar to the cool CGM of L^* galaxies in the

COS-Halos survey (Werk et al. 2013); however, the chance of our sightlines intercepting a very-high density clump at large distance from the host galaxy is rare. Future work on the patchiness of M31's CGM and those of L^* galaxies may help to confirm or dispute our argument for no association between the VHVC and M31.

4.5.3 An M33 CGM Cloud or an M33 Outflow?

M33 has a systemic velocity of $v_{LSR} \sim -180$ km s^{-1} (Corbelli & Schneider 1997), therefore the VHVC would be moving at $\delta v \sim -170$ km s^{-1} in the galaxy's rest frame. If we simplify M33's gravitational potential as a point mass $\sim 5.5\times10^{10}$ M$_\odot$ (dark matter+baryon; Corbelli 2003), the VHVC should be within $\sim$ 16 kpc of the galaxy to remain gravitationally bound. This calculation certainly omits the complex mechanisms (ionization, cooling, equilibrium, etc.) that regulate clouds' survivability in a galaxy's CGM, however, it hints that the VHVC is most likely to be near M33's disk if it has some M33 origins. Observationally, the COS-Halos survey (Werk et al. 2013) found that most of the CGM clouds of $L \sim L^*$ galaxies at $z \sim 0.2$ were within $\sim$ 100 km s^{-1} of their host galaxies' systemic velocities and only a few exceed 200 km s^{-1}. Therefore, it is unlikely that our VHVC is a CGM cloud of M33 at large radius given its high velocity. As for the possibility that the VHVC exists in the vicinity of M33's disk, we have shown in § 4.5.1 that the VHVC is unlikely to be HVC-like features due to its smooth column density distribution. In the following, we consider two other near-the-disk scenarios: (1) the VHVC represents an outflow from M33 (Case E in Figure 4.1), which we discuss in the rest of this section; (2) the VHVC could be an ionized extension of M33's northern warp (Case D in Figure 4.1; see § 4.5.4).

The VHVC should lie in front of M33's disk since our background targets are UV-bright stars in M33. If we use these M33 stars as the reference points, the VHVC is moving at $\sim [-180, -100]$ km s^{-1}. These negative velocities with respect to M33 indicate that the VHVC could be regional outflows from the disk but remain in the vicinity of the disk; the outflows could be driven by stellar winds or supernova feedback (Case E in Figure 4.1) – Outflows powered by an active galactic nuclei are not considered since M33 does not host a massive central black hole (Merritt et al. 2001). In the following, we evaluate the possibility of outflow by comparing the ion properties of the VHVC with those of galactic outflows seen in absorption in other galaxies.

First, we find that our COS spectra do not show a detection of Fe II – an ion that is commonly reported in galactic outflow observations of both nearby (e.g., LMC; Lehner et al. 2009) and $z \sim 1$ star-forming galaxies (Martin et al. 2012; Rubin et al. 2010, 2014). The non-detection is unlikely to be due to the sensitivity limit of our COS spectra, which is sensitive to Fe II absorption lines with log N(Fe II)$\gtrsim$13.5. If M33 indeed has an outflow similar to those in nearby and z~1 galaxies (e.g., Martin et al. 2012; Rubin et al. 2014), the Fe II column densities should be log N(Fe II)$\gtrsim$ 14.0, well above our sensitivity limit.

Secondly, we investigate the possibility based on ion absorption line widths and profile shapes. Galactic outflows have been detected in several different ions, such as Na I, Mg II, and Fe II with broad absorption lines (FWHM$\gtrsim$ 100 km s^{-1}; Heckman et al. 2000; Martin 2005; Martin et al. 2012; Weiner et al. 2009; Chen et al. 2010c; Rubin et al. 2010, 2014). Recently, Chisholm et al. (2016, hereafter C16) studied Si II/Si III-tracing outflows in 37 nearby star-forming galaxies observed with *HST*/COS G130M.

They generalized that galactic outflows detected in Si II and Si III commonly have FWHM values of $\sim 230-500$ km s^{-1} and the outflows' line profiles tend to exhibit more extended, gradually shallowing blue absorption edges compared to the red edges. This profile asymmetry may be explained by outflows being continuously accelerated with more diffuse gas columns at larger distances. Since our spectra were observed with the same instrument, we can directly compare our Si II/Si III measurements with C16's. As we show in § 4.3.2, except S2 that is blended with absorption from M33, the absorption lines of the VHVC have a mean FWHM $\lesssim 70$ km s^{-1}, which is at least a factor of 3 narrower than those of galactic outflows reported by C16. In addition, our absorption line profiles are mostly symmetric relative to the line centroids as are shown in Figure 4.2. We note that the 37 galaxies in C16 span distances of 3 – 880 Mpc, corresponding to COS aperture physical sizes of 0.04 – 11 kpc. Within this dynamical range C16 found no correlation between the COS aperture physical sizes and galactic wind line widths. Therefore, although the physical COS aperture size in our observation (~ 0.01 kpc) is smaller, this difference is not likely to cause the distinct line widths and line profile shapes. We conclude that the VHVC is unlikely to represent an outflow from M33's disk.

4.5.4 M33's Extended Warp Material?

The northern warp of M33 moves at negative velocities of $v_{\rm LSR} \sim [-300, -200]$ km s^{-1} (Putman et al. 2009; Corbelli & Schneider 1997), which is close to the velocity of the VHVC. Although the northern warp's orientation is unclear, it is possible that the warp folds toward the MW and cause the ionized gas absorption along our line of sight (see Case

D in Figure 4.1). That M33's northern warp may have a diffuse extension is hinted by the deeper H I maps shown in Putman et al. (2009; Figures 3 & 7) and in Keenan et al. (2016; Figure 1), which both detected some diffuse H I emission at $v_{\rm LSR} \lesssim -250$ km s^{-1} km near the warp. In particular, Putman et al. (2009) suggested the diffuse H I structures cannot be reproduced in M33's tilted-ring model (Corbelli & Schneider 1997) and an additional component is in need to explain these features.

To examine the possible connection between the VHVC and the northern warp, in Figure 4.7 we show the position-velocity map of M33's H I disk and warp projected along its major axis. The major axis is defined based on M33's central optical disk with a position angle (PA) $\sim 21^\circ$ as adopted in Corbelli & Schneider (1997). We show the relative positions of M33's warp and central disk in contours in Figure 4.8, along with a straight line indicating its major axis. To generate the position-velocity map in Figure 4.7, we project all the H I signals within $26^\circ >$ RA $> 21^\circ$ and $28.6^\circ <$ Dec $< 32^\circ$ along M33's major axis and compute the mean T_b. From Figure 4.7, we find that the VHVC could be potentially associated with M33's northern warp as revealed by their proximity in the position-velocity space.

If the VHVC is part of M33's northern warp, then the warp folds toward the MW and is stable as inferred from the smooth column density and velocity distributions of the VHVC (Figure 4.6). In addition, the VHVC's metallicity of [O I/H I] $= -0.56 \pm 0.17$ dex implies that the warp has a similar oxygen abundance to M33's ISM ([O I/H I] $= -0.42 \pm 0.06$ dex; Crockett et al. 2006). This similarity rules out the possibility that M33's warp represents the accretion of primordial H I from outside of the disk. Instead, it favors the scenario that

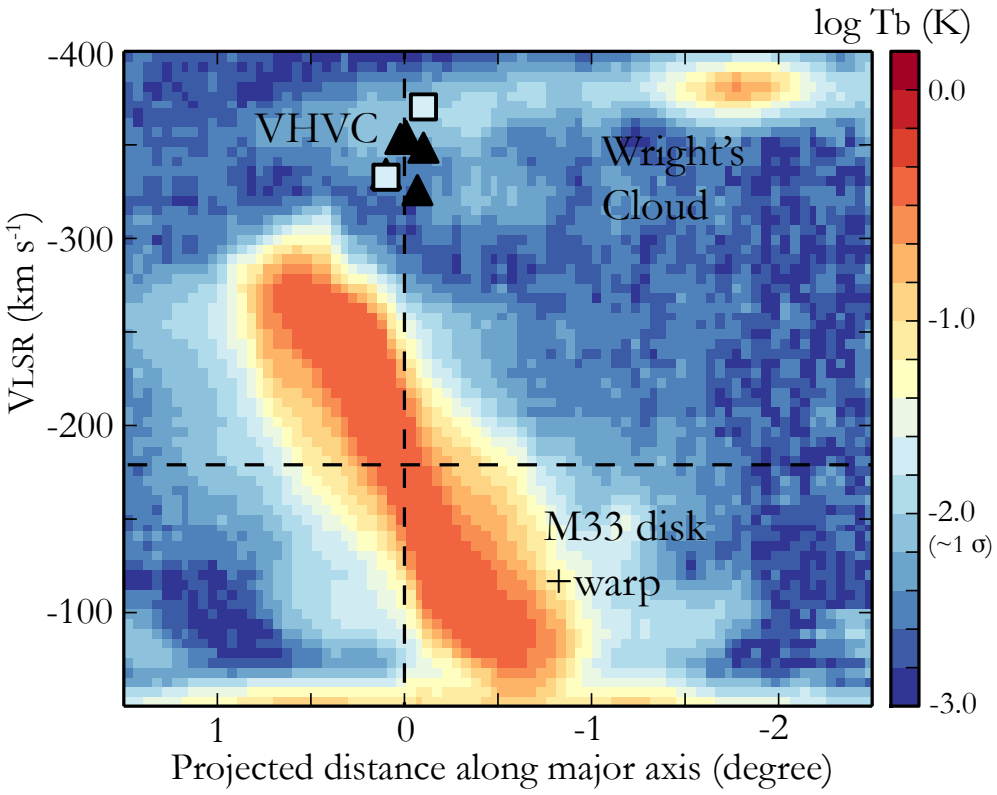

Figure 4.7: Position-velocity map projected along the major axis of M33. The color represents the mean H I brightness temperature on a logarithmic scale (log T_b); the 1σ value of T_b is ~0.008 K (Auld et al. 2006). The major axis is defined based on M33's central optical disk (PA~ 21°; Corbelli & Schneider 1997); we show the relative positions of M33's disk, warp and its major axis in Figure 4.8. X axis shows the angular distance along the major axis, with positive values to the north-east. The bottom emission is the H I from the MW's ISM. The elongated orange-red feature dominating the center of the figure is M33's disk, and the diffuse, light-blue emission in its surroundings shows the extended warp of M33 (Wright 1974; W79). The VHVC is indicated by light-blue squares (H I emission) and black triangles (Si II absorption) with other ions at a similar position-velocity. The colors of the blue squares indicate the peak brightness temperature (≈ 0.015 K) of the VHVC detected along S2 and S7 (see Table 4.1). Note that this figure makes it appear as if there is an H I bridge-like feature between the VHVC and Wright's Cloud. This is a diffuse H I cloud identified by Keenan et al. (2016, numbered as AGESM33-31; see also Grossi et al. 2008), which we annotate as"K16 cloud" in Figure 4.8. The K16 Cloud is on the opposite side of M33 (see Figure 4.8) and therefore does not have a physical spatial connection to Wright's Cloud.

M33 closely interacted with M31 in the past which resulted in a distorted gaseous warp (Putman et al. 2009) and stellar disk (McConnachie et al. 2009). This contradicts a recent dynamical study of M33's orbit history (Patel et al. 2016) that suggests a rare chance (< 1% at 4σ) of an M33-M31 close encounter in the past.

4.5.5 Wright's Cloud Association?

Wright's Cloud is composed of north-south and east-west arms as shown in Figure 4.8. It is $\sim 2^\circ$ from our VHVC and moves at $v_{\rm LSR} \sim [-450, -330]$ km s^{-1}, similar to our VHVC. These two clouds' similar velocities and close angular distance suggest a potential connection. In the bottom position-velocity panel, Wright's Cloud can be found with several noticeable H I concentrations at RA $\sim 17 - 22^\circ$. The VHVC is represented by its H I emission and Si II absorption at RA $\sim 23.5^\circ$, generally following the velocity gradient of Wright's Cloud.

The distance to Wright's Cloud is unknown. Some authors have indicated that Wright's Cloud could be part of the Magellanic Stream based on position-velocity proximity (e.g., W79; Braun & Thilker 2004; Putman et al. 2009; Nidever et al. 2010). However, if the VHVC is related to Wright's Cloud, its metallicity of Z = 0.28 $Z_\odot$ (§ 4.3.1) implies that Wright's Cloud, together with the VHVC, is unlikely to be related to the Magellanic Stream.

If the VHVC is part of Wright's Cloud, then Wright's Cloud could be a nearby H I feature in the MW's inner halo (see § 4.5.1). On the other hand, if we combine Figures 4.7 and 4.8, there is a possibility that our VHVC is forming an ionized bridge that connects Wright's Cloud and M33's northern warp. If Wright's Cloud is in M33's CGM, it would contain a total mass of M(H I)$\approx 4.8 \times 10^8$ $M_\odot$(d/840kpc)^2 as calculated using GALFA-H I data (see also W79, ;Braun & Thilker 2004). Wright's Cloud would be $\sim$ 70 kpc wide in size and $\sim$ 10 kpc at its nearest point to M33 if put at the galaxy's distance, as have been pointed out in W79. In such case, Wright's Cloud would be a Magellanic-like H I complex in M33's CGM.

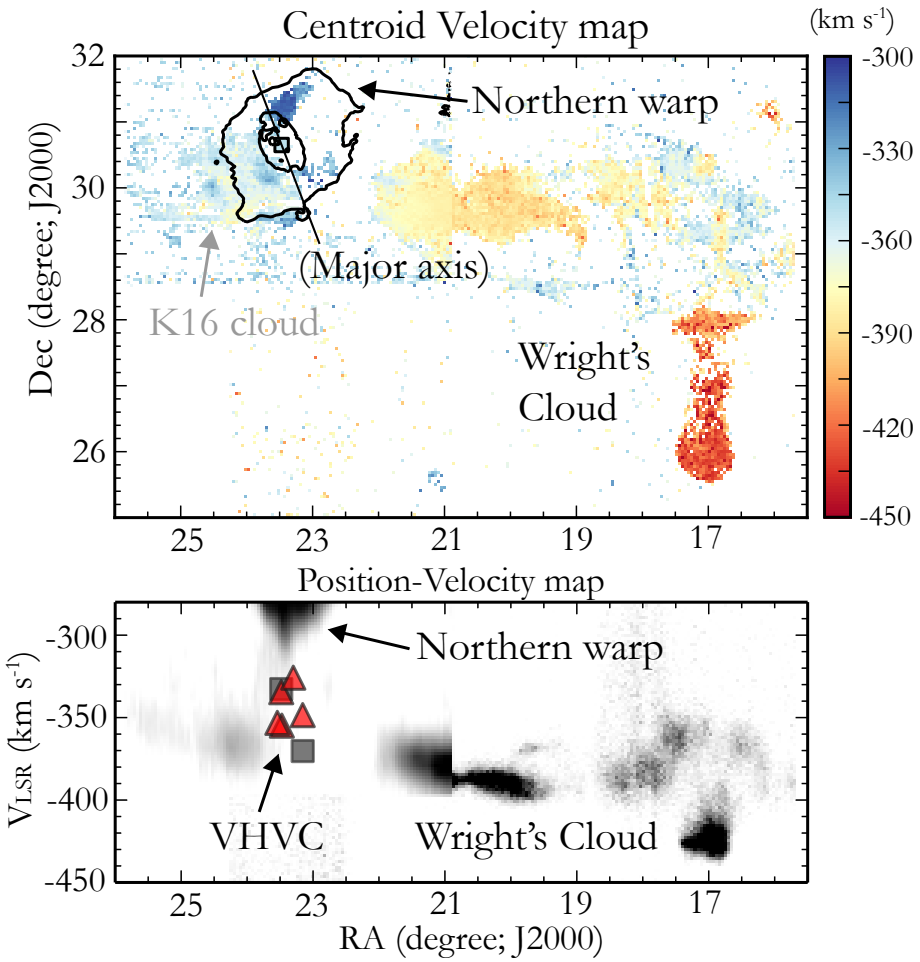

Figure 4.8: Top: the velocity distribution of the VHVC, Wright's Cloud, and M33's northern warp. The map includes AGES H I data (DEC > 28.5°, RA > 21°) and GALFA-HI DR2 data (the rest). The AGES (GALFA-HI DR2) map is shown with log N(H I) ≥ 18.0 (log N(H I) ≥ 19.0) for better illustration. The maps are integrated from $v_{\rm LSR}$ = −450 to −300 km s^{-1}, therefore M33's velocity field (−300 $\lesssim v_{\rm LSR} \lesssim$ −50 km s^{-1}; see Figure 4.7) is not shown here. Instead, we overlay two H I column-density contours to show the positions of M33's warp (outer contour; log$N$ = 19.3) and central disk (inner counter; log$N$ = 21.0). In addition, we show M33's major axis, which is used in producing the position-velocity map in Figure 4.7. The VHVC is noted as a small square near M33's disk center. Bottom: position-velocity map. The VHVC is indicated by its H I emission (grey squares) and Si II absorption (red triangles). There exists a discontinuity at RA~ 21° which is artificial due to the different column density levels we adopted for AGES and GALFA-HI data.

With an estimated H I mass of ~ 10^8 M$_\odot$ at the distance of M33, Wright's Cloud may then have an optical counterpart. However, there is no obvious optical counterpart in Wright's Cloud in the Pan-STARRS1 database (Bernard et al. 2016; Chambers et al.

2016). In addition, we briefly search the GALEX map and Planck dust map (Planck Collaboration et al. 2016) on the MAST archive but do not find any UV or dust emission excess. If Wright's Cloud does not have an optical counterpart, it is an outlier from those H I sources ($M_{HI} \gtrsim 10^7\ M_\odot$) found in Pisano et al. (2007, 2012) which have stellar components. It is more likely to be similar to the Magellanic Stream or other H I features surrounding galaxies as noted by Sancisi et al. (2008; and references therein).

4.6 Conclusion

We report the detection of a VHVC in direction of M33. The detection was made along five *HST*/COS sightlines targeted at UV-bright stars in M33's disk. The VHVC was found in O I, C II, Si II, and Si III absorption lines at $v_{LSR} \sim -350 \pm 154$ km s^{-1}. We do not find Fe II, P II, S II, or Si IV absorption at similar velocities even though our COS spectra cover these ionic species. The mean ion column densities of the VHVC are log N(O I)= 14.00 ± 0.07, <log N(C II)>= 14.13 ± 0.08, <log N(Si II)>= 13.29 ± 0.15, and <log N(Si III)>= 13.27 ± 0.11.

We measure a metallicity [O I/H I]= −0.56 ± 0.17 (Z = 0.28 ± 0.11 $Z_\odot$) for the VHVC, which is 0.68 dex (4σ) higher than the metallicity found for the tip of the Magellanic Stream. The higher metallicity and stronger C II, Si II, and Si III absorption suggest that the VHVC is most likely not associated with the Magellanic Stream. Furthermore, this lack of association may signify that the ionized envelope of the Magellanic Stream is less extended than previously reported in the direction toward M33.

We find that the VHVC is unlikely to be related to M31's CGM since it would be ∼ 200 kpc from M31's disk in projection but its ionic lines are much stronger than those

detected beyond 50 kpc of M31's disk. We also rule out the possibility that the VHVC resides in M33's CGM at large radius given its high velocity ($\delta v \sim -170$ km s^{-1}) with respect to M33's systemic velocity. If the VHVC has some M33 origins, it has to be within $\sim$ 16 kpc from the galaxy to remain gravitationally bound. In the vicinity of M33's disk, we find that the VHVC is unlikely to represent an outflow from M33. This is because the ionic lines of the VHVC are narrower and more symmetric than those detected in galactic outflows seen down the barrel of nearby galaxies.

There remain three intriguing possibilities highlighted by our analysis. First, the VHVC could be a normal ionized absorber sitting in MW's CGM. Second, it could be associated with the nearby Wright's Cloud, which would indiate that Wright's Cloud does not belong to the Magellanic Stream. Third, it could be part of M33's northern warp given the similar metallicity and proximity in position-velocity space. If true, the data indicate that M33's northern warp is folding toward the MW. The VHVC's metallicity would imply an ISM origin for the warp, favoring the scenario that M33's warp was formed during a past interaction between M33 and M31. Furthermore, the proximity of the VHVC with Wright's Cloud and M33's northern warp may hint that these three objects are physically connected. In this case, Wright's Cloud would be a Magellanic-like structure in M33's CGM, which would have important implications on the dynamical history of M33. To break the degeneracy of all these scenarios, further deep H I observations to map diffuse H I gas in this Magellanic-M33-M31 overlapping area would be highly valuable. Absorption-line experiments using MW halo stars toward this direction would also help to bracket (or yield lower/upper limits on) the distance.

Acknowledgement. We thank the referee for the useful comments in improving our manuscript. We thank R. F. Minchin and the AGES team for their generosity in providing us the high-sensitivity H I data of M33. We thank A. J. Fox and the COS team for their help in providing information about the night-only data reduction. We appreciate A. J. Fox's great feedback on § 4.4 where we discuss the origin of the VHVC with respect to the Magellanic Stream. This work is based on observations made with the NASA/ESA Hubble Space Telescope (program ID: 13706). Support for HST-GO-13706 was provided by NASA through a grant from the Space Telescope Science Institute (STScI). STScI is operated by the Association of Universities for Research in Astronomy, Inc., under NASA contract NAS5-26555. Some of the data presented in this paper were obtained from the Mikulski Archive for Space Telescopes (MAST). We also acknowledge support from the National Science Foundation under Grant No. AST-1410800. J.E.G. Peek and J.K. Werk were supported in part by Hubble Fellowship grants 51295 and 51332, respectively, provided by NASA to STScI. This research made use of the IPython package (Pérez & Granger 2007), matplotlib (Hunter 2007) which is a Python library for publication quality graphics, and Astropy (Astropy Collaboration et al. 2013) which is a community-developed core Python package for Astronomy. CalCOS is a product of the Space Telescope Science Institute, which is operated by AURA for NASA.

Chapter 5

Gas Accretion at the Disk-halo Interface of M33

5.1 Introduction

Chemical studies in the solar neighborhood have shown that the star formation rate (SFR) of the Milky Way (MW; $1.9 \pm 0.4\ M_{\odot} \mathrm{yr}^{-1}$; Chomiuk & Povich 2011) has been nearly constant for many billions of years (Chiappini et al. 1997, 2001). Since the total molecular gas mass in the disk is only $\sim 5 \times 10^9\ M_{\odot}$, this reservoir would be exhausted on a significantly shorter timescale without replenishment. Observations of nearby spirals have found the star formation rate (SFR) of a galaxy is tightly related to its molecular gas surface density. This relationship indicates that the molecular gas is consumed at constant efficiency and will be depleted in nearly two Gyrs (Bigiel et al. 2008). The common inference drawn

This chapter is a reproduction of a paper by Zheng, Peek, Werk & Putman (2017) published on ApJ.

from these calculations is that there has to be gas replenishment from an external medium in order to sustain the star-forming activity in a galaxy disk. Analytic studies of galaxies at redshift $z \sim$ 2-3 with high SFRs also show that accretion of additional gas is critical in galaxy formation (Erb 2008).

Observational constraints on the physics of gas accretion onto galaxies are notoriously difficult to obtain. Thus far, the best constraints have been provided by observations of gas in our own MW halo. Absorption- and emission-line studies of the halo reveal complex signatures of multiple-phase gas accretion. H I high-velocity clouds (HVCs; $|v_{\rm LSR}| >$ 90 km s^{-1})* and intermediate-velocity clouds (IVCs; 30 $< |v_{\rm LSR}| <$ 90 km s^{-1}) appear to be predominantly falling toward the disk (Wakker 2001; van Woerden et al. 2004; Putman et al. 2012). However, estimates of the total accretion rate of H I complexes find a value below the SFR of the Galaxy even with the inclusion of ionized gas envelopes surrounding H I complexes (Putman et al. 2012). On the other hand, ultraviolet (UV) spectroscopy of bright halo stars and distant quasars (QSOs) reveal ubiquitous strong absorption from ionized gas (Sembach et al. 2003; Collins et al. 2009; Shull et al. 2009; Lehner et al. 2012; Wakker et al. 2012). Using the distances to halo stars as upper limits on the foreground absorbing gas cloud distances, Lehner & Howk (2011b) place a lower limit on the mass accretion rate of 0.4 – 1.4 $M_{\odot}$yr^{-1} in the MW halo. This accretion rate is comparable to the SFR of the MW. However, having only the radial velocity component along lines of sight with large physical separations ($\gtrsim$ 2 kpc) leads to uncertainties regarding the physical arrangement and three-dimensional motions of halo gas. In addition, mass estimates of the MW halo gas could miss $\sim$ 50% of the gas which has velocities close to the systemic

*$v_{\rm LSR}$ is the velocity in the rest frame of the Local Standard of Rest at the solar circle (LSR).

velocity of the disk, as is found in synthetic observations of a MW-mass galaxy from a cosmological simulation (Chapter 2).

In external galaxies, absorption-line experiments using bright background sources, often QSOs, to study diffuse halo gas have established the existence of an extended, ionized, gaseous halo (aka the circumgalactic medium, or CGM; e.g., Lanzetta et al. 1995; Chen et al. 1998, 2001a; Prochaska et al. 2011). Recent work indicates that the CGM comprises a massive ($M > 10^{10}\ M_{\odot}$), spatially extended ($\sim$ 200 kpc) reservoir of fuel for future star formation and the byproducts of stellar evolution (e.g., Tumlinson et al. 2011; Werk et al. 2014). Our neighbour, M31, is also likely to have a massive CGM, as is found by Lehner et al. (2015) who studied several QSO sightlines with significant M31-related detections within the virial radii of the galaxy. One major limitation of these QSO absorption-line studies is their inability to detect gas flowing into and out of galaxies. Another unavoidable shortcoming is that such studies are often limited to a single sightline per galaxy (except e.g., Keeney et al. 2013; Chen et al. 2014; Lehner et al. 2015), providing incomplete information on the spatial distribution of gas around galaxies.

Recent cosmological simulations of MW-mass galaxies lend further support to this emerging picture of a dynamic, gaseous baryon cycle within galaxy halos. A hydrodynamical cosmological simulation of a MW-mass galaxy finds that within the virial radius the H I accretion rate is $\sim 0.2\ M_{\odot}\mathrm{yr}^{-1}$ and the ionized gas accretion rate is $\sim 3-5\ M_{\odot}\mathrm{yr}^{-1}$ (Joung et al. 2012c; Fernández et al. 2012). Broadly speaking, the simulations incorporate a range of feedback prescriptions, yet are unanimous in indicating the presence of ionized gas extending to a galaxy's virial radius (Joung et al. 2012c; Shen et al. 2012; Oppenheimer

et al. 2012; Ford et al. 2013; Hummels et al. 2013; Suresh et al. 2015; Muratov et al. 2015).

To eventually feed star-forming activities in a galaxy's disk, additional gas fuel needs to be obtained from beyond the disk. Cool gas accretion has been observed in star-forming galaxies in Fe II and Mg II at redshift $z \sim 0.35 - 1$ (Rubin et al. 2012). The gas should be accreted through the disk-halo interface of the galaxy either radially via the edge of the disk (Stewart et al. 2011) or by directly falling down from above the disk. Therefore, the disk-halo interface serves as a key transition region where the mixing of primordial inflowing gas and metal-enriched outflowing gas occurs. In the MW, it has been observed in multiple phases (e.g., H I, Hα, C IV, Si IV, O VI) extending to various heights ranging from a few hundred parsecs to several kiloparsecs (Dickey & Lockman 1990; Reynolds 1993; Haffner et al. 2003; Sembach et al. 2003; Levine et al. 2006; Wakker et al. 2008; Shull et al. 2009; Putman et al. 2012). A hierarchy of increasing temperature and ionization states with increasing scale height has been observed: cold H I mostly dominates at lower z-heights while warm and hot ionized gas fills most of the volume at greater distances from the plane (Dickey & Lockman 1990; Gaensler et al. 2008; Savage & Wakker 2009; Putman et al. 2012). The densest ionized component of this interface, observed in emission, is called the Reynolds layer or the warm ionized medium layer in the MW (Reynolds 1993; Rand 1997; Haffner et al. 2003).

Kinematically, gas with lagging rotation has been found at the disk-halo interface of both the MW and other spiral galaxies in which the rate of halo gas rotation decreases with z-height (Lockman 2002; Ford et al. 2010; Saul et al. 2012; Putman et al. 2012). Such a lagging component shows a typical velocity drop-off of $15 - 30$ km s^{-1} kpc^{-1} as observed

in deep H I observations of external galaxies (Sancisi et al. 2001; Fraternali et al. 2002; Oosterloo et al. 2007; Heald et al. 2011). That is to say, gas at the disk-halo interface has been found to move at velocities very close to the systemic velocity of a galaxy. For the MW observations, the fact that we are residing inside the ISM increases the difficulty in separating the low-velocity disk-halo component from the ISM component. For extragalactic absorption-line observations, low spectral resolutions (typically $\gtrsim 50-100$ km s^{-1}) is a major problem (Heckman et al. 2000; Weiner et al. 2009; Chen et al. 2010d; Martin et al. 2012; Rubin et al. 2012); it would be challenging, if not impossible, to detect infalling IVC- and HVC-like clouds such as those found in the MW halo if they exist in external galaxies.

In this paper we investigate the low- and intermediate-velocity gas flows at the disk-halo interface of M33 with medium-resolution spectra (FWHM $\sim 14-19$ km s^{-1}) from the Cosmic Origins Spectrograph (COS) on the *Hubble Space Telescope (HST)*. M33 is a late-type Sc galaxy at a distance of 840 kpc (Freedman et al. 1991) and it moves toward the MW at $v_{\rm LSR} = -179$ km s^{-1} (Corbelli & Schneider 1997). Its proximity makes UV-bright stars in the disk of M33 observable in a reasonable amount of integration time using *HST*/COS. The galaxy has an inclination of 56° (Paturel et al. 2003), ensuring that a fair fraction of the velocity will be projected along the line of sight if vertical gas inflows or outflows exist. The dark matter halo mass of M33 is 5×10^{10} $M_\odot$ while its stellar mass is $3-6 \times 10^9$ $M_\odot$ (Corbelli 2003). It has atomic H I mass of $1-3 \times 10^9$ $M_\odot$ (Deul & van der Hulst 1987; Corbelli & Schneider 1997; Putman et al. 2009; Gratier et al. 2010) and molecular mass of $3-4 \times 10^8$ $M_\odot$ (e.g., Corbelli 2003; Gratier et al. 2010). M33 is actively forming stars with

a SFR of $0.2 - 0.5\ M_{\odot}\mathrm{yr}^{-1}$ based on a variety of observations (e.g., Engargiola et al. 2003; Gratier et al. 2010). Deep H I observations and galactic chemical evolution models suggest gas accretion could account for its ongoing star formation (Magrini et al. 2007a; Putman et al. 2009). Such gas accretion can be detected with our *HST*/COS UV absorption-line studies, as has been shown in observations of the MW ionized HVCs (Collins et al. 2009; Savage & Wakker 2009; Shull et al. 2009; Lehner et al. 2012).

Our *HST*/COS observations toward M33 provide detailed kinematic information of gas flows on one side of the M33 disk, thus have the great advantage over typical extragalactic observations. In our study, we use UV-bright M33 disk stars as background sources, which helps to unambiguously determine the relative gas motions with respect to the disk. In the rest frame of the M33 gas disk (see § 5.2.4), we define the *low-velocity* gas as that with observed velocities (i.e., without an inclination correction) of $-40 \lesssim v_{\mathrm{d}} \lesssim +40$ km s^{-1} and the *intermediate-velocity* gas with $v_{\mathrm{d}} \gtrsim +40$ km s^{-1}; v_{d} shall be defined in § 5.2.4. By observing multiple sightlines toward different locations of the disk, we are able to differentiate between various accretion models, obtain a better understanding of how gas is flowing, and assess the overall accretion rate. Similar techniques to study disk-wide gas kinematics have also been applied to the observations of multi-phase gas associated with the Large Magellanic Cloud (LMC; Howk et al. 2002; Danforth & Blair 2006; Lehner et al. 2009; Pathak et al. 2011; Barger et al. 2016) and the Small Magellanic Cloud (SMC; Hoopes et al. 2002).

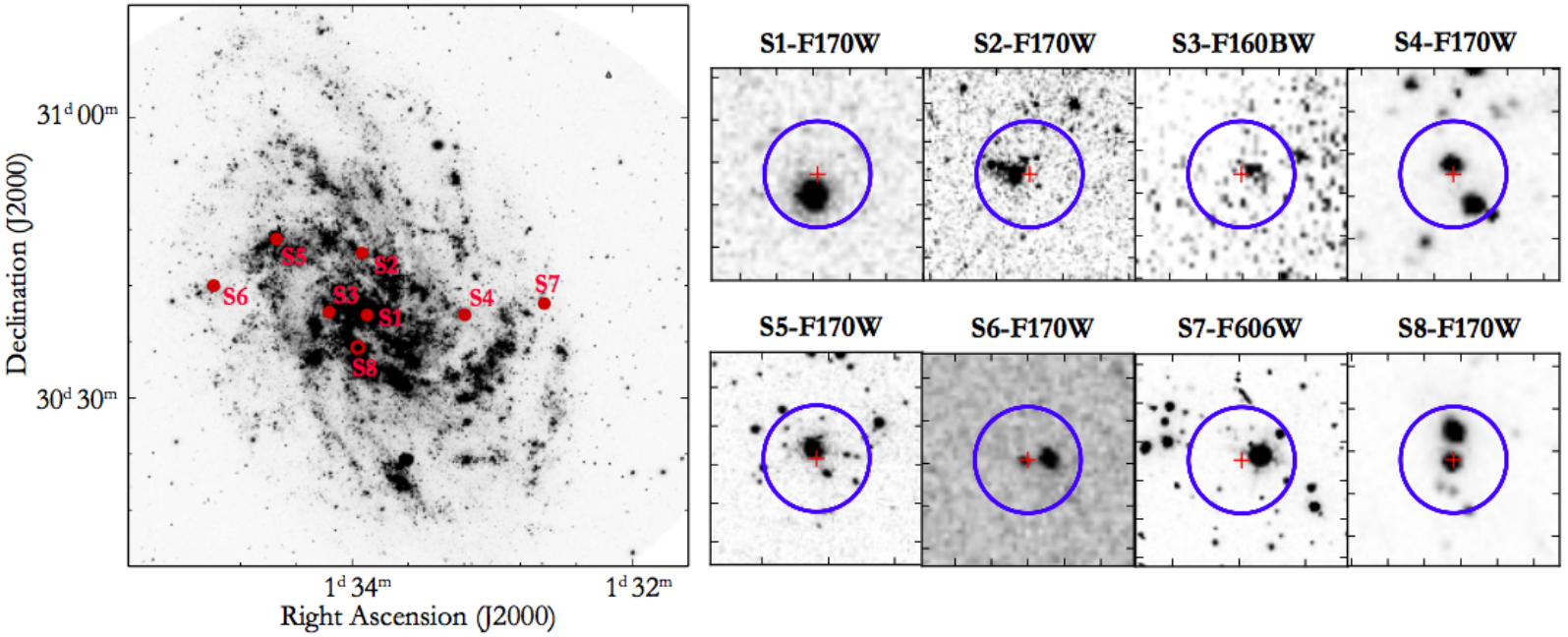

Figure 5.1: Left: The distribution of the target stars (S1-S8) in the disk of M33. The background image is from the *Galaxy Evolution Explorer* (*GALEX*). S8, indicated by an open circle, is not used in our analysis (see § 5.2.1). Right: The number of stars within the COS aperture along each sightline. The background *HST*/WFPC images were retrieved from MAST archive. Images taken with F170W filter are used when they exist. The red cross indicates the center of the COS aperture and the blue circle shows its size (2.5″ in diameter). At the distance of M33 (840 kpc), 2.5″ ~ 10 pc.

This chapter is structured as follows. § 5.2 outlines the sample selection criteria and spectral reduction processes (including continuum fitting and Voigt-profile fitting), and addresses the CalCOS wavelength calibration uncertainty. We calculate the systemic velocity of M33's ISM along each sightline, define the $v_{\rm d}$ frame (the rest frame of M33's ISM), and estimate M33's hydrogen content along each sightline in this section. § 5.3 describes the ion properties. We show that the detected absorbers are indeed associated with M33 in § 5.4. In § 5.5 we perform kinematic modeling of the consistently redshifted Si IV absorption lines, and in § 5.6 address the metal enrichment level of detected gas inflow using our absorption-line measurements and photoionization modeling. In § 5.7 we discuss the accretion rate, the origin(s) of the inflowing gas, and the possibility of galactic outflows from M33. We conclude with a summary of our main findings in § 5.8.

5.2 Observations and Measurements

5.2.1 Sample Selection and COS Spectroscopy

We targeted UV-bright stars in massive OB associations in the disk of M33. Each star was required to have *Far Ultraviolet Spectroscopic Explorer* (*FUSE*) spectra available in the Mikulski Archive for Space Telescopes (MAST), and its UV continuum flux at 1300 Å was required to be $> 5\times10^{-15}$ erg s^{-1} cm^{-2} Å^{-1} to achieve a S/N of 15 – 20. These criteria limited us to only 14 stars. Among all the candidates, we selected seven stars evenly distributed across the disk of M33. This helps sample the gas disk rotation at different locations and galactocentric radii, and thus distinguish among different accretion models (see § 5.5).

The seven targeted stars were observed in 2014 – 2016 during *HST* Cycle 22 (proposal ID: 13706) using the G130M FUV grating with a central wavelength of 1291 Å and coverage from 1134 Å to 1431 Å. The resolving power of COS/G130M centering at 1291 Å is $R = 16,000 - 20,000$, resulting in a spectral resolution (FWHM) of $\sim 14 - 19$ km s^{-1} (COS data handbook; Fox & et al. 2015). The observations were conducted using the FUV XDL detector under TIME-TAG mode with the Primary Science Aperture (2.5″; ~ 10 pc at the distance of M33). Each star was observed with four exposures with a total integration time of $\sim 11,000$ s (see Table 5.1). We retrieved the calibrated and co-added spectra from MAST, which have been processed by the standard CalCOS (version 3.0) pipeline. To supplement our sample, we also retrieved the *HST*/COS spectrum of M33-UIT-236 – a Wolf-Rayet (WR) star near the disk center. The observation of M33-UIT-236 was carried out in 2011 under the *HST* Cycle 18 COS Guaranteed Time observation program (proposal ID: 12026), with a similar spectrograph setting as ours (Welsh & Lallement 2013).

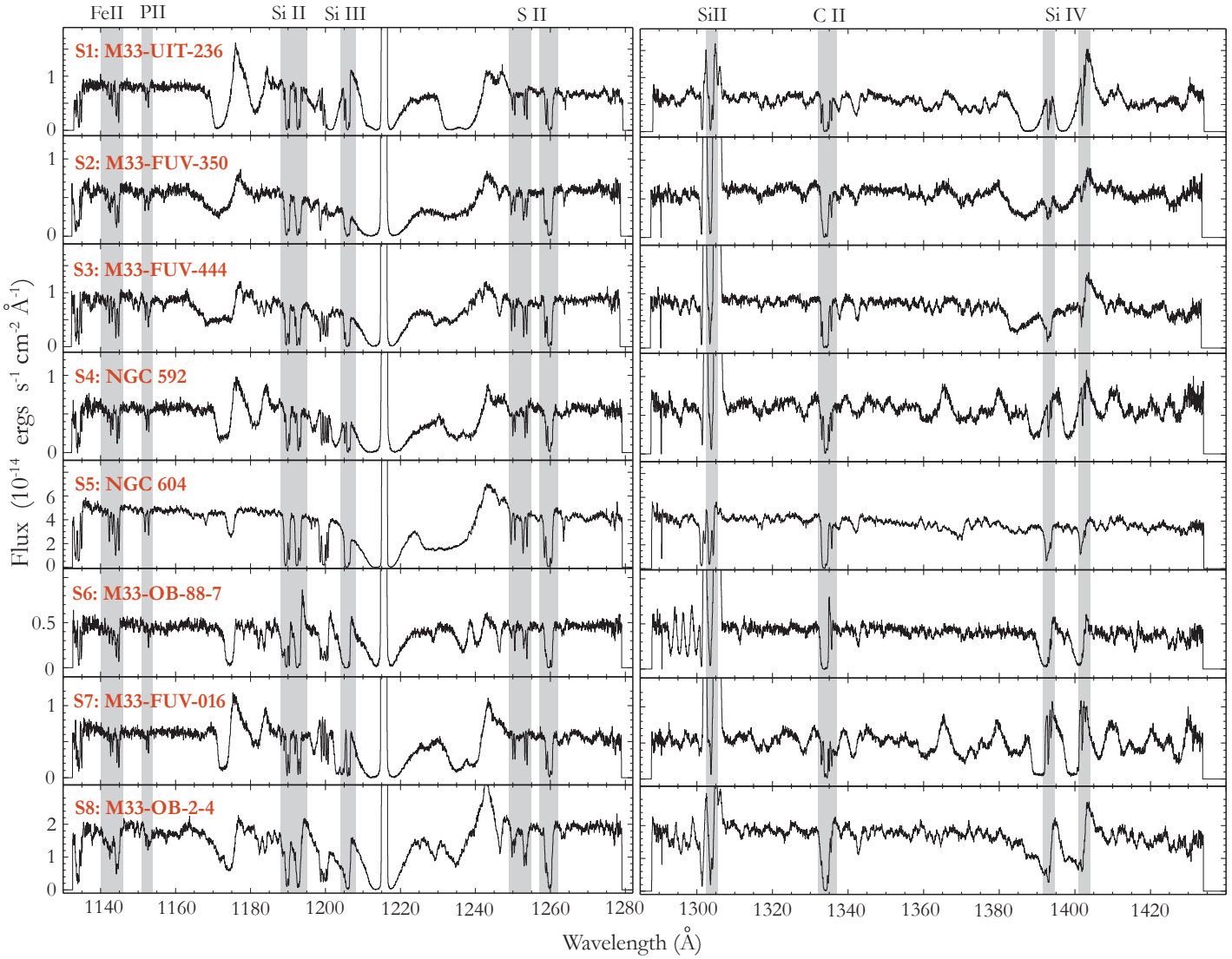

Figure 5.2: CalCOS co-added stellar spectra. We bin the spectra by five pixels for better illustration. Interstellar lines are highlighted in gray, including Fe II λ1142, 1143, 1144, P II λ1152, Si II λ1190, 1193, 1304, Si III λ1206, S II λ1250, 1253, C II λ1334, Si IV λ1393, 1402. Note that Si II λ1304 is dominated by the airglow emission; for the continuum-normalized spectra shown in the following figures, we use the night-only data retrieved from the original observation for this line. We describe the night-only data reduction in detail in Chapter 4. Due to the wide wavelength span of the spectra, M33 and MW components of the same line are usually very close to each other in this figure. For a better illustration of line sub-structures, please see Figures 3-6 . We do not use sightline S8 in our analysis since its interstellar lines are strongly affected by stellar activities and, the spectrum is likely a combination of a WR star and a blue supergiant (see § 5.2.1).

Table 5.1 lists the position (RA, DEC), rotation velocity of the gas disk at the position of a given sightline $v_{\rm rot}$ (§ 5.2.4), projected galactocentric distance R and inclination-corrected galactocentric distance $R_{\rm G}$, total exposure time, and spectral type. For clarity, we assign to each sightline an ID S1–S7 in the order of increasing $R_{\rm G}$, with S1 being the closest to the disk center and S7 the most distant. S8 (M33-OB-2-4) does not follow this rule since it is not included in our analysis (see below for explanation).

Emission- and absorption-line studies in the literature show that our targets have active stellar winds and are fast rotators (e.g., Humphreys et al. 2013; Drissen et al. 2008; Tenorio-Tagle et al. 2000). Such activity generates stellar and photospheric lines that can be easily distinguished from interstellar lines because of their unique line shapes (e.g., P Cygni profiles) and large line widths. We describe the treatment of stellar lines and the normalization of stellar continua in § 5.2.3 and Appendix 6.

The left panel of Figure 5.1 shows the locations of S1-S8 in the disk of M33. They are mostly associated with spiral arms and/or H II regions. For each sightline, we retrieve the *HST*/F170W[†] images from MAST archive and, examine the number of stars within the *HST*/COS aperture. The right panels of Figure 5.1 show that most sightlines have only one UV-bright star dominating the COS aperture except for S4 and S8.

S4 is associated with a giant H II region that has several WR stars identified in the field. Based on coordinate coincidence, one of the two stars in S4 is likely the NGC592-WR2 identified in Drissen et al. (2008). Since the *HST*/COS spectrum of S4 is similar to others shown in Figure 5.2 and 5.3, the two stars within the aperture are not likely to cause significant blending and smearing of the spectral lines. We therefore decided to keep this

[†]Other *HST* filters are chosen when F170W is not available.

sightline in our analysis.

Along sightline S8, two bright stars are present within the COS aperture. Spectroscopic analysis indicates that one is a WN-type WR star and the other is a B supergiant (Massey et al. 1995, 1996). Our *HST*/COS spectra suggests a combination of the two stars, as shown in the bottom panel in Figure 5.2. The interstellar lines of interest along sightline S8, as highlighted in gray, are clearly dominated by stellar features such as P Cygni profiles. This makes the continuum normalization and Voigt-profile fitting highly unreliable. Therefore, we exclude this sightline from our analysis. Note that this does not represent a non-detection in our sample. Our final target list includes seven sightlines that are listed as S1–S7 in Table 5.1.

In addition, we retrieved the *FUSE* spectra for our sightlines from MAST. The spectra span a wavelength range of 905 – 1187 Å within which an important absorption line O VI λ1032 lies. Since O VI is not the focus of this work and we only use it for a comparison with Si IV, a simpler spectral reduction was performed. The stellar continuum within ±1000 km s^{-1} of 1032 Å was normalized using first- and second-order polynomial functions. We did not attempt to run Voigt-profile decomposition for O VI λ1032 given the low S/N of the *FUSE* data. The normalized O VI absorption lines and relevant discussion are presented in § 5.6.1.

All the *HST*, *FUSE* and *GALEX* data used in this paper can be found in MAST: [DOI: 10.17909/T9FG6R].

Table 5.1: M33 Sample

Name	S-ID[a]	RA (J2000) (hh mm ss)	DEC (J2000) (dd mm ss)	$v_{\rm rot}$[b] (km s^{-1})	R[c] (kpc)	$R_{\rm G}$[c] (kpc)	Exp. T. (s)	Sp. Type[d]	Note
M33-UIT-236	S1	01 33 53.60	+30 38 51.60	-177.0	0.2	0.4	10,651	Ofpe/WN9	WR
M33-FUV-350	S2	01 33 56.00	+30 45 31.00	-233.7	1.5	1.5	11,172	A8-F0Ia	Late A type supergiant[e]
M33-FUV-444	S3	01 34 09.90	+30 39 11.00	-194.7	1.2	1.7	11,200	O6III	Star
NGC592	S4	01 33 12.30	+30 38 49.00	-160.1	2.4	3.4	11,168	WN3+neb	H II region; WR2[f]
NGC604	S5	01 34 32.50	+30 47 04.00	-240.3	3.1	3.6	11,221	WN10	H II region; WR12[f]
M33-OB-88-7	S6	01 34 59.40	+30 42 01.10	-210.6	4.2	5.9	11,156	O8Iaf	blue supergiant
M33-FUV-016	S7	01 32 37.70	+30 40 06.00	-157.6	4.5	6.6	11,220	Ofpe/WN9	WR
M33-OB-2-4	S8	01 33 58.70	+30 35 27.00	-147.0	1.1	1.5	11,222	Ofpe/WN9	WR + B supergiant

(*a*): S-ID is in the order of increasing $R_{\rm G}$ with S1 being the closest and S7 the most distant. S8 does not follow this convention since it is not used in our analysis. See Section 5.2.1 for the explanation.
(*b*): $v_{\rm rot}$: the rotation velocity of the gas disk of M33 at the position of a given sightline. See Section 5.2.4 for the derivation of $v_{\rm rot}$.
(*c*): R: the projected galactocentric distance. $R_{\rm G}$: the inclination-corrected galactocentric distance.
(*d*): Spectral type. S1, S4, S5, S7: Neugent & Massey (2011); S2: Humphreys et al. (2013); S3, S6, S8: Massey et al. (2006).
(*e*): Humphreys et al. (2013).
(*f*): Several WR stars are reported in these H II regions; based on coordinate coincidence, we find sightline S4 is likely pointing at NGC592-WR2 and S5 at NGC604-WR12 as identified in Drissen et al. (2008).

5.2.2 Wavelength Calibration and Spectral Co-addition

As mentioned in § 5.2.1, each sightline was observed with four exposures which produce four spectra that need to be co-added. The standard CalCOS pipeline provides data reduction for spectral co-addition and wavelength calibration with an uncertainty of nearly one resolution element. We show the original CalCOS-processed stellar spectra in Figure 5.2. In the following work, we process and present the spectra in their original resolution; we do not perform any binning to the spectra unless otherwise specified.

Several authors have pointed out that problems may arise with CalCOS wavelength calibration and spectral co-addition, and thus have written their own pipelines to process *HST*/COS spectra in order to minimize the uncertainties. To justify that CalCOS products are reliable for our scientific analysis, we used three other pipelines to calibrate and co-add the original spectra and compared the results with those from CalCOS. The three pipelines we investigated are: (1) an IDL routine x1d_coadd.pro by Danforth et al. (2010), (2) a spectral co-add code by Wakker et al. (2015), and (3) the PyCOS pipeline by Liang & Chen (2014) (& private communication). We discuss the details of these pipelines and compare them with CalCOS in Appendix 6. All the coadded spectra processed by these three methods can be found in Zheng et al. (2016).

In brief, our investigation shows consistency between CalCOS products and those from other pipelines. A couple of lines using the method of Wakker et al. (2015) have minor wavelength shifts with respect to the CalCOS spectra but all within one resolution element. We note that such good agreement between CalCOS and the other three pipelines is mainly due to the straightforward setup of our observations. For each of our sightlines,

the observation was completed with four exposures in one single visit and the spectra were taken under the same setting. The background stars are all UV-bright to ensure high S/N. Thus the possibility of spectral miss-alignment is largely reduced. CalCOS pipeline is most likely to become problematic in situations where faint QSO observations and multiple spectra are obtained at different epochs. We proceed with our analysis using the CalCOS co-added spectra that we have tested to be scientifically reliable by direct comparisons with three other different methods.

5.2.3 Line Identification, Continuum Fitting and Voigt-Profile Fitting

Our observations include interstellar absorption lines of S II λ1250, 1253[‡], Fe II λ1142, 1143, 1144, P II λ1152, Si IV λ1393, 1402, Si II λ1190, 1193, 1304[§], Si III λ1206, and C II λ1334. In Figure 5.2, we highlight these lines in gray. Due to the broad wavelength span, M33 and MW absorption components of the same line are very close to each other in this figure. Please see Figures 3–6 for a better illustration of the line structures.

Line identification is made according to wavelength coincidence at the rest frame of the gas disk at the position of the corresponding sightline. For each absorption line, we confirm its detection in each of the four exposures to ensure that it is not an artifact due to spectral co-addition or fixed pattern noise (COS data handbook; Fox & et al. 2015). Our spectra also cover N V $\lambda\lambda$1238, 1242, but we do not detect related absorption features with

[‡]S II lines are in fact triplet: 1250 Å, 1253 Å, and 1259 Å. However, S II λ1259 is blended with a $v_{\rm LSR} \sim -350$ km s^{-1} component of Si II λ1260 that we will discuss in § 5.7.3 and Appendix 6. We do not include S II λ1259 in our analysis. We also exclude Si II λ1260 and only use Si II λ1190, 1193, 1304.

[§]In each of our COS spectra, Si II λ1304 is strongly affected by nearby airglow emission O I λ1302, 1304 due to oxygen atoms in the exosphere of the Earth. For this line, we retrieve night-only photons from the spectra, the process of which is described in Chapter 4.

reliable significance in any of our sightlines.

Table 5.2: Voigt Profile Fitting

S-ID	$v_{\rm d}^{a}$ (km s^{-1})	b^{b} (km s^{-1})	$\log_{10}N^{c}$ (cm^{-2})	$\lambda^{2}_{\rm red}{}^{d}$
S II: 1250.58 Å, 1253.81 Å				
S1	-15.0± 5.7	41.3± 4.5	15.07±0.07	0.94
	20.0± 1.0	17.0± 2.3	14.87±0.10	
S2	-10.7± 5.5	35.0± 4.9	15.18±0.16	0.62
	51.2±17.6	52.6±14.7	15.15±0.18	
S3	-18.6± 0.5	30.2± 0.7	15.34±0.01	0.92
S4	29.2± 0.8	31.5± 1.3	15.24±0.02	0.71
S5	-20.6± 9.5	52.1± 3.8	15.14±0.18	0.92
	-4.0± 1.9	33.5± 3.4	15.13±0.17	
	52.8± 1.4	13.3± 3.4	14.01±0.18	
S6	-2.3± 4.5	39.4± 7.6	15.10±0.08	0.65
	68.7±10.6	29.3±13.6	14.54±0.25	
S7	15.2± 0.7	18.3± 1.0	15.02±0.02	0.95
P II: 1152.82 Å				
S1	-37.0±29.8	26.4±23.7	13.10±0.86	0.64
	9.1±24.0	34.1±20.2	13.46±0.38	
S2	-10.9± 7.6	37.5± 9.4	13.66±0.11	0.54
	69.9±15.1	38.3±28.5	13.31±0.28	
S3	-18.8± 2.9	34.0± 4.0	13.62±0.04	0.91
S4	32.3± 3.4	37.9± 4.7	13.77±0.05	0.57
S5	2.6± 1.4	40.9± 2.1	13.69±0.02	1.00
S6	[-80, 80]^{e}	-	$\leq$13.3^{e}	
S7	19.9± 3.3	25.9± 4.7	13.47±0.06	0.72
Fe II: 1142.37 Å, 1143.23 Å, 1144.94 Å				
S1	-41.1±9.8	31.2±7.4	14.34±0.20	0.81
	10.7±10.4	34.6±8.1	14.42±0.16	
S2	1.0±6.2	39.2±6.4	14.56±0.08	0.76
	68.3±4.8	31.0±4.9	14.51±0.08	
S3	-25.6±3.8	18.5±9.7	13.96±0.39	0.86
	-23.4±2.6	46.2±6.7	14.52±0.11	
S4	42.2±2.9	24.2±4.0	14.31±0.06	0.70
S5	-39.9±2.5	12.9±5.9	13.37±0.29	1.11
	8.9±1.8	40.4±4.2	14.63±0.04	
	74.6±4.8	32.5±3.9	14.11±0.09	
S6	-7.2±11.8	30.0±10.8	14.39±0.21	0.80
	39.5±10.5	23.7±10.4	14.23±0.30	
	96.0± 8.1	14.2±12.6	13.42±0.27	
S7	9.9±1.3	18.6±1.8	14.34±0.04	0.87
Si IV: 1393.76 Å, 1402.77 Å				
S1	3.0±0.8	32.8± 1.0	14.17±0.01	0.84
	*67.9±1.8^{f}	22.3± 2.0	13.38±0.04	
S2	10.4±20.3	44.8±14.6	13.33±0.54	0.69
	*75.6±32.4	60.9±21.7	13.57±0.31	
S3	-14.9±2.3	44.3± 3.2	13.67±0.03	0.96
	*75.9±3.1	34.2± 4.4	13.35±0.05	
S4	-29.3±3.5	14.7± 3.8	12.94±0.13	0.65

Table 2. – *Continued*

S-ID	$v_{\rm d}^{a}$	b^{b}	$\log_{10}N^{c}$	$\chi^{2}_{\rm red}{}^{d}$
	8.4±2.3	20.4± 4.5	13.43±0.14	
	*50.8±13.3	34.5±11.8	13.19±0.20	
S5	-35.6±2.0	34.1± 2.2	13.47±0.03	0.92
	5.0±1.5	12.9± 2.8	12.78±0.12	
	*39.1±2.8	11.3± 4.5	12.29±0.12	
S6	-8.9±5.4	19.2± 7.4	13.20±0.14	0.35
	*70.6±4.0	17.5± 5.7	13.25±0.12	
	*106.2±3.9	14.5± 4.4	13.13±0.14	
S7	-19.8±2.0	19.8± 1.9	13.52±0.05	0.70
	13.8±2.0	15.6± 3.4	13.25±0.14	
	*48.2±15.0	30.6±15.4	12.80±0.28	

[a]: Centroid velocity.
[b]: Doppler width.
[c]: Logarithmic column density of the Voigt-profile fits.
[d]: The reduced χ^2 of the fit that is calculated within $[-150, 150]$ km s^{-1} of the respective spectral line.
[e]: No P II detection along this sightline; a 3σ upper limit over the $[-80, 80]$ km s^{-1} range is quoted.
[f]:The * sign indicates the intermediate-velocity/non-disk Si IV component. See § 5.3 for description.

The narrow interstellar absorption lines of interest are found superimposed on stellar features that have much broader line widths and commonly have P Cygni profiles. We treat the stellar features as continua such that interstellar line profiles can be normalized. First, we model the continua using Legendre polynomials within ±1000 km s^{-1} from the centroids of the lines of interest. The fitting is evaluated such that the polynomial order is kept as low as possible while the reduced χ^2 ($\chi^2_{\rm red}$) is minimized to ~ 1.0. For ions (Fe II, S II, Si IV) that have multiple transition lines available and the lines are not saturated, we use their oscillator strengths f to scale their normalized profiles and compare the f-scaled line shapes. This f-scale matching helps to simultaneously constrain the continuum fitting of different transition lines of the same ion, and ensures that we have filtered out the stellar features plaguing the interstellar lines of interest at different wavelengths.

We note that unresolved saturation may exist in the non-saturated lines even though their minimum fluxes have not yet reached zero, which will make the f-scale matching not valid. To evaluate the level of unresolved saturation, we perform another independent

continuum fitting for each non-saturated line of S II and Si IV. We use a different pipeline – the linetools package(Prochaska et al. 2016)[¶], which applies Akima Spline to regenerate the continua of non-absorption region of each line. We compare the column densities of S II (Si IV) derived from λ1250 and λ1253 (λ1393 and λ1402), and find that the values agree well. For S II lines, the log $N_{\rm SII}$ derived from λ1253 are generally consistent with those from λ1250 within $\sim$ 0.05 dex; only in S2 and S7 we find an offset of $\sim 0.1 - 0.2$ dex. For Si IV lines, the $N_{\rm SiIV}$ derived from λ1393 and λ1402 are also consistent within 0.05 dex. Therefore, we conclude that the unresolved saturation is well controlled in our COS data and only along a couple of sightlines (e.g., S7-S II) the unresolved saturation may affect the column density estimates by up to 0.2 dex. We refer the reader to Figures 3–6 for a close inspection on the continuum fitting and f-scaled profile matching of each line.

After continuum normalization, we perform Voigt-profile fitting to decompose the interstellar absorption lines by taking into account both the profile shapes and line saturation. By doing so, we resolve the underlying kinematic components of detected absorption lines. We use the same method as described in Tumlinson et al. (2013). First, visual inspection is required to determine the number of kinematic components and unrelated nuisance absorption lines (e.g., absorption due to MW's ISM). Using the MPFIT[‖] software (Markwardt 2009), we optimize the fit of each component and derive the best-fit column density log N, Doppler width b and centroid velocity $v_{\rm d}$ for each component. $v_{\rm d}$ is defined as the velocity in the rest frame of M33's ISM at the position of each sightline; we will define this $v_{\rm d}$ in § 5.2.4. The errors for the fit are computed from parameter covariance

[¶]https://github.com/linetools/linetools
[‖]http://purl.com/net/mpfit

matrices by MPFIT. Specifically, if an ion has multiple transitions, such as Si IV $\lambda\lambda$1393, 1402, the same number of kinematic components and the same set of parameters (log N, b, $v_{\rm d}$) will be simultaneously applied to all observed lines. The parameters are eventually determined when the values converge after iteratively fitting. This approach reduces the risk that visual inspection could be biased by artifacts at certain wavelengths. For this simultaneous multi-line fitting, our procedure also takes into account potential velocity shifts and geometric distortion of line profiles at different locations on the grating. The modeled Voigt profiles are convolved with the COS line-spread-function that is given at the nearest observed wavelength grid point in the compilation (Ghavamian et al. 2009). We refer the reader to Tumlinson et al. (2013) for a detailed discussion on the methodology and the profile fitting algorithm. We tabulate the Voigt-profile fitting results in Table 5.2 and discuss the interpretation in § 5.3.

The above multi-component and/or multi-line fitting is performed only for ions with non-saturated absorption lines, including those of P II, S II, Fe II, and Si IV. For ions with saturated and blended lines – i.e., C II, Si II, and Si III – we do not attempt to recover the underlying kinematic components. As shown in Figure 7, Si II λ1304 has the lightest saturation among these lines, even so, the core of the line (M33's ISM) can be still found saturated. Therefore, we only derive the column densities of these ions by integrating the spectra over the M33 velocity ranges using the AOD method (Savage & Sembach 1991, 1996). Since the lines are saturated, these derived values should be lower limits. We describe the AOD method and show the results in Appendix 6. A full display of the detected absorption lines along each sightline can be found in Figure 7. In Appendix 6,

we discuss in detail the continuum- and Voigt-profile fitting of specific lines.

5.2.4 Rotation Velocity of M33's ISM at the Position of Each Sightline

Throughout this paper, we use a velocity frame, $v_{\rm d}$, which is defined as the velocity in the rest frame of M33's ISM at the position of each sightline: $v_{\rm d} \equiv v_{\rm LSR}$-$v_{\rm rot}$, where $v_{\rm LSR}$ is a spectral line's LSR velocity with respect to the Sun and $v_{\rm rot}$ is the rotation velocity of the M33 gas disk at the position of each sightline in the LSR frame. We emphasize that the gas kinematics we investigate is with respect to the M33's ISM, the rotation of which will be determined from H I 21-cm spectra as shown in the following paragraphs. The exact positions of the background stars in the gas disk do not change our determination of gas inflows and outflows.

To compute $v_{\rm rot}$, we use the H I 21-cm emission-line observation from the Very Large Array (VLA; Gratier et al. 2010); the spectral resolution is 1.29 km s^{-1} and the angular resolution is 25″ ($\sim$ 100 pc at the distance of M33). The H I 21-cm spectrum at the position of each sightline is shown in the first row of Figure 5.3. We fit a single Gaussian function to each spectrum to decide the centroid velocity of the line, which we adopt as $v_{\rm rot}$ (Table 5.1). Note that we do not attempt to shift the UV absorption-line centroids to line up with the H I 21-cm peak emission, since it is not clear whether the neutral and the ionized gas associated with M33's ISM are co-spatial and/or kinetically connected.

In addition, we make use of the H I 21-cm spectra from the Arecibo Galaxy Environment Survey (AGES; Auld et al. 2006; Keenan et al. 2015) that has a spectral resolution of $\sim$ 5 km s^{-1} and angular resolution of $\sim$ 4′. The AGES data reaches a column density

limit of $\sim 1.5 \times 10^{17}$ cm^{-2} over 10 km s^{-1}. Its large beam size and high sensitivity helps to map the diffuse gas pervading M33's ISM and its disk-halo interface. We also examine the H I 21-cm spectra obtained from the GALFA-H I survey (Peek et al. 2011) that has the same angular resolution as the AGES data. Similar H I 21-cm emission line profiles are found. We use the AGES spectra for later analysis since they have better column density sensitivity than GALFA-H I. The AGES spectra are shown in the second row of Figure 5.3. We discuss the use of these spectra in § 5.6.2.

5.2.5 Hydrogen Column Density in Front of the Stars

To assess the metallicity of M33's ISM and the disk-halo interface as discussed in § 5.6.2 and 5.6.3, here we calculate the total column density of neutral hydrogen (both in atomic and molecular forms) along the lines of sight in front of our target stars. We cannot pursue this hydrogen measurement with H I 21-cm emission since it would include all of the H I both in front of and behind the stars. In addition, the H I 21-cm spectra were obtained with larger beam size than that of the COS aperture, thus may introduce up to a factor of ten uncertainty in H I column density due to unresolved sub-structures within the beam (e.g., Tumlinson et al. 2002; Welty et al. 2012). On the other hand, estimates based on Lyα λ1215 absorption line are not reliable since this line is saturated and, distorted due to stellar P Cygni profiles and the dominant Galactic emission (see Figure 5.2).

Here we use a method first introduced by Bohlin et al. (1978), which correlates the column density of neutral hydrogen $N_{\rm H}(= N_{\rm HI} + 2N_{\rm H_2})$ in front of the corresponding stars with their color excess E(B-V) – the gas-to-dust ratio. The relation is established linearly

as

$$N_{\rm H} = f \times 5.8 \times 10^{21}\ {\rm E(B-V)\ cm^{-2}\ mag^{-1}}. \quad (5.1)$$

where $f = 1.0$ for the Galactic value (Bohlin et al. 1978), and $f = 2.8$ (5.0) for the LMC (SMC) gas-to-dust ratio (Welty et al. 2012; Tumlinson et al. 2002).

Using E(B-V) to infer $N_{\rm H}$ relies on the assumption that local environment does not change dramatically from sightline to sightline. This is reasonable as the gas-to-dust ratio is relatively constant over a galaxy's disk (Sandstrom et al. 2013) and the dust extinction curve only weakly varies across kpc scales (Schlafly et al. 2016). Since the metal content of M33's ISM is not yet well understood, in Table 5.3 we provide log $N_{\rm H}$ values in three cases assuming M33 is MW-, LMC-, or SMC-like. The MW-like log $N_{\rm H}$ has uncertainty of $\lesssim 0.2$ dex (Bohlin et al. 1978), while the LMC- and SMC-like log $N_{\rm H}$ have rms deviations of 0.22 and 0.34 dex, respectively (Welty et al. 2012). We suggest the LMC-like values are likely to be the closest to the M33's since these two galaxies are similar in galaxy mass and metallicity (Crockett et al. 2006; D'Onghia & Fox 2015). The MW-like and SMC-like values serve as the metal-rich and metal-poor guesses, respectively; they provide lower and upper log $N_{\rm H}$ estimates, which are consistent with the quoted LMC-like rms deviation. In § 5.6.3 and Table 5.5, we provide metallicity estimates using the LMC-like log $N_{\rm H}$ values. We note that the total H I column density (integrated from $v_{\rm d} = -30$ km s^{-1} to +30 km s^{-1} for each sightline) is log $N_{\rm HI} \sim 21.0$ cm^{-2}, consistent with the ones derived from E(B-V). Overall, the LMC-like scenario is an approximation given the current limited knowledge of the actual metal content of M33s ISM. The reader should interpret our provided $N_{\rm H}$ and metallicity values (§ 5.6.3) with caution.

Table 5.3: E(B-V) and log $N_{\rm H}$

ID	(B-V)[a] (mag)	$(B-V)_0$[b] (mag)	E(B-V)[c] (mag)	log $N_{\rm H}$ (cm^{-2}) (MW)	log $N_{\rm H}$ (cm^{-2}) (LMC)	log $N_{\rm H}$ (cm^{-2}) (SMC)
S1	-0.21	-0.32	0.07	20.6	21.1	21.3
S2	0.43	N/A	0.24	21.1	21.6	21.8
S3	-0.16	-0.30	0.10	20.8	21.2	21.5
S4	0.48	N/A	0.20	21.1	21.5	21.8
S5[d]	0.24	N/A	0.20	21.1	21.5	21.8
S6	-0.14	-0.30	0.12	20.8	21.3	21.5
S7	-0.13	-0.32	0.15	20.9	21.4	21.6

[a]Observed B-V color including the Galactic extinction. S1, S2, S3, S6, S8: Massey et al. (2006); S7: Neugent & Massey (2011); S4, S5: B mag is from Drissen et al. (2008) and V mag from Neugent & Massey (2011).

[b]Intrinsic color. S3, S6: Wegner (1994). S1, S7: see Section 5.2.5 for the derivation.

[c]E(B-V) corrected for the foreground Galactic value.

[d]For S5, L06 found log $N_{\rm HI}$ = 20.75 ± 0.3 (log $N_{\rm HI}$ = $21.07^{+0.17}_{-0.24}$) by fitting the damping wing of the Lyβ (Lyα) line. These numbers are consistent with our MW-like value, given that the molecular gas content is negligible along S5 as indicated by L06. See Section 5.2.5 for detailed discussion.

We find the E(B-V) values from a number of sources. For S2, which was named B324 in their paper, Humphreys et al. (2013) found a V-band total extinction of $A_{\rm v}$ = 0.9 mag. Assuming $R_{\rm v}$ = 3.2 mag as suggested (Humphreys et al. 2013), we obtain a total color excess of 0.28 mag, which gives E(B-V)=0.24 mag for S2 after correcting for foreground Galactic extinction (∼0.04 mag; Schlegel et al. 1998; Schruba et al. 2010). For S3 and S6, their color excesses are directly calculated using E(B-V)=(B-V)-$(B-V)_0$-0.04 mag. For S4, its E(B-V) is from Úbeda & Drissen (2009) who provided the measurement of E(4405-5495) that is the monochoromatic equivalent of E(B-V) assuming 4405 Å and 5495 Å are the central wavelengths of the B and V filters. For S5, it is from Bruhweiler et al. (2003) who measured the E(B-V) of two O-type stars (690A and 690B) in the same COS aperture as S5.

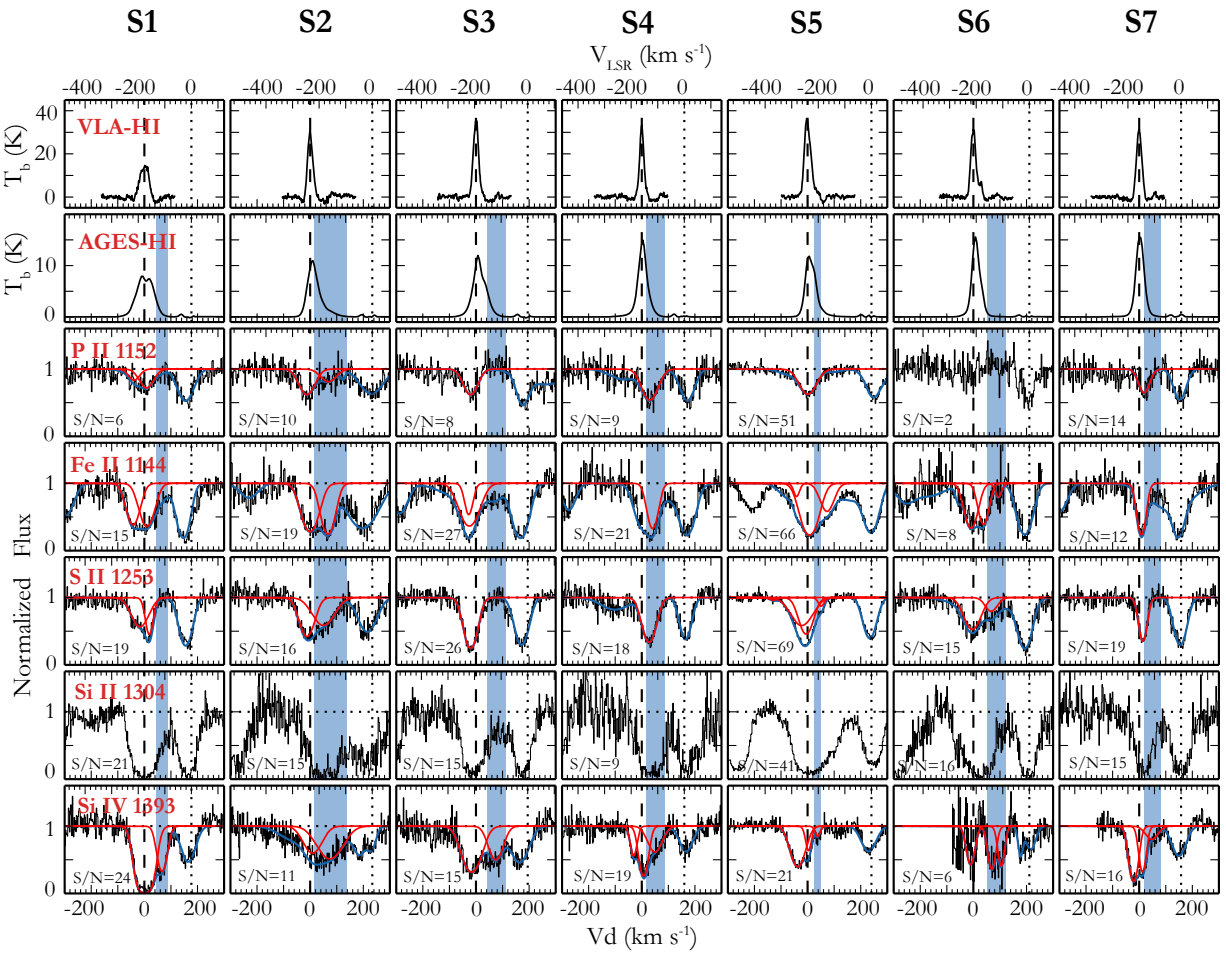

Figure 5.3: The first and second row show the H I 21-cm spectra from the VLA and the AGES, respectively. Note that the brightness temperature T_b is on a different scale. The bottom four rows show the continuum-normalized *HST*/COS spectra of P II λ1152, Fe II λ1144, S II λ1253, and Si IV λ1393. Velocity on the bottom x-axis, v_d, is with respect to the M33 gas disk rotation velocity at the position of each sightline (see § 5.2.4); velocity on the top x-axis in the LSR frame at solar circle. The absorption lines from M33's ISM with $v_d = 0$ km s^{-1} are shown by dashed lines, while those from MW's ISM with $v_{LSR} = 0$ km s^{-1} are indicated by dotted lines. The red curves in each panel indicate the Voigt-profile fitted components, while the underlying blue curves show the overall fitted profiles including additional nuisance components. For example, the M33 Fe II λ1144 along S4 is blended with the MW Fe II λ1143, thus a nuisance is added at $v_d \sim 0$ km s^{-1}. The blue shaded areas highlight the redshifted non-disk Si IV components (§ 5.3). The S/N ratio of each line is shown in the bottom left corner, which is measured locally using the line-free normalized continuum region near the absorption line. It is the rms dispersion over one resolution element. For FUV XDL detector, one resolution element consists of six pixels in segment A and ten pixels in segment B (COS instrument handbook; Debes & et al. 2016).

For S1 and S7, neither a direct measurement of E(B-V) nor an intrinsic color $(B\text{-}V)_0$ can be found in the literature. We calculate their E(B-V) as follows. We first infer $(B\text{-}V)_0$ for S1 and S7 by searching for WR stars in LMC that have the same spectral type WN9 as S1 and S7. We found two WN9-type stars (BR18 and BR64) with color excess of E(b-v)=0.12 mag and 0.31 mag, respectively (Breysacher 1981; Torres-Dodgen & Massey 1988). Using E(B-V)=1.21×E(b-v) (Turner 1982; Torres-Dodgen & Massey 1988), we obtain E(B-V)=0.15 (0.38) mag for star BR18 (BR64). Knowing that the observed color (B-V) of these two stars are -0.16 mag and 0.06 mag respectively, we find the intrinsic color $(B\text{-}V)_0$=-0.32 mag for S1 and S7. Then taking into account the observed (B-V) values of S1 and S7, and correcting for foreground Galactic extinction, we find their E(B-V)=0.07 mag and 0.15 mag, respectively.

We note that the log $N_{\rm HI}$ value along S5 has been determined by Lebouteiller (2006; henceforth L06) in a study of the neutral ISM of M33. L06 observed Lyβ (Lyα) with the *FUSE* (*IUE*) instrument, and found log $N_{\rm HI}$ = 20.75 ± 0.3 (log $N_{\rm HI}$ = $21.07^{+0.17}_{-0.24}$) by fitting the damping wing of the saturated Lyβ (Lyα) along S5. These values are similar to our MW-like value for S5 (log $N_{\rm H}$ = 21.1) derived using the E(B-V) method, but significantly lower than the LMC- and SMC-like numbers, as shown in Table 5.3. The difference is not likely due to a significant presence of H_2, since L06 found only a small contribution from molecular gas along S5, log $N_{\rm H_2}$ = 16.86, from H_2 absorption lines in the *FUSE* spectra. We suggest that the log $N_{\rm HI}$ estimates from L06 may be lower limits due to: (1) contamination by complicated stellar O VI (N V) P-Cygni profiles contaminating the Lyβ (Lyα) damping wings and, (2) saturated Lyβ (Lyα) absorption due to MW's ISM separated from M33's ISM absorption by only $\sim$ 200 km s^{-1}. While our MW-like value is consistent with their

estimates within the uncertainty, such a comparison may not be overly informative due to the unavoidably large systematic uncertainties inherent in both methods.

5.3 General Ion Properties

In this section, we discuss the ion properties as inferred from the Voigt-profile fitting. In row 3 – 7 of Figure 5.3, we show the continuum-normalized absorption lines of P II, Fe II, S II, Si II, and Si IV[**]. Among these transition lines, P II, Fe II, S II, and Si IV are not saturated, thus they are fitted with Voigt profiles as discussed in § 5.2.3. Si II λ1304 is not Voigt-profile fitted since this line has saturated core at $v_{\rm d} \sim 0$ km s^{-1} along each sightline. We do not show other Si II lines or C II, Si III lines in Figure 5.3 because they are all heavily saturated and blended both at the velocity of M33's ISM as well as MW's ISM; therefore, they are not informative in evaluating the ion properties at intermediate velocities as we show in the following. For an inspection of these saturated lines, please see Figures 1 and 7.

Since Si IV requires $\sim$ 33.5eV to ionize from Si III, while S II, P II, Fe II, and Si II only need $\sim$ 10eV to produce from their neutral forms, hereafter we address Si IV as the "warm ion" and, S II, P II, Fe II, and Si II the "cool ions"[††]. Both the warm and cool ions show strong absorption lines from MW's ISM at $v_{\rm d} \gtrsim 150$ km s^{-1} ($v_{\rm LSR} \sim 0$ km s^{-1}), as noted by the dotted lines in Figure 5.3. The M33-associated absorption lines are at $v_{\rm d} \sim 0$ km s^{-1} ($v_{\rm LSR} \lesssim -150$ km s^{-1}), consistent with the peaks of the corresponding H I 21-cm emission

[**]Note that absorption lines of S II, Fe II, Si II, and Si IV are actually multiplets; in Figure 5.3 we only show one line for each ion for clarity. A full display of all the lines can be found in Figure 7.

[††]The "warm" and "cool" do not necessarily correspond to the temperature ranges used by other authors (e.g., Werk et al. 2014); we use the two terms here to reflect the different ionization states of the ions.

from M33's ISM (row 1–2). In the following, we summarize the main properties of the M33-associated absorption lines:

1. On all sightlines, apart from the $v_{\rm d} \sim 0$ km s^{-1} components associated with M33's ISM, we fit additional velocity component(s) at intermediate velocities to the warm and cool ion lines. We find that the warm ion Si IV consistently shows additional absorption components along each sightline, with $v_{\rm d}$ ranging from +39 km s^{-1} to +106 km s^{-1} (indicated by "*" sign in Table 5.2). The mean value is $v_{\rm d}$ = +67 km s^{-1}. Once corrected for inclination, this corresponds to a warm-ionized inflow toward M33 at +67/cos(56°) $\sim$ +120 km s^{-1} (shown by the dotted line in the left panel of Figure 5.4; see point 7). In Figure 5.3, we highlight these Si IV components with intermediate velocities in blue. We also find absorption features at similar intermediate velocities in cool ions, such as those ions along S6 and Fe II along S5, although they do not consistently exist among all the sightlines. Since these intermediate-velocity absorption components have mean $v_{\rm d}$(= +67 km s^{-1}) noticeably separated from the M33's ISM absorption ($v_{\rm d} \sim 0$ km s^{-1}), hereafter we call these features the "non-disk" components. And we call the absorption components at $v_d \sim 0$ km s^{-1} the "disk" components. *The consistently present non-disk components in Si IV suggests that there exists a disk-wide, warm-ionized gas accreting toward M33.* This accreting flow is most likely multi-phase, as the non-disk components can also be observed in the cool ions (Fe II, S II, and P II) along some sightlines, and may as well be commonly present in saturated C II, Si II, and Si III lines (also see Point 3).

2. The AGES H I 21-cm spectra in row 2 show extended H I wings at the intermediate

velocities where the non-disk Si IV are detected, also supporting the multi-phase scenario of the accreting gas. The VLA spectra on the top row indicate there may be some H I emission within the highlighted ranges; however, after fitting baselines and checking the sensitivity of the VLA data, we find there is no signal above the noise level given by Gratier et al. (2010).

3. The saturated ions (i.e., Si II, Si III, and C II) are consistent with the accreting flow being multi-phase. In row 6, we show the continuum-normalized profiles of Si II λ1304 (night-only data). We do not Voigt-profile fit this line as the core is saturated. Along some sightlines (e.g., S1, S3, S6) where the non-disk velocity ranges (blue shades) fall out of the core, we find significant Si II absorption, consistent with the non-disk Si IV components.

4. The line profiles and line widths of the non-disk Si IV components vary from sightline to sightline. Such discrepancy is unlikely due to contamination by stellar winds since those stellar features are much broader and have been fitted as continua (see § 5.2.3). In addition, the continuum-normalized Si IV $\lambda\lambda$1393, 1402 show similar line profiles despite their different wavelengths (see Figure 7), which also suggests that local stellar features are unlikely to cause the variation seen in the data.

5. S6 shows two non-disk Si IV components. With limited S/N ratio (=6), it is less certain whether the line has one broad component or two narrower ones but, in general, both components are consistent with the non-disk components seen along other sightlines. S6 is of particular interest since within the Si IV non-disk velocity

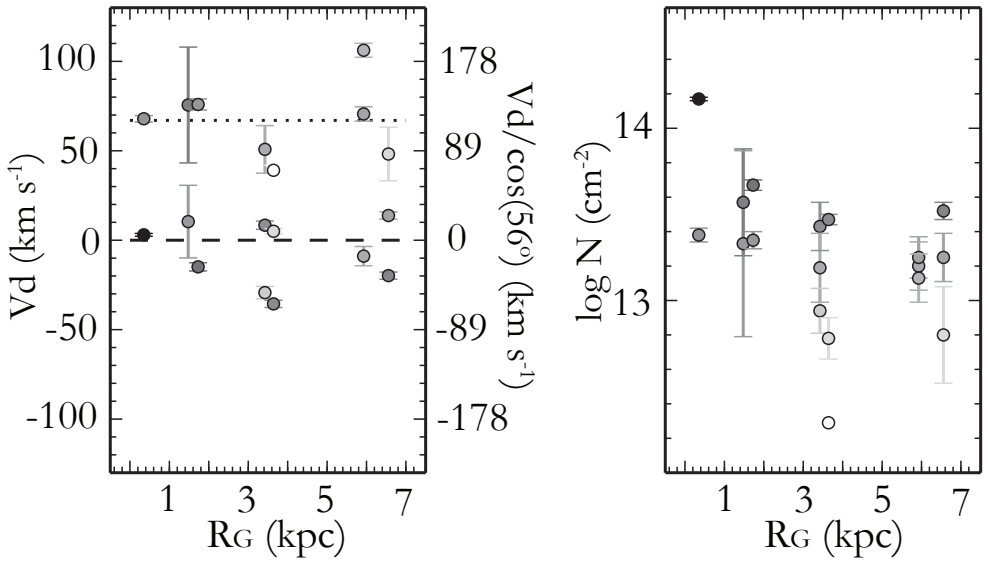

Figure 5.4: Radial distribution of $v_{\rm d}$ (left) and log N (right) for Si IV. Data points are color-coded in gray scale such that darker color means larger log N. The $R_{\rm G}$ on the x-axis shows the inclination-corrected galactocentric distance. In the left panel, the left y-axis indicates the observed/projected velocity for each absorption component $v_{\rm d}$ while the right y-axis shows the inclination-corrected values $v_{\rm d}$/cos(56°). The dotted line shows the mean velocity $v_{\rm d}$=+67 km s^{-1} (or +67/cos(56°) $\sim$ +120 km s^{-1} if corrected for inclination) of the non-disk Si IV components.

range, its H I 21-cm spectrum shows the least contamination from the dominant disk emission. We make use of this sightline to calculate the H I column density of the non-disk component in § 5.6.2.

6. In Table 5.2, we show the Voigt-profile fitted ($v_{\rm d}$, b, log N) for each sightline. For the warm ion Si IV, the non-disk component has mean $\langle N_{\rm SiIV}\rangle = 10^{13.24\pm0.21}$ cm^{-2}, and the disk component has $\langle N_{\rm SiIV}\rangle = 10^{13.55\pm0.08}$ cm^{-2}. As a comparison, we find that MW IVCs have $\langle N_{\rm SiIV}\rangle = 10^{13.17\pm0.07}$ cm^{-2} (Shull et al. 2009), which suggests the non-disk Si IV components of M33 are consistent with IVC-like clouds. For the cool ions, we find mean column densities of $\langle N_{\rm SiII}\rangle = 10^{15.07\pm0.04}$ cm^{-2}, $\langle N_{\rm FeII}\rangle = 10^{14.34\pm0.04}$ cm^{-2} and $\langle N_{\rm PII}\rangle = 10^{13.55\pm0.06}$ cm^{-2}, respectively, taking into account both the disk and non-disk components. The Voigt-profile fits of these cool ions show considerably large b

values along a few sightlines, which might result from the COS spectral resolution that fails to resolve underlying narrower components.

7. Specifically, we show the radial distribution of $v_{\rm d}$ and log N of the warm ion Si IV in Figure 5.4. Each data point is color-coded in gray scale according to its log N: darker color means higher log N. For example, at $R_{\rm G} \sim 0.5$ kpc, a Si IV component with $v_{\rm d} \sim 0$ km s^{-1} in the left panel can be found with log $N \sim 14.2$ cm^{-2} in the right. Clearly Si IV shows a significant asymmetric distribution of $v_{\rm d}$ toward positive (inflow) velocities. Along each sightline, the disk component generally has larger column density than the non-disk component. We also examine the radial distribution $v_{\rm d}$ and log N for the cool ions S II, P II, and Fe II. Their centroid velocities $v_{\rm d}$ mostly concentrate near $v_{\rm d} \sim 0$ km s^{-1}, and there is no obvious radial trend in column density.

Apart from the disk-wide accreting flow detected in the warm ion Si IV, our sightlines show some low-velocity, blue-shifted components with $-40 \lesssim v_{\rm d} \lesssim 0$ km s^{-1} in both warm and cool ions, indicating a tentative detection of slow winds or disk turbulence in M33; we discuss this in § 5.7.3.1. In addition, we find a very high-velocity absorption feature with $-200 \lesssim v_{\rm d} \lesssim -100$ km s^{-1} (or $v_{\rm LSR} \sim -350$ km s^{-1}) in C II, Si II, and Si III. This could potentially be the outflows from M33, however, the scenario is complicated by other origin possibilities as discussed in § 5.7.3.2 and Appendix 6.

We note that the same COS spectrum of S1 was analyzed by Welsh & Lallement (2013; henceforth WL13), finding multiple narrow components in cool ions for which we are only be able to fit broad Voigt-profiles. In their work, the multiple narrow-component

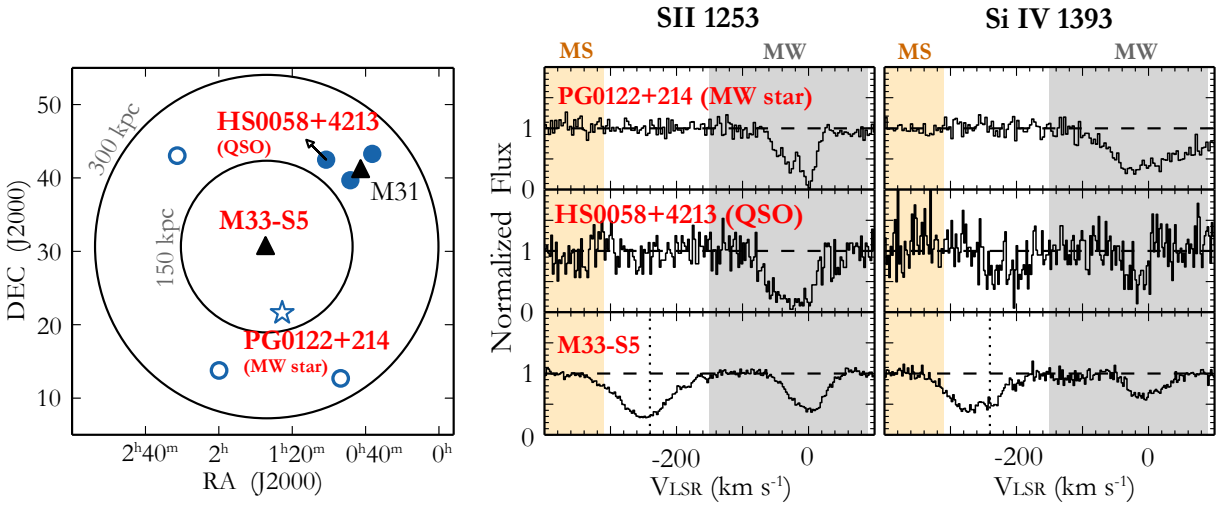

Figure 5.5: Left: The positions of the MW halo star PG0122+214 (open star), QSO sightlines (open and solid circles) within ~ 300 kpc of M33, the M31 disk (triangle), and S5 toward M33 are shown. The M33 sightlines S1–S7 are at almost the same spot as S5. For QSO sightlines, solid (open) circles indicate detection (non-detection) of Si IV at $v_{\rm LSR} < -150$ km s^{-1}; we show one of the QSOs (HS0058+4213) spectra in the middle row of the right panel. Right: Normalized S II λ1253 and Si IV λ1393 absorption lines of the MW halo star PG0122+214 (top), of the QSO HS0058+4213 (middle), and of M33-S5 (bottom). Note that the velocities of these spectra are in the LSR frame. Our M33 absorption lines appear at $v_{\rm LSR} \lesssim -180$ km s^{-1} while the MW's absorption lines are at $v_{\rm LSR} \geq -90$ km s^{-1}. The dotted lines in the bottom indicate the systemic velocity ($v_{\rm LSR} = -240.3$ km s^{-1}) of M33's gas disk at the position of sightline S5 (Table 5.1). The highlighted light yellow and gray shades are the "MS-related" and "MW-related" components as defined in Lehner et al. (2015).

fits were achieved by restricting five components at fixed velocities (varying by only ±10 km s^{-1}) as indicated from Ca II lines (Welsh et al. 2009). Since it is unclear whether the Ca II-bearing gas and the low-ion-bearing gas are kinematically similar, this fixed-velocity fitting procedure is likely to lead to artificial components. Therefore, we do not compare our component fits to the results shown in WL13. In addition, we note that their continuum fittings for O I λ1302 and Si II λ1304 are inaccurate due to the omission of recognizing the air-glow emissions at nearby location. We provide in Figure 1 the night-only spectra of Si II λ1304, which are weaker than those shown in WL13.

5.4 Association of The Non-Disk Components with M33

As we show in § 5.3, we find consistently redshifted non-disk components in Si IV, suggesting that there exists a disk-wide, warm-ionized accreting flow toward M33. The accreting flow is most likely multi-phase as non-disk components can also be seen in cool ions (Fe II, S II, and P II) along some sightlines and may as well commonly exist in saturated C II, Si II, and Si III lines. The non-disk components follow the overall rotation of M33 and are almost certainly associated with this galaxy; however, given the Local Group spatial and kinematic environment, other sources should be considered. Apart from the M33 disk-halo accreting layer and M33 halo cloud scenarios modeled in § 5.5, here we focus on the possibilities of ion absorbers from MW's ISM, MW HVCs, the Magellanic Stream, or M31's CGM.

First, MW's ISM and the Magellanic Stream are unlikely to have created the absorption lines. We show in Figure 5.5 that, in the LSR frame, MW's ISM is at only a few tens of km s^{-1} and the Magellanic Stream is at -310 to -450 km s^{-1} in directions near M33 as shown in Figure 5.5 (Fox et al. 2014; Lehner et al. 2015). Our M33 absorption lines fall in between these two velocity ranges.

Second, absorbers from MW HVCs are unlikely intercepting our sightlines toward M33 at the intermediate velocities. We compare our spectra with those from a nearby MW halo star, PG0122+214, which is at a distance $\sim$ 10 kpc from us. In the right panel of Figure 5.5, we display the S II and Si IV lines[‡‡] from PG0122+214 in the top row, and those from sightline S5 toward M33 in the bottom row; clearly the MW halo star does not

[‡‡]We use S II λ1253 and Si IV λ1393 because 1. they generally have high S/N than other ion lines, and 2. they have higher oscillator strengths among their available multiplets.

have S II and Si IV absorption lines at $v_{\rm LSR} < -150$ km s^{-1} where M33-S5 shows strong absorption. Since the angular separation between PG0122+214 and M33-S5 is only $\sim 9°$, if there exists an HVC within 10 kpc of the MW halo that covers all our M33 sightlines but not PG0122+214, the HVC's physical size should only be $\lesssim 1.6$ kpc. This is contrary to current knowledge of classic MW HVCs, which finds them to be large H I complexes (Wakker & van Woerden 1991) with extended ionized gas (e.g., Lehner & Howk 2011b; Fox et al. 2004). Thus, within 10 kpc there are no MW HVCs with $v_{\rm LSR} < -150$ km s^{-1} in direction toward M33. In addition, MW HVCs beyond 10 kpc are unlikely as we do not find relevant strong absorption from nearby QSOs (shown as open circles in Figure 5.5).

Third, we investigate the situation that the non-disk warm and cool absorbers are from M31's CGM. We examine the QSO sightlines that are within 300 kpc of M33. These sightlines were studied by Lehner et al. (2015), who found three QSO sightlines (solid circle in Figure 5.5) with M31-related Si IV absorption within 50 kpc of M31's disk, while others beyond this radius (open circles) do not have significant detection. In the middle row of the right panel, we plot the S II and Si IV lines from HS0058+4213 – one of the three QSOs with M31-related Si IV detection. The S II line does not show absorption at M33's velocity while the Si IV does indicate some overlap at $v_{\rm LSR} \sim -240$ km s^{-1}. The Si IV column density of the overlapped portion along this QSO sightline is $\sim 10^{13.1}$ cm^{-2} (Lehner et al. 2015), lower than the mean non-disk Si IV value ($10^{13.24}$ cm^{-2}) that we have found toward M33. Given that our M33 sightlines are $\gtrsim 200$ kpc from M31, we expect the Si IV column density of M31's CGM should be lower than $\sim 10^{13.1}$ cm^{-2} at M33's position, as inferred from other CGM studies (e.g., Werk et al. 2013). Our strong detection of the

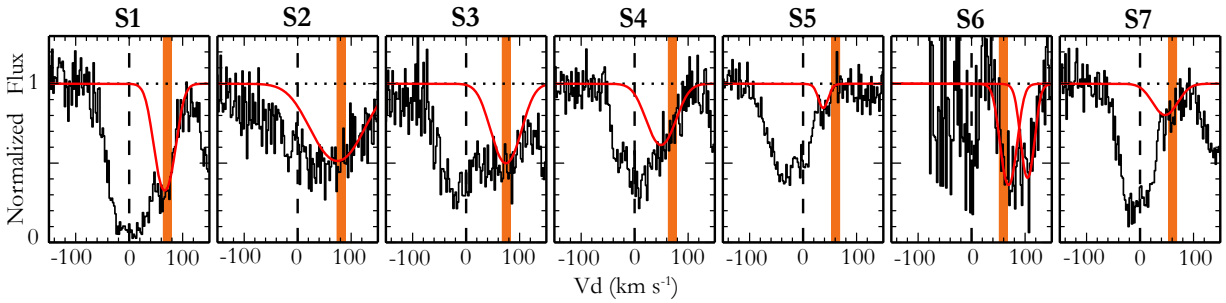

Figure 5.6: The Voigt-profile fitted non-disk Si IV components (red curves) and the model-predicted centroid velocities (vertical lines) from the Accreting Layer model. The Si IV spectra and the fitted Voigt-profiles are the same as those in Figure 5.3.

non-disk Si IV toward M33 suggests that the M31 origin is highly unlikely. In addition, the fact that our Si IV lines clearly follow the rotation of M33 disk as modelled in § 5.5 also state their association with M33.

To conclude, we find that the non-disk warm and cool absorption lines we have observed are unlikely to be associated with MW's ISM, MW HVCs, the Magellanic Stream, or the M31 halo. In the next section, we perform kinematic modeling and study if the ions could be related to the M33 disk-halo interface or a gas cloud in the M33 halo.

5.5 Kinematic Modeling

In this section, we model the kinematics of the accreting flows onto M33 as observed in warm and cool ions. Since the red-shifted, non-disk components are consistently found in Si IV, they provide a complete picture of the flows across the disk and we hereafter focus our analysis on Si IV lines. We consider two scenarios: 1) an accreting layer on top of M33's gas disk, representing the disk-halo interface, and 2) a cloud in the halo of M33 that intercepts all of our sightlines. Hereafter, we refer to these two models as the "Accreting

Layer" model and the "M33 Halo Cloud" model.

5.5.1 The Accreting Layer Model

The Accreting Layer model is a layer of warm ionized gas at the disk-halo interface of M33 moving toward the disk. It starts with an H I tilted-ring model (Corbelli & Schneider 1997), simulating the H I disk of M33 as a set of concentric tilted rings with each ring gradually differing in inclination, position angle and rotation velocity. The model recovers the velocity field of the H I disk. We then lift the whole set of tilted rings to some height above the disk to represent the accreting layer.

Using polar coordinates that originate from the disk center, the line of sight velocity $v(r, \theta)$ of a parcel of ionized gas at position (r, θ) in the accreting layer can be written as,

$$\begin{aligned} v(r,\theta) &= v(r) cos\theta sin\phi(r) + v_{\rm acc} cos\phi(r) \\ v(r) &= (v_\infty + v_{\rm lag} z_{\rm acc}) tanh(r/\Delta_v) \end{aligned} \tag{5.2}$$

where v_∞ is the rotation velocity of the gas disk at infinity, Δ_v is the difference of the rotational velocity between adjacent tilted rings, and $\phi(r)$ is the inclination of each tilted ring. We adopt $\phi(r) \approx \phi_{\rm M33}$ =56°, since $\phi(r)$ varies very little within the star-forming disk. We refer the reader to the work by Corbelli & Schneider (1997) for a detailed discussion of each of these parameters.

The Accreting Layer model differs from the tilted ring model in that it includes three additional parameters, $v_{\rm acc}$, $z_{\rm acc}$, and $v_{\rm lag}$. $v_{\rm acc}$ is the inflow velocity of the accreting layer perpendicular to the gas disk. We do not model $v_{\rm acc}$ faster than $\sim$ 180 km s^{-1} as beyond

this velocity the absorbers would be obscured by absorption from MW's ISM. Note that we use a positive sign for the accretion velocities in our modeling. $z_{\rm acc}$ is the height of the layer above the disk. $v_{\rm lag}$ is the drop-off of the rotation velocity above the disk plane (halo lagging). Here, we model the accreting layer with $v_{\rm lag}$ = 0 km s^{-1} kpc^{-1} (non-halo-lagging) and, with $v_{\rm lag}$ = −15 km s^{-1} kpc^{-1} (halo-lagging) which is a typical value found from observations of the MW and external edge-on galaxies, as well as from numerical simulations (Levine et al. 2008; Marasco & Fraternali 2011; Marasco et al. 2012).

The model predicts line-of-sight velocity $v_{\rm l,\,i}$ of the layer at the position of each sightline with i representing the sightline ID 1–7. We compare $v_{\rm l,\,i}$ with the observed centroid velocity $v_{\rm d,\,i}$ of the non-disk Si IV components along each sightline, and use χ^2 minimization to find the best fit parameters ($v_{\rm acc}$, $z_{\rm acc}$, $v_{\rm lag}$). The χ^2 is computed as,

$$\chi^2 = \sum_{\rm i=1}^{\rm M=7} \frac{(v_{\rm l,\,i} - v_{\rm d,\,i})^2}{\sigma_{\rm cos}^2 + \sigma_{\rm d,\,i}^2} \tag{5.3}$$

where $\sigma_{\rm cos}$ = 15 km s^{-1} is the COS velocity calibration uncertainty, and $\sigma_{\rm d,\,i}$ is the uncertainty of velocity centroid from the Voigt-profile fitting[§§]. We find that for the non-halo-lagging case ($v_{\rm lag}$ = 0 km s^{-1} kpc^{-1}), the minimum χ^2 is reached when $v_{\rm acc}$ = 110 km s^{-1}, $z_{\rm acc}$ =1.5 kpc; its reduced χ^2 value is $\chi^2_{\rm red}$ =1.3, indicating a good fit. The halo-lagging case ($v_{\rm lag}$ = −15 km s^{-1} kpc^{-1}) finds similar results, suggesting our models are not sensitive to velocity drop-off with z-height at the disk-halo interface of M33. Hereafter we only discuss the non-halo-lagging case.

[§§]S6 has two non-disk components: one is at v_1 = 70.6±4.0 km s^{-1}, and the other at v_2 = 106.2±3.9 km s^{-1}. For the kinematic model fitting, we use a mean value $\langle v \rangle$ = 88.4 km s^{-1}, and calculate its 1σ value through error propagation $\sigma_{\rm d,\,6} = \frac{1}{2}\sqrt{3.9^2 + 4.0^2}$ km s^{-1}

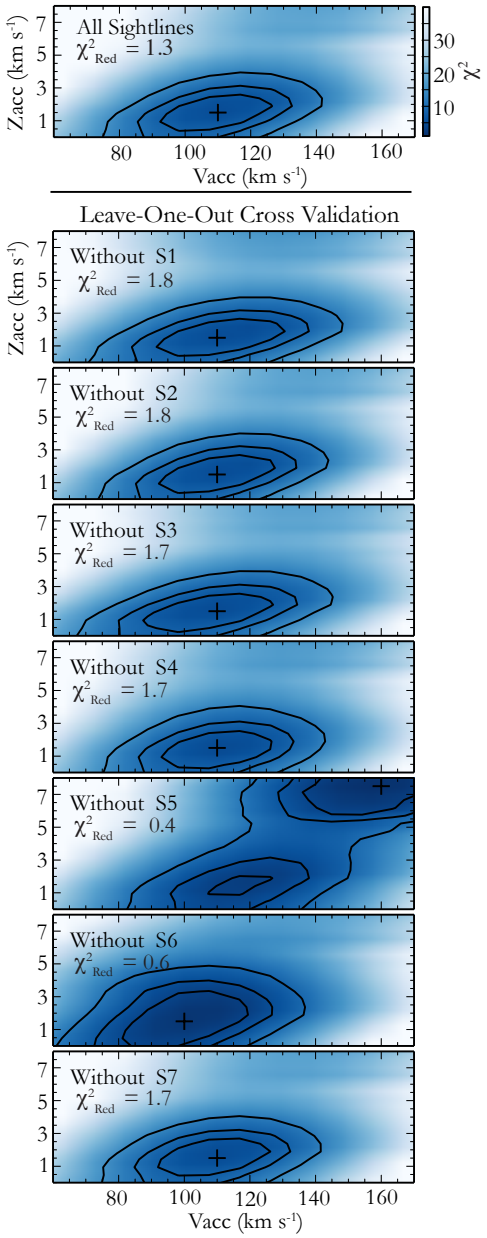

Figure 5.7: The top panel shows the χ^2 distribution of the non-halo-lagging case of the Accreting Layer model using all the sightlines. The minimum χ^2 value is indicated by a cross, and its $\chi^2_{\rm red}$ value is shown in the top left corner. Contours represent 1/2/3 σ (68%/95%/99%) confidence levels. The bottom seven panels show the LOOCV of the model as described in § 5.5.1; color-coding and labeling are the same as the top panel.

In Figure 5.6, we show the performance of the best fit model that has $v_{\rm acc}$ = 110 km s^{-1} and $z_{\rm acc}$ = 1.5 kpc. The figure visualizes the model-predicted velocity $v_{\rm l,\,i}$ of each sightline

in comparison with the respective Voigt-profile fitted non-disk component of Si IV. The model shows a good match with the observed spectra, except that along S6 the model favors the lower velocity component and along S5 the model indicates an absorption component with velocity $\sim$ 20 km s^{-1} higher than that of the observed.

The top panel in Figure 5.7 shows the distribution of χ^2 as a function of $v_{\rm acc}$ and $z_{\rm acc}$ for the non-halo-lagging case. Contours indicate the confidence limits (P= 0.68/0.95/0.99) for the best fit model with $v_{\rm acc}$ = 110 km s^{-1} and $z_{\rm acc}$ =1.5 kpc. The probability P that the minimum $\chi^2_{\rm red}$ has a certain increment δ_α can be expressed as

$$\text{Probability}(\chi^2_{\rm red} - \chi^2_{\rm red,min} \leq \delta) \equiv \text{P} \tag{5.4}$$

. At confidence limits of P= 0.68 (1σ), 0.95 (2σ) and 0.99 (3σ), the increment δ is 2.30, 4.61, 9.21 for a model with 2 parameters (Avni 1976). The top panel in Figure 5.7 shows that at 1 σ confidence level, the best fit parameters are $v_{\rm acc} = 110^{+15}_{-20}$ km s^{-1} and $z_{\rm acc} = 1.5^{+1.0}_{-1.0}$ kpc.

We use the Leave-One-Out Cross Validation (LOOCV) to evaluate the robustness of our model fitting. The method is performed by training the model parameters ($v_{\rm acc}$, $z_{\rm acc}$) using all the sightlines except for one that will be treated as a validation set. When the best fit parameters are found, a prediction is made for the sightline in the validation set; a good set of parameters will predict a velocity similar to the observed one of the validating sightline. In general, this method tests whether the best fit parameters are sensitive to certain sightline(s). We perform LOOCV seven times, each with six sightlines in the training set and the remaining one in the validation set. Every time when a $\chi^2_{\rm red,min}$ value is found at certain ($v_{\rm acc}$, $z_{\rm acc}$), we check if these parameters predict a velocity that

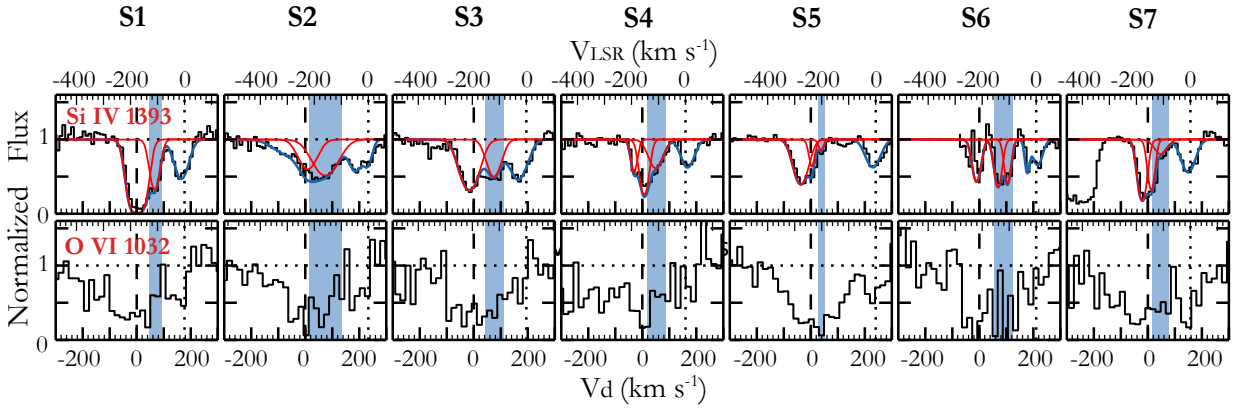

Figure 5.8: The Si IV spectra from *HST*/COS (top) compared to the O VI lines observed by *FUSE* (bottom). The absorption lines from M33's ISM with $v_{\rm d} = 0$ km s^{-1} are shown by dashed lines, while those from MW's ISM with $v_{\rm LSR} = 0$ km s^{-1} are indicated by dotted lines. The O VI spectra have been binned by five pixels to increase the S/N. The Si IV spectra and the fitted Voigt-profiles are the same as those in Figure 5.3, but binned by five pixels here to keep the consistency with the *FUSE* O VI spectra. The blue patch in each panel highlights the non-disk Si IV components.

matches the observed velocity of the validating sightline.

The result of LOOCV is shown in panels 2–8 of Figure 5.7. It is shown that when S1/S2/S3/S4/S6/S7 are individually used as the validation set, the model prediction and its χ^2 distribution are very similar to the result ran with all the sightlines (the top panel), and for each experiment the predicted velocity and the observed of the validation sightline show a good match. However, when adopting S5 as the validation set (panel 5), the χ^2 distribution changes dramatically. It predicts two possible minimum χ^2 values: one is similar to that in other panels while the other indicates some fast-moving medium at higher z height. We find that the former can reproduce the centroid velocity as observed in S5, while the latter one fails. This indicates that S5, and its clear non-detection of Si IV above $v_{\rm d} \sim 50$ km s^{-1}, is critical for our model fitting in distinguishing different scenarios and it justifies that the original best-fit parameters are robust.

To conclude, we find the observed centroid velocities of the non-disk Si IV compo-

nents can be well reproduced by assuming an accreting layer at the disk-halo interface of M33. The Accreting Layer model finds the best fit parameters at $v_{\rm acc} = 110^{+15}_{-20}$ km s^{-1} and $z_{\rm acc} = 1.5^{+1.0}_{-1.0}$ kpc.

5.5.2 The M33 Halo Cloud Model

Alternatively, we consider an M33 halo cloud may exist and cause the non-disk absorption features. We assume the cloud is large enough to cover all the sightlines and, there is no velocity variation across the cloud. If the cloud is at a distance of 10 kpc from the M33 disk, its size should be $\sim$ 7.5 kpc; if it is 100 kpc away in M33's halo, its size reduces to $\sim$ 6.5 kpc.

We vary the velocity of the halo cloud toward M33 ($v_{\rm hc}$) and calculate the model-predicted absorption velocity at the position of each sightline. Since the cloud is far from the M33 disk, its velocity is not influenced by the disk rotation; therefore, the potential absorption lines along different sightlines created by this halo cloud should have the same velocities in the LSR frame. We derive the χ^2 value between the predicted and the observed velocities using Eq 5.3 and study the overall χ^2 distribution. The best fit model is found at $v_{\rm hc} = 45^{+10}_{-5}$ km s^{-1} with a minimum χ^2 of 27.07 and the corresponding $\chi^2_{\rm red,min}$ of 5.41. This indicates an M33 halo cloud with a uniform velocity does not yield a good fit to the non-disk Si IV component absorption lines. This is because the velocities of our detected non-disk Si IV components consistently indicate the influences of the M33 rotation, a disk-wide, different velocity pattern that an M33 cloud in the distant halo with only uniform velocity would not be able to reproduce.

With our limited number of sightlines, we are unable to place further constraints on whether a non-uniform cloud would cause the observed absorption lines. Different velocity fields across the cloud surface and potentially arbitrary turbulent velocities may cause the variation of centroid velocity seen in the non-disk Si IV components. In addition, future models that incorporate the clumpiness of the halo cloud would be helpful since density variation has been intentionally excluded in our kinematic modeling.

5.6 Ionization Condition and Gas-Phase Abundances

In this section, we investigate the ionization sources and the gas metallicity of the accreting flow. Specifically, we study the properties of the non-disk Si IV components since they are consistently found among all the sightlines and their accreting velocities are well reproduced by the Accreting Layer model. In § 5.6.1 we assess the role of shocks and collisional ionization in creating the non-disk Si IV components. In § 5.6.2 and 5.6.3 we put constraints on the metallicity of the non-disk gas at the disk-halo interface and the ISM of M33, respectively. This helps to determine whether the disk-halo gas has been metal-enriched.

5.6.1 The Ionization Mechanism of Si IV

The accreting layer discussed in the previous section well reproduces the observed velocities of the non-disk Si IV components. In this model, shocks could be induced as the disk-halo gas accretes at a velocity of $v_{\rm acc}$ = 110 km s^{-1} onto the disk and, Allen et al. (2008)

showed that slow radiative shocks moving at $v_s \lesssim$170 km s^{-1} would produce collisionally ionized gas behind the shocks (see also Dopita & Sutherland 1996). This is of particular interest as we find that the Si IV absorption-line profiles are similar to those of the O VI despite the difference of aperture size of *HST*/COS and *FUSE* data (see Figure 5.8). The similarity between the profiles may suggest some physical connection. Since Si IV requires 34 eV to produce while O VI needs 114 eV, it is unlikely both ions are created under the same ionization conditions; however, it is worth considering whether these two ions are created by collisional ionization behind shocked gas as the accreting layer plummets toward the disk.

In their models, Allen et al. (2008) predicted ion column densities as a function of shock velocity, gas metallicity, gas density, and magnetic field strength. Their models show that for $v_s \lesssim 170$ km s^{-1}, the O VI column density is $\lesssim 10^{14.0}$ cm^{-2} while the Si IV column density is $\lesssim 10^{12.30}$ cm^{-2}. As a comparison, we calculate the Si IV and O VI column densities of the non-disk gas which are highlighted in blue in Figure 5.8. For Si IV, the column densities can be found in Table 5.2; for O VI, the column densities are integrated over the highlighted velocity ranges using the AOD method[¶¶] (see Appendix 6; Savage & Sembach 1996). The mean values are $\langle N_{\rm SiIV} \rangle = 10^{13.24}$ cm^{-2} and $\langle N_{\rm OVI} \rangle = 10^{14.16}$ cm^{-2}, both larger than those predicted by shock models, suggesting that shocks are not the dominant mechanism in creating these two ions.

From a broader point of view, we investigate whether general collisional ionization processes could be the dominant producer of Si IV at the disk-halo interface. It has been

[¶¶]The quality of the *FUSE* spectra does not allow for a reliable Voigt-profile decomposition of the O VI line profiles.

suggested that if an ion is collisionally ionized in radiatively cooling flows, its total column density is proportional to the Doppler width b of the corresponding absorption lines (e.g., Heckman et al. 2002; Lehner et al. 2011). Following Heckman et al. (2002) and Lehner et al. (2011), the column density of an ion X_i in a cooling flow is $N_{X_i} = v_{cool} t_{cool} n_{cool}$, where v_{cool} is the velocity, t_{cool} the cooling time, and n_{cool} the number density. Assuming the ideal gas law and introducing the cooling function Λ to solve for t_{cool} and n_{cool}, one would find $N_{X_i} = 4.34 \times (3/2 + s) k_B T v_{cool} \frac{Z f_i}{\Lambda}$, where s equals to 0 (1) for isochoric (isobaric) cooling, f_i the gas fraction of the corresponding ion, and Z the metallicity. Heckman et al. (2002) suggested that v_{cool} could be identified as the non-thermal broadening b_{nth} such that the Doppler width is $b^2 = b_{th}^2 + b_{nth}^2 = 2k_B T/A m_p + v_{cool}^2$, where A is the mass number and m_p the proton mass. Combining the above equations to solve for N_{X_i} and b, an analytical relation can be laid out as

$$N_{X_i} = 4.34 \times (3/2 + s) k_B T \sqrt{b^2 - \frac{2k_B T}{A m_p}} \frac{Z f_i}{\Lambda}. \tag{5.5}$$

To test whether the non-disk Si IV can be produced under collisional ionization, we compare the observed log N_{SiIV} and b with the theoretical relation from Eq 5.5 in Figure 5.9. The Λ and f_i values are from Gnat & Sternberg (2007) assuming collisional ionization equilibrium (CIE) and $Z = 0.1\ Z_\odot$ is adopted which is within the metallicity range we derive in the following section. Figure 5.9 shows that in both cases, log N_{SiIV} increases as b becomes larger. For the CIE models, Si IV is mostly produced when log T is 4.8 K, the temperature at which Si IV collisional ionization fraction reaches its maximum (Gnat & Sternberg 2007). However, even the highest production of Si IV from the CIE modeling is still $\sim$ 0.5 dex less than the vast majority of the observed data points.

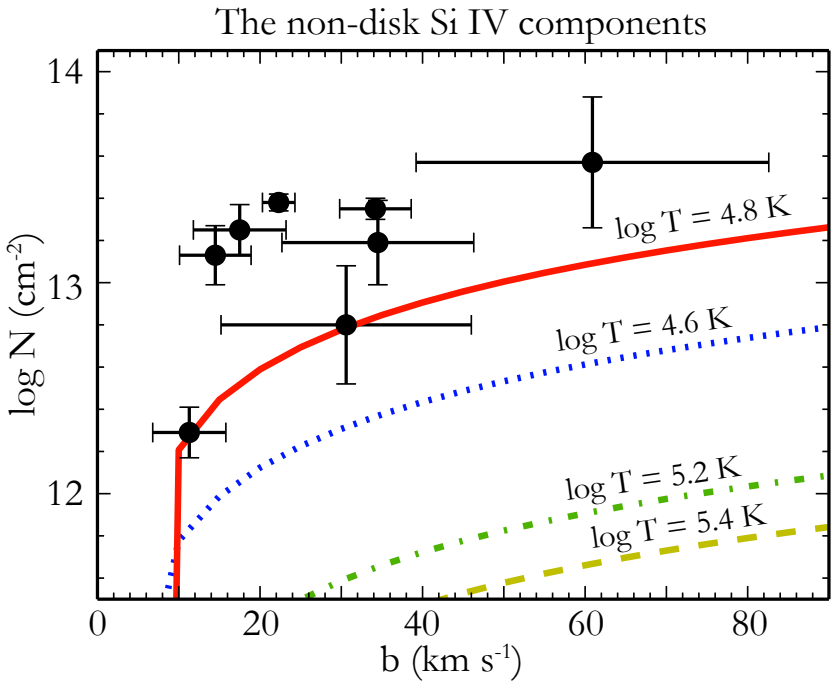

Figure 5.9: The observed log *N*-*b* correlation of the non-disk (disk-halo) components of Si IV. The colored curves show four CIE models derived using Eq 5.5 assuming a metallicity of $Z = 0.1\ Z_{\odot}$ and at log $T = 4.6$ K (blue dotted), 4.8 K (red solid), 5.2 K (green dash-dotted), and 5.4 K (yellow dash).

Our investigations indicate shocks and collisional ionization under CIE are unlikely the dominant mechanisms of producing Si IV at the disk-halo interface of M33. Photoionization is necessary to explain the large column density of Si IV. We proceed in the following section to discuss the role of photoionization in producing the observed Si IV. Note that non-equilibrium collisional ionization processes, such as turbulent mixing layers (Slavin et al. 1993; Kwak et al. 2011) and conductive interfaces (Borkowski et al. 1990; Gnat et al. 2010), could contribute in producing Si IV although current data is unable to distinguish among these scenarios.

5.6.2 Photoionization Modeling and the Metallicity of the Disk-Halo Interface

In this section, we consider the Si IV at the disk-halo interface being created by radiation from M33's starlight and extragalactic UV background (EUVB). We run two photoionization models for the M33 disk-halo interface using CLOUDY (v13.03; Ferland et al. 1998, 2013), which is a radiative transfer code assuming the gas is in a plane-parallel slab with uniform density and in thermal equilibrium. We refer to the first model as "pureEUVB", in which the gas is photoionized only by the assumed EUVB (Haardt & Madau 2001). It has an ionizing photon flux of $\Phi_\gamma = 1.52 \times 10^5$ s^{-1} cm^{-2} (Haardt & Madau 2001), representing the minimum incident radiation field received by the disk-halo interface[***].

The second model is called the "EUVB+star" model, with ionizing flux from both EUVB and M33's starlight (SFR = 0.5 $M_\odot$yr^{-1}). We assume a photon escape fraction of 10% and a gas slab distance of 5 kpc. The model has $\Phi_\gamma = 7.86 \times 10^7$ s^{-1} cm^{-2}, which is a combination of the EUVB (Haardt & Madau 2001) and the stellar radiation using a L$_*$ galaxy's spectral energy distribution (SED) from Starburst99 (Leitherer et al. 1999) as in Werk et al. (2014). In this EUVB+star framework, the extent to which the galaxy's SED contributes to the photoionization rate depends on the escape fraction of ionizing photons $f_{\rm esc}$, the SFR of the galaxy, and the distance of the slab from the galaxy. The integrated flux from the EUVB+star model thus scales as $(f_{\rm esc} \times {\rm SFR})/d^2$. Given the uncertainties in estimating $f_{\rm esc}$ for M33 (Hoopes & Walterbos 2000), the SFR (Engargiola et al. 2003; Gratier

[***]But see Kollmeier et al. (2014), Shull et al. (2015), and Emerick et al. (2015) for discussions of the discrepancy of photon production between the Haardt & Madau (2001) model and the Haardt & Madau (2012) model.

et al. 2010), and the height of the accreting layer (§ 5.5.1), the EUVB+star model provides a rough but reasonable evaluation of the ionization condition of the disk-halo interface of M33.

The models require an input of $N_{\rm HI}$ as a stopping condition. For the disk-halo gas, we obtain $N_{\rm HI}$ values by fitting Gaussian components to the AGES H I 21-cm spectra within the integrated velocity ranges as indicated by the non-disk Si IV components. For each sightline, we show the non-disk Si IV and the corresponding H I velocity ranges in blue in Figure 5.3. S6 shows the minimum contamination from the main disk emission while the others all have substantially large disk H I wings entering the disk-halo velocity ranges. Given the importance of the H I value, we only apply our pureEUVB and EUVB+star models to S6. The integrated non-disk H I column density along S6 is $N_{\rm HI} = 10^{19.0}$ cm^{-2}. This value may have uncertainties due to (1) the potential unresolved gas moving at similar velocities from behind star S6, and (2) H I sub-structures within the beam of the radio observations (Wakker et al. 2001; Tumlinson et al. 2002; Welty et al. 2012). We repeat our CLOUDY modeling on a set of varying input log $N_{\rm HI}$ values from 17.0 to 21.0 cm^{-2} (in step of 1.0 dex), and find that our derived [Si/H] (described below) values do not vary significantly for a range of log $N_{\rm HI}$ from 18.0 to 21.0 cm^{-2}. Therefore, the uncertainties related to $N_{\rm HI}$ do not affect our assessment of gas metallicity at the disk-halo interface of M33.

The models predict Si IV column densities on $f_{\rm SiIV}$ - log U - [X/H] grids, where $f_{\rm SiIV}$ is the gas fraction of Si IV, log U the logarithm of the dimensionless ionization parameter U, and [X/H] the logarithm of the metallicity Z. [X/H] is also called the gas-phase abundance,

Table 5.4: CLOUDY Modeling using S6

	EUVB+star	pureEUVB
Φ_γ[a] (s^{-1} cm^{-2})	7.86×10^7	1.52×10^5
log U[b]	$[-2.4, -2.8]$	$[-2.7, -3.3]$
n_H[c] (cm^{-3})	$[0.7, 1.7]$	$[0.003, 0.010]$
f_{HI}[d]	$[0.026, 0.081]$	$[0.042, 0.158]$
f_{SiIV}[d]	$[0.030, 0.007]$	$[0.085, 0.018]$
log (Si/H)[e]	$[-5.57, -4.45]$	$[-5.82, -4.57]$
[Si/H][f]	$[-1.08, 0.04]$	$[-1.33, -0.08]$

Table Note: (a) Ionizing photon flux. The pureEUVB value is from Haardt & Madau (2001), and the EUVB+star one is a combination of the EUVB (Haardt & Madau 2001) and the stellar ionization background (Leitherer et al. 1999). (b) Logarithm of ionization parameter $U \equiv \Phi_\gamma/(cn_H)$ where c is the speed of light. (c) Hydrogen number density $n_H = \Phi_\gamma/(cU)$. (d) Gas fraction of H I and Si IV, respectively. (e) Gas-phase abundance of Si with ionization correction. (f) Gas-phase abundance of Si normalized to the solar value.

which is normalized to a solar value: [X/H]≡log (N_X/N_H)-log $(X/H)_\odot$. For Silicon, we adopt $(Si/H)_\odot = 10^{-4.49\pm0.04}$ from Asplund et al. (2005), which is the abundance reference of CLOUDY. The log U and f_{SiIV} parameters of the disk-halo interface are solved by matching the predicted log N_{SiIV} with the observed one of S6, log N_{SiIV}[†††](= 13.50 ± 0.09 cm^{-2}). We apply the gas fraction f_{SiIV}, f_{HI} to the observed log N_{SiIV} and log N_{HI} values to make ionization correction and calculate the metallicity [Si/H].

Table 5.4 shows the CLOUDY modeling results. The EUVB+star model predicts a higher log U than the pureEUVB by ∼ 0.4 dex. The hydrogen volume density n_H of the EUVB+star model is $0.7 - 1.7$ cm^{-3}, which is typical of H II gas in the disk, while n_H = $0.003 - 0.01$ cm^{-3} from the pureEUVB model represents typical values of diffuse coronal gas (Draine 2011). Both models show small values of f_{HI}, indicating that the hydrogen

[†††]S6 has two disk-halo Si IV components with one at 70.6 km s^{-1} and the other at 106.2 km s^{-1} as shown in Figure 5.3 and Table 5.2. Here we use the sum of their column densities and calculate the error through error propagation. Note that the combined column density is within the maximum value as found from other individual components.

at the disk-halo interface is mostly ionized. The EUVB+star model shows [Si/H]=[-1.08, 0.04] and the pureEUVB model finds a similar range. Although the EUVB+star model has a much higher photon flux than the pureEUVB field, their SED slopes between the H I ionization potential (1 Ryd) and the Si IV's (2.5 Ryd) are similar (see Figure 13 in Werk et al. 2014). This causes similar values of ($f_{\rm HI}/f_{\rm SiIV}$) and thus similar [Si/H] values despite the different $f_{\rm HI}$ and $f_{\rm SiIV}$ given by each model at a particular log U.

The [Si/H] value we derive for the disk-halo interface of M33 is similar to that found by Lebouteiller et al. (2006) for the H II region NGC 604 (i.e., S5) using Si II λ1020.7. Their value is [Si/X] = [$-1.2, \gtrsim -0.2$]. Since they use Si II λ1020.7 with line centering at $v_{\rm LSR} = -245.4$ km s^{-1} (Lebouteiller et al. 2006), consistent with the systemic velocity of the gas disk at the position of S5 ($v_{\rm LSR} = -240.3$ km s^{-1}; Table 5.1), their measurement represents a [Si/H] value for M33's ISM. This indicates the disk-halo interface of M33 may have a metallicity similar to that of its ISM. In the next section, we calculate the metallicity of M33's ISM using the S II abundance ratio. It should be noted that studies on MW's ISM show that Si is normally depleted by at least a factor of five in the ISM, and the depletion level may change as varying gas phases (Savage & Sembach 1996). Overall, it is clear that M33's disk-halo interface has been previously enriched since its Si IV column density ($\langle N_{\rm SiIV}\rangle = 10^{13.24}$ cm^{-2}) is comparable to both the disk's and the disk-halo interface gas of the MW that is known to be enriched ($\langle N_{\rm SiIV}\rangle = 10^{13.17}$ cm^{-2}; Shull et al. 2009).

5.6.3 The Metallicity of M33's ISM

To assess the relative enrichment level of the disk-halo interface gas, we can compare the disk-halo metallicity with that of the ISM. Since the current M33's ISM metallicity measurements are mostly based on emission-line observations (e.g., Crockett et al. 2006; Magrini et al. 2007b; Rubin et al. 2008), here we decide to derive the ISM abundance from our absorption-line data to avoid any systematic difference. We do not perform CLOUDY modeling for the ISM which would involve additional assumptions on SFR and incident radiation fields; instead, we use the abundance ratio [S II/H] as S is not readily depleted onto interstellar dust (Savage & Sembach 1996) and the multiple transitions we detect are not saturated in our data.

The total hydrogen column $N_{\rm H}$ in front of each star is obtained from the color excess E(B-V) as we have calculated in § 5.2.5. Here we use the LMC-like $\log N_{\rm H}$ values since M33 and LMC are more similar in terms of galaxy mass and metal content than the MW or SMC (D'Onghia & Fox 2015; Crockett et al. 2006). The reader should interpret the provided values with caution given the current limited knowledge of the actual metal content of M33's ISM. If M33 is MW- (SMC-) like, the provided abundance ratios in Table 5.5 would be higher (lower) by $\sim$ 0.5 (0.2) dex, while the relative abundance ratios [Fe II/S II] and [P II/S II] remain the same. Since the $N_{\rm H}$ value includes all the neutral hydrogen in front of a given star, we use the total ion column density of those lines that were fit with multiple kinematic components. This may slightly increase the derived ISM metallicity if some components are non-disk; however, this effect should be minor as ISM components usually dominate the absorption lines.

Table 5.5: Metallicity of M33's ISM from Absorption Line

ID	[S II/H][a]	[P II/H][a]	[Fe II/H][a]	[Fe II/S II] [b]	[P II/S II][b]
S1	-1.0	-0.8	-1.9	-0.9±0.2	0.1±0.4
S2	-1.3	-1.1	-2.2	-0.9±0.2	0.1±0.2
S3	-1.0	-0.9	-2.0	-1.0±0.1	0.1±0.1
S4	-1.4	-1.1	-2.6	-1.2±0.1	0.3±0.1
S5	-1.2	-1.2	-2.2	-1.0±0.1	0.0±0.1
S6	-1.2	<-1.4	-2.1	-0.9±0.2	<-0.1
S7	-1.5	-1.3	-2.5	-1.0±0.1	0.2±0.1

[a]Gas-phase abundance. [X/H]≡log(N_X/N_H)-(X/H)$_\odot$ where X represents species S II, P II and Fe II, respectively. For the solar values, we adopt (S/H)$_\odot$ = $10^{-4.86\pm0.05}$, (P/H)$_\odot$ = $10^{-6.64\pm0.04}$, and (Fe/H)$_\odot$ = $10^{-4.55\pm0.05}$ (Asplund et al. 2005). N_H is the LMC-like values in Table 5.3. If M33 is MW (SMC) like, the provided abundance ratios would be higher (lower) by ∼ 0.5 (0.2) dex, while the relative abundance ratios [Fe II/S II] and [P II/S II] remain the same. The reader should interpret the provided metallicities with caution given the current limited knowledge of the actual metal content of M33's ISM.

[b]The relative abundance ratio, defined as [X/S II]≡log(N_X/N_{SII})-(X/S)$_\odot$ where X represents Fe II and P II, respectively.

The [S II/H] and [P II/H] values in Table 5.5 show that the metallicity of M33's ISM is ∼ 0.1 solar if M33 is LMC like. This is consistent with the derived metallicity range that we have found at the disk-halo interface with [Si/H]=[-1.08, 0.04], indicating that the disk-halo interface of M33 is as similarly metal-enriched as the ISM. [Fe II/H] shows a mean value ∼ 1.0 dex lower than the other two, suggesting Fe is strongly depleted in M33's ISM. We additionally calculate the [P II/S II] and [Fe II/S II] abundance ratios. These values do not require the input of N_H, thus provide unbiased measurements of the abundance pattern of M33's ISM. Fe again shows a relative depletion with respect to S.

We note that our S and P metallicity is consistently lower than those values based on emission-line measurements. For example, Rubin et al. (2008) found [S/H] ∼ −0.5 dex and Crockett et al. (2006) indicated [O/H] ∼ −0.4 dex, both based on emission-line observations of H II regions in M33. This may reflect a systematic difference between emission-line-

and absorption-line-based metallicity measurements. We do not attempt to analyze M33's ISM further as the focus of this work is the disk-halo gas. However, we tabulate the data in Table 5.5 for researchers who are interested in the metal content of M33's ISM.

5.7 Discussion

Using UV-bright M33 stars as background targets, we detect an unambiguous accreting ionized gas flow towards the disk of M33. The ionized gas flow is multi-phase, as it is consistently seen in the warm ion Si IV and it is also found in the cool ions (Fe II, S II, and P II) along some sightlines. It is also possibly present in the saturated Si II, Si III, and C II lines. § 5.5 shows that the inflow can be well explained by an accreting layer with an inflow velocity of 110^{+15}_{-20} km s^{-1} and at a z-height of $1.5^{+1.0}_{-1.0}$ kpc from the galactic plane. In § 5.6, we find that the disk-halo interface gas of M33 is metal-enriched. An estimate of the metallicity of this accreting layer is [Si/H]=[-1.08, 0.04], consistent with the metallicity of M33's ISM measured via similar absorption-line methods. In this section, we calculate the mass and the accretion rate of the accreting layer and discuss its origin(s). We discuss the potential existence of outflows from M33 in the final part of this section.

5.7.1 Accretion Mass and Gas Accretion Rate

The kinematic modeling in § 5.5 predicts an accreting layer with an inflow velocity of $v_{\rm acc}$ = 110 km s^{-1} at height of $z_{\rm acc}$ = 1.5 kpc. Assuming a cylindrical geometry for the accreting layer with height $z_{\rm acc}$ and radius $R_{\rm acc}$, the total mass of the detected accreting

layer is,

$$
\begin{aligned}
M_{\rm acc} &= 1.3 \times (\pi R_{\rm acc}^2 z_{\rm acc}) m_{\rm H} N_{\rm H} / z_{\rm acc} \\
&= 1.3 \pi R_{\rm acc}^2 m_{\rm H} N_{\rm SiIV} [\frac{\rm Si}{\rm H}]_{\odot}^{-1} Z^{-1} f_{\rm SiIV}^{-1} \\
&\approx 3.9 \times 10^7 \ M_{\odot} \\
&(\frac{R_{\rm acc}}{7 \ {\rm kpc}})^2 (\frac{N_{\rm SiIV}}{10^{13.2} {\rm cm}^{-2}}) (\frac{Z}{0.2 \ Z_{\odot}})^{-1} (\frac{f_{\rm SiIV}}{0.1})^{-1}
\end{aligned}
\tag{5.6}
$$

where 1.3 accounts for the helium mass using a primordial He/H ratio of 1/12 and $m_{\rm H}$ is the proton mass. For $R_{\rm acc}$, we adopt the maximum inclination-corrected galactocentric distance $R_{\rm G} \sim 7$ kpc (Table 5.1) assuming the accreting layer covers the whole star-forming disk. The term $\pi R_{\rm acc}^2 z_{\rm acc}$ is the total volume of the layer in front of the stars, and $m_{\rm H} N_{\rm H} / z_{\rm acc}$ is the mass density. Since large uncertainties are associated with the estimation of $N_{\rm H}$ for the disk-halo gas, here we substitute $N_{\rm H}$ with the measured $N_{\rm SiIV}$: $N_{\rm H} = N_{\rm SiIV} (\frac{\rm Si}{\rm H})_{\odot}^{-1} Z^{-1} f_{\rm SiIV}^{-1}$. We adopt $N_{\rm SiIV} = 10^{13.2}$ cm^{-2} which is the mean Si IV column density of the disk-halo gas, $Z \sim 0.2 \ Z_{\odot}$ which is within the metallicity derived in § 5.6.2, and $f_{\rm SiIV} \sim 0.1$ which is the maximum gas fraction of Si IV from both ionization fields (Table 5.4). Note that our calculation is conservative and the actual accretion mass and the accretion rate could be higher if we use a smaller gas fraction $f_{\rm SiIV}$ value. If a symmetric accreting layer exists on the other side of the disk, the total mass of accreting material will double from the value above to $\sim 7.8 \times 10^7 \ M_{\odot}$.

The closest observed analogs to this accreting layer are the denser H I IVCs ($d \leq 3-4$ kpc; Albert & Danly 2004) and the Hα Reynolds layer ($1-2$ kpc; Reynolds 1993; Haffner et al. 2003) in the MW, or the H I extraplanar gas (e.g., Fraternali et al. 2002; Oosterloo

et al. 2007; Gentile et al. 2013) and diffuse ionized gas (e.g., Collins et al. 2000; Heald et al. 2006b) in external galaxies. The M33 accreting layer is much less massive than these (at least a factor of ten less than the H I extraplanar gas in other galaxies; e.g., NGC 2403; Fraternali et al. 2002) and is clearly infalling, while these observed analogs are only known to be lagging in rotation. It is interesting that our Accreting Layer model (§ 5.5.1) is not sensitive to halo lagging since the lagging rotational velocity is found along the vertical direction out to a few kpc in both H I and Hα in the MW and external galaxies (e.g., Heald et al. 2006a; Levine et al. 2008). Future observations that are capable of observing more direct analogs to our accreting layer would be useful, in particular, observations that can kinematically resolve the extraplanar gas and identify inflow motions.

We derive the accretion rate for the accreting layer on the front side of the disk,

$$\begin{aligned} \dot{M} &= M_{\rm acc} v_{\rm acc}/z_{\rm acc} \\ &\approx 2.9\ M_\odot {\rm yr}^{-1} (\frac{M_{\rm acc}}{3.9\times10^7\ M_\odot})(\frac{v_{\rm acc}}{110\ \ {\rm km\ s^{-1}}})(\frac{z_{\rm acc}}{1.5\ {\rm kpc}})^{-1}. \end{aligned} \tag{5.7}$$

Again, if there is a symmetric layer on the other side of the disk, the total accretion rate will be $\sim 5.8\ M_\odot {\rm yr}^{-1}$. This accretion rate is much higher than the M33's SFR ($\lesssim 0.5\ M_\odot {\rm yr}^{-1}$; Engargiola et al. 2003; Gratier et al. 2010). In the next section, we discuss two potential scenarios that may account for the large accretion rate. We note that the covering fraction of the gas may play a critical role in evaluating the accreting mass and the accretion rate. In our calculation, we assume a 100% coverage since all seven sightlines have detected Si IV inflow. However, since our sightlines are all targeted at star-forming regions, we do not have the comparison with non-star-forming regions in M33 disk. The $M_{\rm acc}$ and $\dot{M}$ would

be lower or higher if the accreting inflow has lower or higher column density in non-star-forming regions. Future observations using QSO sightlines through non-star-forming regions may help to evaluate the structure of the accreting gas.

5.7.2 The Origin of the Ionized Gas Inflow

As discussed in § 5.6, the disk-halo gas of M33 is metal-enriched. This enrichment could result from some disk-wide gas mixing processes as we find a 100% detection rate of infalling Si IV and our sightlines have sampled the disk rather evenly, including both the very center of the disk and its star-forming outskirts. We propose two scenarios that could account for the detected gas inflows at the disk-halo interface of M33.

First, the accreting layer may be the cooling stage of the galactic fountain model (Shapiro & Field 1976). The model starts with hot gas in the ISM losing pressure support from its surrounding cool medium and streaming upward and radially outward to a height of a few kpc (Bregman 1980; Houck & Bregman 1990). Then it condenses into cold clouds via non-linear instability (Joung et al. 2012a). Once the cold clouds can no longer feel pressure support from the hot corona, they fall downward and inward due to gravity and centrifugal forces and can dissolve into the warm ionized medium after travelling several kpc (Heitsch & Putman 2009; Joung et al. 2012a).

Bregman (1980) ran a 2D hydrodynamic simulation incorporating the galactic fountain scenario to explain the existence of HVCs in the MW halo. He found that if the cold clouds fall ballistically, their vertical highest velocities could reach -80 km s^{-1} and up to -150 km s^{-1}. Similar results are found if we use the terminal velocity equation from

Benjamin & Danly (1997) to calculate the terminal velocities of free-falling clouds at the disk-halo interface. This is consistent with the high velocity $v_{\rm acc}$ = 110 km s^{-1} found in our Accreting Layer model.

A number of authors (e.g., Fraternali & Binney 2006, 2008; Marinacci et al. 2011; Marasco et al. 2012) suggest that the cold fountain clouds would seed the condensation of the hot corona and trigger a net inflow of halo gas. The total inflow includes the fountain return, and the ambient halo material that contributes 10 – 20% of the inflow mass and feeds the star formation. Taking into account the fountain return and the newly accreted halo gas, the total accretion rate should be $\sim$ 5 – 10 times the SFR of the galaxy. If we apply this fountain model to M33, which has a SFR $\lesssim$ 0.5 $M_{\odot}$yr^{-1}, one would expect a total accretion rate of $\dot{M} \lesssim$ 2.5 – 5.0 $M_{\odot}$yr^{-1}, consistent with the number we derive in § 5.7.1. The galactic fountain model predicts changes of gas phases at different circulation stages; this is likely our case as warm and cool ions are both found with accreting velocities. However, we are unable to fully address whether the accreting flow consistently bears a cool-phase gas as the non-disk components in Fe II, S II, and P II are only detected along a few sightlines and the Si II, Si III, and C II lines are saturated.

Alternatively, the accreting gas could be associated with stripped material raining back down that was pulled from the disk of M33 during a close passage with M31. The M31-M33 interaction is hinted by its large warps, diffuse H I features, and extended stellar disk (van der Marel & Guhathakurta 2008; Putman et al. 2009; McConnachie et al. 2009). Heitsch & Putman (2009) showed that if falling from 10 kpc, the maximum velocity a free-falling cloud could reach is $\lesssim$ 150 km s^{-1}, which is consistent with the accretion

velocity $v_{\rm acc}$ = 110 km s^{-1} of our fast accreting layer. In this case, the large accretion rate of $\sim 2.9\ M_{\odot}{\rm yr}^{-1}$ would be temporary and result in an increase in star formation in the disk, but may not have a long-term influence.

Apart from these two scenarios, there may exist other kinematic processes that have not been accounted for in order to fully understand M33's accretion. For future work, more sophisticated kinematic models incorporating radial gas flows (e.g., Schmidt et al. 2016) would be helpful to disentangle the degeneracy of different gas motions. Detailed galactic fountain modeling that takes into account the distribution of local star-forming regions in the disk would shed light upon the influence of stellar activities in shaping the disk-halo interface of M33. Observationally, more sightlines using bright stars in the disk and background QSOs through non-star-forming regions will help to address whether there exists a correlation between gas inflows and local star formation.

5.7.3 Outflows from M33

Galactic outflows driven by stellar and/or AGN feedback are ubiquitously observed in star-forming and starburst galaxies both in the local universe and at higher redshifts (e.g., Lehner et al. 2009; Heckman et al. 2000; Shapley et al. 2003; Chen et al. 2010d; Weiner et al. 2009; Martin et al. 2012; Rubin et al. 2014). Winds have been observed in multiple phases traced by CO emission, Hα emission, UV and optical absorption lines (e.g., Mg II, Fe II, Na I) and X-ray (e.g., Martin 1999; Walter et al. 2002; Strickland et al. 2004a,b). Galactic outflows are generally found moving at several hundred km s^{-1} and can be seen out to $\sim$ 1000 km s^{-1} (e.g., Weiner et al. 2009; Coil et al. 2011; Rubin et al. 2014).

One may expect the presence of such galactic outflows in M33 since it is actively forming stars (e.g., Engargiola et al. 2003; Gratier et al. 2010) and has a relatively high SFR surface density (Heyer et al. 2004; Magrini et al. 2007a) that could potentially drive winds out of the disk (e.g., Rubin et al. 2014). In addition, the metallicity of M33's ISM is abnormally low in terms of its stellar mass ($3 - 6{\times}10^9$ $M_\odot$; Corbelli 2003) according to the mass-metallicity relation (Tremonti et al. 2004), also suggesting the presence of outflows in M33 to efficiently remove metals from its ISM. Accordingly, we now discuss whether the M33 COS data show any evidence for ionized gas outflows along our seven sightlines.

5.7.3.1 Tentative Detection of Slow Winds

We detect weak blueshifted absorption components ($-40 \lesssim v_{\rm d} \lesssim 0$ km s^{-1}) in low and/or warm ions along our sightlines (see Figure 5.3). As shown in Table 5.2, the mean column densities for these blueshifted components are $N_{\rm S\ II} = 10^{15.17}$ cm^{-2}, $N_{\rm P\ II} = 10^{13.52}$ cm^{-2}, $N_{\rm Fe\ II} = 10^{14.26}$ cm^{-2}, and $N_{\rm Si\ IV} = 10^{13.43}$ cm^{-2}, and their mean Doppler widths are $b \sim 25 - 40$ km s^{-1}. We find that these blueshifted components could be due to the expansion of local H II regions into M33's ISM, since both their b values and measured velocities are consistent with the large velocity dispersions found in the ionized gas of H II regions ($\sigma \sim 20 - 30$ km s^{-1}; Kam et al. 2015) and in the H I 21-cm emission across the M33 disk ($\sigma \sim 18.5$ km s^{-1}; Putman et al. 2009). In particular, the giant H II region NGC 604 (i.e., S5) has been found to be undergoing multiple blowouts (Tenorio-Tagle et al. 2000), consistent with the blue-shifted components we detect for S5. We note that these blueshifted components have velocities that are close to our CalCOS spectral uncertainty

(14 – 19 km s^{-1}), thus they only tentatively exhibit evidence for slow winds. In general, these slow-velocity features indicate gas activities that are closely related to M33's ISM.

5.7.3.2 Potential Fast Outflows at $v_{\rm d} \lesssim -100$ km s^{-1}?

As indicated in § 5.3, we find strong absorption signatures in C II, Si II, and Si III along all our available sightlines at negative high velocities of $-200 \lesssim v_d \lesssim -100$ km s^{-1} (see Figure 1); however, such absorption is not found in Si IV, P II, S II, or Fe II. In this section, we discuss the possible origins for these negative high-velocity C II, Si II, and Si III absorbers, while in the following section (5.7.3.3), we address the non-detection of relevant absorption in Si IV, P II, S II, or Fe II.

The C II, Si II, and Si III absorbers could potentially be fast outflows that have originated from the disk of M33, as their velocities are broadly consistent with those measured in extragalactic down-the-barrel studies (e.g., Rubin et al. 2014). If such outflows indeed exist in M33, they can only be driven by stellar winds or supernova explosions (such as those in LMC; Lehner et al. 2009) as M33 does not have a central massive black hole (Merritt et al. 2001). This would be an unusual detection however, as these absorbers generally have narrow line widths (FWHM < 100 km s^{-1}) compared to the ionized galactic outflows with FWHM values of $\sim 200 - 500$ km s^{-1} found in star-forming regions (e.g., Chisholm et al. 2016).

On the other hand, the C II, Si II, and Si III absorbers may have other origins. First, the absorbers may be part of the northern warp of M33 that folds back over the disk thus to intercept our sightlines, given that M33 has a large extended northern H I warp

with velocity up to $v_{\rm LSR} \sim -300$ km s^{-1} (Rogstad et al. 1976; Corbelli & Schneider 1997; Putman et al. 2009). Second, this low-ionization state absorption may be due to stripped debris from M33 if the galaxy orbited close to M31 in the past several Gyrs (Putman et al. 2009; McConnachie et al. 2009). Third, even though their velocities differ in the M33's $v_{\rm d}$ frame, these C II, Si II, and Si III absorbers have nearly constant $v_{\rm LSR}(\sim -350$ km s$^{-1})$, suggesting that they may come from the ionized extension of a nearby high-velocity cloud – the Wright's Cloud (Wright 1979; Braun & Thilker 2004; Putman et al. 2009). In a deep H I 21-cm emission map of the cloud (Keenan et al. 2015), the ionized gas absorption appears well-aligned in position space and, its velocity matches the observed gradient of the cloud.

In all, we find that the C II, Si II, and Si III absorbers at $-200 \lesssim v_d \lesssim -100$ km s^{-1} ($v_{\rm LSR} \sim -350$ km s^{-1}) could be a mixture of multiple sources given the complex surrounding environments. Their presence certainly helps to provide a more complete picture of ionized gas environment near M33, thus an intricate analysis on its origin should be carried out, which is beyond the scope of this work. We will extend our investigation on the origin(s) of these negative high-velocity C II, Si II, and Si III absorbers in (Zheng et al. 2017).

5.7.3.3 Covering Fraction of the Potential Fast Outflows

If the blue-shifted absorption seen in C II, Si II, and Si III have origins other than outflowing gas, then M33 exhibits a lack of fast outflows in low-ionization states. This scenario is also supported by the non-detections of fast outflows in Fe II, a frequently detected ion in

down-the-barrel wind studies (e.g., Rubin et al. 2014), as well as in P II, S II, or Si IV. In this section, we discuss the possible reasons for the non-detections in these ions, and use the non-detections to constraint the upper limit of the covering fraction of the potential outflows.

First, we find that the non detection of outflows among these ions cannot be explained by the potential geometry of the outflows or the inclination of M33's disk. Generally speaking, outflows having collimated and/or bi-conical geometry are easier to observe in face-on galaxies (e.g., Martin et al. 2012; Rubin et al. 2014); thus, the inclination of M33 of 56°, could preclude the detection of outflows in our study. However, we observed seven sightlines that evenly sampled different areas of the disk. Three of them are within two kpc from the galactic center. If such collimated outflows have a large covering fraction (as discussed below), we would have been able to detect them even though M33 is moderately inclined.

Second, the non-detection is unlikely due to data's sensitivity limit. Our *HST*/COS spectra are sensitive to Fe II column density above $10^{13.5}$ cm^{-2} while the typical $N_{\rm FeII}$ value found for the galactic outflows in star-forming galaxies at redshift ~ 0.5 is $\gtrsim 10^{14.0}$ cm^{-2} (Rubin et al. 2014). The fast outflows in M33 could potentially be in a hotter phase than we can detect as the disk could blow out hot and diffuse gas as pictured in the galactic fountain model (see § 5.7.2). However, this speculation is inconsistent with most observations that commonly find outflows in colder phases traced by cool ions such as Fe II (e.g., Chen et al. 2010d; Coil et al. 2011; Rubin et al. 2014).

Third, the small aperture size of our COS observations (~10 pc) would not cause the

non-detection if the outflows have covering fraction (C_f) of 1.0 over the disk. However, it is possible that the outflows from M33 have a substantially low covering fraction C_f thus elude our detections. With the seven non-detections in our COS data, we can assess the upper limit to C_f. In this framework, the likelihood of a non-detection along a given sightline is $1 - C_f$. Assuming that the seven non-detection events are independent, which is reasonable given the typical projected separation between sightlines of $\sim$ 2 kpc, the probability of seven non-detections is then $(1 - C_f)^7$. To constrain the upper limit to the covering fraction at 95% confidence level, we then expect $(1 - C_f)^7 \geq (1 - 0.95)$. Thus, we find that the covering fraction of outflows from M33 with $N_{\rm FeII} > 10^{13.5}$ cm^{-2} is constrained to be $C_f \leq 0.35$ at a 95% confidence. This suggests the covering fraction of outflows (in S II, S II, P II, and Si IV) from M33 have to be less than 35% if they indeed exist.

The derived covering fraction for M33's outflows lies at the low-end C_f ranges (0.24–0.98) of the ubiquitous outflows found in star-forming galaxies at z $\sim$ 0.5 (Rubin et al. 2014). In their sample, the galaxies with winds exhibit a mean covering fraction of $C_f = 0.59 \pm 0.17$. The mean C_f would be lower (0.37±0.32) if we include those galaxies that do not have wind detection and assign them C_f values of 0. Similar results are found if we only consider galaxies with inclination of $50 - 60^\circ$ (M33 has $i = 56^\circ$). Therefore, the low covering fraction of the potential outflows from M33 is consistent with observations of outflows from star-forming galaxies based on larger data sample.

Note that this direct comparison may be complicated by the varying column density limits of Rubin et al. (2014) at different covering fraction. Beside the above statistical argument, it is worth noticing that our sightlines are through major star forming regions

in the disk where one would expect to detect galactic outflows if they were present. We suggest that for future work an increased number of sightlines through the disk at different locations or an increase of aperture size will help to increase the outflow detection probability or solidify that M33 does not host galactic outflows.

5.8 Conclusion

We present a UV absorption-line study of the ionized gas inflow at the disk-halo interface of M33. In contrast to common approaches of using background QSOs, we choose a sample of seven UV-bright stars in the disk of M33. This allows us to unambiguously identify gas inflow onto the disk. Our main results are summarized as follows.

We detect consistently redshifted non-disk Si IV absorption along all of our sightlines that extend evenly across the disk of M33 (§ 5.3). Their centroid velocities $v_{\rm d}$ range from +39 km s^{-1} to +106 km s^{-1} with a mean value of +67 km s^{-1} (or +67/cos56° $\sim$ +120 km s^{-1} if corrected for inclination), suggesting that there exists a disk-wide, warm-ionized gas accreting toward M33. This accreting flow is most likely multi-phase, since similar non-disk components can also be observed in cool ions (Fe II, S II, and P II) along some sightlines. They may also commonly exist in saturated ion lines (C II, Si II, and Si III). The mean column density of the non-disk ionized gas is $\langle N_{\rm SiIV} \rangle = 10^{13.24 \pm 0.21}$ cm^{-2}. We find that shocks and collisional ionization under CIE cannot account for the total non-disk Si IV column and, we conclude that the majority of Si IV is produced via photoionization (§ 5.6.1).

To interpret the consistently redshifted non-disk Si IV absorption components, we

construct two kinematic models - the Accreting Layer model and the M33 Halo Cloud model (§ 5.5). We find the Accreting Layer model provides the best explanation of the observed non-disk Si IV velocities if the layer accretes toward the disk at $v_{\rm acc} = 110^{+15}_{-20}$ km s^{-1} at a height of $z_{\rm acc} = 1.5^{+1.0}_{-1.0}$ kpc. The mass of the accreting layer on the near side of the disk is 3.9×10^7 $M_\odot$, and the accretion rate is 2.9 $M_\odot$yr^{-1} (§ 5.7.1). If symmetric accreting flows exist on both sides of the disk, the total accretion mass is 7.8×10^7 $M_\odot$ and the accretion rate is 5.8 $M_\odot$yr^{-1}.

We find an abundance ratio of [Si/H]=[-1.08, 0.04] for the accreting gas at the disk-halo interface of M33. Although there are uncertainties that make it somewhat unclear if M33's disk-halo gas has a higher or lower metallicity than its ISM ([S II/H] $\sim$ -1.0 dex), its Si IV column density ($10^{13.24\pm0.21}$ cm^{-2}) is comparable to the M33 disk gas and the enriched disk-halo interface of the MW ($10^{13.17}$ cm^{-2}; Shull et al. 2009).

We invoke two processes in the discussion of the origin of the metal-enriched, fast-accreting gas at the disk-halo interface of M33. First, we find that a galactic fountain model is able to explain the metal enrichment via gas recycling, the high inflow velocity by ballistic motions, and the large accretion rate by bringing back more material from the hot corona. Second, we speculate that the accreting layer could include free-falling material that was previously stripped from the disk of M33 as it orbited close to M31. In this case, the large accretion rate would be temporary. More sophisticated modeling is needed to better understand the gas accretion at the disk-halo interface of M33.

We detect negative high-velocity absorption in C II, Si II, and Si III. Their origin is so far unclear – M33's fast outflows, M33's H I warp or a nearby HVC, could all be possible.

We defer the detailed analysis of the origins of these ion absorbers in a future paper (Zheng et al. 2017, in prep.). We do not have detection at negative high velocities in Fe II, S II, P II, or Si IV along any of our sightlines. This is unlikely due to geometric effects with the outflows being collimated and bi-conical, as our sightlines extend across the star-forming disk. We suggest that the covering fraction of the potential galactic outflows has to be less than 35% at a 95% confidence level (at a $N_{\rm FeII} > 10^{13.5}$ cm^{-2} sensitivity limit) if M33 indeed hosts such fast-moving winds.

Our study of M33 is one of the first to clearly reveal the existence of an ionized gas inflow onto the disk of a galaxy beyond the MW. Our analysis provides a better understanding of gas accretion in the vicinity of a galaxy disk; however, there are several ways we can further our understanding in the future. 1) The sample of sightlines should be enlarged to assess the clumpiness and sub-structure of the inflowing gas. 2) It would be ideal to have QSO sightlines that do not go through H II regions and/or spiral arms to determine the effects of local star formation activities. 3) With only COS/G130M grating, a critical ion C IV, which traces collisional processes, is missed. It would be helpful to use the G160M grating to expand the detected line library and form a clearer picture of the ionization state of the gas. 4) Finally, in the future more detailed models that incorporate different kinematic processes would be helpful in interpreting the gas motions.

Acknowledgement. We thank the anonymous referee for the detailed comments to improve this work. We appreciate B.P. Wakker's generosity of providing us the co-added spectra of S7 ran with his program. We thanks C. Liang, H.W. Chen and A.J. Fox for discussions on *HST*/COS wavelength calibration and comments on the draft, J. Tumlinson,

J.M. Shull and C.W. Danforth for discussions on Si IV and O VI line profiles, N. Lehner for questioning and reviewing § 5.4, K.H.R. Rubin for discussions on our non-detection of galactic-scale outflows in Fe II, and J.X. Prochaska, Filippo Fraternali and David J. Helfand for useful comments on the draft. J. Werk and Y. Zheng gratefully acknowledge the peaceful and beautiful setting offered by the Esalen institute during the drafting of this manuscript.

This work is based on observations made with the NASA/ESA Hubble Space Telescope (program ID: 13706). Support for HST-GO-13706 was provided by NASA through a grant from the Space Telescope Science Institute (STScI). STScI is operated by the Association of Universities for Research in Astronomy, Inc., under NASA contract NAS5-26555. Some of the data presented in this paper were obtained from the Mikulski Archive for Space Telescopes (MAST). Support for MAST for non-HST data is provided by the NASA Office of Space Science via grant NNX13AC07G and by other grants and contracts. We also acknowledge support from the National Science Foundation under Grant No. AST-1410800. J.E.G. Peek and J.K. Werk were supported in part by Hubble Fellowship grants 51295 and 51332, respectively, provided by NASA to STScI.

This research made use of the IPython package (Pérez & Granger 2007), matplotlib (Hunter 2007) and Astropy (Astropy Collaboration et al. 2013). CalCOS is a product of the Space Telescope Science Institute operated by AURA for NASA. This research also made use of the SIMBAD database, operated at CDS, Strasbourg, France. The M33 image is made with the NASA Galaxy Evolution Explorer. GALEX is operated for NASA by the California Institute of Technology under NASA contract NAS5-98034.

Chapter 6

Concluding Remarks

This dissertation mainly investigates the gas distribution and kinematics in the CGM of the MW and M33. Multiple methods and datasets are used, including H I 21cm observations from the Arecibo Observatory, UV spectra of QSOs and stars from HST/COS, and a simulated MW-mass galaxy from a cosmological simulation. I show that nearly half of the mass in the MW's CGM is moving at low velocity ($|v_{\rm lsr}| \lesssim 100$ km s^{-1}), a component that has been largely omitted by previous studies due to contamination of foreground gas. Furthermore, I find that M33's star-forming disk is replenished by a layer of ionized gas at an inflow rate of $\dot{M}_{\rm in} = 2.9\ M_\odot\ {\rm yr}^{-1}$ in the near side of the disk. This M33 work is among the first to provide unambiguous evidence of gas accretion in extragalactic systems, and it justifies the methodology of using pencil-beam observations of disk stars to study inflows/outflows in galaxies beyond the MW and LMC/SMC. Briefly, the studies of $z = 0$ CGM as examined in this dissertation, together with the findings of CGM at higher redshifts, imply that the CGM of $< L >\sim L^*$ galaxies is massive, multiphase, metal-rich,

and complex in kinematics.

My future work is aimed at better understanding how the baryon cycle between the CGM and galaxy is formed via inflows and outflows. In theory, the disks are fed by inflows from the CGM to constantly form stars, while the CGM are heated and stirred by outflows from the disks. Recent years have seen great progress in detecting outflows; however, inflow detection remains rare and it is unclear how ionized gas cools out of the CGM and enters the disks. From the observational perspective, one of the keys to the CGM-disk mutualism is to obtain high-quality data to spatially and kinematically resolve the gas motions at the disk-halo interfaces of galaxies.

The techniques and methodology established in this dissertation can be further used and developed. For example, our own MW is a convenient (but no less challenging) target to study the gas kinematics at the disk-halo interface due to its proximity. In Chapter 3, I have studied the gas distribution in the MW's CGM with background QSOs. One major shortcoming is that no distance information for gas absorbers in the CGM can be inferred from the QSO data. This can be overcome by including UV-bright halo star sightlines to provide better constraints on the gas distribution in the foreground. The distances to target halo stars can be obtained thanks to the precise parallax measurements of the Gaia mission. A 3D kinematic model of the MW's disk-halo interface can therefore be built to investigate whether the MW hosts inflows and outflows, and how they alter the CGM gas kinematics projected onto local observers' viewing positions.

In a broader context, statistically analyses should be conducted to evaluate the occurrence rate of gas inflow and its relation with the properties of host galaxies. As I

have shown in Chapter 5, pencil-beam observations with high-resolution spectra provide insightful details of gas kinematics in the vicinity of galaxy disks. However, such observations are often limited to only a few available background sources such as UV-bright stars in star-forming regions or QSO sightlines passing through galaxy halos. The integral field unit (IFU) will be an useful tool to obtain 3D (i.e., position-position-velocity) information of gas kinematics in and near the star-forming disks. For example, the Sydney-AAO Multi-object IFU (SAMI) Galaxy Survey (Bryant et al. 2015) will generate 3D optical datacubes for 3,400 galaxies over a wide range of stellar mass and environment. Although gas emission faints quickly beyond galaxy disks and these IFU datacubes will mainly detect signals from the disks, stacking techniques can be adopted to get statistical assessment of gas inflow/outflow signatures.

To summarize, the knowledge of the CGM is rapidly evolving thanks to the developments of various observational instruments and simulation techniques. The work presented in this dissertation shows the complexity of the gas distribution in the CGM of MW and M33, which is only the tip of the iceberg. Much work needs to be done to better understand how the baryon cycle between the CGM and disk is formed through inflows and outflows, which will be the focus of my future research.

Bibliography

Ackermann, M., Albert, A., Atwood, W. B., Baldini, L., Ballet, J., Barbiellini, G., Bastieri, D., Bellazzini, R., Bissaldi, E., Blandford, R. D., Bloom, E. D., Bottacini, E., Brandt, T. J., Bregeon, J., Bruel, P., Buehler, R., Buson, S., Caliandro, G. A., Cameron, R. A., Caragiulo, M., Caraveo, P. A., Cavazzuti, E., Cecchi, C., Charles, E., Chekhtman, A., Chiang, J., Chiaro, G., Ciprini, S., Claus, R., Cohen-Tanugi, J., Conrad, J., Cutini, S., D'Ammando, F., de Angelis, A., de Palma, F., Dermer, C. D., Digel, S. W., Di Venere, L., Silva, E. d. C. e., Drell, P. S., Favuzzi, C., Ferrara, E. C., Focke, W. B., Franckowiak, A., Fukazawa, Y., Funk, S., Fusco, P., Gargano, F., Gasparrini, D., Germani, S., Giglietto, N., Giordano, F., Giroletti, M., Godfrey, G., Gomez-Vargas, G. A., Grenier, I. A., Guiriec, S., Hadasch, D., Harding, A. K., Hays, E., Hewitt, J. W., Hou, X., Jogler, T., Jóhannesson, G., Johnson, A. S., Johnson, W. N., Kamae, T., Kataoka, J., Knödlseder, J., Kocevski, D., Kuss, M., Larsson, S., Latronico, L., Longo, F., Loparco, F., Lovellette, M. N., Lubrano, P., Malyshev, D., Manfreda, A., Massaro, F., Mayer, M., Mazziotta, M. N., McEnery, J. E., Michelson, P. F., Mitthumsiri, W., Mizuno, T., Monzani, M. E., Morselli, A., Moskalenko, I. V., Murgia, S., Nemmen, R., Nuss, E., Ohsugi, T., Omodei, N., Orienti, M., Orlando, E., Ormes, J. F., Paneque, D., Panetta, J. H., Perkins, J. S., Pesce-Rollins, M., Petrosian, V., Piron, F., Pivato, G., Rainò, S., Rando, R., Razzano, M., Razzaque, S., Reimer, A., Reimer, O., Sánchez-Conde, M., Schaal, M., Schulz, A., Sgrò, C., Siskind, E. J., Spandre, G., Spinelli, P., Stawarz, Ł., Strong, A. W., Suson, D. J., Tahara, M., Takahashi, H., Thayer, J. B., Tibaldo, L., Tinivella, M., Torres, D. F., Tosti, G., Troja, E., Uchiyama, Y., Vianello, G., Werner, M., Winer, B. L., Wood, K. S., Wood, M., & Zaharijas, G. 2014, ApJ, 793, 64

Adelberger, K. L., Steidel, C. C., Shapley, A. E., & Pettini, M. 2003, ApJ, 584, 45

Albert, C. E. & Danly, L. 2004, in Astrophysics and Space Science Library, Vol. 312, High Velocity Clouds, ed. H. van Woerden, B. P. Wakker, U. J. Schwarz, & K. S. de Boer, 73

Allen, J. T., Schaefer, A. L., Scott, N., Fogarty, L. M. R., Ho, I.-T., Medling, A. M., Leslie, S. K., Bland-Hawthorn, J., Bryant, J. J., Croom, S. M., Goodwin, M., Green, A. W., Konstantopoulos, I. S., Lawrence, J. S., Owers, M. S., Richards, S. N., & Sharp, R. 2015, MNRAS, 451, 2780

Allen, M. G., Groves, B. A., Dopita, M. A., Sutherland, R. S., & Kewley, L. J. 2008, ApJS, 178, 20

Anderson, M. E. & Bregman, J. N. 2010, ApJ, 714, 320

Asplund, M., Grevesse, N., & Sauval, A. J. 2005, in Astronomical Society of the Pacific Conference Series, Vol. 336, Cosmic Abundances as Records of Stellar Evolution and Nucleosynthesis, ed. T. G. Barnes, III & F. N. Bash, 25

Asplund, M., Grevesse, N., Sauval, A. J., & Scott, P. 2009, ARA&A, 47, 481

Astropy Collaboration, Robitaille, T. P., Tollerud, E. J., Greenfield, P., Droettboom, M., Bray, E., Aldcroft, T., Davis, M., Ginsburg, A., Price-Whelan, A. M., Kerzendorf, W. E., Conley, A., Crighton, N., Barbary, K., Muna, D., Ferguson, H., Grollier, F., Parikh, M. M., Nair, P. H., Unther, H. M., Deil, C., Woillez, J., Conseil, S., Kramer, R., Turner, J. E. H., Singer, L., Fox, R., Weaver, B. A., Zabalza, V., Edwards, Z. I., Azalee Bostroem, K., Burke, D. J., Casey, A. R., Crawford, S. M., Dencheva, N., Ely, J., Jenness, T., Labrie, K., Lim, P. L., Pierfederici, F., Pontzen, A., Ptak, A., Refsdal, B., Servillat, M., & Streicher, O. 2013, A&A, 558, A33

Auld, R., Minchin, R. F., Davies, J. I., Catinella, B., van Driel, W., Henning, P. A., Linder, S., Momjian, E., Muller, E., O'Neil, K., Sabatini, S., Schneider, S., Bothun, G., Cortese, L., Disney, M., Hoffman, G. L., Putman, M., Rosenberg, J. L., Baes, M., de Blok, W. J. G., Boselli, A., Brinks, E., Brosch, N., Irwin, J., Karachentsev, I. D., Kilborn, V. A., Koribalski, B., & Spekkens, K. 2006, MNRAS, 371, 1617

Avni, Y. 1976, ApJ, 210, 642

Barger, K. A., Lehner, N., & Howk, J. C. 2016, ApJ, 817, 91

Behroozi, P. S., Conroy, C., & Wechsler, R. H. 2010, ApJ, 717, 379

Benjamin, R. A. & Danly, L. 1997, ApJ, 481, 764

Bernard, E. J., Ferguson, A. M. N., Schlafly, E. F., Martin, N. F., Rix, H.-W., Bell, E. F., Finkbeiner, D. P., Goldman, B., Martínez-Delgado, D., Sesar, B., Wyse, R. F. G., Burgett, W. S., Chambers, K. C., Draper, P. W., Hodapp, K. W., Kaiser, N., Kudritzki, R.-P., Magnier, E. A., Metcalfe, N., Wainscoat, R. J., & Waters, C. 2016, MNRAS, 463, 1759

Besla, G., Kallivayalil, N., Hernquist, L., van der Marel, R. P., Cox, T. J., & Kereš, D. 2010, ApJL, 721, L97

—. 2012, MNRAS, 421, 2109

Bigiel, F., Leroy, A., Walter, F., Brinks, E., de Blok, W. J. G., Madore, B., & Thornley, M. D. 2008, AJ, 136, 2846

Binney, J. & Tremaine, S. 2008, Galactic Dynamics: Second Edition (Princeton University Press)

Bizyaev, D., Walterbos, R. A. M., Yoachim, P., Riffel, R. A., Fernández-Trincado, J. G., Pan, K., Diamond-Stanic, A. M., Jones, A., Thomas, D., Cleary, J., & Brinkmann, J. 2017, ApJ, 839, 87

Bland-Hawthorn, J. & Gerhard, O. 2016, ARA&A, 54, 529

Boettcher, E., Zweibel, E. G., Gallagher, III, J. S., & Benjamin, R. A. 2016, ApJ, 832, 118

Bohlin, R. C., Savage, B. D., & Drake, J. F. 1978, ApJ, 224, 132

Bordoloi, R., Fox, A. J., Lockman, F. J., Wakker, B. P., Jenkins, E. B., Savage, B. D., Hernandez, S., Tumlinson, J., Bland-Hawthorn, J., & Kim, T.-S. 2017, ApJ, 834, 191

Bordoloi, R., Lilly, S. J., Knobel, C., Bolzonella, M., Kampczyk, P., Carollo, C. M., Iovino, A., Zucca, E., Contini, T., Kneib, J.-P., Le Fevre, O., Mainieri, V., Renzini, A., Scodeggio, M., Zamorani, G., Balestra, I., Bardelli, S., Bongiorno, A., Caputi, K., Cucciati, O., de la Torre, S., de Ravel, L., Garilli, B., Kovač, K., Lamareille, F., Le Borgne, J.-F., Le Brun, V., Maier, C., Mignoli, M., Pello, R., Peng, Y., Perez Montero, E., Presotto, V., Scarlata, C., Silverman, J., Tanaka, M., Tasca, L., Tresse, L., Vergani, D., Barnes, L., Cappi, A., Cimatti, A., Coppa, G., Diener, C., Franzetti, P., Koekemoer, A., López-Sanjuan, C., McCracken, H. J., Moresco, M., Nair, P., Oesch, P., Pozzetti, L., & Welikala, N. 2011, ApJ, 743, 10

Bordoloi, R., Tumlinson, J., Werk, J. K., Oppenheimer, B. D., Peeples, M. S., Prochaska, J. X., Tripp, T. M., Katz, N., Davé, R., Fox, A. J., Thom, C., Ford, A. B., Weinberg, D. H., Burchett, J. N., & Kollmeier, J. A. 2014, ApJ, 796, 136

Borisova, E., Cantalupo, S., Lilly, S. J., Marino, R. A., Gallego, S. G., Bacon, R., Blaizot, J., Bouché, N., Brinchmann, J., Carollo, C. M., Caruana, J., Finley, H., Herenz, E. C., Richard, J., Schaye, J., Straka, L. A., Turner, M. L., Urrutia, T., Verhamme, A., & Wisotzki, L. 2016, ApJ, 831, 39

Borkowski, K. J., Balbus, S. A., & Fristrom, C. C. 1990, ApJ, 355, 501

Borthakur, S., Heckman, T., Tumlinson, J., Bordoloi, R., Thom, C., Catinella, B., Schiminovich, D., Davé, R., Kauffmann, G., Moran, S. M., & Saintonge, A. 2015, ApJ, 813, 46

Bouché, N., Hohensee, W., Vargas, R., Kacprzak, G. G., Martin, C. L., Cooke, J., & Churchill, C. W. 2012, MNRAS, 426, 801

Bowen, D. V., Blades, J. C., & Pettini, M. 1995, ApJ, 448, 634

Bowen, D. V., Jenkins, E. B., Tripp, T. M., Sembach, K. R., Savage, B. D., Moos, H. W., Oegerle, W. R., Friedman, S. D., Gry, C., Kruk, J. W., Murphy, E., Sankrit, R., Shull, J. M., Sonneborn, G., & York, D. G. 2008, ApJS, 176, 59

Braun, R. & Thilker, D. A. 2004, A&A, 417, 421

Bregman, J. N. 1980, ApJ, 236, 577

—. 2007, ARA&A, 45, 221

Breysacher, J. 1981, A&AS, 43, 203

Bruhweiler, F. C., Miskey, C. L., & Smith Neubig, M. 2003, AJ, 125, 3082

Brüns, C., Kerp, J., Staveley-Smith, L., Mebold, U., Putman, M. E., Haynes, R. F., Kalberla, P. M. W., Muller, E., & Filipovic, M. D. 2005, A&A, 432, 45

Bryan, G. L. & Norman, M. L. 1998, ApJ, 495, 80

Bryant, J. J., Owers, M. S., Robotham, A. S. G., Croom, S. M., Driver, S. P., Drinkwater, M. J., Lorente, N. P. F., Cortese, L., Scott, N., Colless, M., Schaefer, A., Taylor, E. N., Konstantopoulos, I. S., Allen, J. T., Baldry, I., Barnes, L., Bauer, A. E., Bland-Hawthorn, J., Bloom, J. V., Brooks, A. M., Brough, S., Cecil, G., Couch, W., Croton, D., Davies, R., Ellis, S., Fogarty, L. M. R., Foster, C., Glazebrook, K., Goodwin, M., Green, A., Gunawardhana, M. L., Hampton, E., Ho, I.-T., Hopkins, A. M., Kewley, L., Lawrence,

J. S., Leon-Saval, S. G., Leslie, S., McElroy, R., Lewis, G., Liske, J., López-Sánchez, Á. R., Mahajan, S., Medling, A. M., Metcalfe, N., Meyer, M., Mould, J., Obreschkow, D., O'Toole, S., Pracy, M., Richards, S. N., Shanks, T., Sharp, R., Sweet, S. M., Thomas, A. D., Tonini, C., & Walcher, C. J. 2015, MNRAS, 447, 2857

Bundy, K., Bershady, M. A., Law, D. R., Yan, R., Drory, N., MacDonald, N., Wake, D. A., Cherinka, B., Sánchez-Gallego, J. R., Weijmans, A.-M., Thomas, D., Tremonti, C., Masters, K., Coccato, L., Diamond-Stanic, A. M., Aragón-Salamanca, A., Avila-Reese, V., Badenes, C., Falcón-Barroso, J., Belfiore, F., Bizyaev, D., Blanc, G. A., Bland-Hawthorn, J., Blanton, M. R., Brownstein, J. R., Byler, N., Cappellari, M., Conroy, C., Dutton, A. A., Emsellem, E., Etherington, J., Frinchaboy, P. M., Fu, H., Gunn, J. E., Harding, P., Johnston, E. J., Kauffmann, G., Kinemuchi, K., Klaene, M. A., Knapen, J. H., Leauthaud, A., Li, C., Lin, L., Maiolino, R., Malanushenko, V., Malanushenko, E., Mao, S., Maraston, C., McDermid, R. M., Merrifield, M. R., Nichol, R. C., Oravetz, D., Pan, K., Parejko, J. K., Sanchez, S. F., Schlegel, D., Simmons, A., Steele, O., Steinmetz, M., Thanjavur, K., Thompson, B. A., Tinker, J. L., van den Bosch, R. C. E., Westfall, K. B., Wilkinson, D., Wright, S., Xiao, T., & Zhang, K. 2015, ApJ, 798, 7

Burchett, J. N., Tripp, T. M., Bordoloi, R., Werk, J. K., Prochaska, J. X., Tumlinson, J., Willmer, C. N. A., O'Meara, J., & Katz, N. 2016, ApJ, 832, 124

Cantalupo, S., Arrigoni-Battaia, F., Prochaska, J. X., Hennawi, J. F., & Madau, P. 2014, Nature, 506, 63

Cen, R. & Ostriker, J. P. 1999, ApJ, 514, 1

—. 2006, ApJ, 650, 560

Chambers, K. C., Magnier, E. A., Metcalfe, N., Flewelling, H. A., Huber, M. E., Waters, C. Z., Denneau, L., Draper, P. W., Farrow, D., Finkbeiner, D. P., Holmberg, C., Koppenhoefer, J., Price, P. A., Saglia, R. P., Schlafly, E. F., Smartt, S. J., Sweeney, W., Wainscoat, R. J., Burgett, W. S., Grav, T., Heasley, J. N., Hodapp, K. W., Jedicke, R., Kaiser, N., Kudritzki, R.-P., Luppino, G. A., Lupton, R. H., Monet, D. G., Morgan, J. S., Onaka, P. M., Stubbs, C. W., Tonry, J. L., Banados, E., Bell, E. F., Bender, R., Bernard, E. J., Botticella, M. T., Casertano, S., Chastel, S., Chen, W.-P., Chen, X., Cole, S., Deacon, N., Frenk, C., Fitzsimmons, A., Gezari, S., Goessl, C., Goggia, T., Goldman, B., Grebel, E. K., Hambly, N. C., Hasinger, G., Heavens, A. F., Heckman, T. M., Henderson, R., Henning, T., Holman, M., Hopp, U., Ip, W.-H., Isani, S., Keyes, C. D., Koekemoer, A., Kotak, R.,

Long, K. S., Lucey, J. R., Liu, M., Martin, N. F., McLean, B., Morganson, E., Murphy, D. N. A., Nieto-Santisteban, M. A., Norberg, P., Peacock, J. A., Pier, E. A., Postman, M., Primak, N., Rae, C., Rest, A., Riess, A., Riffeser, A., Rix, H. W., Roser, S., Schilbach, E., Schultz, A. S. B., Scolnic, D., Szalay, A., Seitz, S., Shiao, B., Small, E., Smith, K. W., Soderblom, D., Taylor, A. N., Thakar, A. R., Thiel, J., Thilker, D., Urata, Y., Valenti, J., Walter, F., Watters, S. P., Werner, S., White, R., Wood-Vasey, W. M., & Wyse, R. 2016, ArXiv e-prints

Chen, H.-W., Gauthier, J.-R., Sharon, K., Johnson, S. D., Nair, P., & Liang, C. J. 2014, MNRAS, 438, 1435

Chen, H.-W., Helsby, J. E., Gauthier, J.-R., Shectman, S. A., Thompson, I. B., & Tinker, J. L. 2010a, ApJ, 714, 1521

Chen, H.-W., Lanzetta, K. M., & Webb, J. K. 2001a, ApJ, 556, 158

Chen, H.-W., Lanzetta, K. M., Webb, J. K., & Barcons, X. 1998, ApJ, 498, 77

—. 2001b, ApJ, 559, 654

Chen, H.-W. & Tinker, J. L. 2008, ApJ, 687, 745

Chen, H.-W., Wild, V., Tinker, J. L., Gauthier, J.-R., Helsby, J. E., Shectman, S. A., & Thompson, I. B. 2010b, ApJL, 724, L176

Chen, S.-F. S., Simcoe, R. A., Torrey, P., Bañados, E., Cooksey, K., Cooper, T., Furesz, G., Matejek, M., Miller, D., Turner, M., Venemans, B., Decarli, R., Farina, E. P., Mazzucchelli, C., & Walter, F. 2017, ApJ, 850, 188

Chen, Y.-M., Tremonti, C. A., Heckman, T. M., Kauffmann, G., Weiner, B. J., Brinchmann, J., & Wang, J. 2010c, AJ, 140, 445

—. 2010d, AJ, 140, 445

Chiappini, C., Matteucci, F., & Gratton, R. 1997, ApJ, 477, 765

Chiappini, C., Matteucci, F., & Romano, D. 2001, ApJ, 554, 1044

Chisholm, J., Tremonti, C. A., Leitherer, C., Chen, Y., & Wofford, A. 2016, MNRAS, 457, 3133

Chomiuk, L. & Povich, M. S. 2011, AJ, 142, 197

Coil, A. L., Weiner, B. J., Holz, D. E., Cooper, M. C., Yan, R., & Aird, J. 2011, ApJ, 743, 46

Collins, J. A., Rand, R. J., Duric, N., & Walterbos, R. A. M. 2000, ApJ, 536, 645

Collins, J. A., Shull, J. M., & Giroux, M. L. 2005, ApJ, 623, 196

—. 2009, ApJ, 705, 962

Connors, T. W., Kawata, D., & Gibson, B. K. 2006, MNRAS, 371, 108

Cooksey, K. L., Kao, M. M., Simcoe, R. A., O'Meara, J. M., & Prochaska, J. X. 2013, ApJ, 763, 37

Corbelli, E. 2003, MNRAS, 342, 199

Corbelli, E. & Schneider, S. E. 1997, ApJ, 479, 244

Corlies, L. & Schiminovich, D. 2016, ApJ, 827, 148

Courteau, S. & van den Bergh, S. 1999, AJ, 118, 337

Crockett, N. R., Garnett, D. R., Massey, P., & Jacoby, G. 2006, ApJ, 637, 741

Daddi, E., Bournaud, F., Walter, F., Dannerbauer, H., Carilli, C. L., Dickinson, M., Elbaz, D., Morrison, G. E., Riechers, D., Onodera, M., Salmi, F., Krips, M., & Stern, D. 2010, ApJ, 713, 686

Dame, T. M., Hartmann, D., & Thaddeus, P. 2001, ApJ, 547, 792

Danforth, C. W. & Blair, W. P. 2006, ApJ, 646, 205

Danforth, C. W., Keeney, B. A., Stocke, J. T., Shull, J. M., & Yao, Y. 2010, ApJ, 720, 976

Debes, J. & et al. 2016

Deul, E. R. & van der Hulst, J. M. 1987, A&AS, 67, 509

Dickey, J. M. & Lockman, F. J. 1990, ARA&A, 28, 215

Diehl, R., Halloin, H., Kretschmer, K., Lichti, G. G., Schönfelder, V., Strong, A. W., von Kienlin, A., Wang, W., Jean, P., Knödlseder, J., Roques, J.-P., Weidenspointner, G., Schanne, S., Hartmann, D. H., Winkler, C., & Wunderer, C. 2006, Nature, 439, 45

D'Onghia, E. & Fox, A. J. 2015, ArXiv e-prints

Dopita, M. A. & Sutherland, R. S. 1996, ApJS, 102, 161

Draine, B. T. 2011, Physics of the Interstellar and Intergalactic Medium (Princeton University Press, 2011. ISBN: 978-0-691-12214-4)

Drissen, L., Crowther, P. A., Úbeda, L., & Martin, P. 2008, MNRAS, 389, 1033

Emerick, A., Bryan, G., & Putman, M. E. 2015, MNRAS, 453, 4051

Engargiola, G., Plambeck, R. L., Rosolowsky, E., & Blitz, L. 2003, ApJS, 149, 343

Erb, D. K. 2008, ApJ, 674, 151

Erb, D. K., Steidel, C. C., Shapley, A. E., Pettini, M., Reddy, N. A., & Adelberger, K. L. 2006, ApJ, 647, 128

Ferland, G. J., Korista, K. T., Verner, D. A., Ferguson, J. W., Kingdon, J. B., & Verner, E. M. 1998, PASP, 110, 761

Ferland, G. J., Porter, R. L., van Hoof, P. A. M., Williams, R. J. R., Abel, N. P., Lykins, M. L., Shaw, G., Henney, W. J., & Stancil, P. C. 2013, Rev. Mexicana Astron. Astrofis., 49, 137

Fernández, X., Joung, M. R., & Putman, M. E. 2012, ApJ, 749, 181

Fernández, X., van Gorkom, J. H., Hess, K. M., Pisano, D. J., Kreckel, K., Momjian, E., Popping, A., Oosterloo, T., Chomiuk, L., Verheijen, M. A. W., Henning, P. A., Schiminovich, D., Bershady, M. A., Wilcots, E. M., & Scoville, N. 2013, ApJL, 770, L29

Ford, A. B., Oppenheimer, B. D., Davé, R., Katz, N., Kollmeier, J. A., & Weinberg, D. H. 2013, MNRAS, 432, 89

Ford, H. A., Lockman, F. J., & McClure-Griffiths, N. M. 2010, ApJ, 722, 367

Fox, A. J., Bordoloi, R., Savage, B. D., Lockman, F. J., Jenkins, E. B., Wakker, B. P., Bland-Hawthorn, J., Hernandez, S., Kim, T.-S., Benjamin, R. A., Bowen, D. V., & Tumlinson, J. 2015, ApJL, 799, L7

Fox, A.-J. & et al. 2015

Fox, A. J., Richter, P., Wakker, B. P., Lehner, N., Howk, J. C., Ben Bekhti, N., Bland-Hawthorn, J., & Lucas, S. 2013, ApJ, 772, 110

Fox, A. J., Savage, B. D., & Wakker, B. P. 2006, ApJS, 165, 229

Fox, A. J., Savage, B. D., Wakker, B. P., Richter, P., Sembach, K. R., & Tripp, T. M. 2004, ApJ, 602, 738

Fox, A. J., Wakker, B. P., Barger, K. A., Hernandez, A. K., Richter, P., Lehner, N., Bland-Hawthorn, J., Charlton, J. C., Westmeier, T., Thom, C., Tumlinson, J., Misawa, T., Howk, J. C., Haffner, L. M., Ely, J., Rodriguez-Hidalgo, P., & Kumari, N. 2014, ApJ, 787, 147

Fox, A. J., Wakker, B. P., Savage, B. D., Tripp, T. M., Sembach, K. R., & Bland-Hawthorn, J. 2005, ApJ, 630, 332

Fox, A. J., Wakker, B. P., Smoker, J. V., Richter, P., Savage, B. D., & Sembach, K. R. 2010, ApJ, 718, 1046

Fox, A.-J., e. a. 2015

Fraternali, F. & Binney, J. J. 2006, MNRAS, 366, 449

—. 2008, MNRAS, 386, 935

Fraternali, F., Oosterloo, T., Sancisi, R., & van Moorsel, G. 2001, ApJL, 562, L47

Fraternali, F., Oosterloo, T. A., Sancisi, R., & Swaters, R. 2005, in Astronomical Society of the Pacific Conference Series, Vol. 331, Extra-Planar Gas, ed. R. Braun, 239

Fraternali, F., van Moorsel, G., Sancisi, R., & Oosterloo, T. 2002, AJ, 123, 3124

Freedman, W. L., Wilson, C. D., & Madore, B. F. 1991, ApJ, 372, 455

Fukugita, M., Hogan, C. J., & Peebles, P. J. E. 1998, ApJ, 503, 518

Gaensler, B. M., Madsen, G. J., Chatterjee, S., & Mao, S. A. 2008, PASA, 25, 184

Garcia-Appadoo, D. A., West, A. A., Dalcanton, J. J., Cortese, L., & Disney, M. J. 2009, MNRAS, 394, 340

Gardiner, L. T., Sawa, T., & Fujimoto, M. 1994, MNRAS, 266, 567

Gauthier, J.-R., Chen, H.-W., & Tinker, J. L. 2010, ApJ, 716, 1263

Gentile, G., Józsa, G. I. G., Serra, P., Heald, G. H., de Blok, W. J. G., Fraternali, F., Patterson, M. T., Walterbos, R. A. M., & Oosterloo, T. 2013, A&A, 554, A125

Genzel, R., Tacconi, L. J., Gracia-Carpio, J., Sternberg, A., Cooper, M. C., Shapiro, K., Bolatto, A., Bouché, N., Bournaud, F., Burkert, A., Combes, F., Comerford, J., Cox, P., Davis, M., Schreiber, N. M. F., Garcia-Burillo, S., Lutz, D., Naab, T., Neri, R., Omont, A., Shapley, A., & Weiner, B. 2010, MNRAS, 407, 2091

Ghavamian, P., Aloisi, A., Lennon, D., Hartig, G., Kriss, G. A., Oliveira, C., Massa, D., Keyes, T., Proffitt, C., Delker, T., & Osterman, S. 2009, Preliminary Characterization of the Post- Launch Line Spread Function of COS, Tech. rep.

Gibson, B. K., Giroux, M. L., Penton, S. V., Putman, M. E., Stocke, J. T., & Shull, J. M. 2000, AJ, 120, 1830

Giovanelli, R., Haynes, M. P., Kent, B. R., Perillat, P., Saintonge, A., Brosch, N., Catinella, B., Hoffman, G. L., Stierwalt, S., Spekkens, K., Lerner, M. S., Masters, K. L., Momjian, E., Rosenberg, J. L., Springob, C. M., Boselli, A., Charmandaris, V., Darling, J. K., Davies, J., Garcia Lambas, D., Gavazzi, G., Giovanardi, C., Hardy, E., Hunt, L. K., Iovino, A., Karachentsev, I. D., Karachentseva, V. E., Koopmann, R. A., Marinoni, C., Minchin, R., Muller, E., Putman, M., Pantoja, C., Salzer, J. J., Scodeggio, M., Skillman, E., Solanes, J. M., Valotto, C., van Driel, W., & van Zee, L. 2005, AJ, 130, 2598

Gnat, O. & Sternberg, A. 2007, ApJS, 168, 213

Gnat, O., Sternberg, A., & McKee, C. F. 2010, ApJ, 718, 1315

Gratier, P., Braine, J., Rodriguez-Fernandez, N. J., Schuster, K. F., Kramer, C., Xilouris, E. M., Tabatabaei, F. S., Henkel, C., Corbelli, E., Israel, F., van der Werf, P. P., Calzetti, D., Garcia-Burillo, S., Sievers, A., Combes, F., Wiklind, T., Brouillet, N., Herpin, F., Bontemps, S., Aalto, S., Koribalski, B., van der Tak, F., Wiedner, M. C., Röllig, M., & Mookerjea, B. 2010, A&A, 522, A3

Grcevich, J. & Putman, M. E. 2009, ApJ, 696, 385

Grossi, M., Giovanardi, C., Corbelli, E., Giovanelli, R., Haynes, M. P., Martin, A. M., Saintonge, A., & Dowell, J. D. 2008, A&A, 487, 161

Gupta, A., Mathur, S., Krongold, Y., Nicastro, F., & Galeazzi, M. 2012, ApJL, 756, L8

Haardt, F. & Madau, P. 2001, in Clusters of Galaxies and the High Redshift Universe Observed in X-rays, ed. D. M. Neumann & J. T. V. Tran

Haardt, F. & Madau, P. 2012, ApJ, 746, 125

Haffner, L. M., Dettmar, R.-J., Beckman, J. E., Wood, K., Slavin, J. D., Giammanco, C., Madsen, G. J., Zurita, A., & Reynolds, R. J. 2009, Reviews of Modern Physics, 81, 969

Haffner, L. M., Reynolds, R. J., Tufte, S. L., Madsen, G. J., Jaehnig, K. P., & Percival, J. W. 2003, ApJS, 149, 405

Haiman, Z., Spaans, M., & Quataert, E. 2000, ApJL, 537, L5

Hartmann, D. & Burton, W. B. 1997, Atlas of Galactic Neutral Hydrogen

Hayashino, T., Matsuda, Y., Tamura, H., Yamauchi, R., Yamada, T., Ajiki, M., Fujita, S. S., Murayama, T., Nagao, T., Ohta, K., Okamura, S., Ouchi, M., Shimasaku, K., Shioya, Y., & Taniguchi, Y. 2004, AJ, 128, 2073

Heald, G., Józsa, G., Serra, P., Zschaechner, L., Rand, R., Fraternali, F., Oosterloo, T., Walterbos, R., Jütte, E., & Gentile, G. 2011, A&A, 526, A118

Heald, G. H., Rand, R. J., Benjamin, R. A., & Bershady, M. A. 2006a, ApJ, 647, 1018

Heald, G. H., Rand, R. J., Benjamin, R. A., Collins, J. A., & Bland-Hawthorn, J. 2006b, ApJ, 636, 181

Heckman, T. M., Lehnert, M. D., Strickland, D. K., & Armus, L. 2000, ApJS, 129, 493

Heckman, T. M., Norman, C. A., Strickland, D. K., & Sembach, K. R. 2002, ApJ, 577, 691

Heitsch, F. & Putman, M. E. 2009, ApJ, 698, 1485

Hennawi, J. F., Prochaska, J. X., Cantalupo, S., & Arrigoni-Battaia, F. 2015, Science, 348, 779

Heyer, M. H., Corbelli, E., Schneider, S. E., & Young, J. S. 2004, ApJ, 602, 723

HI4PI Collaboration, Ben Bekhti, N., Flöer, L., Keller, R., Kerp, J., Lenz, D., Winkel, B., Bailin, J., Calabretta, M. R., Dedes, L., Ford, H. A., Gibson, B. K., Haud, U., Janowiecki, S., Kalberla, P. M. W., Lockman, F. J., McClure-Griffiths, N. M., Murphy, T., Nakanishi, H., Pisano, D. J., & Staveley-Smith, L. 2016, A&A, 594, A116

Ho, I.-T., Medling, A. M., Bland-Hawthorn, J., Groves, B., Kewley, L. J., Kobayashi, C., Dopita, M. A., Leslie, S. K., Sharp, R., Allen, J. T., Bourne, N., Bryant, J. J., Cortese, L., Croom, S. M., Dunne, L., Fogarty, L. M. R., Goodwin, M., Green, A. W., Konstantopoulos, I. S., Lawrence, J. S., Lorente, N. P. F., Owers, M. S., Richards, S., Sweet, S. M., Tescari, E., & Valiante, E. 2016, MNRAS, 457, 1257

Ho, S. H., Martin, C. L., Kacprzak, G. G., & Churchill, C. W. 2017, ApJ, 835, 267

Hoopes, C. G., Sembach, K. R., Howk, J. C., Savage, B. D., & Fullerton, A. W. 2002, ApJ, 569, 233

Hoopes, C. G. & Walterbos, R. A. M. 2000, ApJ, 541, 597

Houck, J. C. & Bregman, J. N. 1990, ApJ, 352, 506

Howk, J. C., Savage, B. D., Sembach, K. R., & Hoopes, C. G. 2002, ApJ, 572, 264

Howk, J. C., Sembach, K. R., & Savage, B. D. 2006, ApJ, 637, 333

Hsu, W.-H., Putman, M. E., Heitsch, F., Stanimirović, S., Peek, J. E. G., & Clark, S. E. 2011, AJ, 141, 57

Hummels, C. B., Bryan, G. L., Smith, B. D., & Turk, M. J. 2013, MNRAS, 430, 1548

Humphreys, R. M., Davidson, K., Grammer, S., Kneeland, N., Martin, J. C., Weis, K., & Burggraf, B. 2013, ApJ, 773, 46

Hunter, J. D. 2007, Computing In Science & Engineering, 9, 90

Jenkins, E. B. 1978, ApJ, 219, 845

—. 2009, ApJ, 700, 1299

Jin, S. & Lynden-Bell, D. 2008, MNRAS, 383, 1686

Joung, M. R., Bryan, G. L., & Putman, M. E. 2012a, ApJ, 745, 148

Joung, M. R., Putman, M. E., Bryan, G. L., Fernández, X., & Peek, J. E. G. 2012b, ApJ, 759, 137

—. 2012c, ApJ, 759, 137

Kacprzak, G. G., Churchill, C. W., Ceverino, D., Steidel, C. C., Klypin, A., & Murphy, M. T. 2010, ApJ, 711, 533

Kacprzak, G. G., Churchill, C. W., Steidel, C. C., & Murphy, M. T. 2008, AJ, 135, 922

Kalberla, P. M. W., Burton, W. B., Hartmann, D., Arnal, E. M., Bajaja, E., Morras, R., & Pöppel, W. G. L. 2005, A&A, 440, 775

Kallivayalil, N., van der Marel, R. P., Besla, G., Anderson, J., & Alcock, C. 2013, ApJ, 764, 161

Kam, Z. S., Carignan, C., Chemin, L., Amram, P., & Epinat, B. 2015, MNRAS, 449, 4048

Keenan, O., Davies, J., Taylor, R., & Minchin, R. 2015, ArXiv e-prints

Keenan, O. C., Davies, J. I., Taylor, R., & Minchin, R. F. 2016, MNRAS, 456, 951

Keeney, B. A., Stocke, J. T., Danforth, C. W., Shull, J. M., Pratt, C. T., Froning, C. S., Green, J. C., Penton, S. V., & Savage, B. D. 2017, ApJS, 230, 6

Keeney, B. A., Stocke, J. T., Rosenberg, J. L., Danforth, C. W., Ryan-Weber, E. V., Shull, J. M., Savage, B. D., & Green, J. C. 2013, ApJ, 765, 27

Kennicutt, Jr., R. C. 1998, ApJ, 498, 541

Kim, C.-G., Ostriker, E. C., & Kim, W.-T. 2014, ApJ, 786, 64

Klypin, A. A., Trujillo-Gomez, S., & Primack, J. 2011, ApJ, 740, 102

Kollmeier, J. A., Weinberg, D. H., Oppenheimer, B. D., Haardt, F., Katz, N., Davé, R., Fardal, M., Madau, P., Danforth, C., Ford, A. B., Peeples, M. S., & McEwen, J. 2014, ApJL, 789, L32

Kuno, N., Sato, N., Nakanishi, H., Hirota, A., Tosaki, T., Shioya, Y., Sorai, K., Nakai, N., Nishiyama, K., & Vila-Vilaró, B. 2007, PASJ, 59, 117

Kwak, K., Henley, D. B., & Shelton, R. L. 2011, ApJ, 739, 30

Lanzetta, K. M., Bowen, D. V., Tytler, D., & Webb, J. K. 1995, ApJ, 442, 538

Lebouteiller, V., Kunth, D., Lequeux, J., Aloisi, A., Désert, J.-M., Hébrard, G., Lecavelier Des Étangs, A., & Vidal-Madjar, A. 2006, A&A, 459, 161

Lehner, N. & Howk, J. C. 2007, MNRAS, 377, 687

—. 2010, ApJL, 709, L138

—. 2011a, Science, 334, 955

—. 2011b, Science, 334, 955

Lehner, N., Howk, J. C., Thom, C., Fox, A. J., Tumlinson, J., Tripp, T. M., & Meiring, J. D. 2012, MNRAS, 424, 2896

Lehner, N., Howk, J. C., & Wakker, B. P. 2015, ApJ, 804, 79

Lehner, N., Staveley-Smith, L., & Howk, J. C. 2009, ApJ, 702, 940

Lehner, N., Zech, W. F., Howk, J. C., & Savage, B. D. 2011, ApJ, 727, 46

Leitherer, C., Schaerer, D., Goldader, J. D., Delgado, R. M. G., Robert, C., Kune, D. F., de Mello, D. F., Devost, D., & Heckman, T. M. 1999, ApJS, 123, 3

Leroy, A. K., Walter, F., Bigiel, F., Usero, A., Weiss, A., Brinks, E., de Blok, W. J. G., Kennicutt, R. C., Schuster, K.-F., Kramer, C., Wiesemeyer, H. W., & Roussel, H. 2009, AJ, 137, 4670

Leroy, A. K., Walter, F., Brinks, E., Bigiel, F., de Blok, W. J. G., Madore, B., & Thornley, M. D. 2008, AJ, 136, 2782

Levine, E. S., Blitz, L., & Heiles, C. 2006, ApJ, 643, 881

Levine, E. S., Heiles, C., & Blitz, L. 2008, ApJ, 679, 1288

Liang, C. J. & Chen, H.-W. 2014, MNRAS, 445, 2061

Lockman, F. J. 2002, ApJL, 580, L47

Lockman, F. J., Free, N. L., & Shields, J. C. 2012, AJ, 144, 52

Lockman, F. J., Murphy, E. M., Petty-Powell, S., & Urick, V. J. 2002, ApJS, 140, 331

Magrini, L., Corbelli, E., & Galli, D. 2007a, A&A, 470, 843

Magrini, L., Vílchez, J. M., Mampaso, A., Corradi, R. L. M., & Leisy, P. 2007b, A&A, 470, 865

Marasco, A. & Fraternali, F. 2011, A&A, 525, A134

Marasco, A., Fraternali, F., & Binney, J. J. 2012, MNRAS, 419, 1107

Marasco, A., Marinacci, F., & Fraternali, F. 2013, MNRAS, 433, 1634

Marinacci, F., Fraternali, F., Nipoti, C., Binney, J., Ciotti, L., & Londrillo, P. 2011, MNRAS, 415, 1534

Markwardt, C. B. 2009, in Astronomical Society of the Pacific Conference Series, Vol. 411, Astronomical Data Analysis Software and Systems XVIII, ed. D. A. Bohlender, D. Durand, & P. Dowler, 251

Martin, C. L. 1999, ApJ, 513, 156

—. 2005, ApJ, 621, 227

Martin, C. L., Shapley, A. E., Coil, A. L., Kornei, K. A., Bundy, K., Weiner, B. J., Noeske, K. G., & Schiminovich, D. 2012, ApJ, 760, 127

Massey, P., Armandroff, T. E., Pyke, R., Patel, K., & Wilson, C. D. 1995, AJ, 110, 2715

Massey, P., Bianchi, L., Hutchings, J. B., & Stecher, T. P. 1996, ApJ, 469, 629

Massey, P., Olsen, K. A. G., Hodge, P. W., Strong, S. B., Jacoby, G. H., Schlingman, W., & Smith, R. C. 2006, AJ, 131, 2478

Matejek, M. S. & Simcoe, R. A. 2012, ApJ, 761, 112

Matsuda, Y., Yamada, T., Hayashino, T., Tamura, H., Yamauchi, R., Ajiki, M., Fujita, S. S., Murayama, T., Nagao, T., Ohta, K., Okamura, S., Ouchi, M., Shimasaku, K., Shioya, Y., & Taniguchi, Y. 2004, AJ, 128, 569

McConnachie, A. W., Irwin, M. J., Ibata, R. A., Dubinski, J., Widrow, L. M., Martin, N. F., Côté, P., Dotter, A. L., Navarro, J. F., Ferguson, A. M. N., Puzia, T. H., Lewis, G. F., Babul, A., Barmby, P., Bienaymé, O., Chapman, S. C., Cockcroft, R., Collins, M. L. M., Fardal, M. A., Harris, W. E., Huxor, A., Mackey, A. D., Peñarrubia, J., Rich, R. M., Richer, H. B., Siebert, A., Tanvir, N., Valls-Gabaud, D., & Venn, K. A. 2009, Nature, 461, 66

McGaugh, S. S. 2005, ApJ, 632, 859

McMillan, P. J. 2011, MNRAS, 414, 2446

Meiring, J. D., Tripp, T. M., Werk, J. K., Howk, J. C., Jenkins, E. B., Prochaska, J. X., Lehner, N., & Sembach, K. R. 2013, ApJ, 767, 49

Ménard, B., Wild, V., Nestor, D., Quider, A., Zibetti, S., Rao, S., & Turnshek, D. 2011, MNRAS, 417, 801

Merritt, D., Ferrarese, L., & Joseph, C. L. 2001, Science, 293, 1116

Miller, M. J. & Bregman, J. N. 2013, ApJ, 770, 118

—. 2015, ApJ, 800, 14

Morton, D. C. 2003, ApJS, 149, 205

Murai, T. & Fujimoto, M. 1980, PASJ, 32, 581

Muratov, A. L., Kereš, D., Faucher-Giguère, C.-A., Hopkins, P. F., Quataert, E., & Murray, N. 2015, MNRAS, 454, 2691

Murphy, E. M., Lockman, F. J., & Savage, B. D. 1995, ApJ, 447, 642

Neugent, K. F. & Massey, P. 2011, ApJ, 733, 123

Nicastro, F., Zezas, A., Elvis, M., Mathur, S., Fiore, F., Cecchi-Pestellini, C., Burke, D., Drake, J., & Casella, P. 2003, Nature, 421, 719

Nidever, D. L., Majewski, S. R., & Butler Burton, W. 2008, ApJ, 679, 432

Nidever, D. L., Majewski, S. R., Butler Burton, W., & Nigra, L. 2010, ApJ, 723, 1618

Nielsen, N. M., Churchill, C. W., & Kacprzak, G. G. 2013, ApJ, 776, 115

Nielsen, N. M., Churchill, C. W., Kacprzak, G. G., Murphy, M. T., & Evans, J. L. 2016, ApJ, 818, 171

Oosterloo, T., Fraternali, F., & Sancisi, R. 2007, AJ, 134, 1019

Oppenheimer, B. D., Davé, R., Katz, N., Kollmeier, J. A., & Weinberg, D. H. 2012, MNRAS, 420, 829

Pachat, S., Narayanan, A., Khaire, V., Savage, B. D., Muzahid, S., & Wakker, B. P. 2017, MNRAS, 471, 792

Patel, E., Besla, G., & Sohn, T. 2016, ArXiv e-prints

Pathak, A., Pradhan, A. C., Sujatha, N. V., & Murthy, J. 2011, MNRAS, 412, 1105

Paturel, G., Petit, C., Prugniel, P., Theureau, G., Rousseau, J., Brouty, M., Dubois, P., & Cambrésy, L. 2003, A&A, 412, 45

Peek, J. E. G., Babler, B. L., Zheng, Y., Clark, S. E., Douglas, K. A., Korpela, E. J., Putman, M. E., Stanimirović, S., Gibson, S. J., & Heiles, C. 2018, ApJS, 234, 2

Peek, J. E. G., Bordoloi, R., Sana, H., Roman-Duval, J., Tumlinson, J., & Zheng, Y. 2016, ApJL, 828, L20

Peek, J. E. G., Heiles, C., Douglas, K. A., Lee, M.-Y., Grcevich, J., Stanimirović, S., Putman, M. E., Korpela, E. J., Gibson, S. J., Begum, A., Saul, D., Robishaw, T., & Krčo, M. 2011, ApJS, 194, 20

Peek, J. E. G., Heiles, C., Putman, M. E., & Douglas, K. 2009, ApJ, 692, 827

Peek, J. E. G., Putman, M. E., & Sommer-Larsen, J. 2008, ApJ, 674, 227

Peeples, M., Tumlinson, J., Fox, A., Aloisi, A., Fleming, S., Jedrzejewski, R., Oliveira, C., Ayres, T., Danforth, C., Keeney, B., & Jenkins, E. 2017, The Hubble Spectroscopic Legacy Archive, Tech. rep.

Peeples, M. S. & Shankar, F. 2011, MNRAS, 417, 2962

Peeples, M. S., Werk, J. K., Tumlinson, J., Oppenheimer, B. D., Prochaska, J. X., Katz, N., & Weinberg, D. H. 2014, ApJ, 786, 54

Pérez, F. & Granger, B. E. 2007, Computing in Science and Engineering, 9, 21

Persic, M. & Salucci, P. 1992, MNRAS, 258, 14P

Pisano, D. J., Barnes, D. G., Gibson, B. K., Staveley-Smith, L., Freeman, K. C., & Kilborn, V. A. 2007, ApJ, 662, 959

Pisano, D. J., Barnes, D. G., Staveley-Smith, L., Gibson, B. K., Kilborn, V. A., & Freeman, K. C. 2012, ApJS, 201, 39

Planck Collaboration, Ade, P. A. R., Aghanim, N., Alves, M. I. R., Arnaud, M., Ashdown, M., Aumont, J., Baccigalupi, C., Banday, A. J., Barreiro, R. B., & et al. 2016, A&A, 594, A25

Prochaska, J. X. 1999, ApJL, 511, L71

Prochaska, J. X., Tejos, N., Crighton, N., Burchett, J., & Tuo-Ji. 2016, linetools/linetools: Second major release

Prochaska, J. X., Weiner, B., Chen, H.-W., Mulchaey, J., & Cooksey, K. 2011, ApJ, 740, 91

Prochaska, J. X., Werk, J. K., Worseck, G., Tripp, T. M., Tumlinson, J., Burchett, J. N., Fox, A. J., Fumagalli, M., Lehner, N., Peeples, M. S., & Tejos, N. 2017, ApJ, 837, 169

Putman, M. E. 2017, in Astrophysics and Space Science Library, Vol. 430, Gas Accretion onto Galaxies, ed. A. Fox & R. Davé, 1

Putman, M. E., Peek, J. E. G., & Joung, M. R. 2012, ARA&A, 50, 491

Putman, M. E., Peek, J. E. G., Muratov, A., Gnedin, O. Y., Hsu, W., Douglas, K. A., Heiles, C., Stanimirovic, S., Korpela, E. J., & Gibson, S. J. 2009, ApJ, 703, 1486

Putman, M. E., Staveley-Smith, L., Freeman, K. C., Gibson, B. K., & Barnes, D. G. 2003, ApJ, 586, 170

Qu, Z. & Bregman, J. N. 2016, ApJ, 832, 189

Rand, R. J. 1997, ApJ, 474, 129

—. 2000, ApJL, 537, L13

Rauch, M. 1998, ARA&A, 36, 267

Reid, M. J., Menten, K. M., Brunthaler, A., Zheng, X. W., Dame, T. M., Xu, Y., Wu, Y., Zhang, B., Sanna, A., Sato, M., Hachisuka, K., Choi, Y. K., Immer, K., Moscadelli, L., Rygl, K. L. J., & Bartkiewicz, A. 2014, ApJ, 783, 130

Reynolds, R. J. 1993, in American Institute of Physics Conference Series, Vol. 278, Back to the Galaxy, ed. S. S. Holt & F. Verter, 156–165

Richter, P., Fox, A. J., Wakker, B. P., Lehner, N., Howk, J. C., Bland-Hawthorn, J., Ben Bekhti, N., & Fechner, C. 2013, ApJ, 772, 111

Richter, P., Nuza, S. E., Fox, A. J., Wakker, B. P., Lehner, N., Ben Bekhti, N., Fechner, C., Wendt, M., Howk, J. C., Muzahid, S., Ganguly, R., & Charlton, J. C. 2016, ArXiv e-prints

—. 2017, A&A, 607, A48

Robitaille, T. P. & Whitney, B. A. 2010, ApJL, 710, L11

Rogstad, D. H., Wright, M. C. H., & Lockhart, I. A. 1976, ApJ, 204, 703

Rubin, K. H. R., Prochaska, J. X., Koo, D. C., & Phillips, A. C. 2012, ApJL, 747, L26

Rubin, K. H. R., Prochaska, J. X., Koo, D. C., Phillips, A. C., Martin, C. L., & Winstrom, L. O. 2014, ApJ, 794, 156

Rubin, K. H. R., Weiner, B. J., Koo, D. C., Martin, C. L., Prochaska, J. X., Coil, A. L., & Newman, J. A. 2010, ApJ, 719, 1503

Rubin, R. H., Simpson, J. P., Colgan, S. W. J., Dufour, R. J., Brunner, G., McNabb, I. A., Pauldrach, A. W. A., Erickson, E. F., Haas, M. R., & Citron, R. I. 2008, MNRAS, 387, 45

Rudie, G. C., Steidel, C. C., Trainor, R. F., Rakic, O., Bogosavljević, M., Pettini, M., Reddy, N., Shapley, A. E., Erb, D. K., & Law, D. R. 2012, ApJ, 750, 67

Sancisi, R., Fraternali, F., Oosterloo, T., & van der Hulst, T. 2008, A&A Rev., 15, 189

Sancisi, R., Fraternali, F., Oosterloo, T., & van Moorsel, G. 2001, in Astronomical Society of the Pacific Conference Series, Vol. 230, Galaxy Disks and Disk Galaxies, ed. J. G. Funes & E. M. Corsini, 111–118

Sandstrom, K. M., Leroy, A. K., Walter, F., Bolatto, A. D., Croxall, K. V., Draine, B. T., Wilson, C. D., Wolfire, M., Calzetti, D., Kennicutt, R. C., Aniano, G., Donovan Meyer, J., Usero, A., Bigiel, F., Brinks, E., de Blok, W. J. G., Crocker, A., Dale, D., Engelbracht, C. W., Galametz, M., Groves, B., Hunt, L. K., Koda, J., Kreckel, K., Linz, H., Meidt, S., Pellegrini, E., Rix, H.-W., Roussel, H., Schinnerer, E., Schruba, A., Schuster, K.-F., Skibba, R., van der Laan, T., Appleton, P., Armus, L., Brandl, B., Gordon, K., Hinz, J., Krause, O., Montiel, E., Sauvage, M., Schmiedeke, A., Smith, J. D. T., & Vigroux, L. 2013, ApJ, 777, 5

Saul, D. R., Peek, J. E. G., Grcevich, J., Putman, M. E., Douglas, K. A., Korpela, E. J., Stanimirović, S., Heiles, C., Gibson, S. J., Lee, M., Begum, A., Brown, A. R. H., Burkhart, B., Hamden, E. T., Pingel, N. M., & Tonnesen, S. 2012, ApJ, 758, 44

Saul, D. R., Peek, J. E. G., & Putman, M. E. 2014, MNRAS, 441, 2266

Savage, B. D., Edgar, R. J., & Diplas, A. 1990, ApJ, 361, 107

Savage, B. D. & Lehner, N. 2006, ApJS, 162, 134

Savage, B. D., Lehner, N., Wakker, B. P., Sembach, K. R., & Tripp, T. M. 2005, ApJ, 626, 776

Savage, B. D. & Sembach, K. R. 1991, ApJ, 379, 245

—. 1996, ARA&A, 34, 279

Savage, B. D., Sembach, K. R., & Lu, L. 1997, AJ, 113, 2158

Savage, B. D., Sembach, K. R., Wakker, B. P., Richter, P., Meade, M., Jenkins, E. B., Shull, J. M., Moos, H. W., & Sonneborn, G. 2003, ApJS, 146, 125

Savage, B. D. & Wakker, B. P. 2009, ApJ, 702, 1472

Schiminovich, D., Catinella, B., Kauffmann, G., Fabello, S., Wang, J., Hummels, C., Lemonias, J., Moran, S. M., Wu, R., Giovanelli, R., Haynes, M. P., Heckman, T. M., Basu-Zych, A. R., Blanton, M. R., Brinchmann, J., Budavári, T., Gonçalves, T., Johnson, B. D., Kennicutt, R. C., Madore, B. F., Martin, C. D., Rich, M. R., Tacconi, L. J., Thilker, D. A., Wild, V., & Wyder, T. K. 2010, MNRAS, 408, 919

Schlafly, E. F., Meisner, A. M., Stutz, A. M., Kainulainen, J., Peek, J. E. G., Tchernyshyov, K., Rix, H.-W., Finkbeiner, D. P., Covey, K. R., Green, G. M., Bell, E. F., Burgett, W. S., Chambers, K. C., Draper, P. W., Flewelling, H., Hodapp, K. W., Kaiser, N., Magnier, E. A., Martin, N. F., Metcalfe, N., Wainscoat, R. J., & Waters, C. 2016, ApJ, 821, 78

Schlegel, D. J., Finkbeiner, D. P., & Davis, M. 1998, ApJ, 500, 525

Schmidt, T. M., Bigiel, F., Klessen, R. S., & de Blok, W. J. G. 2016, MNRAS, 457, 2642

Schruba, A., Leroy, A. K., Walter, F., Sandstrom, K., & Rosolowsky, E. 2010, ApJ, 722, 1699

Sembach, K. R., Wakker, B. P., Savage, B. D., Richter, P., Meade, M., Shull, J. M., Jenkins, E. B., Sonneborn, G., & Moos, H. W. 2003, ApJS, 146, 165

Shapiro, P. R. & Field, G. B. 1976, ApJ, 205, 762

Shapley, A. E., Steidel, C. C., Pettini, M., & Adelberger, K. L. 2003, ApJ, 588, 65

Shen, S., Madau, P., Aguirre, A., Guedes, J., Mayer, L., & Wadsley, J. 2012, ApJ, 760, 50

Shull, J. M. 2014, ApJ, 784, 142

Shull, J. M., Jones, J. R., Danforth, C. W., & Collins, J. A. 2009, ApJ, 699, 754

Shull, J. M., Moloney, J., Danforth, C. W., & Tilton, E. M. 2015, ApJ, 811, 3

Shull, J. M., Smith, B. D., & Danforth, C. W. 2012, ApJ, 759, 23

Shull, J. M., Stevans, M., Danforth, C., Penton, S. V., Lockman, F. J., & Arav, N. 2011, ApJ, 739, 105

Slavin, J. D., Shull, J. M., & Begelman, M. C. 1993, ApJ, 407, 83

Smoker, J. V., Fox, A. J., & Keenan, F. P. 2011, MNRAS, 415, 1105

Somerville, R. S. & Davé, R. 2015, ARA&A, 53, 51

Sommer-Larsen, J. 2006, ApJL, 644, L1

Spekkens, K., Urbancic, N., Mason, B. S., Willman, B., & Aguirre, J. E. 2014, ApJL, 795, L5

Stanimirović, S., Hoffman, S., Heiles, C., Douglas, K. A., Putman, M., & Peek, J. E. G. 2008, ApJ, 680, 276

Steidel, C. C. 1990, ApJS, 74, 37

Steidel, C. C., Adelberger, K. L., Shapley, A. E., Pettini, M., Dickinson, M., & Giavalisco, M. 2000, ApJ, 532, 170

—. 2003, ApJ, 592, 728

Stern, J., Hennawi, J. F., Prochaska, J. X., & Werk, J. K. 2016, ApJ, 830, 87

Stewart, K. R., Kaufmann, T., Bullock, J. S., Barton, E. J., Maller, A. H., Diemand, J., & Wadsley, J. 2011, ApJ, 738, 39

Stinson, G. S., Brook, C., Prochaska, J. X., Hennawi, J., Shen, S., Wadsley, J., Pontzen, A., Couchman, H. M. P., Quinn, T., Macciò, A. V., & Gibson, B. K. 2012, MNRAS, 425, 1270

Stocke, J. T., Keeney, B. A., Danforth, C. W., Shull, J. M., Froning, C. S., Green, J. C., Penton, S. V., & Savage, B. D. 2013, ApJ, 763, 148

Stocke, J. T., Penton, S. V., Danforth, C. W., Shull, J. M., Tumlinson, J., & McLin, K. M. 2006, ApJ, 641, 217

Strickland, D. K., Heckman, T. M., Colbert, E. J. M., Hoopes, C. G., & Weaver, K. A. 2004a, ApJS, 151, 193

—. 2004b, ApJ, 606, 829

Suresh, J., Bird, S., Vogelsberger, M., Genel, S., Torrey, P., Sijacki, D., Springel, V., & Hernquist, L. 2015, MNRAS, 448, 895

Tacconi, L. J., Genzel, R., Neri, R., Cox, P., Cooper, M. C., Shapiro, K., Bolatto, A., Bouché, N., Bournaud, F., Burkert, A., Combes, F., Comerford, J., Davis, M., Schreiber, N. M. F., Garcia-Burillo, S., Gracia-Carpio, J., Lutz, D., Naab, T., Omont, A., Shapley, A., Sternberg, A., & Weiner, B. 2010, Nature, 463, 781

Tenorio-Tagle, G., Muñoz-Tuñón, C., Pérez, E., Maíz-Apellániz, J., & Medina-Tanco, G. 2000, ApJ, 541, 720

Thilker, D. A., Braun, R., Walterbos, R. A. M., Corbelli, E., Lockman, F. J., Murphy, E., & Maddalena, R. 2004, ApJL, 601, L39

Thom, C. & Chen, H.-W. 2008, ApJ, 683, 22

Thom, C., Putman, M. E., Gibson, B. K., Christlieb, N., Flynn, C., Beers, T. C., Wilhelm, R., & Lee, Y. S. 2006, ApJL, 638, L97

Tollerud, E. J., Boylan-Kolchin, M., Barton, E. J., Bullock, J. S., & Trinh, C. Q. 2011, ApJ, 738, 102

Torres-Dodgen, A. V. & Massey, P. 1988, AJ, 96, 1076

Tremonti, C. A., Heckman, T. M., Kauffmann, G., Brinchmann, J., Charlot, S., White, S. D. M., Seibert, M., Peng, E. W., Schlegel, D. J., Uomoto, A., Fukugita, M., & Brinkmann, J. 2004, ApJ, 613, 898

Tripp, T. M., Wakker, B. P., Jenkins, E. B., Bowers, C. W., Danks, A. C., Green, R. F., Heap, S. R., Joseph, C. L., Kaiser, M. E., Linsky, J. L., & Woodgate, B. E. 2003, AJ, 125, 3122

Tumlinson, J., Peeples, M. S., & Werk, J. K. 2017, ARA&A, 55, 389

Tumlinson, J., Shull, J. M., Rachford, B. L., Browning, M. K., Snow, T. P., Fullerton, A. W., Jenkins, E. B., Savage, B. D., Crowther, P. A., Moos, H. W., Sembach, K. R., Sonneborn, G., & York, D. G. 2002, ApJ, 566, 857

Tumlinson, J., Thom, C., Werk, J. K., Prochaska, J. X., Tripp, T. M., Katz, N., Davé, R., Oppenheimer, B. D., Meiring, J. D., Ford, A. B., O'Meara, J. M., Peeples, M. S., Sembach, K. R., & Weinberg, D. H. 2013, ApJ, 777, 59

Tumlinson, J., Thom, C., Werk, J. K., Prochaska, J. X., Tripp, T. M., Weinberg, D. H., Peeples, M. S., O'Meara, J. M., Oppenheimer, B. D., Meiring, J. D., Katz, N. S., Davé, R., Ford, A. B., & Sembach, K. R. 2011, Science, 334, 948

Turk, M. J., Smith, B. D., Oishi, J. S., Skory, S., Skillman, S. W., Abel, T., & Norman, M. L. 2011, ApJS, 192, 9

Turner, D. G. 1982, in IAU Symposium, Vol. 99, Wolf-Rayet Stars: Observations, Physics, Evolution, ed. C. W. H. De Loore & A. J. Willis, 57–60

Turner, M. L., Schaye, J., Steidel, C. C., Rudie, G. C., & Strom, A. L. 2015, MNRAS, 450, 2067

Úbeda, L. & Drissen, L. 2009, MNRAS, 394, 1847

van der Marel, R. P., Fardal, M., Besla, G., Beaton, R. L., Sohn, S. T., Anderson, J., Brown, T., & Guhathakurta, P. 2012, ApJ, 753, 8

van der Marel, R. P. & Guhathakurta, P. 2008, ApJ, 678, 187

van Woerden, H., Wakker, B. P., Schwarz, U. J., & de Boer, K. S., eds. 2004, Astrophysics and Space Science Library, Vol. 312, High Velocity Clouds

Wakker, B. P. 1991a, A&A, 250, 499

Wakker, B. P. 1991b, in IAU Symposium, Vol. 144, The Interstellar Disk-Halo Connection in Galaxies, ed. H. Bloemen, 27–40

—. 2001, ApJS, 136, 463

Wakker, B. P. 2004, in Astrophysics and Space Science Library, Vol. 312, High Velocity Clouds, ed. H. van Woerden, B. P. Wakker, U. J. Schwarz, & K. S. de Boer, 25

Wakker, B. P., Hernandez, A. K., French, D. M., Kim, T.-S., Oppenheimer, B. D., & Savage, B. D. 2015, ApJ, 814, 40

Wakker, B. P., Kalberla, P. M. W., van Woerden, H., de Boer, K. S., & Putman, M. E. 2001, ApJS, 136, 537

Wakker, B. P. & Savage, B. D. 2009, ApJS, 182, 378

Wakker, B. P., Savage, B. D., Fox, A. J., Benjamin, R. A., & Shapiro, P. R. 2012, ApJ, 749, 157

Wakker, B. P. & van Woerden, H. 1991, A&A, 250, 509

—. 1997, ARA&A, 35, 217

Wakker, B. P., York, D. G., Wilhelm, R., Barentine, J. C., Richter, P., Beers, T. C., Ivezić, Ž., & Howk, J. C. 2008, ApJ, 672, 298

Walter, F., Weiss, A., & Scoville, N. 2002, ApJL, 580, L21

Wegner, W. 1994, MNRAS, 270, 229

Weiner, B. J., Coil, A. L., Prochaska, J. X., Newman, J. A., Cooper, M. C., Bundy, K., Conselice, C. J., Dutton, A. A., Faber, S. M., Koo, D. C., Lotz, J. M., Rieke, G. H., & Rubin, K. H. R. 2009, ApJ, 692, 187

Welsh, B. Y. & Lallement, R. 2013, PASP, 125, 1455

Welsh, B. Y., Wheatley, J., & Lallement, R. 2009, PASP, 121, 606

Welty, D. E., Xue, R., & Wong, T. 2012, ApJ, 745, 173

Werk, J. K., Prochaska, J. X., Cantalupo, S., Fox, A. J., Oppenheimer, B., Tumlinson, J., Tripp, T. M., Lehner, N., & McQuinn, M. 2016, ApJ, 833, 54

Werk, J. K., Prochaska, J. X., Thom, C., Tumlinson, J., Tripp, T. M., O'Meara, J. M., & Meiring, J. D. 2012, ApJS, 198, 3

Werk, J. K., Prochaska, J. X., Thom, C., Tumlinson, J., Tripp, T. M., O'Meara, J. M., & Peeples, M. S. 2013, ApJS, 204, 17

Werk, J. K., Prochaska, J. X., Tumlinson, J., Peeples, M. S., Tripp, T. M., Fox, A. J., Lehner, N., Thom, C., O'Meara, J. M., Ford, A. B., Bordoloi, R., Katz, N., Tejos, N., Oppenheimer, B. D., Davé, R., & Weinberg, D. H. 2014, ArXiv e-prints

Wisotzki, L., Bacon, R., Blaizot, J., Brinchmann, J., Herenz, E. C., Schaye, J., Bouché, N., Cantalupo, S., Contini, T., Carollo, C. M., Caruana, J., Courbot, J.-B., Emsellem, E., Kamann, S., Kerutt, J., Leclercq, F., Lilly, S. J., Patrício, V., Sandin, C., Steinmetz, M., Straka, L. A., Urrutia, T., Verhamme, A., Weilbacher, P. M., & Wendt, M. 2016, A&A, 587, A98

Wolfe, A. M., Gawiser, E., & Prochaska, J. X. 2005, ARA&A, 43, 861

Wolfe, S. A., Lockman, F. J., & Pisano, D. J. 2016, ApJ, 816, 81

Wright, M. C. H. 1974, A&A, 31, 317

—. 1979, ApJ, 233, 35

Zheng, Y., Peek, J. E., Werk, J. K., & Putman, M. E. 2016, Coadded spectra supplement to this work

Zheng, Y., Putman, M. E., Peek, J. E. G., & Joung, M. R. 2015, ApJ, 807, 103

Zheng, Y., Werk, J. K., Peek, J. E. G., & Putman, M. E. 2017, ApJ, 840, 65

Zhu, G. & Ménard, B. 2013, ApJ, 770, 130

Appendix A - Properties of Saturated Ions

Here we show the properties of ions C II, Si II, and Si III that have saturated absorption-line profiles, which we did not discuss in details in Chapter 5. Figure 1 shows the continuum-normalized line profiles. The portion of the absorption lines associated with M33's ISM is highlighted in gray shade based on visual inspection. The high degree of saturation limits our ability to discern the underlying individual kinematic structures, thus we do not attempt to decompose the M33 absorption lines. Instead, we apply the apparent optical depth (AOD) method (Savage & Sembach 1991, 1996) to calculate the column densities of C II, Si II, and Si III that are associated with M33.

The AOD method converts the observed absorption profiles into apparent column density as a function of velocity $N_{\rm a}(v)$, which can be expressed as,

$$N_{\rm a}(v) = 3.768 \times 10^{14} \tau_{\rm a}(v) / [f\lambda(\text{Å})], \tag{1}$$

where f and λ are the oscillator strength and wavelength of the line of interest respectively, and $\tau_{\rm a}(v)$ is the apparent optical depth. For continuum-normalized absorption-line profiles, the apparent optical depth can be calculated as,

$$\tau_{\rm a}(v) = -\ln[I_{\rm obs}(v)/I_{\rm o}(v)], \tag{2}$$

where $I_{\rm o}(v) = 1$ is the continuum intensity and $I_{\rm obs}(v)$ is the strength of the absorption lines. The total column density within a certain velocity range $[v_{\rm min}, v_{\rm max}]$ is $N_{\rm a}(v) = \int_{v_{\rm min}}^{v_{\rm max}} N_{\rm a}(v) dv$.

Table 1: AODM: Saturated Ions

	v_{min}, v_{max} (km s^{-1})	log N_{CII}[a] (cm^{-2})	log N_{SiII}[a] (cm^{-2})	log N_{SiIII}[a] (cm^{-2})
S1	-100, 100	>15.13	>14.98	>14.11
S2	-60, 140	>15.17	>15.02	>14.02
S3	-100, 120	>15.24	>14.85	>14.12
S4	-80, 100	>14.93	>14.85	>13.92
S5	-80, 140	>15.28	>14.98	>14.25
S6	-80, 80	-[b]	>14.97	-
S7	-80, 70	>14.75	>14.62	>13.79

[a]Since the absorption lines are all saturated, these column densities represent the lower limit. C II column density is calculated using C II λ1334, Si II column density is calculated using Si II λ1304 which is the weakest line with the least saturation among other Si II lines, and Si III column density is from Si III λ1206.
[b]See Appendix 6 for explanation of omitting C II and Si III along S6.

Since the C II, Si II, and Si III absorption lines are strongly saturated, here the AOD method only provide lower limits of the ion column densities, which are shown in Table 1.

In addition to the saturated M33 and MW absorption lines, we find an $v_{LSR} \sim -350$ km s^{-1} ($-200 \lesssim v_d \lesssim -100$ km s^{-1}) absorption feature that is commonly present in C II, Si II, and Si III lines. Please see § 5.7.3.2 for the discussion of the potential origins of this feature.

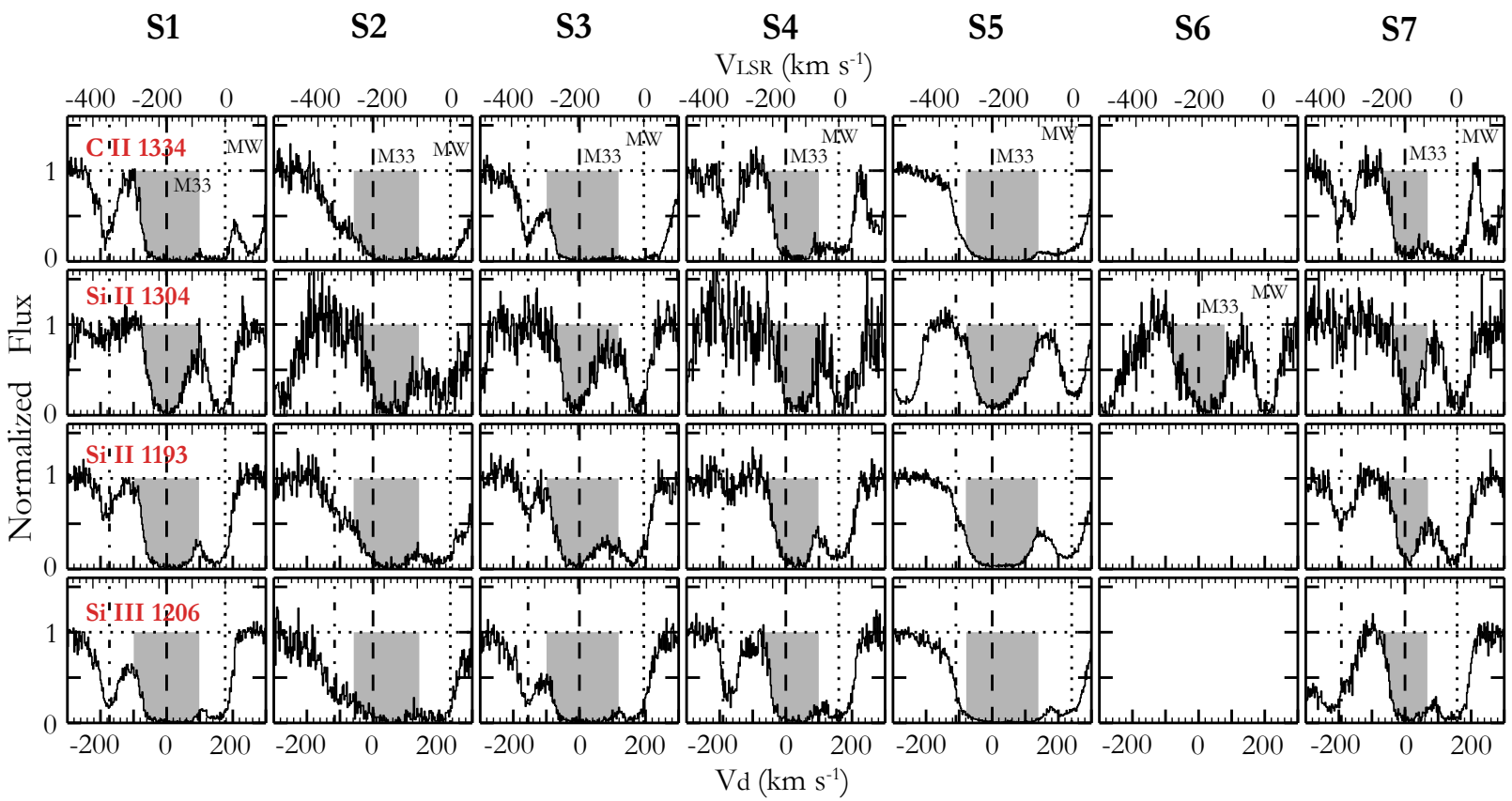

Figure 1: The continuum-normalized *HST*/COS spectra of C II λ1334, Si II $\lambda\lambda$1304, 1193, and Si III λ1206. Velocity on the bottom X axis is shown with respect to the gas disk of M33 at the position of each sightline. The velocity on the top X axis is shown in the LSR frame. The vertical dashed line show the $v_{\rm d}$ = 0 km s^{-1}, which is the systemic velocity of the M33 disk at the position of the corresponding sightline. The dotted line around $v_{\rm d} > +150$ km s^{-1} ($v_{\rm LSR}$ = 0 km s^{-1}) shows the MW absorption, while the dash-dotted line at $v_{\rm d} \sim -200$ km s^{-1} ($v_{\rm LSR} = -350$ km s^{-1}) indicates the negative high-velocity absorption that is discussed in § 5.7.3. The highlighted gray shades show the velocity ranges we use to calculate the M33-associated ion column density via the AOD method. Note that we do not attempt to normalize the C II, Si II, and Si III spectra of S6 (except for Si II λ1304) since they are strongly affected by stellar lines.

Appendix B - CalCOS V.S. Other Spectral Co-addition Pipelines

As mentioned in § 5.2.2, CalCOS pipeline yields an uncertainty in the wavelength solution of 14 – 19 km s^{-1}. Other spectral calibration and co-addition routines exist to minimize this wavelength uncertainty. To ensure that CalCOS products are reliable for our scientific analysis, we use three other pipelines to process the original raw *HST*/COS spectra and compare the results with that of CalCOS (version 3.0). The three pipelines are 1) x1d_coadd.pro by Danforth et al. (2010), 2) a co-add code by Wakker et al. (2015) and 3) the PyCOS pipeline by Liang & Chen (2014) (& private communication). All the coadded spectra processed by these three methods can be found in Zheng et al. (2016, Dataset: `https://doi.org/10.5281/zenodo.168580`)

First we use x1d_coadd.pro (Danforth et al. 2010) to process the spectral co-adding for each of our seven sightlines. Since each sightline has four exposures, the program randomly chooses one exposure as a wavelength reference while the others are cross-correlated with it using strong ISM absorption lines over a 10 Å spectral region. The code assumes a constant wavelength offset within the whole wavelength coverage. The final flux array is exposure-weighted average and the error array is exposure-weighted inverse invariance average. In Figure 2, we compare the co-added lines for S7 using this program with those from CalCOS. Good agreement is reached between the x1d_coadd.pro-processed spectra and CalCOS products. Similar results are found for other sightlines. In the most extreme case, a $\sim$ 10 km s^{-1} offset is seen in S4.

B.P. Wakker kindly processed the raw spectra of S7 using his co-addition pipeline (Wakker et al. 2015) and provided us the final co-added product for comparison. His code is similar to x1d_coadd.pro (Danforth et al. 2010) except that it cross-correlates all

available strong ISM and IGM lines and applies relative offset for each individual line while Danforth et al. (2010) assumes a constant shift for all the lines. The code aligns weakly-ionized ISM metal lines with the corresponding MW H I 21 cm emission lines retrieved from the LAB survey (Kalberla et al. 2005). We show the co-added spectra in Figure 2. Good alignment is found between CalCOS spectra and those by Wakker et al. (2015) except that Si IV $\lambda\lambda$1393, 1402 show a $\sim$ 10 km s^{-1} displacement, which is less than one resolution element. In addition, the error array from his program is also consistent with that from CalCOS.

Thirdly, we process the raw *HST*/COS data using the PyCOS pipeline developed by Liang & Chen (2014) (& private communication). PyCOS provides a user-friendly interface with which one could process spectral alignment for individual lines interactively. The performance of line alignment is based on visual judgement and χ^2 estimates. We use PyCOS to align and co-add the spectra, and also find good agreement between the PyCOS spectrum and the CalCOS one, as is shown in Figure 2.

In all, our investigation shows a consistent result that the CalCOS pipeline provides reliable spectra for our scientific analysis. We have noted in § 5.2.3 that such good agreement between CalCOS and the other three pipelines is mainly due to the simple setup of our observations. For each of our sightlines, the observation was completed with four exposures in one single visit and the spectra were taken under the same setting. The background stars are all bright to ensure high S/N. Thus the possibility of spectral miss-alignment is largely reduced. CalCOS pipeline is most likely to become problematic in the case of faint QSO observations and that the spectra are taken at different epochs.

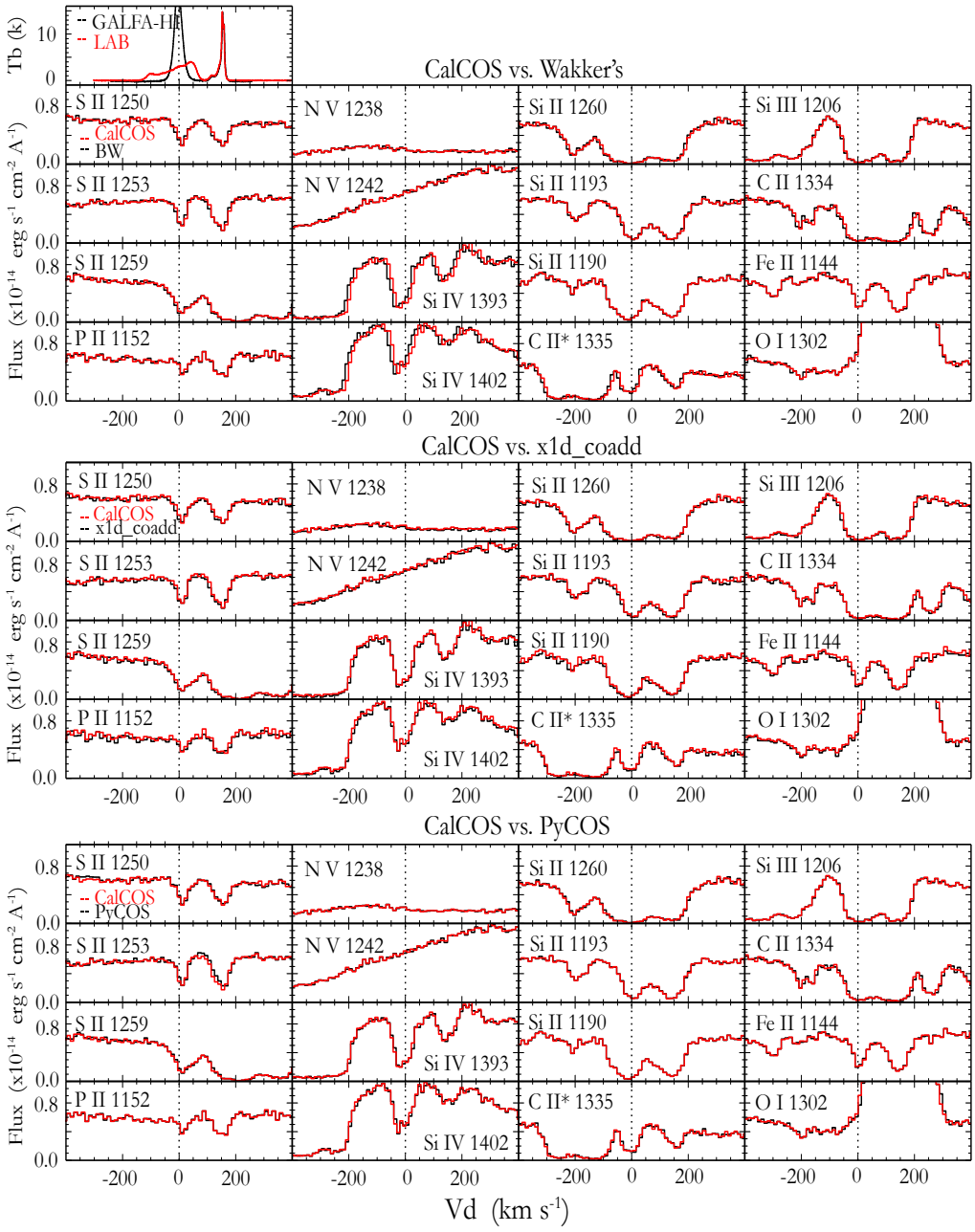

Figure 2: Comparison of spectral alignment and co-addition results of S7 between CalCOS (red) and the other three pipelines (black) developed by Wakker et al. (2015) (top), Danforth et al. (2010) (middle) and C. Liang & H.W. Chen (private communication; bottom), respectively. The panel on the top row shows the H I 21-cm spectrum from the LAB (red; Kalberla et al. 2005) and the GALFA-H I (black; Peek et al. 2011). The velocity on the x axis is with respective to the rotation velocity of the gas disk at the position of S7. Note that all the absorption lines are not continuum-normalized.

Appendix C - Continuum Fitting and Voigt-Profile Fitting

Here we show the continuum fitting for the COS spectra displayed in § 5.2.1. We show the result of each line for each target in Figures 3–6. Most lines have good S/N, thus their continuum fitting and Voigt-profile fitting are straightforward. The f-scaled profiles in the right panels of Figures 3–6 show that the continuum fitting of most non-saturated lines are consistent, while some lines do show non-matching f-scaled profiles that we explain as follows:

1. Along all the sightlines the f-scaled profiles of Fe II λ1143 is stronger than it is supposed to be due to the blending with the Fe II λ 1142 from the MW.

2. For S1, the f-scaled profiles of Si IV $\lambda\lambda$ 1393, 1402 lines do not match perfectly because Si IV λ 1393 may be slightly saturated.

3. For the triplets S II $\lambda\lambda\lambda$1250, 1253, 1259, we only use the first two lines for f-scaled matching since S II λ1259 is severely blended with the $v_{\rm LSR} \sim -350$ km s^{-1} feature from Si II λ1260 as mentioned in Appendix 6 and 5.7.3.1. We do not include S II λ1259 in our analysis.

4. For sightline S6, we do not perform continuum fitting for C II λ1334, Si II $\lambda\lambda$1190, 1193 and Si III λ 1206. These lines are affected by strong P Cgyni profiles due to stellar activities. We show the original spectra of these lines in the bottom panel of Figure 5. The continuum peaks at $v_{\rm d} \sim 300$ km s^{-1} in these lines are likely to be the emission components of the corresponding P Cygni profiles. These emission peaks can be clearly seen in panel 6 of Figure 5.2.

In Figure 7, we show all the non-saturated and saturated lines that were observed in our program. These includes those triplets and doublets that we do not show in Figure 5.3 and 1 for better illustration. In the following, we lay out the details of treatment of Voigt-profile fitting to some specific lines that we do not address in the previous sections:

1. On S3 and S4, the M33 Fe II λ1143 is blended with the MW Fe II λ1142, so a nuisance component is added to the Voigt-profile fitting.

2. On S4, the M33 Fe II λ1144 is blended with the MW Fe II λ1143, so a nuisance component is added.

3. On S6, the P II λ1152 has no detection, thus we do not apply Voigt-profile fitting to this line.

4. On all the sightlines S II λ1259 is blended with a $v_{\rm LSR} \sim -350$ km s^{-1} feature from Si II λ1260, thus we do not include this line in our analysis. For some sightlines when the blending is less severe, we manage to fit Vogit-profile components to this line simultaneously with S II $\lambda\lambda$1250, 1253.

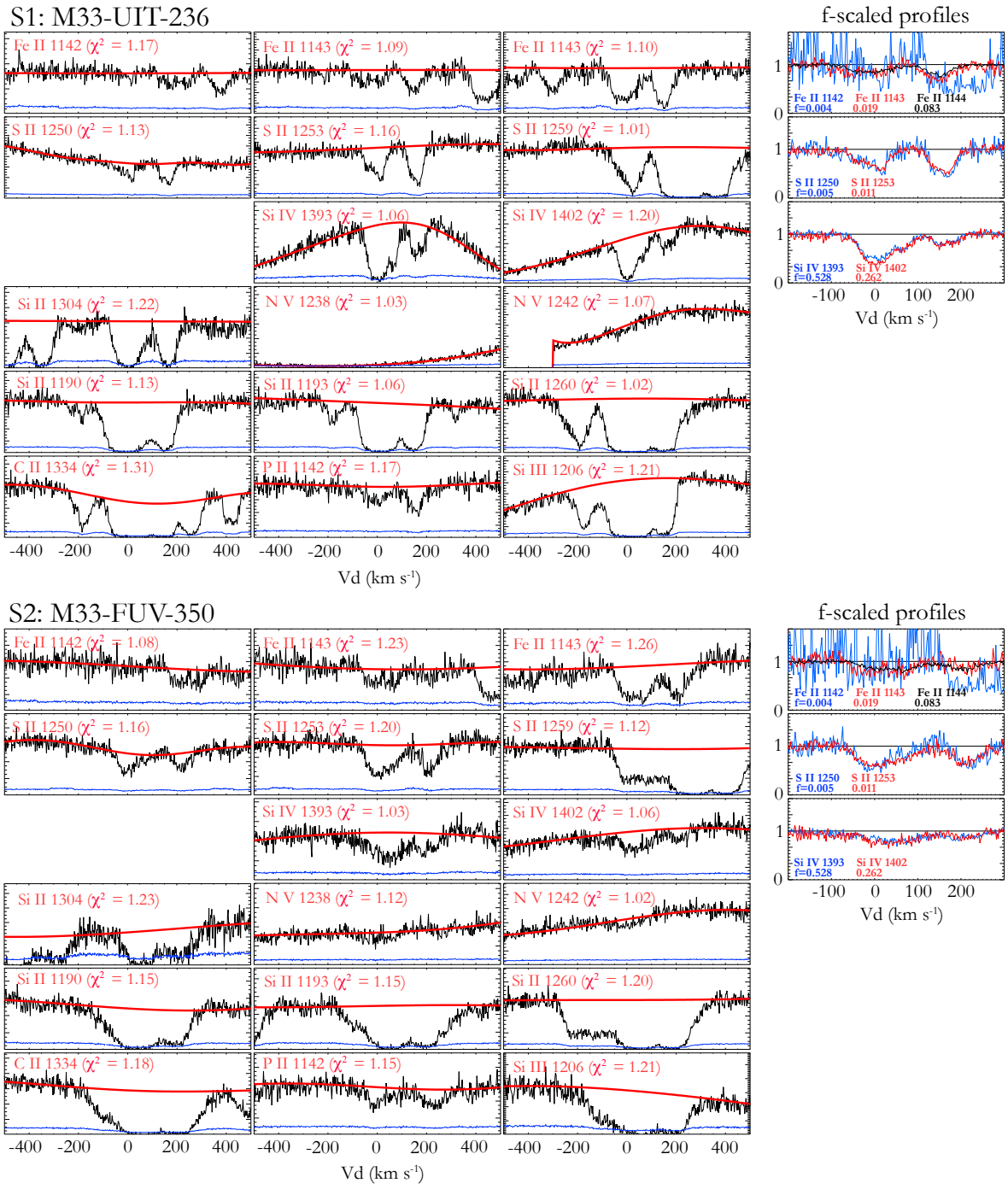

Figure 3: Continuum fiting and f-scaled profiles of S1 (top) and S2 (bottom). The first three columns show the continuum fitting of each line, with black representing the original data, red for the fitted continuum and blue for the error. The right panels show the f-scaled profiles of Fe II, S II, and Si IV, respectively.

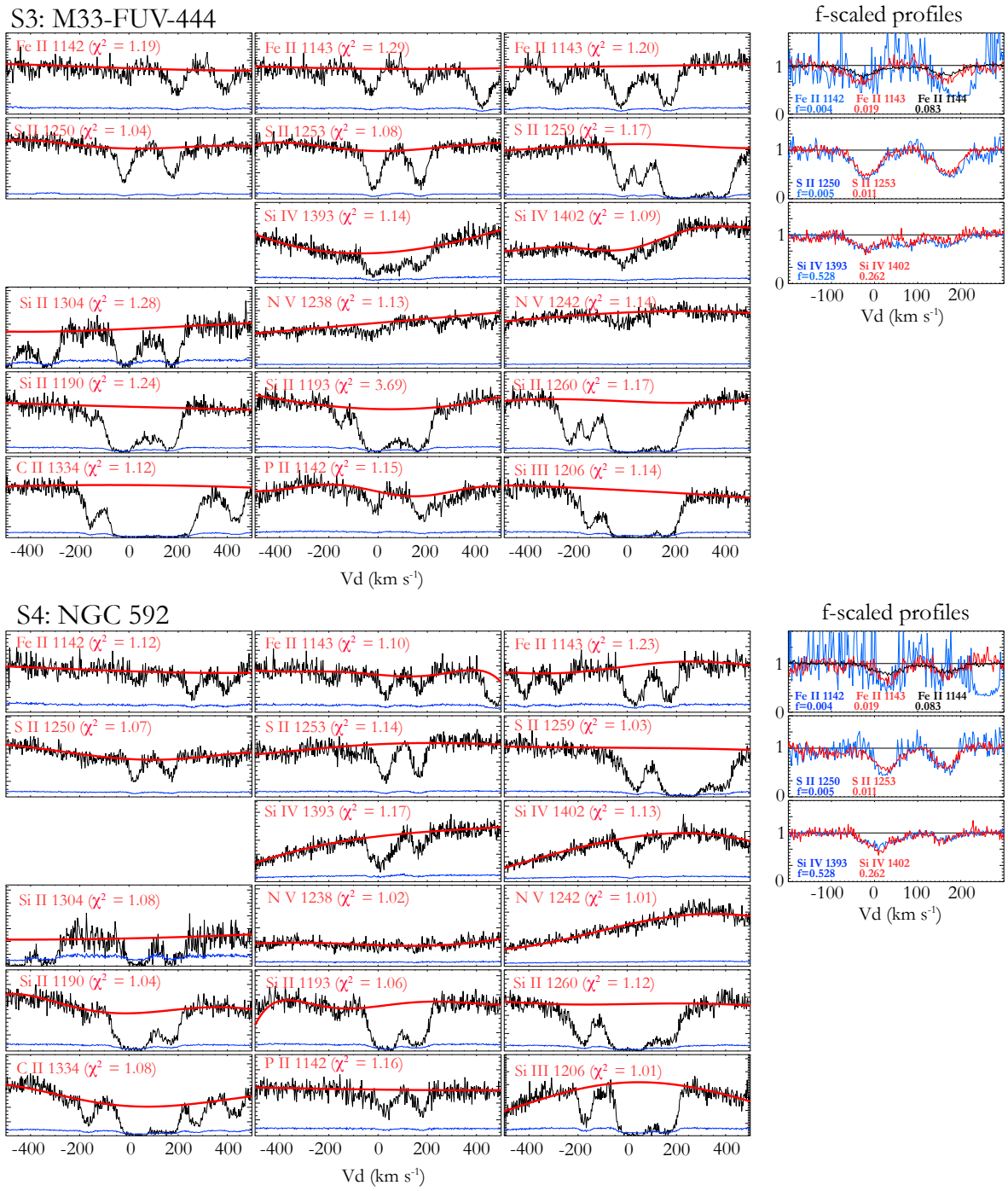

Figure 4: Continuum fiting and f-scaled profiles of sightline S3 (top) and S4 (bottom). See Figure 3 for layout explanation.

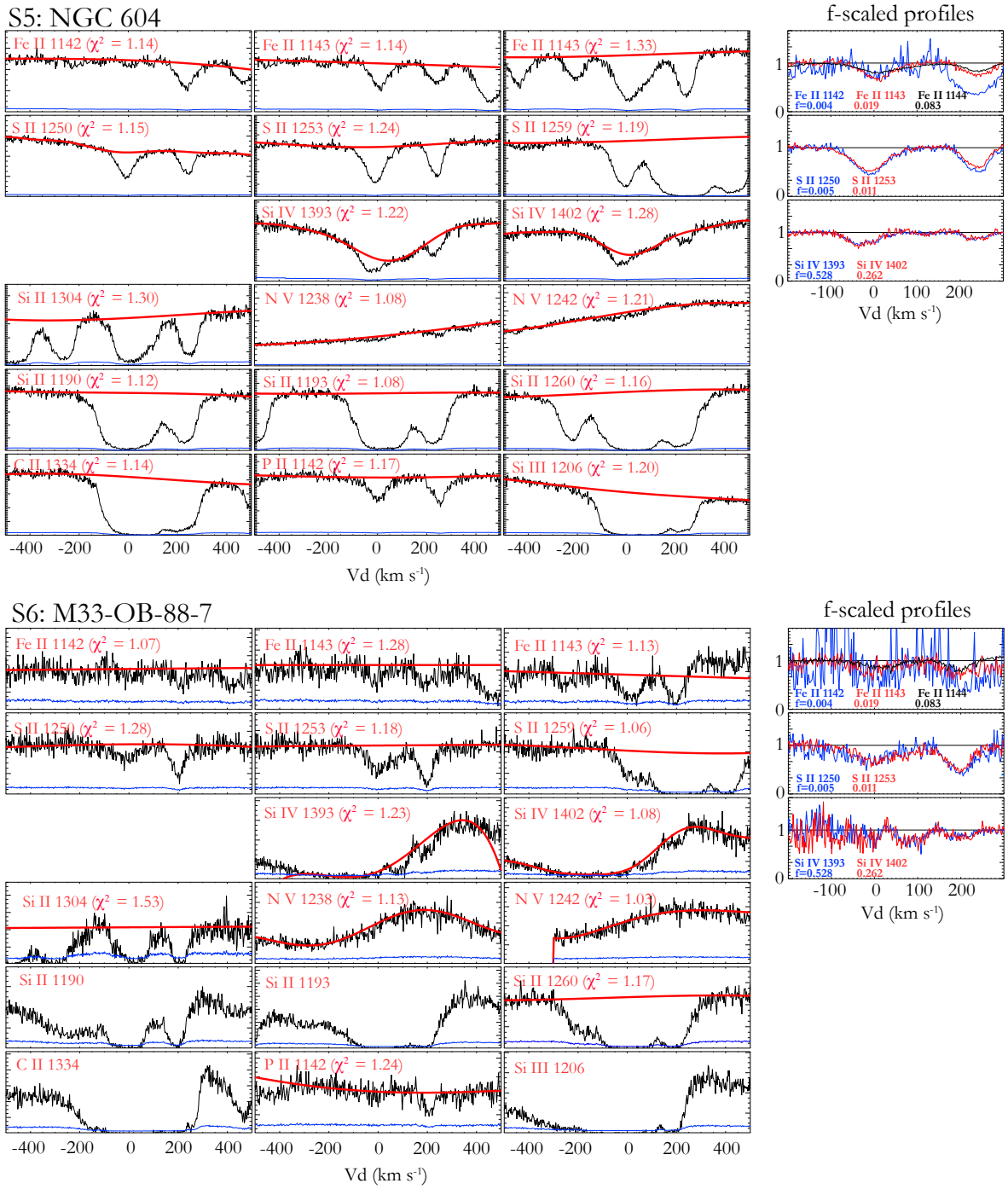

Figure 5: Continuum fiting and f-scaled profiles of sightline S5 (top) and S6 (bottom). See Figure 3 for layout explanation. In S6, C II λ1334, Si II $\lambda\lambda$1190, 1193, and Si III λ1206 are not fitted since they are strongly affected by stellar P Cygni profiles. See Appendix 6 for detailed explanation.

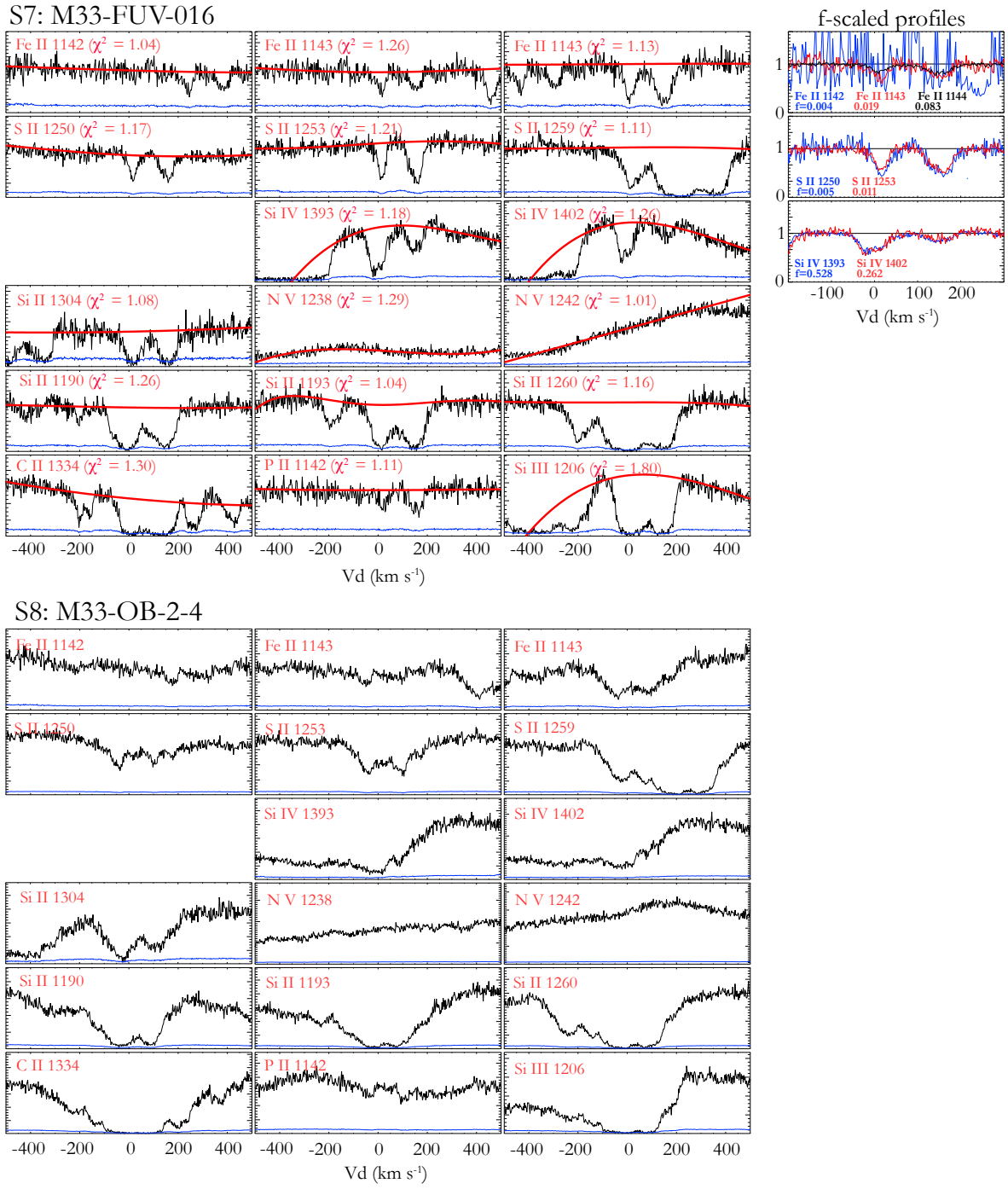

Figure 6: Continuum fiting and f-scaled profiles of sightline S7 (top). See Figure 3 for layout explanation. S8 is not used in our analysis. Here we show the original profile of each line to indicate the great uncertainity of the continuum fitting due to strong stellar activities. Please see § 5.2.1 for discussion of this sightline.

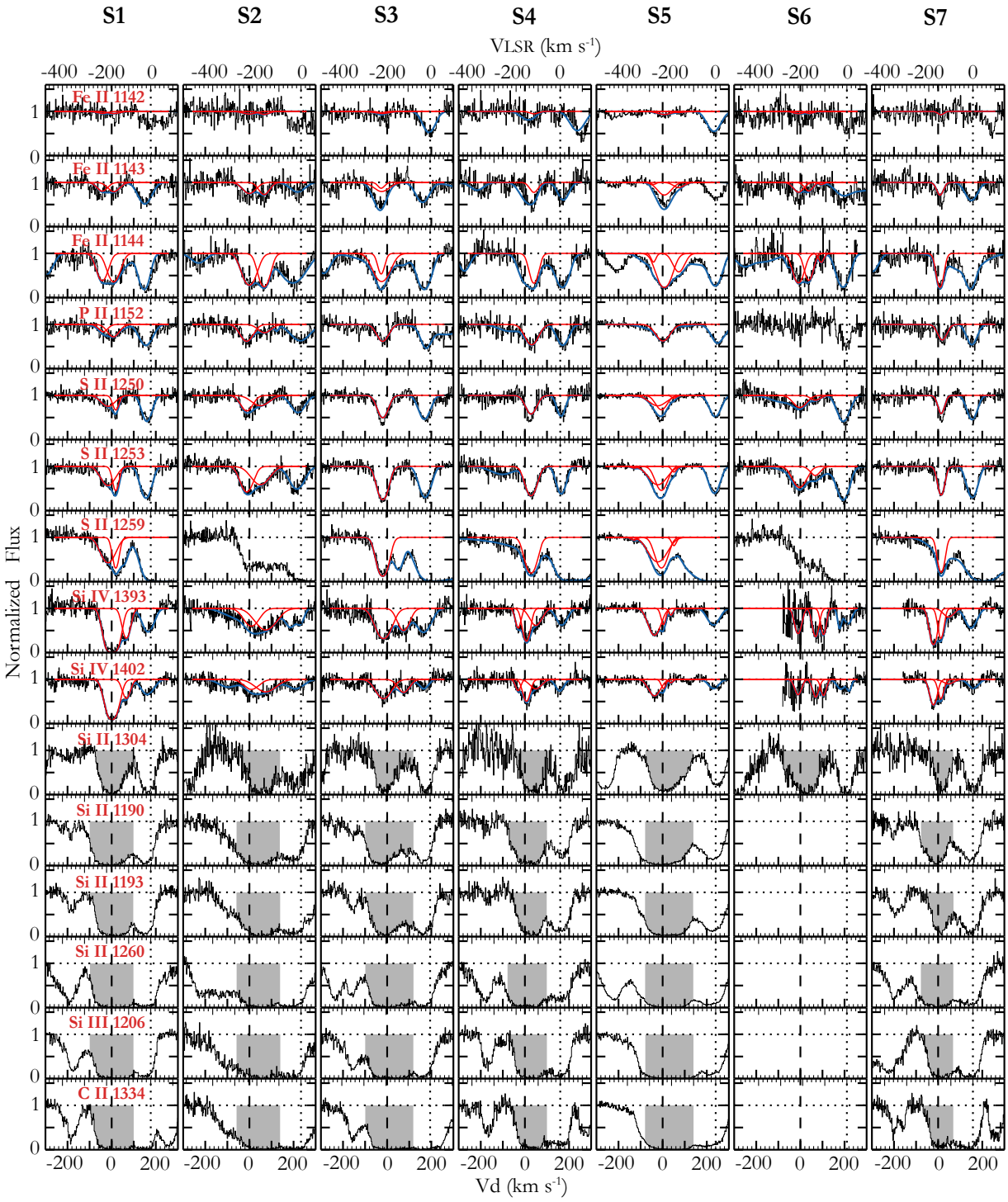

Figure 7: Continuum-normalized spectra and Voigt-profile fitting for all the lines. M33's ISM absorption is shown by dashed line ($v_{\rm d}$ = 0 km s^{-1}), and the MW's absorption is shown by dotted line ($v_{\rm LSR}$ = 0 km s^{-1}). The red curves indicate the Voigt-profile fits, and the blue curves show the overall fitting, including the sum of the red curves and the additional nuisance components (Appendix 6). Gray shades indicate the integrated velocity range used in Appendix 6.